DEVELOPMENT and VALIDATION of a DISCRETE PARTICLE MODEL of a SPOUT-FLUID BED GRANULATOR

Samenstelling promotiecommissie:

Prof. dr. ir. A. Bliek, voorzitter	Universiteit Twente
Prof. dr. ir. J.A.M. Kuipers, promotor	Universiteit Twente
Dr. ir. N.G. Deen, assistent-promotor	Universiteit Twente
Jun.-Prof. Dr.-Ing. S. Heinrich	Universität Magdeburg
Prof. dr. D. Lohse	Universiteit Twente
Prof. dr. ir. G.F. Versteeg	Universiteit Twente
Prof. dr. ir. M.M.C.G. Warmoeskerken	Universiteit Twente
Dr. ir. N.P. Kruyt	Universiteit Twente
Ing. L. Vanmarcke	Yara Technology Centre Sluiskil

The research reported in this thesis was funded by Senter Novem and Yara Technology Centre Sluiskil, and was carried out within BTS project 99162, entitled, ”Fluid Bed Granulatie”.

Publisher: PrintPartners Ipskamp B.V., P.O. Box 333, 7500 AH Enschede, The Netherlands

Link, J. M.
Development and validation of a discrete particle model of a spout-fluid bed granulator
PhD thesis, University of Twente, The Netherlands
ISBN: 90-365-2371-0

DEVELOPMENT AND VALIDATION OF A DISCRETE PARTICLE MODEL OF A SPOUT-FLUID BED GRANULATOR

PROEFSCHRIFT

ter verkrijging van
de graad van doctor aan de Universiteit Twente,
op gezag van de rector magnificus,
prof. dr. W.H.M. Zijm,
volgens besluit van het College van Promoties
in het openbaar te verdedigen
op vrijdag 19 mei 2006 om 16.45 uur

door

Jeroen Martijn Link

geboren op 11 november 1975
te Zevenaar

Dit proefschrift is goedgekeurd door de promotor

Prof. dr. ir. J.A.M. Kuipers

en de assistent-promotor

Dr. ir. N.G. Deen

Aan mijn ouders

Contents

Summary

Spout-fluid beds find a widespread application in the process industry for efficient contacting of large particles with a gas. Since the spout-fluid bed configuration allows for the introduction of a liquid, spout-fluid beds are used for both coating and granulation applications, for example in the fertilizer industry. In this application, the spout-fluid bed has the advantage of producing strong granules over a wide range of particle sizes. However, the particle size distribution obtained in spout-fluid beds can be relatively wide resulting in large recycling requirements.

The objective of this thesis is to improve the control over the particle size distribution resulting from spout-fluid bed granulation by gaining insight into the underlying fundamental processes. As detailed experiments in operating granulators are virtually impossible, it was decided to adopt a modeling approach. Since the flow behavior inside the spout-fluid bed was considered to be most critical, the modeling efforts were focused on the hydrodynamics.

The discrete particle model (DPM) was considered to be the most suitable model to describe the hydrodynamics inside a spout-fluid bed, because the relevant closures for this model are available and it has been successfully applied to regular (bubbling) fluidized beds. The DPM uses the volume-averaged Navier-Stokes equations to compute the flow of the gas, while the interaction between the gas phase and the particles is described using drag closures, three of which are assessed in this thesis. The interaction between the particles is treated using collision models, two of which are used in this thesis.
The functionality of the DPM was improved by introducing a new treatment for the inter-phase coupling, which is independent of the computational grid. This treatment allows the computational grid to reach the level of refinement that is required to treat the large velocity gradients that are present in the vicinity of the spout.

In order to validate the computational model, several experimental techniques have been developed and used to map the behavior of the spout-fluid bed and to supply the necessary experimental data.
The dynamic behavior of the bed was captured in a non-intrusive manner using spectral analysis of the pressure drop fluctuations. The characteristics of the dynamic behavior are obtained by applying a Fourier transformation to a recording of the

fluctuations of the pressure drop over the entire bed. The result of this transformation is rendered into a frequency spectrum, which characterizes the dynamic behavior of the bed.
Several non-intrusive whole-field measuring techniques were employed to record the flow of the particles inside the spout-fluid bed. With positron emission particle tracking (PEPT) three-dimensional particle trajectories were obtained, which were transformed into time-averaged particle velocity fields. With particle image velocimetry (PIV) two-dimensional velocity fields were obtained from digital images. The light intensity levels of these digital images were used to obtain particle concentration fields, which were subsequently combined with the particle velocity fields to calculate particle flux fields.

To facilitate the selection of operating conditions for the validation procedure, the flow regimes in the spout-fluid bed were mapped using spectral analysis of pressure drop fluctuations. Six flow regimes were discerned, the behavior of which is described in detail and illustrated with snapshots and frequency spectra. The manner in which the flow regimes depend on the spout and background velocity was mapped based on the shape and frequency of the characteristic frequency peak(s) in the frequency spectra.
By comparing the results obtained for different geometries, particle size distributions, and particle properties, it was found that these properties have a profound influence on the flow regime map, especially on the exact location of the boundaries between the flow regimes. The distribution of the flow regimes over the regime map however was not affected. It can therefore be concluded that the flow regime map of a spout-fluid bed is not exclusively determined by the spout and background velocities.

The flow regime maps obtained for the pseudo-2D set-up were subsequently used to select operating conditions in different flow regimes for the validation procedure. For the selected cases time-averaged particle flux profiles and pressure drop fluctuations were recorded and computed.
By comparing the time-averaged results from simulations with different initial conditions, the reproducibility of the model results was established.
Simulations with different collision models proved that the spring stiffness was chosen sufficiently large to prevent it from affecting the simulation results of the soft-sphere model. Furthermore, for this value of the spring stiffness the results obtained with the hard and soft sphere model are virtually identical, indicating that the models are interchangeable.
The new treatment of the inter-phase coupling was verified using simulations of a packed bed and a single particle. The results obtained with the new treatment proved

to be independent of the computational grid. Furthermore they resembled the theoretical solution to a significantly larger degree than the results obtained with the conventional method, especially when the grid was refined. Based on the simulation results, a value of 5 is proposed for the ratio between the mapping window and particle diameter. This value is considered to be sufficiently small to capture the details of the flow, while being sufficiently large to reduce the offset to an acceptable level.

Using the new treatment of the inter-phase coupling the grid dependence of the model was assessed in a pseudo-2D set-up. The pressure drop fluctuations, the time-averaged particle flux and the time-averaged gas velocity for different operating regimes showed that even in a system where the width of the spout channel is 10 mm, a numerical grid size of 10 mm (i.e. 4 times the particle diameter) is sufficiently small to obtain grid independent results.

In the pseudo-2D set-up, several drag closures were tested in the DPM to assess their suitability regarding spout-fluid beds. For this purpose, the time-averaged particle flux and the pressure drop fluctuations have been compared with experimental results for different operating regimes. It was found that the most frequently used drag model (i.e. the Ergun equation (1952) for low porosities, and the Wen and Yu relation (1966) for high porosities) produces unsatisfactory results for fluid beds with stable high velocity jets, as encountered in spout(-fluid) beds. The usage of the minimum of the drag given by the relations of Ergun (1952), and Wen and Yu (1966), as well as the relation proposed by Koch and Hill (2001) improves the predictions of the DPM, although the computed frequency of the pressure drop fluctuations is still somewhat too high. Because of its more fundamental nature the use of the Koch and Hill relation (2001) is to be preferred.

After the model was successfully verified and proper closure relations have been selected, a combined experimental and computational study of the various regimes that are typically encountered in spout-fluid bed operation was conducted.

A regime map for a 3D spout-fluid bed was composed employing spectral analysis of pressure drop fluctuations and fast video recordings. In addition, three-dimensional DPM simulations were performed to assess the capability of the model to reproduce the experimentally observed flow regimes.

Spectral analysis of pressure drop fluctuations revealed that for most investigated regimes the model is able to predict the appropriate regime. The frequency, at which the largest power is found, is slightly overpredicted by the model in most cases. Contrary to the experimental observations, the model did not predict any large slugs in the slugging bed regime.

The remaining differences between the simulated and experimentally observed bed behavior are most likely related to the representation of the effective fluid-particle interaction in the model, which relies on a homogeneous distribution of the particles on the length scale that is used to calculate the fluid-particle drag.
The computations were also used to study the particle motion in a 3D spout-fluid bed. Both mono-disperse and bi-disperse systems were investigated. The simulation results were compared with velocity maps determined from particle trajectories acquired using positron emission particle tracking.
The model accurately reproduces measured particle velocities, including their root mean square, for all investigated conditions and is therefore able to capture the details of the particle flow in various flow regimes.
Detailed analysis of the results shows that the model has difficulty predicting the exact shape of the spout channel, which is probably related to the heterogeneity in the solids volume fraction, which was already observed in relation with the pressure drop fluctuations.
A study of the results obtained with the bi-disperse system revealed no difference between the time-averaged particle velocities of the small and large particles, despite the fact that the net force on the small particles, and consequently the acceleration of these particles, is larger. The computed root mean square was generally larger for the small particles, which was not as clearly observed in the experiments. This is probably related to the post-processing method of the experimental results.
The DPM results for a mixture of large and small particles revealed rather small differences between the concentration and flux of large and small particles, although most differences in the particle concentrations disappeared at higher background velocities.
An experimental study of the particle circulation time distribution revealed that it correlates well with the mobility of the particles. Since the jet-in-fluidized-bed regime displays the highest number of particle circulations within a fixed period of time and shows the narrowest particle circulation time distribution, this regime will probably provide the most (homogeneously distributed) growth opportunities in a granulator.

After the model was successfully validated, it was extended to facilitate the description of the droplets in a gas-liquid-solid flow in a spout-fluid bed, including all relevant phenomena for the study of granulation.
The extended model was demonstrated for the case of a granulation process in a flat spout-fluid bed, containing four different initial particle size distributions. For each of the cases it was found that particle growth increases the mean of the particle size distribution, without affecting its standard deviation.

The amount of growth differs significantly for each individual particle and depends strongly on the position of the particle with respect to the nozzle. Particle growth rapidly decreases with increasing distance from the nozzle.

It was found that the growth rate scales with the projected surface area of the particle. Two types of growth have been identified in the simulations, ‘peak growth’ and ‘constant growth’. Peak growth occurs when particles are exposed to droplets over their entire projected surface area. The growth rate for this type of growth is very large, while the period over which this type of growth occurs is very short (< 4 ms), due to the short residence time of the particles in the peak growth region.

Constant growth occurs when only a small fraction of the particle surface is exposed to the droplets, either because of the location of the jet or because other particles are blocking part of its surface. The growth rate for this type of growth is relatively small, but it can be maintained over a longer period than peak growth.

The majority of the growth is caused by constant growth due to the low solids fraction above the nozzle, which is caused by the large drag forces exerted by the gas phase on the particles in this region.

The smaller particles within a mixture of differently sized particles are slightly more likely to display peak growth, which is due to the larger concentration of these particles near the nozzle. In the remainder of the bed all particles display similar growth rates per projected surface area.

For the particle size distributions examined in this work, the ones with a larger average particle size display larger peak growth rates per projected surface area due to longer residence times near the nozzle, which is probably caused by the higher particle inertia.

It can be concluded that the extended discrete particle model can supply valuable information on the growth behavior in a spout-fluid bed. To establish its accuracy, the model results need to be validated by detailed experiments of particle growth within a spout-fluid bed.

Samenvatting

In de procesindustrie worden “spout”-fluïde bedden veelvuldig toegepast om relatief grote (Geldart-D) deeltjes in contact te brengen met een gas. Daarnaast is het relatief eenvoudig om middels atomisatie een vloeistof in “spout”-fluïde bedden te injecteren. Vandaar dat “spout”-fluïde bedden onder andere gebruikt worden voor het coaten en granuleren van materialen, zoals bijvoorbeeld bij de industriële productie van kunstmestgranules. In tegenstelling tot een aantal andere granulatoren kunnen in “spout”-fluïde bedden sterke granules van vrijwel elk formaat geproduceerd worden. Hierbij dient opgemerkt te worden dat “spout”-fluïde bed granulatoren een relatief brede deeltjesgrootteverdeling produceren, waardoor veel materiaal gerecycled moet worden.

Het doel van het onderzoek, dat gepresenteerd wordt in dit proefschrift, is de controle over de groei van de deeltjes, en daarmee de deeltjesgrootteverdeling, in een “spout”-fluïde bed te vergroten door het inzicht in de onderliggende fundamentele principes te verbeteren. Aangezien het in de praktijk vrijwel onmogelijk is om dit inzicht te verkrijgen door middel van experimenten in werkende granulatoren, is er voor gekozen om dit inzicht met behulp van modellen te verkrijgen. Bij de modellering is de nadruk gelegd op het beschrijven van de hydrodynamica, omdat een correcte beschrijving van het stromingsgedrag van cruciaal belang wordt geacht.

Het discrete deeltjes model (DPM) werd het meest geschikt bevonden om de hydrodynamica in een “spout”-fluïde bed te beschrijven, aangezien de relevante sluitingsmodellen voor dit model beschikbaar zijn en omdat het succesvol is toegepast in normale (bubbelende) wervelbedden. In het DPM wordt de stroming van de gasfase berekend aan de hand van de volume-gemiddelde Navier-Stokes vergelijkingen. De interactie tussen de deeltjes en de gasfase wordt beschreven door sluitingsmodellen voor de wrijvingskracht, waarvan er drie in dit proefschrift worden behandeld. De interactie tussen de deeltjes onderling wordt beschreven met behulp van botsingsmodellen, waarvan er in dit proefschrift twee worden gepresenteerd.
De werking van het DPM is verbeterd door de koppeling tussen de fasen op een nieuwe manier te realiseren. Hierdoor is deze koppeling onafhankelijk gemaakt van het tijdens de simulatie gebruikte numerieke rooster. Door deze aanpassing kan het

numerieke rooster voldoende worden verfijnd om de grote snelheidsgradiënten in de nabijheid van de “spout” met voldoende nauwkeurigheid te beschrijven.

Om het numerieke model te valideren zijn er een aantal experimentele technieken ontwikkeld. Deze technieken zijn vervolgens gebruikt om het gedrag van een “spout”-fluïde bed in kaart te brengen en om de voor de validatie benodigde data te genereren.
Het dynamische gedrag van het bed is gekwantificeerd door gebruik te maken van spectraalanalyse van de temporale fluctuaties in de drukval over het gehele bed. Een voordeel van deze meettechniek is dat het dynamische gedrag niet wordt verstoord door de meting zelf. De karakteristieke kenmerken van het dynamische gedrag zijn verkregen door een Fourier transformatie toe te passen op de opgenomen fluctuaties. Om het resultaat van de transformatie inzichtelijker te maken is het omgevormd tot een frequentiespectrum.
Er zijn diverse meettechnieken gebruikt om de stroming van de deeltjes in het “spout”-fluïde bed te bepalen. Deze technieken zijn in staat om in het gehele bed de stroming te bepalen zonder de stroming zelf te verstoren. Driedimensionale trajectoriën van radioactieve deeltjes zijn verkregen met behulp van PEPT (“positron emission particle tracking”). Deze deeltjestrajectoriën zijn vervolgens omgezet in een tijdsgemiddeld snelheidsveld. Met behulp van PIV (“particle image velocimetry”) is uit digitale beelden een tweedimensionaal snelheidsveld bepaald. De deeltjesconcentratie is vervolgens bepaald door gebruik te maken van verschillen in de lichtintensiteit binnen de digitale beelden. Tenslotte is de deeltjesflux bepaald door het snelheidsveld te combineren met de deeltjesconcentratie.

De stromingsregimes, die in een “spout”-fluïde bed voorkomen, zijn in kaart gebracht met behulp van spectraalanalyse van de fluctuaties in de drukval. Er zijn zes stromingsregimes onderscheiden, waarvan het gedrag in detail wordt beschreven en geïllustreerd wordt door digitale beelden en frequentiespectra. De wijze waarop het stromingsregime afhangt van de gassnelheid in de “spout” en in de rest van het bed is in kaart gebracht aan de hand van de vorm en frequentie van de karakteristieke piek(en) in de frequentiespectra. De resultaten zijn weergegeven in een zogenaamd “stromingsregimeschema”. De stromingsregimeschema’s worden onder andere gebruikt om de juiste procescondities voor de validatieprocedure te bepalen.
De resultaten verkregen met verschillende geometriën, deeltjesgrootteverdelingen en deeltjeseigenschappen zijn vergeleken. Daarbij is vastgesteld dat al deze parameters een significante invloed hebben op het stromingsregimeschema, en dan met name op de ligging van de grenzen tussen de stromingsregimes. De verdeling van de stromingsregimes over het stromingsregimeschema verandert echter niet. Er is

derhalve geconcludeerd dat het stromingsregimeschema van een “spout”-fluïde bed niet uitsluitend afhangt van de gassnelheden in de “spout” en in de rest van het bed.

Met behulp van het stromingsregimeschema voor de pseudo-tweedimensionale opstelling zijn er procescondities in verschillende stromingsregimes geselecteerd voor de validatieprocedure. Vervolgens zijn er voor de geselecteerde cases drukvalmetingen uitgevoerd en tijdsgemiddelde deeltjesfluxprofielen bepaald.
Door de resultaten van simulaties, uitgevoerd vanuit verschillende beginsituaties, te vergelijken is de reproduceerbaarheid van het resultaat van de modelberekeningen gecontroleerd.
Simulaties, waarbij verschillende botsingsmodellen gebruikt werden, toonden aan dat de gekozen veerconstante groot genoeg was om de resultaten van het zachte bollen model onafhankelijk te maken van de gekozen veerconstante. Verder liet een vergelijking met de resultaten van het harde bollen model zien, dat de resultaten van het harde en zachte bollen model hetzelfde zijn, zodat geconcludeerd kan worden, dat de botsingsmodellen uitwisselbaar zijn.
De nieuwe methode om de fasen binnen het model aan elkaar te koppelen is geverifieerd door de resultaten van het model te vergelijken met analytische oplossingen voor een gepakt bed en een enkel deeltje. Hieruit bleek, dat de resultaten verkregen met de nieuwe methode onafhankelijk waren van het gekozen numerieke rooster. Daarnaast benaderde de nieuwe methode de theoretische oplossing veel dichter dan de conventionele methode, met name bij het gebruik van fijne numerieke roosters.
De nieuwe methode is vervolgens gebruikt om de invloed van het gekozen numerieke rooster in een pseudo-tweedimensionale geometrie te bepalen. Alle bestudeerde grootheden lieten voor beide geselecteerde cases zien, dat in een “spout”-fluïde bed met een “spout” breedte van 10 mm (= 4 maal de deeltjesdiameters) zelfs een roosterafstand van 10 mm klein genoeg was om resultaten te verkrijgen, die onafhankelijk waren van het gekozen numerieke rooster.
In de pseudo-tweedimensionale geometrie zijn voor beide cases de beschikbare experimentele resultaten vergeleken met de resultaten van simulaties, waarbij verschillende sluitingsmodellen voor de wrijvingskracht zijn gebruikt. Hieruit bleek dat de kwaliteit van de resultaten verkregen met het meest gebruikte sluitingsmodel voor de wrijvingskracht (de Ergun (1952) vergelijking voor hoge deeltjesfracties en de Wen en Yu (1966) relatie voor lage deeltjesfracties) matig was voor fluïde bedden met een stabiele “jet”, zoals “spout”-fluïde bedden. Bij het gebruik van het minimum van de wrijvingskracht voorspeld door de Ergun (1952) vergelijking en de Wen en Yu (1966) relatie zijn de resultaten aanzienlijk beter, net als bij het gebruik van de relatie voorgesteld door Koch en Hill (2001). Aangezien de Koch en Hill (2001) relatie

theoretisch beter onderbouwd is, wordt aan het gebruik van deze relatie de voorkeur gegeven.

Het geverifieerde model met geschikte sluitingsmodellen is gebruikt om de stromingsregimes, die karakteristiek zijn voor “spout”-fluïde bedden, gedetailleerd in kaart te brengen.
Hiertoe zijn er voor deze stromingsregimes met behulp van het stromingsregimeschema cases geselecteerd. Voor al deze cases zijn de fluctuaties in de drukval over het bed gemeten en voor een aantal cases zijn ook PEPT metingen uitgevoerd. Daarnaast zijn er voor alle cases driedimensionale DPM simulaties uitgevoerd om te onderzoeken of het model de experimenteel waargenomen stromingsregimes kan reproduceren.
Spectraalanalyse van de fluctuaties in de drukval toonde aan dat het model in staat was om in het merendeel van de gevallen het stromingsregime met succes te voorspellen. Hierbij dient wel opgemerkt worden dat het model over het algemeen een hogere frequentie voorspelde dan experimenteel werd waargenomen. Het model bleek echter niet in staat om de zeer grote bellen, die in één van de regimes worden waargenomen, te voorspellen.
De geconstateerde verschillen tussen het voorspelde en waargenomen gedrag van het “spout”-fluïde bed worden toegeschreven aan de behandeling van de interactie tussen het gas en de deeltjes. Er wordt namelijk aangenomen, dat de deeltjes homogeen verdeeld zijn op de lengteschaal waarop de wrijvingskracht berekend wordt, hetgeen lang niet altijd het geval is.

De resultaten van de simulaties van de driedimensionale geometrie, voor zowel monodisperse als bidisperse systemen, zijn vergeleken met de deeltjessnelheidsvelden, die met PEPT verkregen zijn. Daarnaast zijn de resultaten van de simulaties gebruikt om de deeltjesbeweging nader te bestuderen.
Uit de vergelijking blijkt dat het model voor alle onderzochte cases de gemeten deeltjessnelheden en de standaarddeviatie nauwkeurig reproduceert. Dit betekent dat het model in staat is om de details van de deeltjesbeweging voor verschillende regimes te berekenen.
Nadere analyse van de resultaten van de simulaties laat zien dat het model enige moeite ondervindt bij het voorspellen van de exacte vorm van het “spout” kanaal. Ook dit wordt toegeschreven aan de al eerder genoemde aanname van locaal homogene verdeling van de deeltjes.
De tijdsgemiddelde resultaten van het bidisperse systeem laten geen snelheidsverschil zien tussen de kleine en grote deeltjes. Dit is verrassend, aangezien de kleine deeltjes een grotere netto kracht, en dus een grotere versnelling, ondervinden. De berekende

standaarddeviatie in de snelheid van de kleine deeltjes was over het algemeen groter dan die voor de grote deeltjes. In de experimentele resultaten was dit verschil veel kleiner. Dit wordt toegeschreven aan de manier waarop de experimentele resultaten verkregen worden.
Bij nadere bestudering van de resultaten van de simulaties voor het bidisperse systeem werd een aantal kleine verschillen in de concentraties en fluxen van kleine en grote deeltjes waargenomen. Deze verschillen verdwenen echter toen de gassnelheden in de omgeving van de “spout” groter werden.
De experimentele resultaten zijn gebruikt om de spreiding van de circulatietijden van de deeltjes te bepalen. Deze spreiding vertoont een goede correlatie met de beweeglijkheid van de deeltjes. Aangezien het “jet-in-fluidized-bed” regime de kortste circulatietijden heeft en de kleinste spreiding, is het waarschijnlijk dat dit stromingsregime de meeste (en meest homogeen verdeelde) groeimogelijkheden biedt in de granulator.

Aan het met succes gevalideerde model is een bewegingsmodel voor druppels toegevoegd, welke de beschrijving van gas-vloeistof-deeltjes stroming in een “spout”-fluïde bed mogelijk maakt, inclusief de voor granulatie relevante fenomenen.
Het uitgebreide model is gedemonstreerd aan de hand van een granulatieproces in een plat “spout”-fluïde bed met vier verschillende deeltjesgrootteverdelingen. Voor elk van deze cases groeide de gemiddelde deeltjesdiameter, terwijl de standaarddeviatie vrijwel niet veranderde.
De mate van groei verschilde aanzienlijk tussen de individuele deeltjes en hing sterk samen met de positie van het deeltje ten opzichte van de sproeier. De mate van groei nam sterk af bij toenemende afstand tot de sproeier.
De groeisnelheid bleek afhankelijk van de grootte van het geprojecteerde oppervlak van het deeltje. Hierbij zijn er twee groeitypes waargenomen: “piekgroei” en “constante groei”. Piekgroei treedt op als de deeltjes over hun gehele geprojecteerde oppervlak bloot worden gesteld aan de druppels. De groeisnelheid is dan erg groot, terwijl de periode, waarover de groei plaats vindt erg klein is (< 4 ms) vanwege de korte verblijftijd van de deeltjes in de zone, waar piekgroei plaats vindt.
Constante groei treedt op wanneer, vanwege de positie van de jet of omdat een gedeelte van het oppervlak afgeschermd wordt door andere deeltjes, slechts een klein gedeelte van het deeltjesoppervlak blootgesteld wordt aan de druppels. De groeisnelheid voor dit groeitype is relatief laag, terwijl de groeiperiode veel langer is dan bij piekgroei.
Het merendeel van de groei vindt plaats door middel van constante groei. De piekgroei vindt slechts beperkt plaats doordat de zone boven de sproeier vanwege de grote wrijvingskrachten relatief weinig deeltjes bevat.

De kleinere deeltjes binnen een deeltjesgrootteverdeling vertonen iets vaker piekgroei, wat veroorzaakt wordt door een hogere concentratie van dit type deeltjes direct boven de sproeier. In de rest van het bed is de groeisnelheid per geprojecteerd oppervlak vergelijkbaar voor alle deeltjes.

Het uitgebreide discrete deeltjes model kan waardevolle informatie over het groeigedrag van deeltjes in een “spout”-fluïde bed opleveren. Het is daarom noodzakelijk om het model te valideren. Hiervoor zijn experimenten nodig, waarin het groeigedrag van de deeltjes in detail gemeten kan worden.

Chapter 1

General introduction

Abstract

In this chapter the principles of gas-fluidized beds and spout-fluid beds are explained, including an overview of their applications. Subsequently the application that serves as the background for this thesis, spout-fluid bed granulation of urea, is described in detail.

An overview of the literature discussing the various aspects of spout-fluid beds is given, together with an overview of the modeling of fluidized beds in general, which is also considered to be of relevance to this thesis.

Furthermore the objective of this thesis is presented, which is to improve the control over the particle size distribution resulting from spout-fluid bed granulation by gaining insight into the underlying fundamental processes. Subsequently, the strategy that was adopted to reach this objective, which is to focus on the description of the flow behavior inside the spout-fluid bed, is described.

The chapter is concluded with the outline of the thesis.

1.1 Introduction

Gas-fluidized beds are widely used for a variety of processes involving particulate solids. They are applied for both chemical applications, like pyrolysis and polymerization, and physical applications, like drying, coating and granulation.
In a gas-fluidized bed the gravitational and inter-particle forces that keep the particles stationary on the bottom of the bed are compensated by the drag forces exerted by the gas phase flowing upward through the voids in-between the particles. As a result the particles can move through the bed and display behavior that is normally encountered in fluids, hence the name “fluidized bed”. The gas velocity, at which this behavior first emerges, is termed the minimum fluidization velocity.
Because of the fluid-like behavior, the particles are easier to handle facilitating continuous processing. Furthermore, it dramatically improves both heat and mass transfer allowing isothermal operation and avoiding hot spots.

The dynamic behavior of fluidized beds depends on particle properties, like size, density and shape, and gas properties, like density and velocity. In general, the size of gas bubbles in fluidized beds increases with particle size and density. For large particles (> 1mm), the size of the gas bubbles is only limited by the dimensions of the bed, which can cause particles to be elutriated from the bed.
Elutriation can be prevented by adapting the design of the fluidized bed to avoid the formation of large bubbles. This is achieved by breaking up the bubbles with high velocity jets, termed “spouts”, thus creating spout-fluid beds.
Spout-fluid beds are generally applied to processes involving large particles, like drying, coating and granulation. Apart from channeling the bubble behavior, the spout also structures the flow behavior of the particles. Furthermore, the spout can be used as a liquid injector in granulation applications.

Spout-fluid bed granulators are generally operating in the coating regime. Consequently they yield high strength layered granules from liquid feeds. The interested reader is referred to the book written by Litster and Ennis (2004) for more information on granulation regimes and processes.
Spout-fluid bed granulation of fertilizer, in particular urea, serves as a background for the work presented in this thesis. The aim of this granulation process is to convert freshly synthesized liquid urea into solid granules that are within a specified size interval and are sufficiently strong to undergo transport and storage. The industrial process is schematically illustrated in Figure 1.1.

In the process, liquid urea is injected into the granulator through a nozzle at a high velocity. This nozzle is usually referred to as the spout. The gas spouting through the nozzle atomizes the liquid into tiny droplets and launches them into the bed, where they encounter the particles already present in the bed. The droplets spread over the surface of the particle and solidify, since the operating temperature of the granulator is below the melting point of urea. The growing particle is subsequently transported through several granulation chambers and downstream cooling chambers, as it is continuously being fluidized by the fluidization air. Ultimately the particles flow out of the granulator after which they are sieved. The particles that are not within the desired particle size interval are recycled, in case of over-sized particles after crushing. The recycled particles are subsequently fed to the granulator to serve as nuclei for the next cycle of the granulation process.

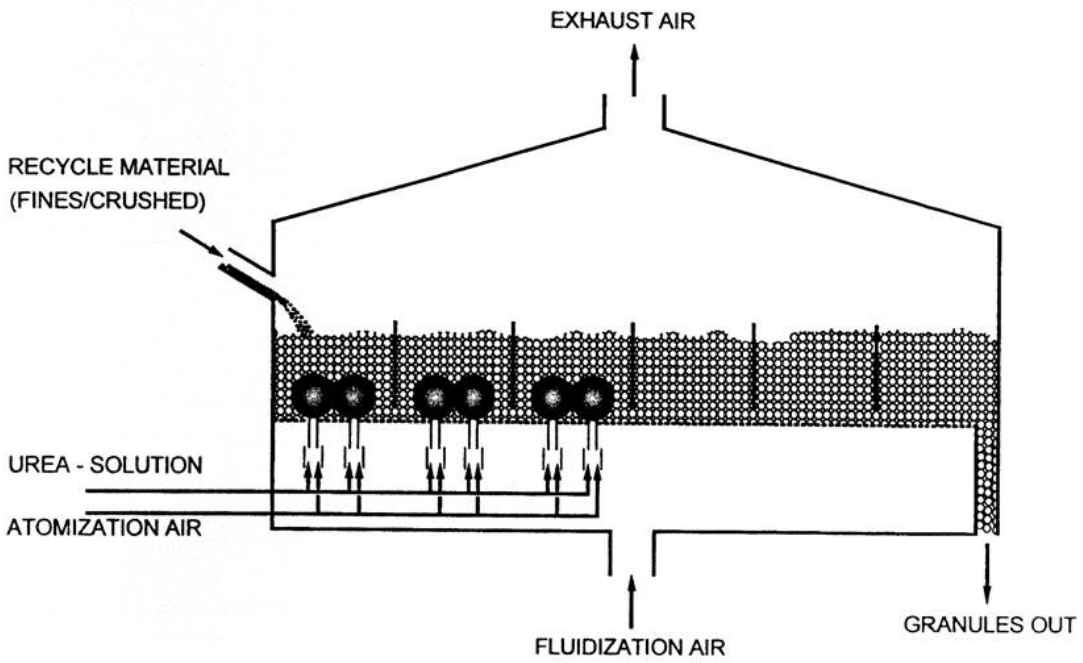

Figure 1.1 Schematic representation of the spout-fluid bed granulation process for liquid urea.

1.2 Overview of previous research

Most of the research on granulation and coating in spouted and spout-fluid beds is based on experiments. Obviously the distribution of growth rates within a particle size distribution has been the focus of most of this work (Kucharski and Kmiec, 1989; Oliveira *et al.*, 1997), sometimes in combination with the particle properties (Pavarini and Coury, 1987). Apart from the experimental work, a few modeling efforts were made to describe the growth rates within a spout-fluid bed. Choi and Meisen (1997) opted for hydrodynamic models, while Liu and Litster (1993a) used a population

balance model. In both papers, the model results were compared with experiments. The behavior of the spout itself, including the stability of the spout channel and the elutriation rate, was studied by Liu and Litster (1993b), who compared the experimental spout behavior with theoretical models.

Since Mathur and Epstein (1974) published a book on spouted bed hydrodynamics, a large number of experimental studies of spouted and spout-fluid bed hydrodynamics have been reported over the years (a.o. Sutanto et al., 1985). The dynamics of spouted and spout-fluid beds were investigated using spectral analysis of pressure drop fluctuations (Xu et al., 2004, Zhang and Tang, 2004, Link et al., 2005). Gas velocity profiles were measured by San José at al. (1995), while solids velocity profiles were obtained using optical probes (He et al., 1994, San José at al., 1998, Pianarosa et al., 2000) and particle tracking (Larachi et al., 2003).

In most early numerical studies of spouted beds (a.o. Littman et al., 1985) only the overall behavior of the particles was modeled neglecting the details of particle motion.
Tsuji *et al.* (1993) introduced a discrete particle model for bubbling fluidized beds, in which they solved the volume-averaged Navier-Stokes equations for the gas phase, taking momentum transfer between the gas and the particles into account. Newton's laws were used to compute the motion of each individual particle. The individual treatment of the particles limits the application of this model to systems of approximately 10^5 particles.
Kawaguchi et al. (2000) were the first to apply the discrete particle model to spouted beds. Other contributions were made by Takeuchi et al. (2004), Limtrakul et al. (2004) and Link et al. (2004), which differ mostly in the treatment of the particle-particle and fluid-particle interaction.
The limitation of the number of particles does not apply to continuum models, which treat the gas phase and the particulate phase as inter-penetrating continua. Lu et al. (2004) used a continuum model to describe the behavior of a spouted bed.

Furthermore a significant fraction of the work published on spouted and spout-fluid beds is related to its application, such as drying (Becker and Sallans, 1961), coating (Jono et al., 2000), coal gasification (Zhao et al., 1988) and catalyzed reactions (Rovero et al., 1983).

1.3 Objective and Strategy

The main objective of most granulators is to produce as many particles as possible within a specific size distribution. Deviating particle sizes will either need to be recycled, decreasing overall granulation capacity, or need to be sold as a byproduct, generally at a lower added value.
The aim of this study is to improve the control over the particle size distribution resulting from spout-fluid bed granulation by gaining insight into the underlying fundamental processes.

A spout-fluid bed granulator comprises three interacting components, i.e. particles, gas and atomized droplets. The performance of the granulator is influenced both by the operating conditions, and by the geometry of the granulator.
Because of all the interactions between the phases, simultaneous information on all components present within the system is required to allow a fundamental study of the behavior of the system itself. Although detailed information on the behavior of a single particle, or the overall result of the granulation process, can be obtained experimentally, it is impossible to monitor all relevant parameters within the system with the experimental equipment that is available at present or in the attainable future.
It is however possible to study the individual interactions within and between the different phases, which has already been done extensively. The fundamentals of the individual interactions within the system are therefore known with an accuracy that appears to be sufficient to allow a detailed study. Consequently all these fundamentals can be combined into a single model, which describes the system as a whole. Unfortunately, the number of calculations required for such a model, for systems with relevant dimensions on a relevant time scale, is beyond the capacity of computers that are available at present or in the attainable future.

The description of the overall flow behavior is considered to be of critical importance for any model describing a spout-fluid bed granulator. Since the flow behavior depends largely on the treatment of the fluid-particle and particle-particle interaction, most of this thesis will be dedicated to the assessment of these interactions. To allow a strong focus on the flow behavior a simple rectangular geometry consisting of a single spout without internals is used.
The treatment of the droplets is only considered to be of relevance after the overall flow behavior is properly described. It will therefore not be discussed until the final chapter.

Models on various scales are available to describe the flow in bubbling gas-fluidized beds. An overview of available models is presented in Figure 1.2. Since the ultimate objective of modeling granulators is to simulate an industrial scale system, continuum models appear to be most suitable. However, these models require closures for the fluid-particle and particle-particle interaction. Several relations that describe the fluid-particle interactions are available, although their suitability needs to be assessed. Closures for the particle-particle interaction within a spout-fluid bed are however unavailable. Consequently, the discrete particle model is more suitable for this study. An advantage of this model is that it also allows a detailed description of the droplet-particle interaction. Once the discrete particle model is developed, it can be used to supply the particle-particle closures for continuum models.

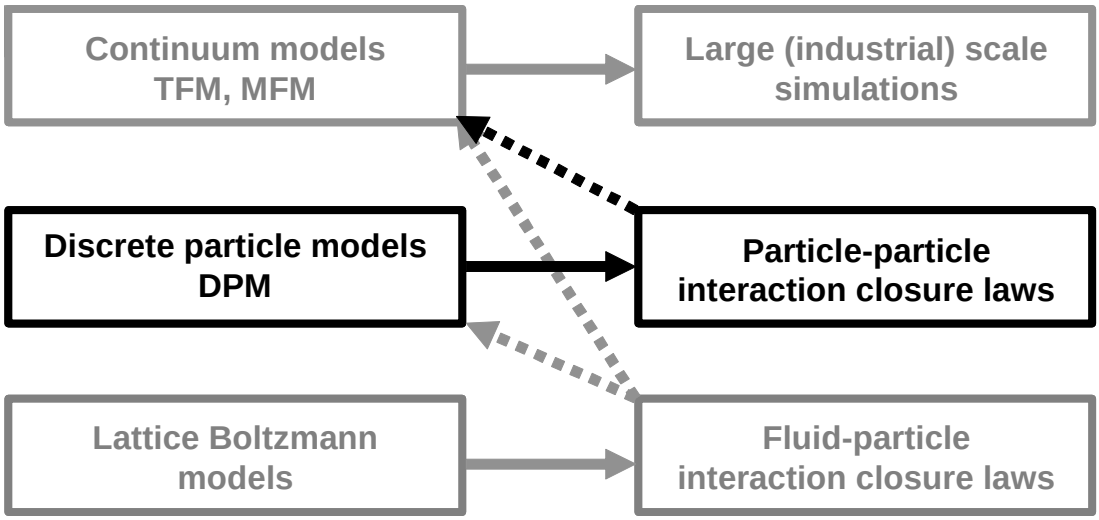

Figure 1.2 Schematic representation of the available models to describe the behavior of fluidized beds, including their relations.

Although the discrete particle model has been successfully applied to gas-fluidized beds, its suitability for spout-fluid beds will need to be established. Therefore the model will need to be developed and the predictions based on this model will need to be validated using dedicated experiments.

Once the discrete particle model is successfully validated, it can be expanded to include droplets, droplet-particle interaction (particle growth) and fluid-droplet interaction. After the model has been successfully validated by carefully designed experiments, it can provide the desired insight into spout-fluid bed granulation.

1.4 Outline of the thesis

Validation of hydrodynamic models is essential to be able to rely on the results produced with discrete particle models. Therefore Chapter 2 presents several experimental techniques that are used for this purpose. Firstly, a technique named particle detection is presented, which yields whole-field two-dimensional solids fraction profiles from digital images. These images are also used to obtain whole-field two-dimensional particle velocity profiles using particle image velocimetry. Subsequently a technique for the spectral analysis of pressure drop fluctuations is introduced. This technique captures the dynamic behavior of a spout-fluid bed. Finally a positron emission particle tracking technique is presented that produces three-dimensional particle velocity profiles.

Chapter 3 presents the discrete particle model, along with two approaches for the particle-particle interaction and three closure models for fluid-particle interaction. The numerical implementation is discussed with special focus on the implementation of a new treatment of the inter-phase coupling.

The behavior of a spout-fluid bed is a function of both the regular fluidization velocity, or background fluidization velocity, and the gas velocity in the spout. In Chapter 4 six different flow regimes are distinguished, the properties of which are described in detail and illustrated with snapshots. A procedure to map these flow regimes is proposed and flow regime maps for a number of systems are presented and discussed. The flow regime maps are used to select proper operating conditions for the experiments.

In Chapter 5 proper closure models and numerical settings are selected by verification and validation of the model in a pseudo-2D set-up. Firstly, the reproducibility of the model is assessed, and the results obtained with the different approaches for the particle-particle interaction are compared. The proposed treatment of the inter-phase coupling is verified and the required grid resolution is determined. In order to select the fluid-particle interaction closure model, results obtained with all closures are compared with several experimental results.

The validated model is subsequently applied to a three-dimensional set-up. In Chapter 6 the validation of both the bed dynamics and the details of the particle flow are continued. Subsequently several properties that can be obtained from the simulations are presented and discussed, along with the additional information that was obtained experimentally.

In Chapter 7 the validated model is expanded to allow the description of granulation. To determine whether the model was able to deliver detailed information on the granulation process, a number of theoretical test cases were simulated. The results of the model were analyzed in detail to establish its potential as a research tool.

Chapter 2

Experimental techniques

Abstract

Several experimental techniques have been developed and used to map the behavior of spout-fluid bed and to supply the experimental data required for validation.
A non-intrusive method is presented that obtains whole-field particle concentration profiles in a pseudo-2D set-up from digital images. This technique uses differences in light intensity levels to distinguish between particles and bubbles.
The light intensity level is not merely a function of the presence of particles and bubbles, but it also varies with position and time. The manner in which the quality of the images is enhanced, along with the methods that were used to compensate for the influence of time and position, are described.

The digital images were also used to obtain whole-field particle concentration profiles in a pseudo-2D set-up using particle image velocimetry (PIV). The method requires two images separated by a short time interval and subsequently uses cross-correlation analysis to determine the spatially-averaged displacement of the particle images between the first and second image. The displacement and the time interval are used to obtain the average velocity of a group of particles.
The methods that were used to ensure and enhance the quality of the results are explained.

Spectral analysis of pressure drop fluctuations is a non-intrusive measurement technique, which supplies information about the dynamic behavior of the particles in a spout-fluid bed through the pressure drop fluctuations. The characteristics of the dynamic behavior are captured by applying a Fourier transformation to a recording of the temporal fluctuations of the pressure drop over the entire bed. The result of this transformation is rendered into a frequency spectrum, which characterizes the dynamic behavior of the bed.

A scaling method is described that can be used to compare results obtained with recordings of different duration.

Positron emission particle tracking (PEPT) is a non-intrusive measurement technique, which supplies detailed information about the particle motion by tracking the position of a single activated particle in the interior of a three-dimensional bed. The activated particle emits positrons, which are annihilated when they encounter electrons, producing back-to-back gamma rays. These gamma rays are simultaneously detected by a pair of detectors. The position of the particle emitting the positrons is reconstructed by calculating the point of intersection of several pairs of gamma rays.
The method that was used to reduce the amount of noise that was present in the signal is described, and the manner in which the particle circulation time was extracted from the signal is explained.

2.1 Introduction

To assess the various aspects of spout-fluid bed behavior, several measurement techniques have been employed. Two image analysis techniques have been used to obtain quantitative information on the particle behavior:

- particle detection, explained in section 2.2, has been used to obtain instantaneous and time-averaged porosity fields;
- particle image velocimetry, explained in section 2.3, has been used to obtain instantaneous and time-averaged particle velocity fields.

Spectral analysis of pressure drop fluctuations, which is described in section 2.4, produced information on the overall dynamic behavior of the spout-fluid bed. Finally, positron emission particle tracking, which is discussed in section 2.5, has been applied to study the bed behavior by tracking an individual particle.

2.2 Particle detection

Particle detection is an optical measurement technique that can a.o. be used to produce the instantaneous spatial distribution of the particles. The technique uses digital images, which can be recorded without influencing the behavior of the particles. In the images, the particle is distinguished from the background based on the intensity. Subsequently, the local particle fraction can be calculated. The main advantages of the particle detection technique are that it is a non-intrusive measurement technique and that the images supply instantaneous information over a large spatial area.

A drawback of using an optical technique in a fluidized bed is that fluidized beds are predominantly opaque due to the presence of particles. Consequently, only the particle behavior in the vicinity of the wall can be captured. To capture the particle behavior in the interior of a fluidized bed, alternative techniques, like positron emission particle tracking, which will be discussed in section 2.5, are required.

Agarwal *et al.* (1996) were the first to use digital image analysis to study a fluidized bed. In their work they positioned a light source behind the bed to visualize the bubbles. The light source was only visible to the camera when a bubble was present. This type of bubble, which extends from the front wall to the back wall is termed a deep bubble and is illustrated in Figure 2.1.

Goldschmidt *et al.* (2003) did not detect the bubbles, but the particles. They illuminated the bed from the front with a diffuse light source. Consequently, the particles in the vicinity of the wall were adequately lighted and are termed bright

particles. Bright particles block part of the incoming light and may consequently prevent the proper illumination of particles further away from the wall, which is illustrated in Figure 2.1. Particles that are not properly illuminated are termed shaded particles. The presence of a shaded particle implies the presence of a bubble located between this particle and the wall. Shaded particles are therefore indicative for bubbles. Since these bubbles do not extend from wall to wall, they are termed shallow bubbles. Goldschmidt *et al.* (2003) distinguished deep bubbles by using a different color for the background of the bed, which they detected by using a color camera.
In this thesis a monochromatic camera is used and by using a background with low intensity (black) the particles can be distinguished from both types of bubbles solely based on intensity information.

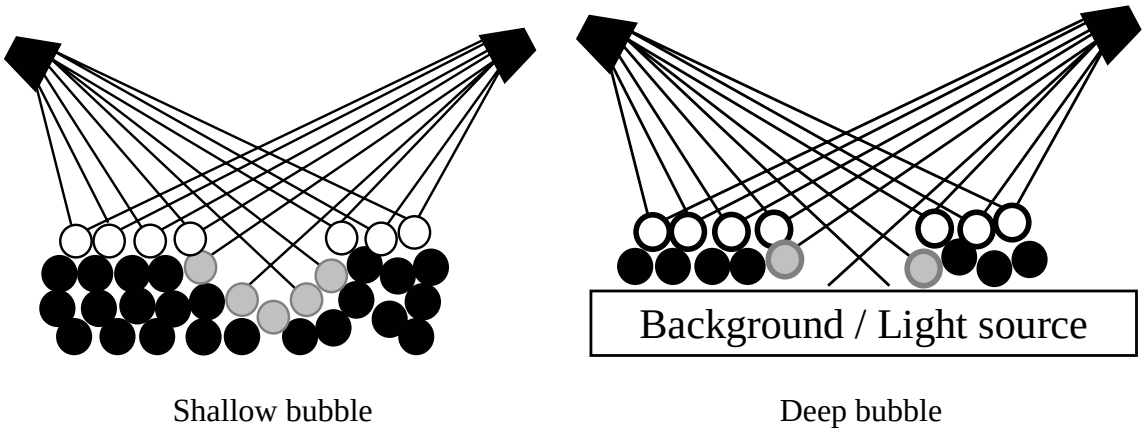

Figure 2.1 An illustration of the illumination of shallow and deep bubbles.

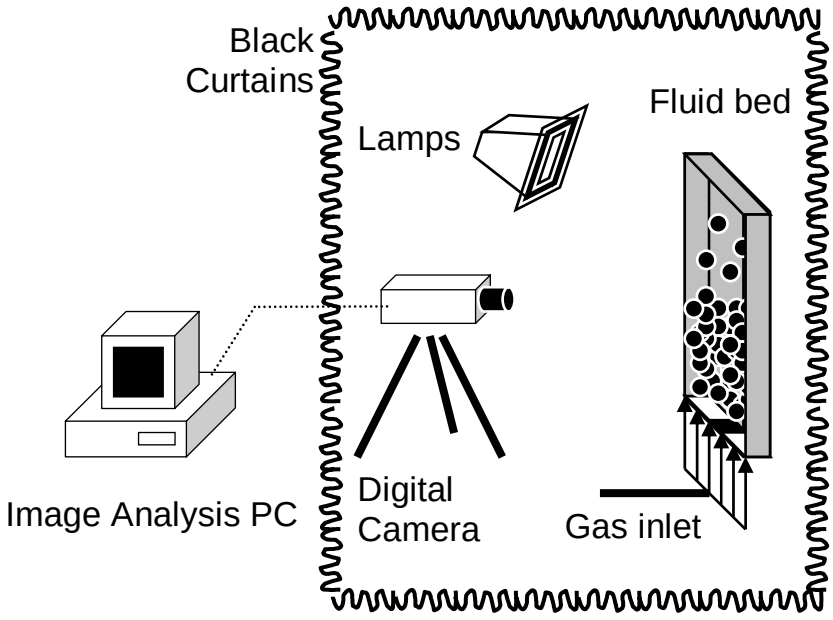

Figure 2.2 Overview of the digital image analysis set-up.

The quality of the results of the image analysis obviously depends on the quality of the individual images. An overview of the set-up that has been used to record the images is presented in Figure 2.2. The quality of the images is negatively affected by reflections, movement of the particles during the exposure time, i.e. motion blurring, and varying illumination conditions.

Reflections are avoided by lighting the bed directly under a small angle (< 45°) and by covering the surroundings of the set-up with black curtains.

Motion blurring can be prevented by minimizing the exposure time, which reduces the amount of lighting. This needs to be compensated for to ensure that the bed is sufficiently illuminated. For this reason two 500 W halogen lamps along each side of the camera were used to illuminate the bed. Apart from that, the amount of lighting can be increased by increasing the aperture of the camera.

The spatial variation of the illumination can be prevented by minimizing the aperture of the camera and by using diffuse lighting.

The temporal variation of the illumination is caused by the alternating current of the power supply of the lamps and needs to be compensated for.

The conflicting requirements for the prevention of motion blurring and the spatial variation of the illumination were reconciled to obtain a reasonably homogeneous, but strong illumination. Consequently, the spatial variation of the illumination needs to be compensated for. The manner in which the temporal and spatial variation of the illumination is handled is discussed below.

In the particle detection algorithm, the intensity of each pixel (I) is compared with a threshold value (I_T):

$$I > I_T \quad \Rightarrow \qquad I \in particle \tag{2.1}$$

$$I < I_T \quad \Rightarrow \qquad I \in bubble \tag{2.2}$$

The determination of the threshold value is unfortunately not straightforward, since, as stated before, the intensity not only depends on the distance between the particle and the wall, but also varies with time and position:

$$I = f\left(x, z, t\right) \Rightarrow I\left(i, j, t\right) \tag{2.3}$$

The intensity of the light emitted by the lamps is affected by the alternating current and therefore varies with time. The temporal correction, that is required to compensate for these fluctuations, is determined by using the difference between the average illumination of the entire bed, $\bar{I}(t)$, and its local time-average, $\langle \bar{I} \rangle$:

$$\Delta I(t) = c_t \left(\bar{I}(t) - \langle \bar{I} \rangle \right) \tag{2.4}$$

where c_t is the temporal correction constant and where the spatial average is defined as:

$$\bar{I}(t) = \frac{1}{N \cdot M} \sum_{i=1}^{N} \sum_{j=1}^{M} I(i, j, t) \tag{2.5}$$

and the temporal average around time t as:

$$\langle I(i, j) \rangle = \frac{1}{2n+1} \sum_{t=-n}^{n} I(i, j, t) \tag{2.6}$$

Furthermore, the intensity of the illumination depends on the orientation of the lamps and the aperture of the camera, and consequently is a function of the position. Both of these disturbances are constant in time and can be compensated for by using a method proposed by Goldschmidt *et al.* (2003). They calculated correction factors for each pixel by evaluating the variation of the intensity with position for a time-averaged recording of a uniformly white sheet:

$$c_x(i, j) = \frac{\langle \bar{I} \rangle}{\langle I(i, j) \rangle} \tag{2.7}$$

Applying both corrections results in:

$$I'(i, j, t) = c_x(i, j) I(i, j, t) - \Delta I(t) \tag{2.8}$$

After the spatial correction has been applied to the images, which is illustrated in Figure 2.3, the threshold value and c_t are determined by examining several situations.
Firstly, a stagnant bed, illustrated in Figure 2.4, is studied. In a stagnant bed all particles are in principle within the field of view (FOV). Therefore the solids volume is known. Furthermore, the width and depth of the bed are known. The height of the bed within the field of view, h_{FOV}, can be determined from the snapshot. Consequently, the volume-averaged solids fraction can be determined:

$$\overline{\varepsilon_{s,3D}} = \frac{N_p V_p}{W \cdot D \cdot h_{FOV}} \tag{2.9}$$

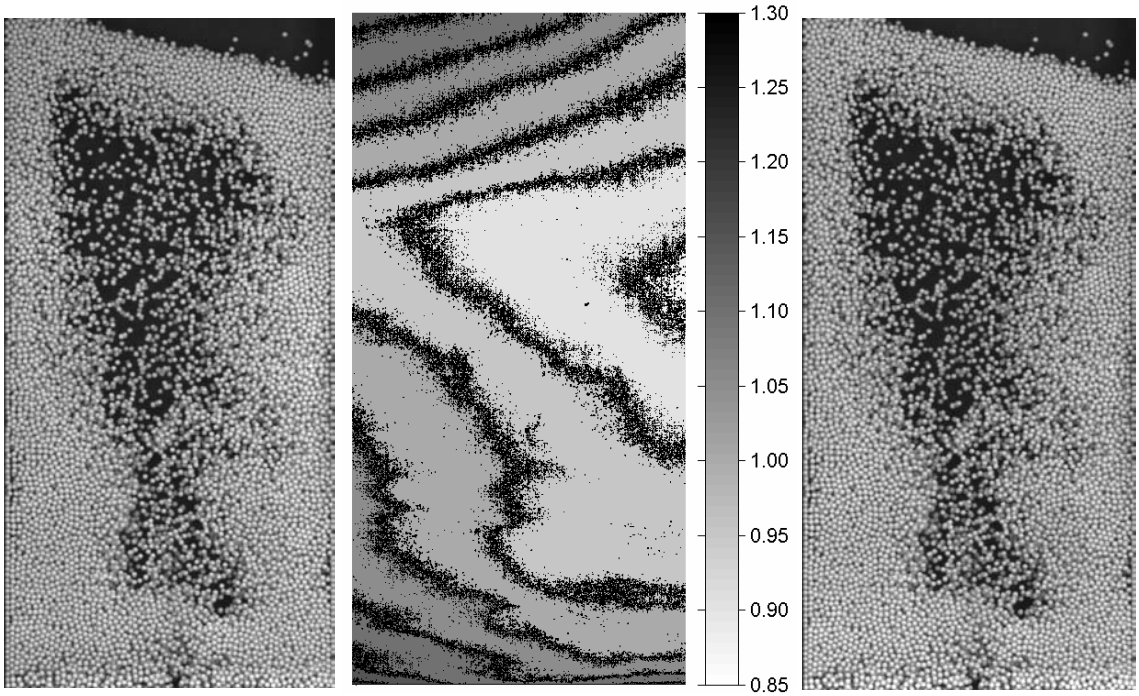

Original image c_x (i,j) Corrected image

Figure 2.3 Illustration of the spatial correction of the illumination.

The height of the bed occupied by solids, h_s, can also be determined from the snapshot. Consequently, the packed bed solids fraction, which is considered to be the maximum solids fraction, can be determined:

$$\varepsilon_{s,3D}^{\max} = \frac{N_p V_p}{W \cdot D \cdot h_s} \tag{2.10}$$

Subsequently a series of images of an operating regime for which all particles remain within the field of view is analyzed. These images are divided into areas of N times M pixels, termed interrogation areas. The solids fraction in each of these areas is determined as follows:

$$\varepsilon_{s,2D} = \frac{1}{N \cdot M} \sum_{i=1}^{N} \sum_{j=1}^{M} \delta(i,j) \quad \text{, where} \quad \begin{matrix} \delta(i,j) = 1 & \text{if } I'(i,j,t) > I_T \\ \delta(i,j) = 0 & \text{if } I'(i,j,t) < I_T \end{matrix} \tag{2.11}$$

For the pseudo-2D configuration that was used in this thesis, it was assumed that the particle configuration in the third dimension, the depth, is equivalent to the two dimensional particle configuration in the interrogation area, the three dimensional solids fraction of the interrogation volume can be obtained:

$$\varepsilon_{s,3D} = \left(\varepsilon_{s,2D}\right)^{3/2} \tag{2.12}$$

When all particles are within the field of view, $\overline{\varepsilon_{s,3D}}$ is known. The threshold value for each image can now be set in such a way that the measured value is in correspondence with the calculated value:

$$\frac{N_p V_p}{W \cdot D \cdot h_{FOV}} = \frac{1}{N_X N_Z} \sum_{i=1}^{N_X} \sum_{j=1}^{N_Z} \left(\varepsilon_{s,2D}(i,j) \right)^{3/2} \tag{2.13}$$

where N_X and N_Z are respectively the number of interrogation areas in the horizontal and vertical direction.
With the following condition:

$$\left(\varepsilon_{s,2D}(i,j) \right)^{3/2} = \varepsilon_{s,3D}^{\max} \quad \text{if} \qquad \left(\varepsilon_{s,2D}(i,j) \right)^{3/2} > \varepsilon_{s,3D}^{\max} \tag{2.14}$$

to reduce the effect of spurious results.
Example input and output images of the particle detection, including the solids fraction distribution, are displayed in Figure 2.5.

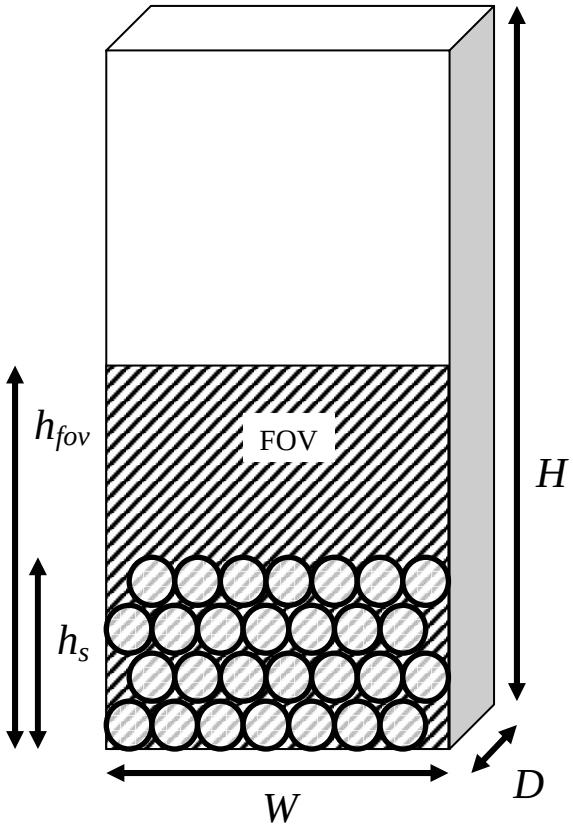

Figure 2.4 Illustration of the analysis of a snapshot of a stagnant bed.

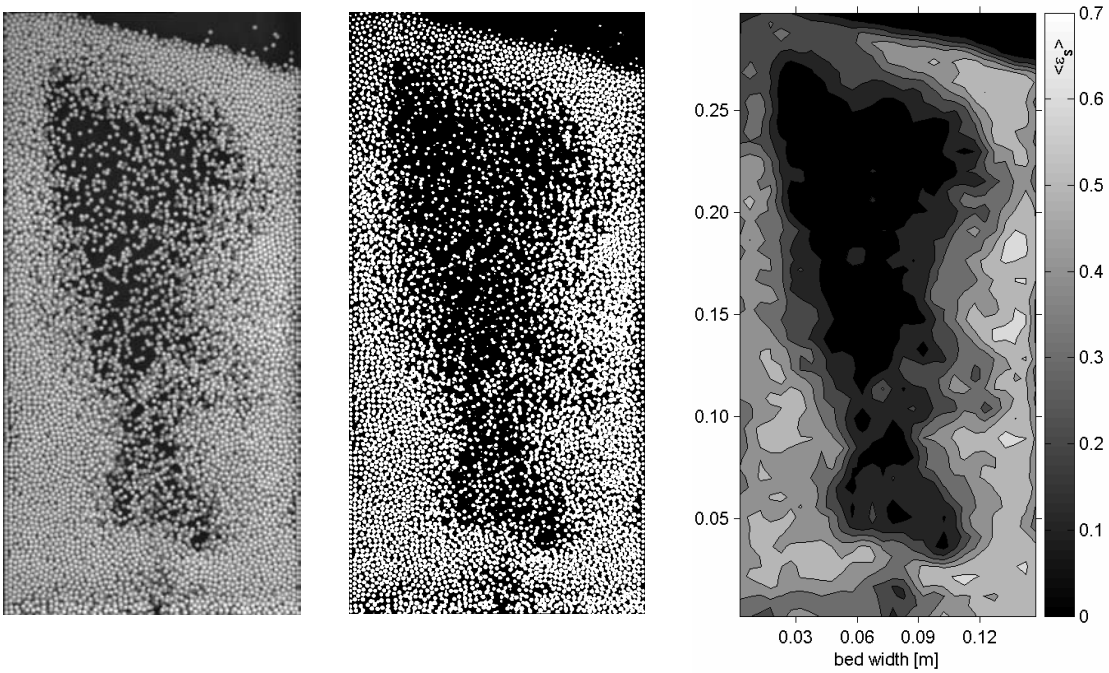

Digital image | Result of particle detection (white = particle, black = bubble) | Solids fraction

Figure 2.5 An example result of the particle detection algorithm.

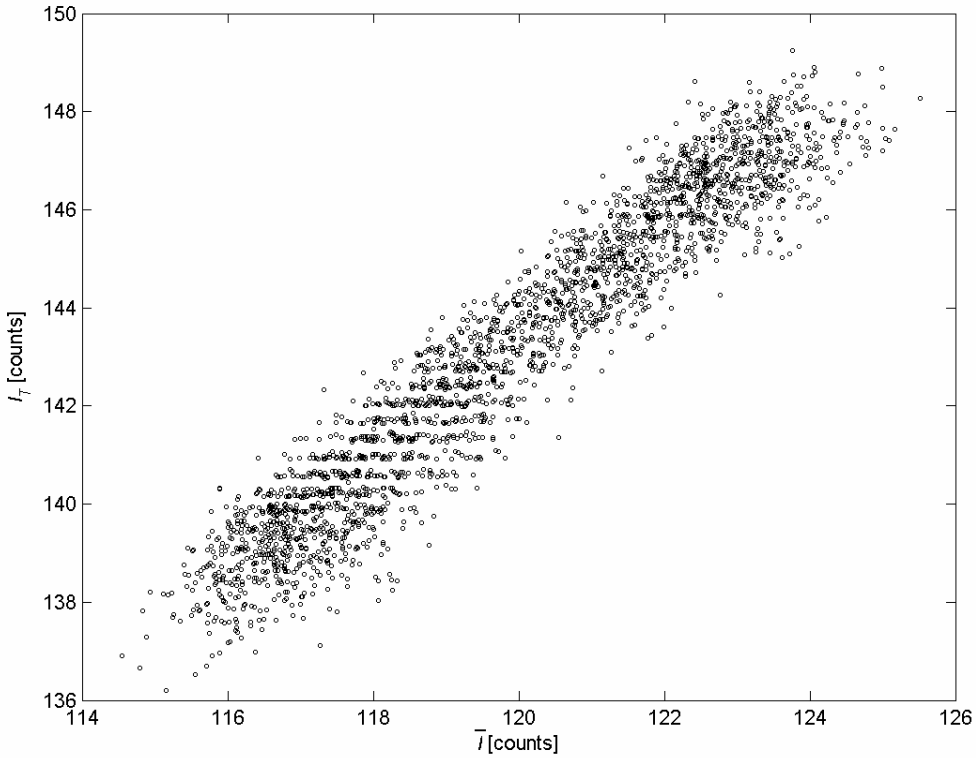

Figure 2.6 Each point shows the spatially-averaged intensity and the corresponding threshold intensity of a single image.

When a series of images is evaluated using the proposed corrections, the same pixels are attributed to particles in a stagnant part of the bed. When a fixed threshold would have been used, the number of pixels representing a particle would have fluctuated with the intensity of the light emitted by the lamps. Consequently, the influence of time on the images is successfully compensated for.

The temporal correction constant, c_t, can be determined from a plot of I_T versus $\bar{I}$, which is shown in Figure 2.6. Since the images can be corrected for the influence of position and time, a single threshold value, which is equal to the average threshold value in Figure 2.6, can be used for all subsequent experiments, even in cases where some particles leave the field of view.

2.3 Particle image velocimetry

Particle image velocimetry (PIV) is an optical, non-intrusive measurement technique that produces instantaneous two dimensional flow velocity data for a whole plane in a three dimensional flow field. The initial groundwork for the PIV technique was laid down by Adrian (1991). Keane and Adrian (1990, 1993) used the PIV technique to experimentally obtain flow velocity fields from photographs. Willert and Gharib (1991) were the first to use images that were recorded with digital cameras. Westerweel (1993) extended the theory to evaluate digital PIV images and developed a method to estimate the displacement at sub-pixel level. Digital PIV has already been used extensively in the field of experimental fluid dynamics, for example to study two-phase flows in dilute systems (Deen *et al.*, 2002).

The PIV technique that was used in this thesis will be discussed in this section and is based on the method developed by Westerweel (1997), to which the interested reader is referred to for further details.

In traditional PIV, the flow is visualized by seeding it with small tracer particles that closely follow the flow. In gas-particle flows, the discrete particles can readily be distinguished, so no additional tracer particles are required to visualize the particle movement. The image acquisition is illustrated in Figure 2.7.

The PIV analysis is illustrated in Figure 2.8. Two subsequent images of the particle flow, separated by a short time delay, d*t*, are divided into small interrogation areas with a size D_I, consisting of N times M pixels.

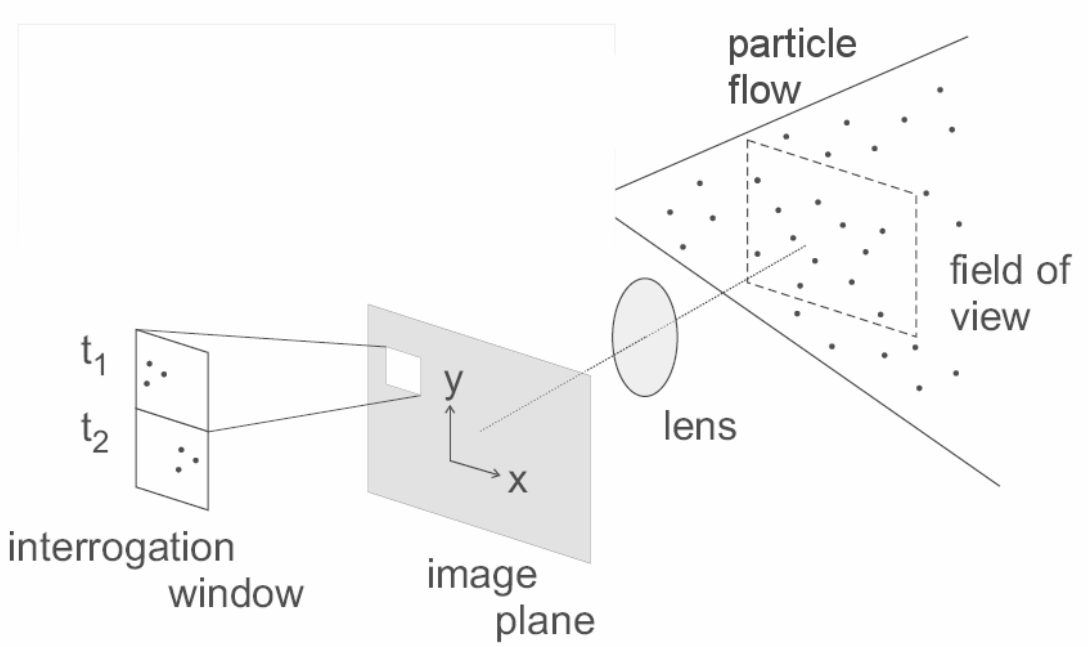

Figure 2.7 Illustration of the image acquisition.

The particle velocity within each of the interrogation areas is assumed to be approximately constant. Cross-correlation analysis is used to determine the spatially-averaged displacement of the particle images, **s**(**x**, *t*), between the interrogation areas in the first and second image:

$$R(\mathbf{s}) = \sum_{i=1}^{N}\sum_{j=1}^{M} I_1(i, j) I_2\left(i + s_x, j + s_y\right) \tag{2.15}$$

which can be split into three contributions:

$$R(\mathbf{s}) = R_C(\mathbf{s}) + R_F(\mathbf{s}) + R_D(\mathbf{s}) \tag{2.16}$$

where R_C is the correlation of the mean intensity, R_F the correlation of the mean with the fluctuating image intensity, and R_D the correlation of the intensity fluctuations. The terms R_C and R_F vanish by subtracting the mean intensity from the image fields. The particle image displacement, $\mathbf{s}_D$, is determined by measuring the location of the tallest peak in R_D. An illustration of a cross-correlation diagram is given in Figure 2.8. The velocity in the interrogation area is then easily determined by dividing the measured displacement by the image magnification, *M*, and the time between two images, d*t*:

$$\mathbf{v}_p(\mathbf{x},t) = \frac{\mathbf{s}_D(\mathbf{x},t)}{M\mathrm{d}t} \tag{2.17}$$

provided that d*t* is sufficiently small. An example result is displayed in Figure 2.9.

To successfully apply PIV a few conditions need to be met. First of all, PIV requires the spatial and temporal scales of the flow to be large with respect to D_I and dt. The former can be expressed by considering the velocity gradient within the interrogation area (Δu), which needs to be small:

$$\frac{M\left|\Delta u\right|\mathrm{d}t}{D_I} < \frac{d_p}{D_I} \tag{2.18}$$

This can be achieved by using small interrogation areas.

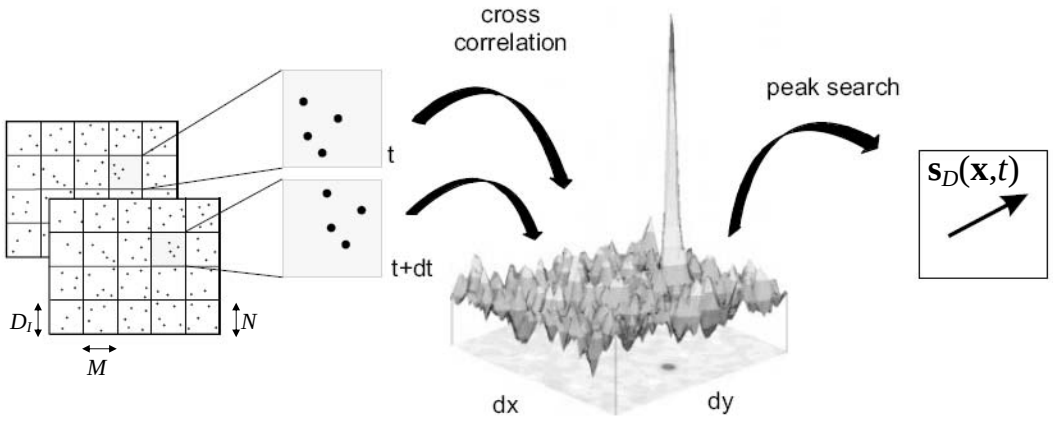

Figure 2.8 Illustration of the PIV analysis.

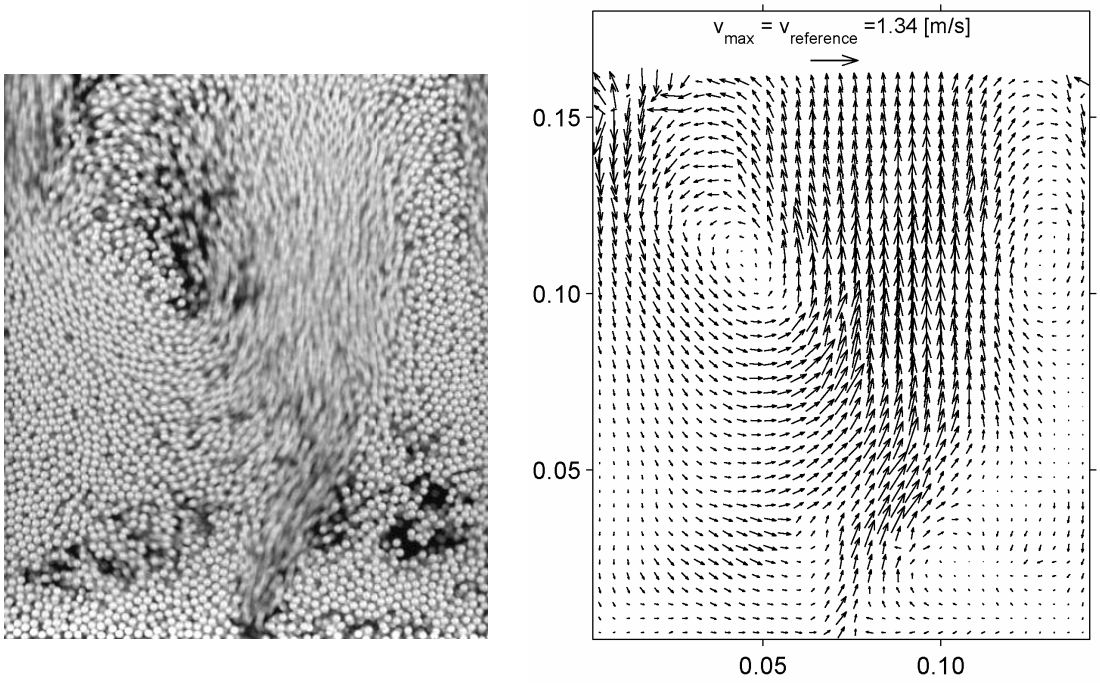

Image Particle velocity profile

Figure 2.9 An example of the input and the result of the PIV analysis.

On the other hand, PIV requires a certain effective number of particle image pairs per interrogation area to produce reliable results. This topic has been addressed by Keane and Adrian (1990). They examined the influence of the effective number of particle image pairs per interrogation area on the accuracy of the measurement.

The effective number of particle image pairs per interrogation area can be expressed as $N_I F_I F_O$, where N_I is the initial number of particles images present in the interrogation area. The factor F_I is a measure for the in-plane displacement, i.e. particles that move out of the interrogation area in the plane of measurement. F_I represents the fraction of particle images remaining in the interrogation area. The factor F_O is a measure for the out-of-plane displacement, i.e. particles that move out of the plane of measurement. F_O represents the fraction of particle images remaining in the measuring plane.

The relative height of the tallest peak in R_D, and consequently the accuracy of the measurement of the particle displacement, $\mathbf{s}_D$, scales linearly with $N_I F_I F_O$:

$$R_D\left(\mathbf{s}_D\right) \sim N_I F_I F_O \tag{2.19}$$

Keane and Adrian (1990) have shown that the following design rule needs to be satisfied in order to have an accuracy larger than 95%:

$$N_I F_I F_O > 7 \tag{2.20}$$

Westerweel (1997) assessed the effect of using digital images for the PIV analysis. In a digital image, a particle image consists of a limited number of pixels. As a consequence, the particle displacement can only be determined in an integer number of pixels, which severely limits the accuracy of the measurement. By applying a peak-fit to the displacement correlation peak, he was able to determine the displacement of the particle images on sub-pixel level. He tested several peak-fit functions of which a Gauss curve was most suitable for the conditions encountered in this study. He found that a minimum of only two pixels was required to represent the diameter of each particle image in order to determine the displacement on sub-pixel level with good precision. He even concluded that increasing the number of pixels per particle image beyond two did not improve the results.

A number of procedures has been developed to improve the results of the PIV analysis. Keane and Adrian (1993) introduced a procedure to reduce the loss of particle images due to in-plane displacement, i.e. to increase the value for F_I. This was achieved by using a window offset, which means that each interrogation area of the first image is not cross-correlated with the same interrogation area of the second image, but with an interrogation area that was shifted by the particle displacement:

$$R(\mathbf{s}) = \sum_{i=1}^{N}\sum_{j=1}^{M} I(i, j) I\left(i + i_{shift} + s_x, j + j_{shift} + s_y\right) \tag{2.21}$$

This procedure implies that the displacement is determined in two steps. In the first step the overall displacement is determined, while this result is refined in the second step. Westerweel *et al.* (1997) concluded that this procedure can also be used to increase the precision and the accuracy of the determination of the displacement.

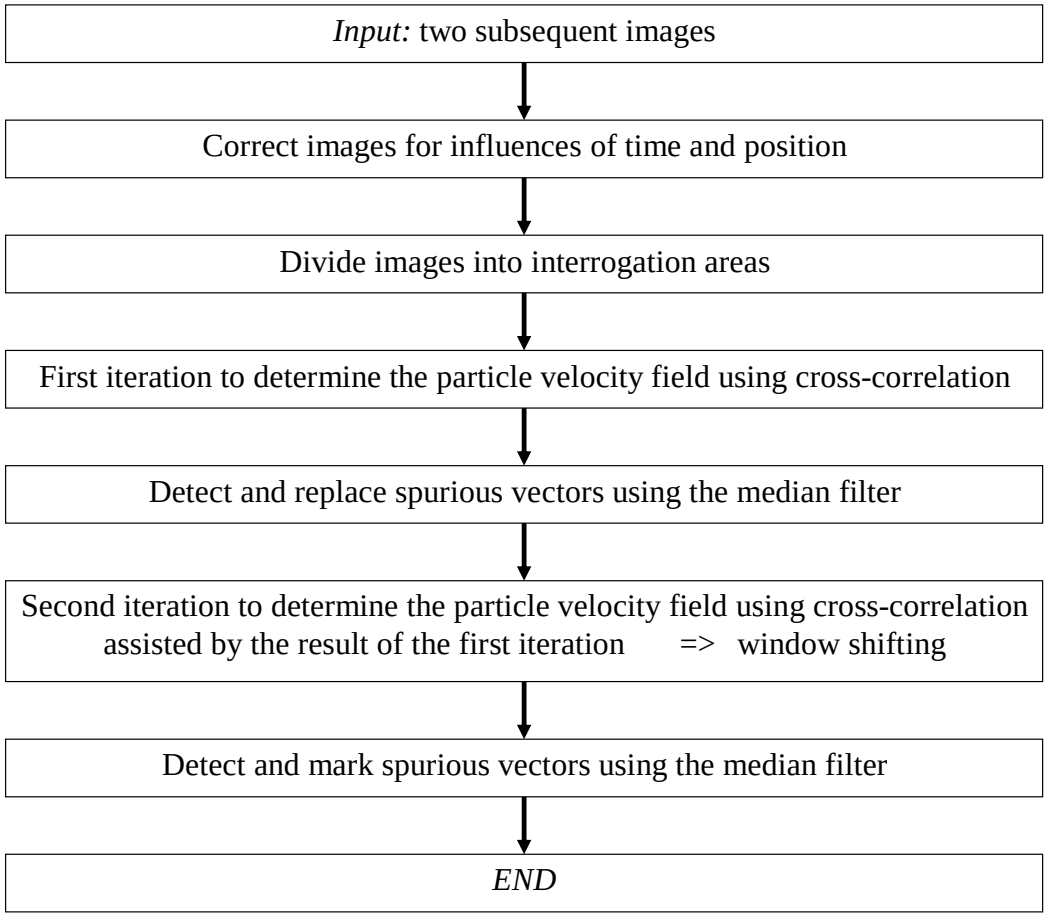

Figure 2.10 Flow diagram of the particle image velocimetry analysis procedure.

Even when the design rules are met and window-shifting is applied, the particle velocity field produced by the PIV analysis contains spurious vectors. These are vectors that significantly deviate from the flow pattern of the particle phase, which should be reasonably continuous. Westerweel (1994) found that a local median test is the most effective method to eliminate these spurious vectors. In this test, each vector is compared with the median of the eight surrounding vectors. This technique was applied in this thesis to improve the results.
The whole PIV analysis procedure is summarized in a flow diagram displayed in Figure 2.10.

2.4 Spectral analysis of pressure drop fluctuations

Spectral analysis of pressure drop fluctuations (SAPDF) is a non-intrusive measurement technique, which supplies information about the dynamic behavior of the particles in a spout-fluid bed.
Fluidized, spout-fluid and spouted beds display dynamic behavior caused by the presence of heterogeneous flow structures. Consequently, the particle configuration changes continuously. Since the particle configuration affects the pressure drop, dynamic behavior involves pressure drop fluctuations. To capture the characteristics of the dynamic behavior, a Fourier transformation is applied to a recording of the temporal fluctuations of the pressure drop over the entire bed. The result of this transformation is rendered into a frequency spectrum, which characterizes the dynamic behavior of the bed.

Van der Schaaf *et al.* (1998) studied the contribution to the pressure drop fluctuations of both local, i.e. in the vicinity of the pressure probe, and global changes in the particle configuration. They concluded that global fluctuations originated from the bottom part of the bed and therefore needed to be caused by bubble formation or coalescence, while the local fluctuations originated from gas bubbles passing the sensor. These authors observed that the local fluctuations can mainly be discerned at high frequencies and are overpowered by the global fluctuations at intermediate frequencies (1-10 Hz). They also observed that the global fluctuations are more easily discerned near the bottom of the bed.

The global pressure drop fluctuations contain most information about the dynamic behavior of the entire bed, and are therefore more relevant for this study. The pressure drop fluctuations are therefore recorded just above the gas distributor. An example pressure drop signal is displayed in Figure 2.11. Furthermore, the spectral analysis will focus on the intermediate frequency range (1 - 10 Hz).

The Fourier transformation decomposes a periodic function into sinusoids of different frequency, which sum into the original function. It identifies the sinusoids of different frequency and their respective amplitudes. The coefficients of the Fourier transform of f(*t*) are defined as:

$$\mathrm{F}(u) = \int_{-\infty}^{\infty} \mathrm{f}(t) \cdot \mathrm{e}^{-i2\pi tu}\, dt \tag{2.22}$$

where i = $\sqrt{-1}$, *t* is time and *u* is termed the frequency variable.
The Fourier transform can be converted with:

$$e^{i\theta} = \cos\theta + i\sin\theta \tag{2.23}$$

into its sinusoidal form:

$$\mathrm{F}(u) = \int_{-\infty}^{\infty} \mathrm{f}(t)\left(\cos(2\pi ut) - i\sin(2\pi ut)\right)dt \tag{2.24}$$

The complex function F(*u*) can be decomposed into a real and an imaginary part according to:

$$\mathrm{F}(u) = \mathrm{R}(u) + i\,\mathrm{I}(u) \tag{2.25}$$

The magnitude of F(*u*) increases with the number of times the period associated with frequency *u* is observed in the signal and with its amplitude in the signal. Therefore F(*u*) represents the contribution of the function with frequency u to the original signal. The contribution of each frequency is usually represented by its power, which is the square of the magnitude of F(*u*):

$$\mathrm{P}(u) = \left|\mathrm{F}(u)\right|^2 = \mathrm{R}^2(u) + \mathrm{I}^2(u) \tag{2.26}$$

In practice, the pressure is not available as a continuous signal, like f(*t*), but measured at regular time intervals on *N* discrete points in time, which are indicated by *j*. Consequently, only *N* frequencies can be discerned, which are indicated by *k*. Therefore, a discrete Fourier transformation, the fast Fourier transfer (FFT) algorithm available in Matlab 6.5, was applied to the pressure drop fluctuations:

$$\mathrm{F}(k) = \sum_{j=1}^{N} \mathrm{f}(j)\, e^{\left(\frac{-i2\pi}{N}\right)(j-1)(k-1)} \tag{2.27}$$

Note that *k*=1 produces the sum of all inputs and consequently contains no information about the periodicity of the signal, and is therefore discarded. Furthermore, *k* and (*N*-*k*+2) produce the same results, which means that the second half of F(*k*) is the same as the first half and therefore redundant.

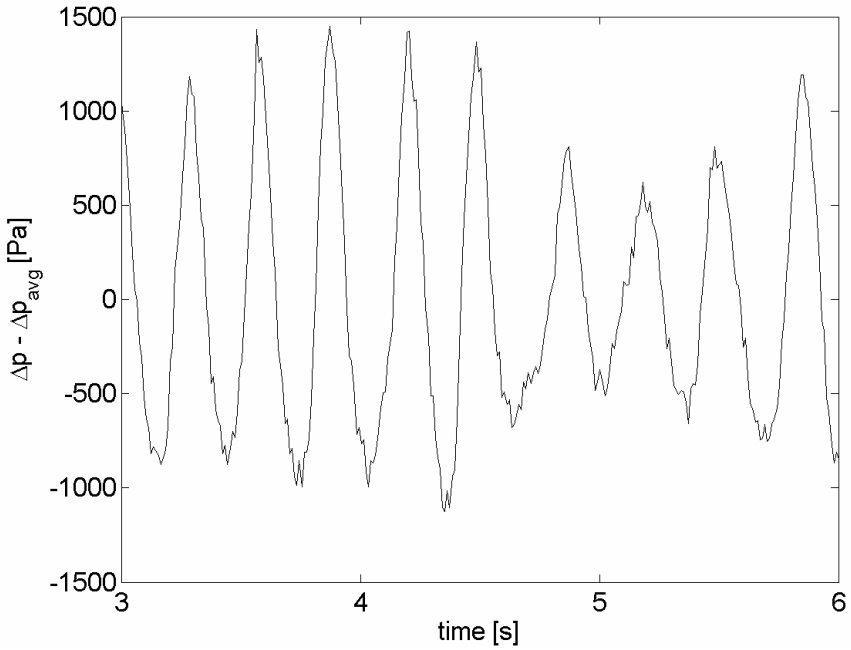

Figure 2.11 A typical recording of the pressure drop over a spout-fluid bed.

Since the magnitude of F is a linear function of *N*, *N* was used to normalize P:

$$\mathrm{P}(k) = \left(\frac{|\mathrm{F}(k)|}{N/2} \right)^2 \tag{2.28}$$

Note that since the first element of F and the second half of F were discarded, P only consists of *N*/2 elements.
Each element of P(k) is associated with the following frequency:

$$\mathrm{freq}(k) = \frac{f_{sample}}{N} k \tag{2.29}$$

where f_{sample} is the sampling rate.
The frequency spectrum consists of a plot of P versus the frequency.

Equation 2.29 shows that the maximum number of frequencies that can be distinguished per Hz depends on $\frac{N}{f_{sample}}$, i.e. the period over which the pressure drop signal is recorded. Consequently, pressure drop signals that are recorded over different periods of time can only be appropriately compared, when the frequency spectra are scaled.

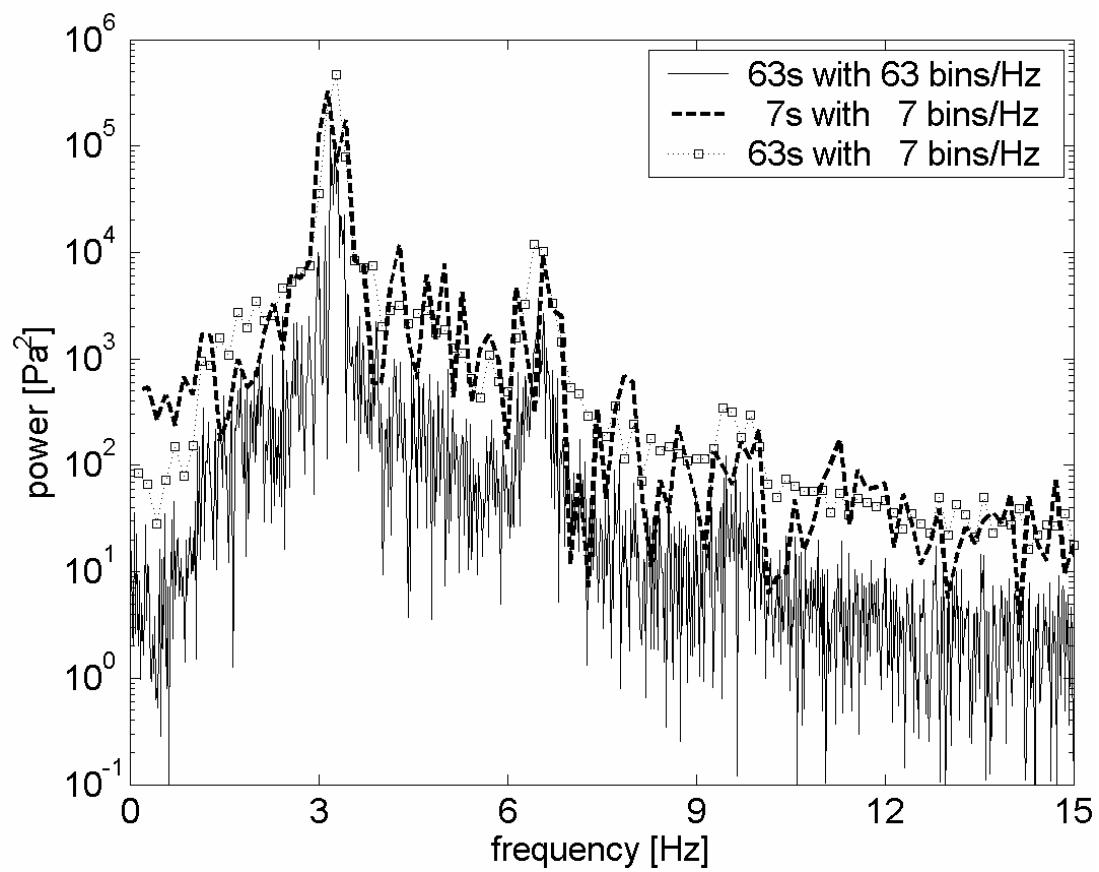

Figure 2.12 Example frequency spectra of pressure drop fluctuations measured over different time intervals.

The scaling procedure is explained using an analogy with a histogram. A larger number of frequencies per Hz is analogous to a smaller bin size in a histogram. When two data sets recorded over different periods of time are considered, the frequency spectra that are based on pressure drop signals that are recorded over the longest period of time consist of a larger number of smaller bins. The contributions, i.e. powers, to several smaller bins can be added to result in bins that have the same size as the bins that are encountered in the pressure drop signal recorded over the shortest period of time.

Example frequency spectra, both scaled and unscaled, are displayed in Figure 2.12. The unscaled frequency spectrum after a period of 7 s does not seem to correspond with the unscaled frequency spectrum obtained after a period of 63 s. When the frequency spectrum obtained after a period of 63 s is scaled to match the number of bins present in the unscaled frequency spectrum after a period of 7 s, it resembles the frequency spectrum obtained after a period of 7 s much more closely.

2.5 Positron emission particle tracking

Positron emission particle tracking (PEPT) is a non-intrusive measurement technique, which supplies detailed information about the particle motion by tracking the position of a single activated particle. PEPT was first applied to engineering equipment by Parker *et al.* (1993) and Parker and McNeil (1996). Stein *et al.* (1997, 2000) and Hoomans *et al.* (2001) were among the first to apply PEPT to fluidized beds.
Contrary to other non-intrusive measurement techniques, like PIV, PEPT supplies information about the particle behavior in the interior of the bed. This allows an experimental study of a three dimensional spout-fluid bed, where the spout is located at the geometrical center. PEPT supplies very detailed information about the behavior of a single particle, which makes it a very useful technique to validate discrete particle models, like the one that will be presented in chapter 3. A drawback of the technique is that it only allows the study of a single particle and therefore requires a long measuring time to produce results that are representative for the entire bed.

PEPT takes advantage of a particular class of radioisotopes, which decay through the emission of positrons. When the positrons encounter electrons, they are annihilated, converting matter into two back-to-back 511 keV gamma rays. These gamma rays are simultaneously detected by a pair of detectors. The position of the particle emitting the positrons is reconstructed by calculating the point of intersection of several pairs of gamma rays, which is illustrated in Figure 2.13.

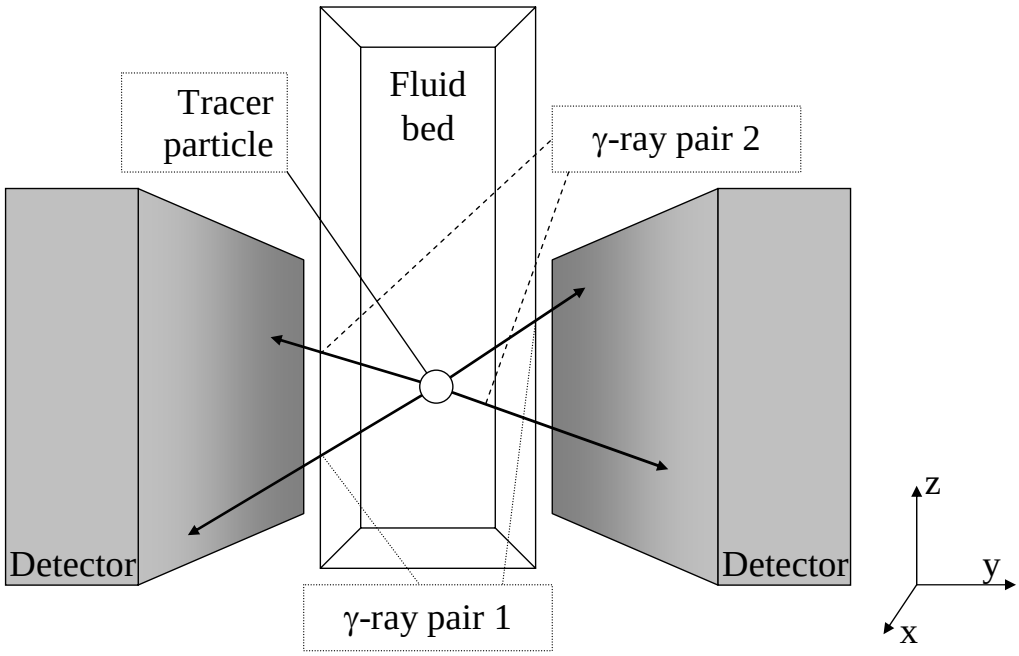

Figure 2.13 Illustration of the detection of a particle based on successive back to back γ-ray pairs emerging from a particle.

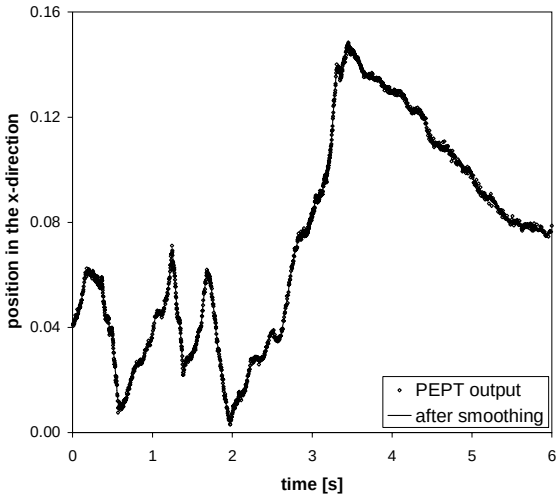

Particle trajectory in the x-direction

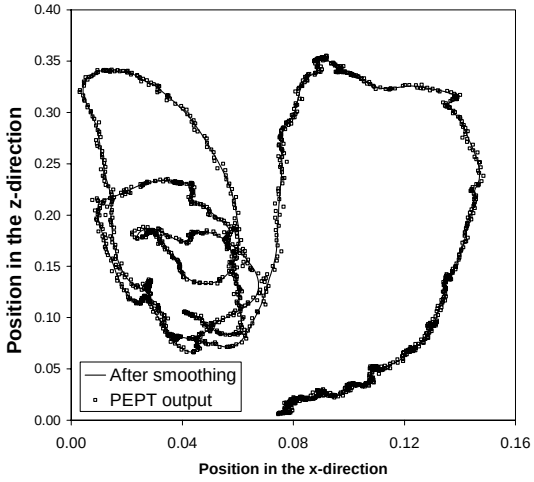

xz-projection of the particle trajectory

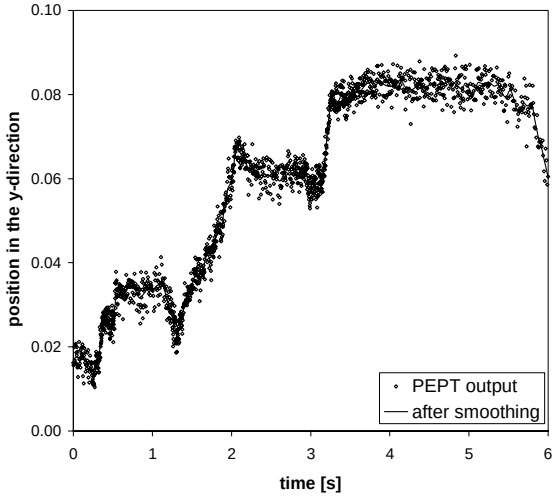

Particle trajectory in the y-direction

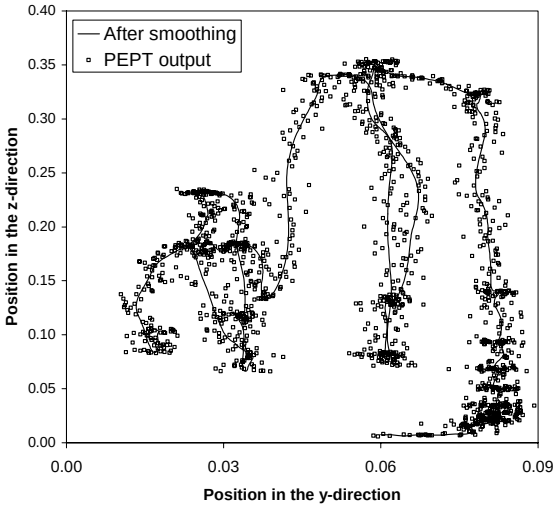

yz-projection of the particle trajectory

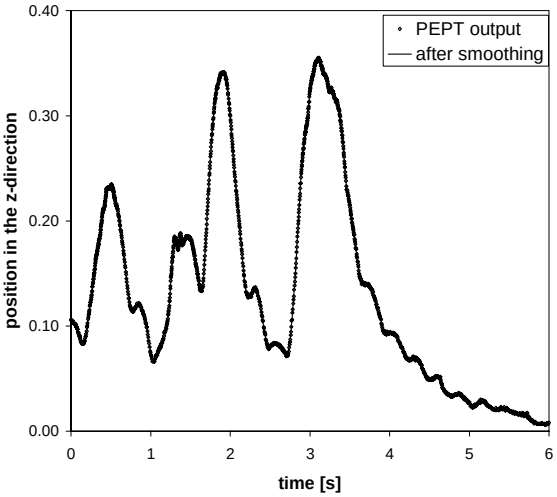

Particle trajectory in the z-direction

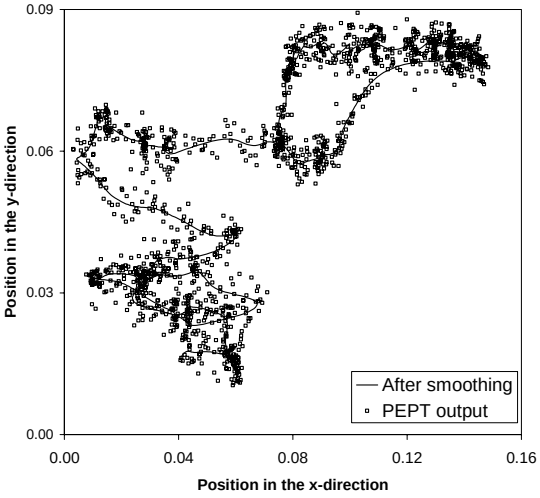

xy-projection of the particle trajectory

Figure 2.14 Particle trajectories in three directions originating from the PEPT measurements and their xz-, yz- and xy-projections along with the associated smoothing splines.

The three dimensional spout-fluid bed was placed in between two PEPT detectors. Depending on the amount of radiation emitted by the single tracer particle that was present in the bed, the space between the detectors and the bed was varied. The tracer particle was produced by exposing one of the glass particles used in the experiments to a ^{3}He beam generated by a cyclotron to produce the positron emitter ^{18}F from reactions involving ^{16}O in the glass.

The primary output of the PEPT measurements consisted of the particle position as a function of time in three directions, which is illustrated in Figure 2.14. The PEPT output contained a certain amount of noise. The amount of noise observed in each direction differed significantly and also depended on the location of the particle within the bed. The noise was most profound in the horizontal plane near the bottom of the bed, which was close to the edge of the PEPT detectors. At the edge of the detectors, the differences in the slopes of the intersecting γ-ray pairs in one or more directions is small. Therefore the accuracy of the point of intersection in those directions, which is representing the location of the tracer particle, is reduced. Consequently, the amount of noise is increased. In order to suppress the noise, a cubic smoothing spline filter was applied to the PEPT output data.
Since the PEPT detectors only covered the lower part of the bed, the tracer particle occasionally left the detectable range. In that case, the readings directly before exit and after return of the particle were discarded.
To diminish the effect of the remaining noise on the time-averaged particle velocities, all instantaneous particle velocities are calculated using the average particle velocity over six subsequent particle locations. The velocity is subsequently assigned to the cell containing the average position over six particle locations. An example velocity field is presented in Figure 2.15.

2.5.1 Particle circulation time

The particle position versus time resulting from the PEPT analysis was also used to determine the amount of time a particle requires to move from the bottom of the bed, up the spout, and back down through the annulus towards the bottom, which is termed the particle circulation time. The particle circulation time can be used to assess differences in the behavior of small and large particles, to compare the extent of circulation for different operating regimes and to study the distribution of particle circulation times within a single experiment.
The detection of a cycle in a spout-fluid bed differs from the methods used for spouted beds, e.g Larachi *et al.*, 2003. This is necessary, since, contrary to spouted beds, the spout-fluid bed is not necessarily operated in a steady state, i.e. due to the influence of bubbles in the annulus, the spout channel does not necessarily

continuously display the same angle with the bottom plate. Furthermore, the bubbles in the annulus of a spout-fluid bed disturb the regular flow patterns generally observed in the annulus of spouted beds.

An example of a cycle is presented in Figure 2.16. A cycle is determined by analyzing the location of the particle in the z-direction, i.e. the particle height. In this case, a cycle starts with a local maximum in the particle height (point A), followed by a local minimum (point B), which is at least 0.05 m below point A. As long as point B is not found, point A can be adjusted, when a new local maximum is found with a higher value than the current local maximum. After a proper point B is found, the cycle is completed when the next local maximum (point C), which is at least 0.05 m above the local minimum, is found. As long as point C is not found, point B can be adjusted, when a new local minimum is found with a smaller value than the current local minimum.

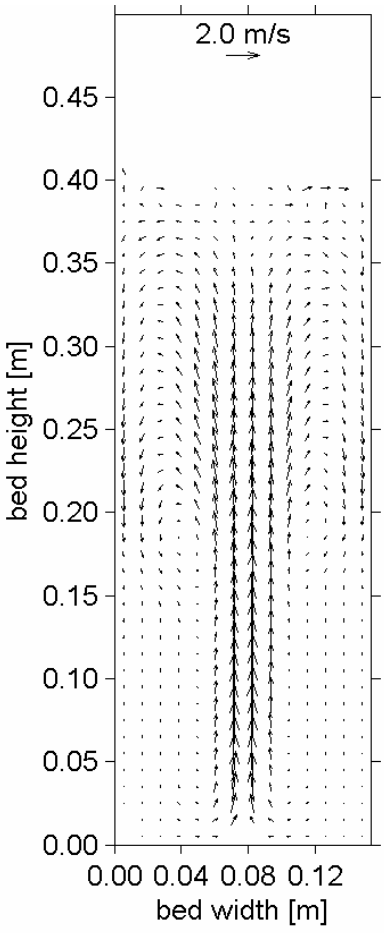

time-averaged particle velocity field

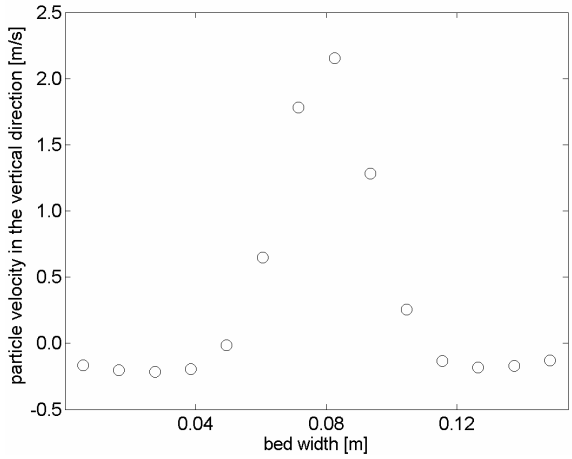

time-averaged particle velocity profile

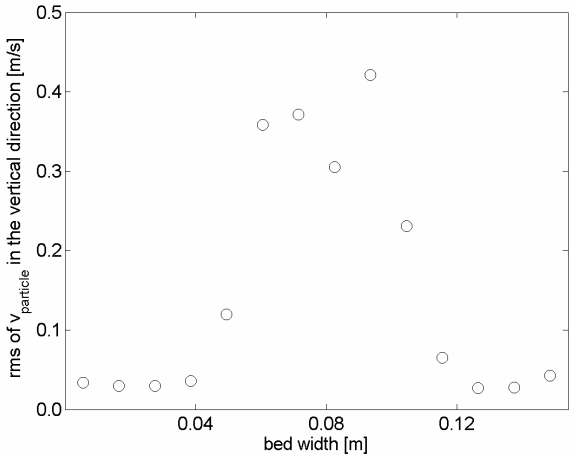

rms of the time-averaged particle velocity profile

Figure 2.15 Example of the time-averaged particle velocities including the rms-component in the vertical direction determined using PEPT.

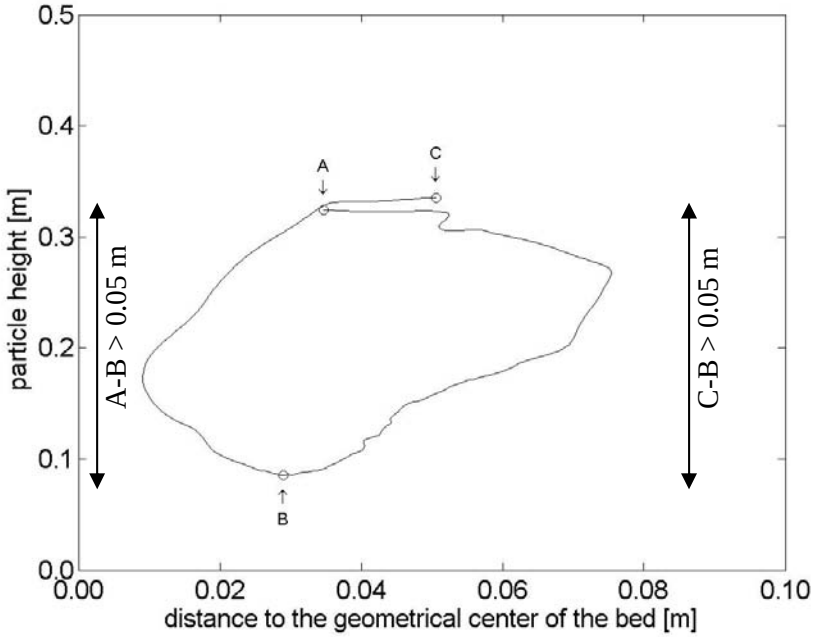

Figure 2.16 Illustration of a cycle and its detection algorithm.

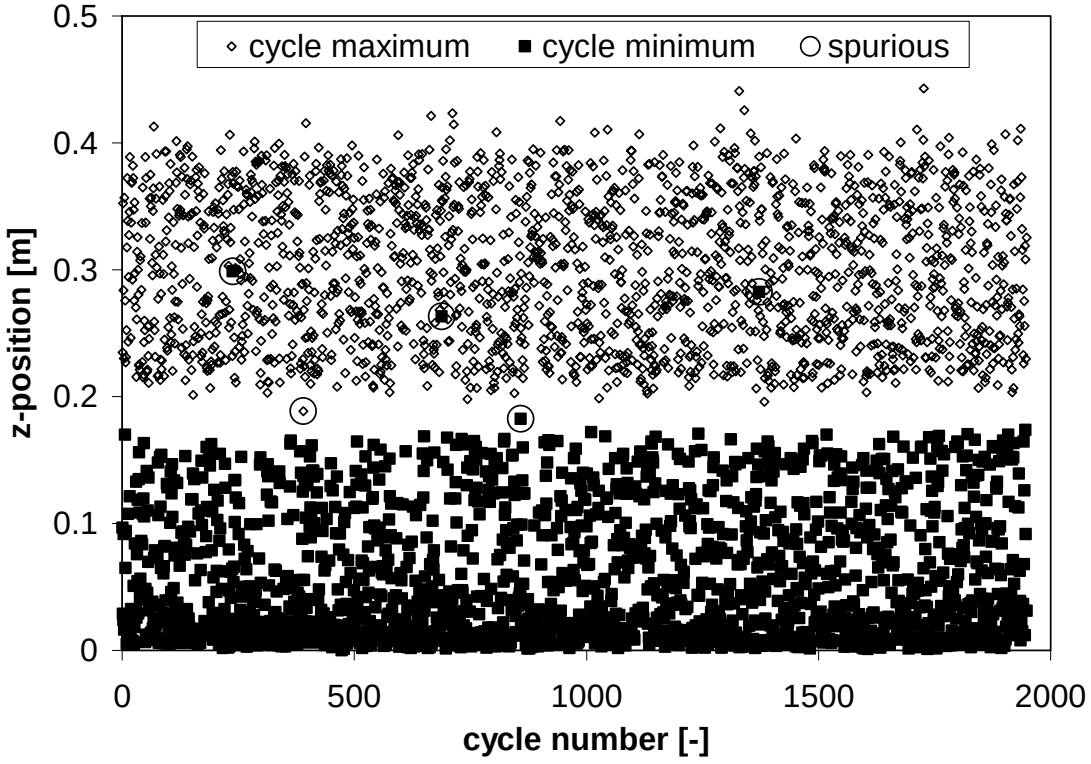

Figure 2.17 Overview of the minimum and maximum particle heights in a cycle for a typical experiment in a spout-fluid bed.

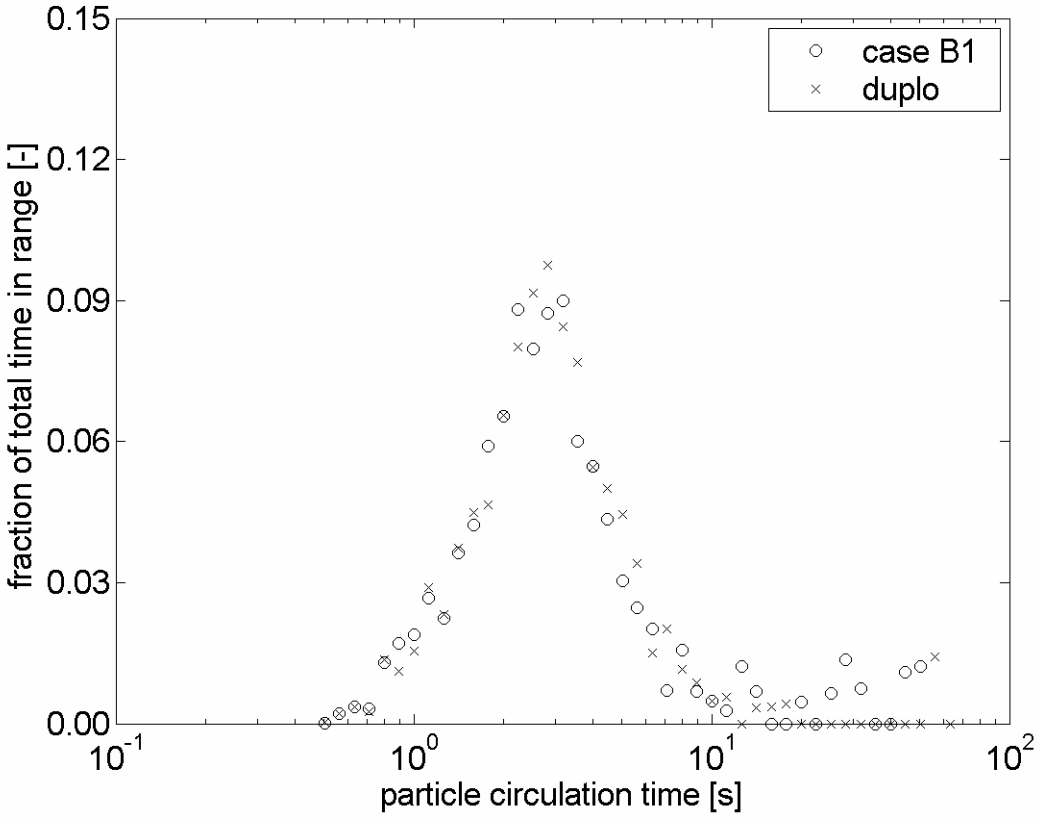

Figure 2.18 Histogram of particle circulation times for a typical experiment in a spout-fluid bed.

The minimum increase or decrease in height of 0.05 m was used to avoid spurious cycles caused by noise in the measurement and by small bubbles, which drag the particle upwards when they pass. After the analysis, pictures of the particle trajectory of each cycle were examined. Virtually all cycles were valid cycles. Rejected valid cycles, which would have been portrayed in these pictures if they existed, were scarcely observed.

The obtained cycles are subsequently validated by evaluating the values of the minimum and maximum z-position of each cycle. An example overview of the minimum and maximum z-position of each cycle in a typical experiment is presented in Figure 2.17. The figure shows that most of the minima are below a certain height (~ 0.18 m) and most maxima can be found above this height. The height dividing the minima and the maxima is virtually the same for all experiments. This implies that the particle needs to pass a certain height to complete a proper cycle. Most spurious cycles can be easily discerned in Figure 2.17 and are subsequently checked manually and eliminated.

Figure 2.18 presents the resulting particle circulation time distribution in the form of a histogram. The figure shows that the distribution of the particle circulation times is quite wide. Since the particle takes more time to pass through long cycles, the impact of these cycles on the overall result should be larger. Therefore the particle circulation time itself is used as a weight factor in the histogram. The horizontal axis of the histogram has a logarithmic scale, as does the bin size used on the x-axis.

Chapter 3

Theoretical model and numerical solution procedures

Abstract

In this chapter the discrete particle model used in this work is presented. The model uses the volume-averaged Navier-Stokes equations to compute the flow of the gas. The interaction between the gas phase and the particles is described using drag relations, three of which are presented in this chapter.
Two approaches towards the particle-particle interaction are used in this work: the hard sphere approach and the soft-sphere approach. In the hard sphere approach particles are assumed to interact through instantaneous binary collisions, while the soft-sphere approach calculates contact forces from the overlap between the particles based on a linear spring/dash-pot model. Both approaches account for energy dissipation through the coefficients of friction, normal and tangential restitution.

The model treats the inter-phase coupling in a manner, which is independent of the computational grid. This was achieved by using a new method, which is presented in this chapter. This method allows the computational grid to reach the level of refinement that is required to treat the large velocity gradients that are present in the vicinity of the spout.
The chapter is concluded by a description of the computational strategy that was employed.

3.1 Introduction

In this chapter the discrete particle model (DPM) is presented, which describes the behavior of gas-particle systems, like fluidized beds, spouted beds and spout-fluid beds.

The DPM resolves the behavior of the gas phase and individual particles in detail, while taking into account the interaction between individual particles and between particles and the gas phase. The gas phase is described by volume-averaged Navier-Stokes equations, while each individual particle obeys Newton's laws of motion. The equations governing the dynamics of both phases are presented in section 3.2, which also includes the three different drag closures that are used to calculate the fluid-particle interaction, which plays a significant role in a spout-fluid bed. Two approaches for the description of the particle-particle interaction are used in this thesis: the hard sphere approach, which was introduced to fluidized bed modeling by Hoomans *et al.* (1996), and the soft sphere approach, which was introduced by Tsuji *et al.* (1993). Both approaches are presented in section 3.3. The mapping of the variables from the Eulerian computational grid to the Lagrangian particle position and vice versa, requires a stencil that is relatively coarse with respect to the particle size. The sharp gradients near the spout however demand for a relatively fine computational grid. In order to solve this issue an alternative grid independent mapping method was developed, which is presented in section 3.4. Finally the computational strategy is presented in section 3.5, together with the algorithm used in the hard sphere approach.

3.2 Model equations

The gas phase flow field is computed from a generalized form of the volume-averaged Navier-Stokes equations for a gas interacting with a solid phase, as originally derived by Anderson and Jackson (1967). The equations for the conservation of mass and momentum are respectively given by:

$$\frac{\partial}{\partial t}(\varepsilon_f \rho_f) + \nabla \cdot (\varepsilon_f \rho_f \mathbf{u}_f) = 0 \tag{3.1}$$

$$\frac{\partial}{\partial t}(\varepsilon_f \rho_f \mathbf{u}_f) + \nabla \cdot (\varepsilon_f \rho_f \mathbf{u}_f \mathbf{u}_f) = -\varepsilon_f \nabla p - \nabla \cdot (\varepsilon_f \boldsymbol{\tau}_f) - \mathbf{S}_p + \varepsilon_f \rho_f \mathbf{g} \tag{3.2}$$

where the density of the fluid phase is calculated using the ideal gas law:

$$\rho_f = \frac{M_f}{RT} p \tag{3.3}$$

and the viscous stress tensor is assumed to obey the general form for a Newtonian fluid (Bird *et al.*, 1960):

$$\boldsymbol{\tau}_f = -\left[\left(\lambda_f - \frac{2}{3}\mu_f\right)\left(\nabla\cdot\mathbf{u}_f\right)\mathbf{I} + \mu_f\left(\left(\nabla\mathbf{u}_f\right) + \left(\nabla\mathbf{u}_f\right)^T\right)\right] \tag{3.4}$$

Two-way coupling is achieved via the sink term, which is computed from:

$$\mathbf{S}_p = \frac{1}{V_{cell}}\sum_{\forall i\in V_{cell}} \frac{V_i\beta}{\varepsilon_p}(\mathbf{u}_f - \mathbf{v}_i)D(\mathbf{r}-\mathbf{r}_i) \tag{3.5}$$

where $\varepsilon_p = 1-\varepsilon_f$.

The distribution function, *D*, distributes the reaction force of the particles exerted on the gas phase to the velocity nodes in the (staggered) Eulerian grid. β represents the inter-phase momentum transfer coefficient due to drag. Several drag closures, which can be used to calculate β, are available, three of which are used in this thesis.

The Ergun equation (1952), which was originally developed for packed beds, is given by:

$$\beta_{Ergun} = 150\frac{\varepsilon_p^2}{\varepsilon_f}\frac{\mu_f}{d_p^2} + 1.75\varepsilon_p\frac{\rho_f}{d_p}\left|\mathbf{u}_f - \mathbf{v}_p\right| \tag{3.6}$$

Wen and Yu (1966) derived the following relation based on the drag caused by a single sphere:

$$\beta_{Wen\&Yu} = \frac{3}{4}C_D\varepsilon_p\frac{\rho_f}{d_p}\left|\mathbf{u}_f - \mathbf{v}_p\right|\varepsilon_f^{-1.65} \tag{3.7}$$

where C_D is based on the drag coefficient for an isolated spherical particle given by Schiller and Naumann (1933):

$$C_D = \begin{cases} \dfrac{24}{\mathrm{Re}_p}(1+0.15\,\mathrm{Re}_p^{0.687}) & \text{if} \quad \mathrm{Re}_p < 1000 \\ 0.44 & \text{if} \quad \mathrm{Re}_p \geq 1000 \end{cases} \tag{3.8}$$

with

$$\mathrm{Re}_p = \frac{\varepsilon_f\rho_f\left|\mathbf{u}_f - \mathbf{v}_p\right|d_p}{\mu_f} \tag{3.9}$$

Koch and Hill (2001) proposed a drag relation obtained from lattice-Boltzmann simulations:

$$\beta_{Koch\&Hill} = \frac{18\mu_f \varepsilon_f^2 \varepsilon_p}{d_p^2}\left(F_0(\varepsilon_p) + \tfrac{1}{2}F_3(\varepsilon_p)\,\mathrm{Re}_p\right) \qquad \text{if} \qquad \mathrm{Re}_p > 40 \tag{3.10}$$

where Re_p is given by equation 3.9 and with:

$$F_0(\varepsilon_p) = \begin{cases} \dfrac{1 + 3\sqrt{\dfrac{\varepsilon_p}{2}} + \dfrac{135}{64}\varepsilon_p \ln(\varepsilon_p) + 16.14\varepsilon_p}{1 + 0.681\varepsilon_p - 8.48\varepsilon_p^2 + 8.16\varepsilon_p^3} & \text{if} \quad \varepsilon_p < 0.4 \\ \dfrac{10\varepsilon_p}{\varepsilon_f^3} & \text{if} \quad \varepsilon_p \geq 0.4 \end{cases} \tag{3.11}$$

$$F_3(\varepsilon_p) = 0.0673 + 0.212\varepsilon_p + \frac{0.0232}{\varepsilon_f^5} \tag{3.12}$$

These relations were derived based on lattice-Boltzmann simulations for Re_p up to $O(10^2)$ and ε_p ranging from 0.1 to the close-packed limit (i.e. 0.64).

The motion of each individual particle present in the system is calculated from the Newtonian equations of motion:

$$m_a \frac{d\mathbf{v}_a}{dt} = -V_a \nabla p + \frac{V_a \beta}{\varepsilon_p}\left(\mathbf{u}_f - \mathbf{v}_a\right) + m_a \mathbf{g} + \sum_{\forall b \in N_{part}} \mathbf{F}_{a \leftrightarrow b} + \sum_{\forall b \in N_{walls}} \mathbf{F}_{a \leftrightarrow b} \tag{3.13}$$

$$I_a \frac{d\boldsymbol{\omega}_a}{dt} = \mathbf{T}_a \tag{3.14}$$

where N_{part} en N_{walls} respectively represent the number of particles and walls in the system. The moment of inertia is defined as:

$$I = \frac{2}{5} m r^2 \tag{3.15}$$

The terms on the right hand side of equation 3.13 respectively represent the forces due to pressure, drag, gravity, particle-particle interaction and particle-wall interaction.

3.3 Particle-particle interaction

Two approaches regarding the treatment of particle-particle interaction have been implemented in the discrete particle model: the hard sphere approach and the soft sphere approach, which are subsequently presented.

In the hard sphere approach the particles are assumed to interact through binary, quasi-instantaneous collisions where contact occurs at a point. The particles are perfect, homogeneous spheres and the interaction forces are impulsive and therefore all other finite forces are negligible during the collision. Campbell and Brennen (1985) introduced collision parameters into the hard sphere approach to account for energy dissipation during the collision.

In the soft-sphere approach the particles are assumed to undergo deformation during their contact, where the contact forces are calculated from a simple mechanical analogue involving a spring, a dash-pot and a slider, which allows for energy dissipation during the contact. In case a particle is in contact with several other particles the resulting contact force follows from the addition of all binary contributions. This approach was originally proposed by Cundall and Strack (1979) for granular matter and is illustrated in Figure 3.1.

Which approach is more suitable to describe the particle-particle interaction depends on the particle velocities. When zones with extremely low particle velocities occur, e.g. defluidized zones, the hard sphere approach will experience significant problems because it, contrary to the soft sphere approach, cannot efficiently handle long term (multiple) particle contacts. These contacts are modeled as a sequence of countless irrelevant collisions, taking up most of the limited number of collisions that can be handled by the hard sphere approach.

On the other hand when particle velocities are high, like in a spout, the soft sphere approach is less efficient than the hard sphere approach. In the soft sphere approach, high particle velocities require relatively small fixed time steps, consequently increasing the required number of time steps and as a result the computation time.

To be able to handle all flow conditions that occur in spout-fluid beds most efficiently, both approaches were implemented in the DPM. Each of these approaches will now be discussed in detail.

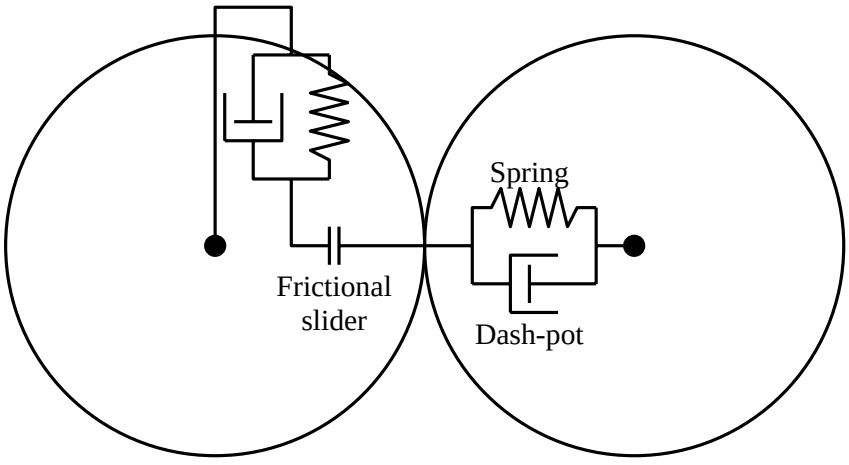

Figure 3.1 The linear spring/dash-pot model.

3.3.1 Hard-Sphere approach

Figure 3.2 shows the coordinate system that was used in the hard sphere approach for two colliding spheres *a* and *b* with position vectors $\mathbf{r}_a$ and $\mathbf{r}_b$. Prior to collision, the spheres with radii r_a and r_b and masses m_a and m_b have translation velocity vectors $\mathbf{v}_a$ and $\mathbf{v}_b$ and rotational velocity vectors $\boldsymbol{\omega}_a$ and $\boldsymbol{\omega}_b$ (clockwise rotation is negative by definition).

The normal unit vector is defined as:

$$\mathbf{n}_{ab} = \frac{\mathbf{r}_a - \mathbf{r}_b}{|\mathbf{r}_a - \mathbf{r}_b|} \tag{3.16}$$

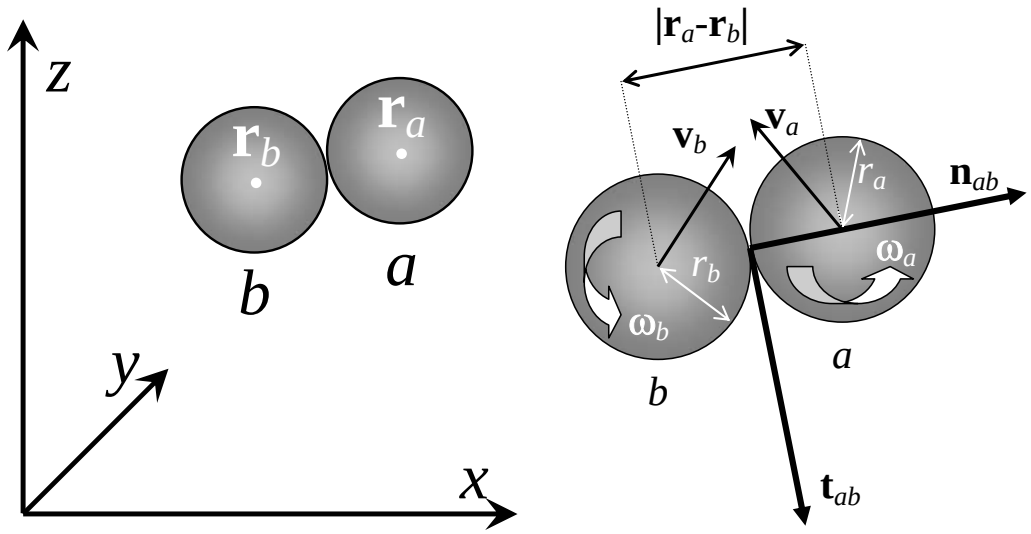

Figure 3.2 The coordinate system used in the hard sphere approach.

Hence the normal unit vector points in the direction from the centre of particle *b* to the centre of particle *a*. The point of origin is located at the contact point between the particles.

The relative velocity at the contact point ($\mathbf{v}_{ab}$) is defined as:

$$\mathbf{v}_{ab} = (\mathbf{v}_a - \mathbf{v}_b) - (r_a\boldsymbol{\omega}_a + r_b\boldsymbol{\omega}_b) \times \mathbf{n}_{ab} \tag{3.17}$$

From the relative velocity and the normal unit vector, the tangential unit vector can be obtained:

$$\mathbf{t}_{ab} = \frac{\mathbf{v}_{ab,0} - \mathbf{n}_{ab}(\mathbf{v}_{ab,0} \cdot \mathbf{n}_{ab})}{\left|\mathbf{v}_{ab,0} - \mathbf{n}_{ab}(\mathbf{v}_{ab,0} \cdot \mathbf{n}_{ab})\right|} \tag{3.18}$$

To determine the post-collision velocities of the particles *a* and *b*, the following equations were derived by applying Newton's second and third laws:

$$m_a(\mathbf{v}_a - \mathbf{v}_{a,0}) = -m_b(\mathbf{v}_b - \mathbf{v}_{b,0}) = \mathbf{J}_{ab} \tag{3.19}$$

$$\frac{I_a}{r_a}(\boldsymbol{\omega}_a - \boldsymbol{\omega}_{a,0}) = \frac{I_b}{r_b}(\boldsymbol{\omega}_b - \boldsymbol{\omega}_{b,0}) = -\mathbf{n}_{ab} \times \mathbf{J}_{ab} \tag{3.20}$$

where $\mathbf{J}_{ab}$ is the impulse vector.

Equations 3.19 and 3.20 can be rearranged using $(\mathbf{n} \times \mathbf{J}) \times \mathbf{n} = \mathbf{J} - \mathbf{n}(\mathbf{J} \cdot \mathbf{n})$ and equation 3.17 to obtain:

$$\mathbf{v}_{ab} - \mathbf{v}_{ab,0} = \frac{7}{2}\frac{\mathbf{J}_{ab}}{m_{ab}} - \frac{5}{2}\frac{\mathbf{n}_{ab}(\mathbf{J}_{ab} \cdot \mathbf{n}_{ab})}{m_{ab}} \tag{3.21}$$

where

$$m_{ab} = \left(\frac{1}{m_a} + \frac{1}{m_b}\right)^{-1} \tag{3.22}$$

In particle-wall collisions the mass of particle *b* (*i.e.* the wall) is infinitely large, resulting in $m_{ab} = m_a$.

To solve equation 3.21 $\mathbf{J}_{ab}$ needs to be known, which requires a description of the physics of the binary collision. In simulations of gas-fluidized beds a large number of collisions (typically 10^6-10^9) is processed. To reduce the amount of time required to process the collisions, without significantly affecting the accuracy, the actual physics of a binary collision is simplified to some extent, and constitutive relations are introduced to close the set of equations, which introduces three parameters to the model:
The coefficient of normal restitution ($0 \le e_n \le 1$):

$$\mathbf{v}_{ab} \cdot \mathbf{n}_{ab} = -e_n\left(\mathbf{v}_{ab,0} \cdot \mathbf{n}_{ab}\right) \tag{3.23}$$

the coefficient of (dynamic) friction ($\mu \ge 0$):

$$\left|\mathbf{n}_{ab} \times \mathbf{J}_{ab}\right| = -\mu\left(\mathbf{n}_{ab} \cdot \mathbf{J}_{ab}\right) \tag{3.24}$$

and the coefficient of tangential restitution ($0 \le \beta_0 \le 1$):

$$\mathbf{v}_{ab} \cdot \mathbf{t}_{ab} = -\beta_0\left(\mathbf{v}_{ab,0} \cdot \mathbf{t}_{ab}\right) \tag{3.25}$$

Combining equations 3.21 and 3.23 yields the following expression for the magnitude of the normal component of the impulse vector:

$$J_n = -(1+e_n)\, m_{ab} \left(\mathbf{v}_{ab,0} \cdot \mathbf{n}_{ab} \right) \tag{3.26}$$

For the tangential component of the impulse vector two types of collisions are distinguished: *sticking* and *sliding*. If gross sliding occurs throughout the whole duration of the contact, the collision is of the *sliding* type. The non-sliding collisions are of the *sticking* type. When β_0 is zero, the tangential component of the relative velocity becomes zero during a sticking collision. When β_0 is greater than zero in such a collision, reversal of the tangential component of the relative velocity will occur.
The magnitude of the tangential impulse vector depends on the type of collision:

$$J_t = \begin{cases} -\frac{2}{7}(1+\beta_0)\, m_{ab} \left(\mathbf{v}_{ab,0} \cdot \mathbf{t}_{ab} \right) & \text{if} \quad \mu J_n \geq \frac{2}{7}(1+\beta_0)\, m_{ab} \left(\mathbf{v}_{ab,0} \cdot \mathbf{t}_{ab} \right) \\ -\mu J_n & \text{if} \quad \mu J_n < \frac{2}{7}(1+\beta_0)\, m_{ab} \left(\mathbf{v}_{ab,0} \cdot \mathbf{t}_{ab} \right) \end{cases} \tag{3.27}$$

where the two equations respectively describe collisions of the sticking and sliding type.
The impulse vector can simply be obtained by vector addition of the normal and tangential contributions:

$$\mathbf{J}_{ab} = J_n \mathbf{n}_{ab} + J_t \mathbf{t}_{ab} \tag{3.28}$$

The post-collision velocities can now be calculated from equations 3.19 and 3.20.

3.3.2 Soft-Sphere approach

Figure 3.3 shows the coordinate system that was used in the soft sphere approach for the two contacting spheres *a* and *b* with position vectors $\mathbf{r}_a$ and $\mathbf{r}_b$. Prior to collision, the spheres with radii r_a and r_b and masses m_a and m_b have translation velocity vectors $\mathbf{v}_a$ and $\mathbf{v}_b$ and rotational velocity vectors $\boldsymbol{\omega}_a$ and $\boldsymbol{\omega}_b$ (clockwise rotation is negative by definition).

The normal unit vector is defined as:

$$\mathbf{n}_{ab} = \frac{\mathbf{r}_b - \mathbf{r}_a}{\left| \mathbf{r}_b - \mathbf{r}_a \right|} \tag{3.29}$$

Hence the normal unit vector points in the direction from the centre of particle *a* to the centre of particle *b*. The point of origin is $\mathbf{r}_a$.

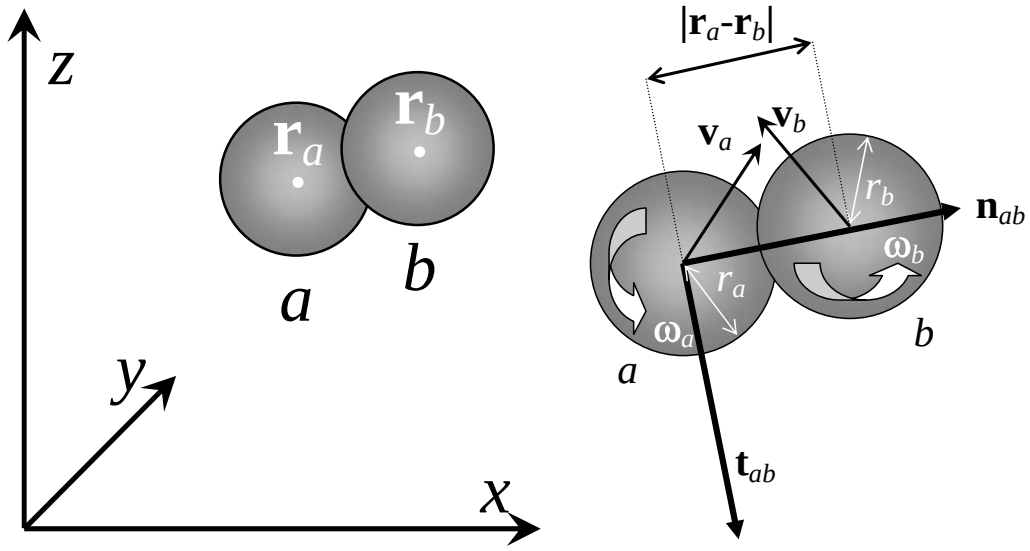

Figure 3.3 The coordinate system used in the soft sphere approach.

The relative velocity of particle a with respect to b is given by:

$$\mathbf{v}_{ab} = (\mathbf{v}_a - \mathbf{v}_b) + (r_a\boldsymbol{\omega}_a + r_b\boldsymbol{\omega}_b)\times\mathbf{n}_{ab} \tag{3.30}$$

and can be split into the normal component:

$$\mathbf{v}_{ab,n} = \left(\mathbf{v}_{ab}\cdot\mathbf{n}_{ab}\right)\mathbf{n}_{ab} \tag{3.31}$$

and the tangential component:

$$\mathbf{v}_{ab,t} = \mathbf{v}_{ab} - \mathbf{v}_{ab,n} \tag{3.32}$$

The tangential unit vector is defined as:

$$\mathbf{t}_{ab} = \frac{\mathbf{v}_{ab,t}}{\left|\mathbf{v}_{ab,t}\right|} \tag{3.33}$$

To determine the post-collision velocities, the Newtonian equations of motion for particle *a* (equations 3.13 and 3.14) need to be resolved. The soft sphere approach considers all particle-particle and particle-wall interactions as contact forces. The contact force on particle *a* is calculated as the sum of the contact forces of all particles in the contact list of particle *a*, i.e. all particles *b*, including walls, which are in contact with particle *a*:

$$\mathbf{F}_{contact,a} = \sum_{\forall b\in contact\ list}\left(\mathbf{F}_{ab,n} + \mathbf{F}_{ab,t}\right) \tag{3.34}$$

where $\mathbf{F}_{ab,n}$ and $\mathbf{F}_{ab,t}$ represent respectively the normal and tangential component of the contact force between particle *a* and *b*.

The torque is defined as:

$$\mathbf{T}_a = \sum_{\forall b \in contact\ list} \left(r_a\, \mathbf{n}_{ab} \times \mathbf{F}_{ab,t} \right) \tag{3.35}$$

In order to solve equations 3.34 and 3.35, the contact force between particles *a* and *b* needs to be determined. With a simple linear spring/dash-pot model the normal component of the contact force is obtained as follows:

$$\mathbf{F}_{ab,n} = -k_n \delta_n\, \mathbf{n}_{ab} - \eta_n \mathbf{v}_{ab,n} \tag{3.36}$$

where k_n is the stiffness of the normal spring.
The overlap is given by:

$$\delta_n = \left(r_a + r_b \right) - \left| \mathbf{r}_a - \mathbf{r}_b \right| \tag{3.37}$$

and the normal damping coefficient is given by:

$$\eta_n = \begin{cases} \dfrac{-2 \ln e_n \sqrt{m_{ab} k_n}}{\sqrt{\pi^2 + \ln^2 e_n}} & if \quad e_n \neq 0 \\ 2\sqrt{m_{ab} k_n} & if \quad e_n = 0 \end{cases} \tag{3.38}$$

where e_n is the coefficient of normal restitution, which has been defined in equation 3.23, and m_{ab} has been defined in equation 3.22. In particle-wall collisions the mass of particle *b* (*i.e.* the wall) is infinitely large, resulting in $m_{ab} = m_a$.

For the tangential component of the contact force the same two types of collisions are distinguished as in the hard sphere approach: *sticking* and *sliding*.
The tangential component of the contact force is defined as:

$$\mathbf{F}_{ab,t} = \begin{cases} -k_t \boldsymbol{\delta}_t - \eta_t\, \mathbf{v}_{ab,t} & \text{if} \quad \left| \mathbf{F}_{ab,t} \right| \leq \mu \left| \mathbf{F}_{ab,n} \right| \\ -\mu \left| \mathbf{F}_{ab,n} \right| \mathbf{t}_{ab} & \text{if} \quad \left| \mathbf{F}_{ab,t} \right| > \mu \left| \mathbf{F}_{ab,n} \right| \end{cases} \tag{3.39}$$

where the two equations respectively describe collisions of the sticking and sliding type. μ is the friction coefficient, which has been defined in equation 3.24, and k_t is the stiffness of the tangential spring.

The tangential damping coefficient is defined as:

$$\eta_t = \begin{cases} \dfrac{-2\ln\beta_0\sqrt{\dfrac{2}{7}m_{ab}k_t}}{\sqrt{\pi^2+\ln^2\beta_0}} & if \quad \beta_0 \neq 0 \\ 2\sqrt{\dfrac{2}{7}m_{ab}k_t} & if \quad \beta_0 = 0 \end{cases} \tag{3.40}$$

where β_0 is the friction coefficient, which has been defined in equation 3.25, and m_{ab} has been defined in equation 3.22.
The tangential displacement is given by:

$$\boldsymbol{\delta}_t = \begin{cases} \boldsymbol{\delta}_{t,0}\mathbf{H} + \int_{t_0}^{t} v_{ab,t}\,dt & \text{if} \quad \left|\mathbf{F}_{ab,t}\right| \leq \mu\left|\mathbf{F}_{ab,n}\right| \\ \dfrac{\mu}{k_t}\left|\mathbf{F}_{ab,n}\right|\mathbf{t}_{ab} & \text{if} \quad \left|\mathbf{F}_{ab,t}\right| > \mu\left|\mathbf{F}_{ab,n}\right| \end{cases} \tag{3.41}$$

with

$$\mathbf{H} = \begin{bmatrix} (1-\cos\varphi)h_x^2 + \cos\varphi & (1-\cos\varphi)h_x h_y - h_z\sin\varphi & (1-\cos\varphi)h_x h_z + h_y\sin\varphi \\ (1-\cos\varphi)h_x h_y + h_z\sin\varphi & (1-\cos\varphi)h_y^2 + \cos\varphi & (1-\cos\varphi)h_y h_z - h_x\sin\varphi \\ (1-\cos\varphi)h_x h_z - h_y\sin\varphi & (1-\cos\varphi)h_y h_z + h_x\sin\varphi & (1-\cos\varphi)h_z^2 + \cos\varphi \end{bmatrix} \tag{3.42}$$

$$\mathbf{h} = \frac{\mathbf{n}_{ab} \times \mathbf{n}_{ab,0}}{\left|\mathbf{n}_{ab} \times \mathbf{n}_{ab,0}\right|} \tag{3.43}$$

$$\varphi = \arcsin\left(\left|\mathbf{n}_{ab} \times \mathbf{n}_{ab,0}\right|\right) \tag{3.44}$$

The post-collision velocities can now be calculated by solving equations 3.13 and 3.14 numerically.

3.4 Inter-phase coupling

In order to resolve the large velocity gradients in the spout region, a sufficiently fine computational mesh is required. This causes the ratio between the size of the computational grid cells and the size of the particles to become relatively low, which is amplified by the generally large size of the particles in spout-fluid beds.
The calculation of the porosity and the two-way coupling between the gas phase and the particles through the fluid-particle interaction requires the ratio between the size of the computational grid cells and the size of the particles to be large. Therefore an

alternative method was developed for the DPM to overcome these contradictory demands regarding the computational grid.
This method, which is subsequently presented, calculates the porosity and the force exerted by the gas phase on the particles in a grid-independent manner, consequently allowing a sufficiently fine solution of the gas flow field.

3.4.1 Calculation of the porosity

A straightforward method for the calculation of the porosity was given by Hoomans *et al.* (1996). In their work, the porosity in an Eulerian grid cell is calculated as follows:

$$\varepsilon_{f,cell} = 1 - \frac{1}{V_{cell}} \sum_{\forall i \in cell} f_{cell}^{i} V_p^i \tag{3.45}$$

where f_{cell}^{i} is the fractional volume of particle i residing in the cell under consideration.
This method works well when the size of the grid cells is much larger than that of the particles (i.e. $V_{cell} >> V_p$). Unfortunately, the method generates problems once V_{cell} approaches V_p. That is, the impact of a particle on the gas-fraction of the grid cells around the center of its mass increases with decreasing grid cell size, eventually reaching a situation, where grid cells can be fully occupied by a single particle, which leads to a porosity of zero and hence numerical problems. In order to overcome these problems, an alternative method to calculate the porosity is suggested in this thesis.
In this alternative method the solid particles are represented as porous cubes with a size taken as:

$$d_{cube} = d_p a \tag{3.46}$$

Where a represents the ratio of the cube diameter and the particle diameter. The porosity of the cube can easily be calculated as:

$$\varepsilon_{cube} = \frac{V_p}{V_{cube}} = \frac{\pi}{6a^3} \tag{3.47}$$

Subsequently the method of Hoomans *et al.* (1996) to calculate the gas fraction in a cell is adapted to facilitate the porous cube representation:

$$\varepsilon_{f,cell} = 1 - \varepsilon_{cube} \sum_{\forall i \in cell} f_{cell}^{i} \tag{3.48}$$

where f_{cell}^{i} is the volume fraction of the cell under consideration that is occupied by cube i.
By representing the particle as a porous cube, its presence is felt only weakly in the same, relatively large, portion of the flow domain, and does not depend on the

computational grid. Consequently, grid refinement will not lead to local extremes in the gas-fraction around the center of mass of the particle. This property is consistent with the approach to model the gas flow on the basis of volume-averaged Navier-Stokes equations.

Due to the local nature of the method developed by Hoomans *et al.* (1996), in their case no special treatment of the porosity calculation near the boundaries is required.

The alternative method however needs to be adapted when a particle is close to a boundary, that is, when the cube representing the particle overlaps the boundary. This can be achieved by folding the cube at the boundary, which is illustrated in Figure 3.4a and b. When a particle is near a corner, the cube is folded back from each boundary it overlaps. The order in which the cube is folded does not influence the result. This concept is illustrated in the bottom part of Figure 3.4c and d.

With this treatment of the boundary, a system, which is filled with particles at an equal spacing in each direction, has a constant porosity throughout the system.

3.4.2 Coupling of the forces between the phases

The force balance for a single particle, which is used in our model to calculate the acceleration of the particle, is given by equation 3.13. The acceleration of the particle is required at the Lagrangian position of the particle. Therefore the properties of the gas phase, which are only available at distinct positions in space, i.e. the Eulerian computational grid, need to be mapped to the position of the particle.

Hoomans *et al.* (1996) used a volume-weighing technique for the mapping. This technique limits the interaction between the particles and the gas phase to eight computational grid cells, which generates local extremes in the fluid-particle drag around the center of mass of a particle when the grid is refined.

The momentum exchange coefficient, β, is calculated using a drag closure that is generally derived for control volumes significantly larger than the size of the particles. This coefficient should therefore be calculated over a large control volume in a way that is independent of the computational grid. Furthermore Newton's third law should be satisfied, which requires a consistent mapping technique.

By mapping the quantities relevant to the calculation of the acceleration of the particle with a method similar to that of the porosity mapping, both requirements can be met. A general variable ϕ_{cell} on the Eulerian grid can be mapped to a property ϕ_p on the Lagrangian position of the particle using the following equation:

$$\phi_p = \frac{1}{V_{cube}} \sum_{\forall j \in cube} f_j^{cube} V_j \phi_j \tag{3.49}$$

where f_j^{cube} is the volume fraction of cell *j* occupied by the cube.

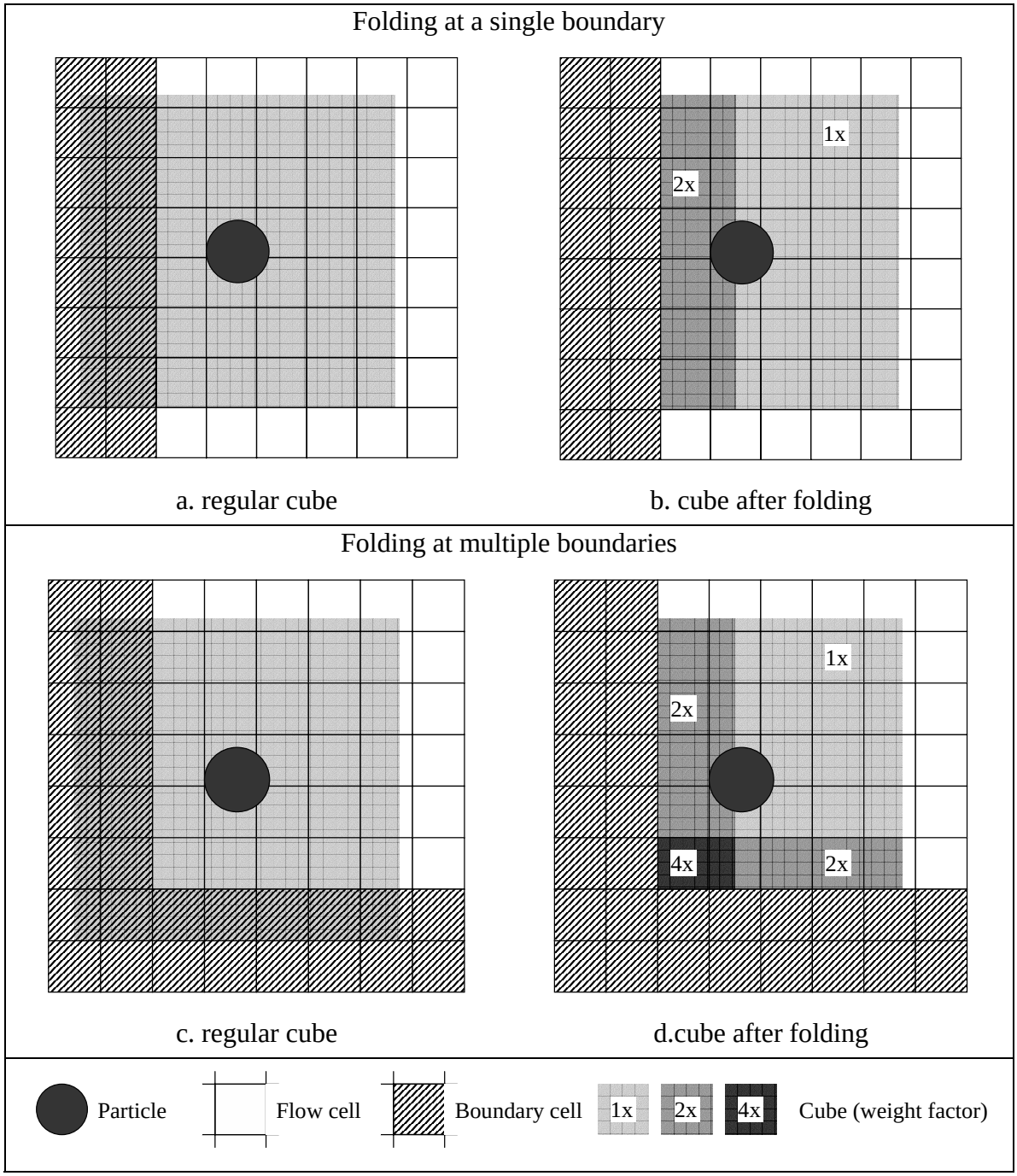

Figure 3.4 Illustration of folding at the boundary.

On the other hand, a general variable ϕ_i at a Lagrangian position can be mapped to an Eulerian property ϕ_{cell} using the following equation:

$$\phi_{cell} = V_{cell} \sum_{\forall i \in cell} \frac{f_{cell}^{i} \phi_i}{V_i} \tag{3.50}$$

where f_{cell}^{i} is the volume fraction of the cell under consideration that is occupied by cube *i*.

The volume weighing method used by Hoomans *et al.* (1996) does not obey Newton's third law at the boundary, since the boundary cells are not influenced by a particle, but do contribute to the force exerted on that particle. The alternative method does satisfy Newton's third law when the folding approach described in section 3.4.1 is used. With this treatment of the boundary the resistance felt by the gas phase is the same throughout a horizontal plane in a system that is filled with particles at an equal spacing in each direction.

3.5 Numerical implementation

The computational strategy, displayed in Figure 3.5, shows a flow diagram of the different modules that constitute the model and the variables that are exchanged between the modules.

To resolve the time-dependent motion of the particles and the gas phase, the DPM uses two different time scales. The main time step, δt_{flow}, is constant and is used to solve the Navier-Stokes equations and the inter-phase coupling. While for the particle-particle interaction a different time step is used, which depends on the particle-particle interaction approach.

In the soft sphere approach δt_{flow} is divided into a number of constant time steps, δt_{soft}, which are used to update the contact forces during the particle-particle contact and the resulting particle velocities. δt_{soft} should be sufficiently small to make sure that the contact lasts for a certain number of time steps to avoid problems concerning energy conservation due to the numerical integration, which is inevitable in the soft sphere approach. During each $\delta t_{soft,}$ the particles are assumed to move at a constant velocity.

The contact time in the normal direction can be determined using:

$$t_{contact,n} = \sqrt{m_{ab} \frac{\pi^2 + \ln^2(e_n)}{k_n}} \tag{3.51}$$

where m_{ab} is defined in equation 3.22 and e_n is defined in equation 3.23.

The contact time in the tangential direction can be determined using:

$$t_{contact,t} = \sqrt{\frac{2}{7} m_{ab} \frac{\pi^2 + \ln^2(\beta_0)}{k_t}} \tag{3.52}$$

where β_0 is defined in equation 3.25.

To maintain the energy balance the normal and tangential contact times should be the same, which yields the following relation for k_t for a given value of k_n:

$$k_t = \frac{2}{7}\frac{\pi^2 + \ln^2(\beta_0)}{\pi^2 + \ln^2(e_n)} k_n \tag{3.53}$$

In the hard sphere approach a significantly smaller varying time step, δt_{ab}, is used. The manner in which each time step is obtained is explained in the next section.

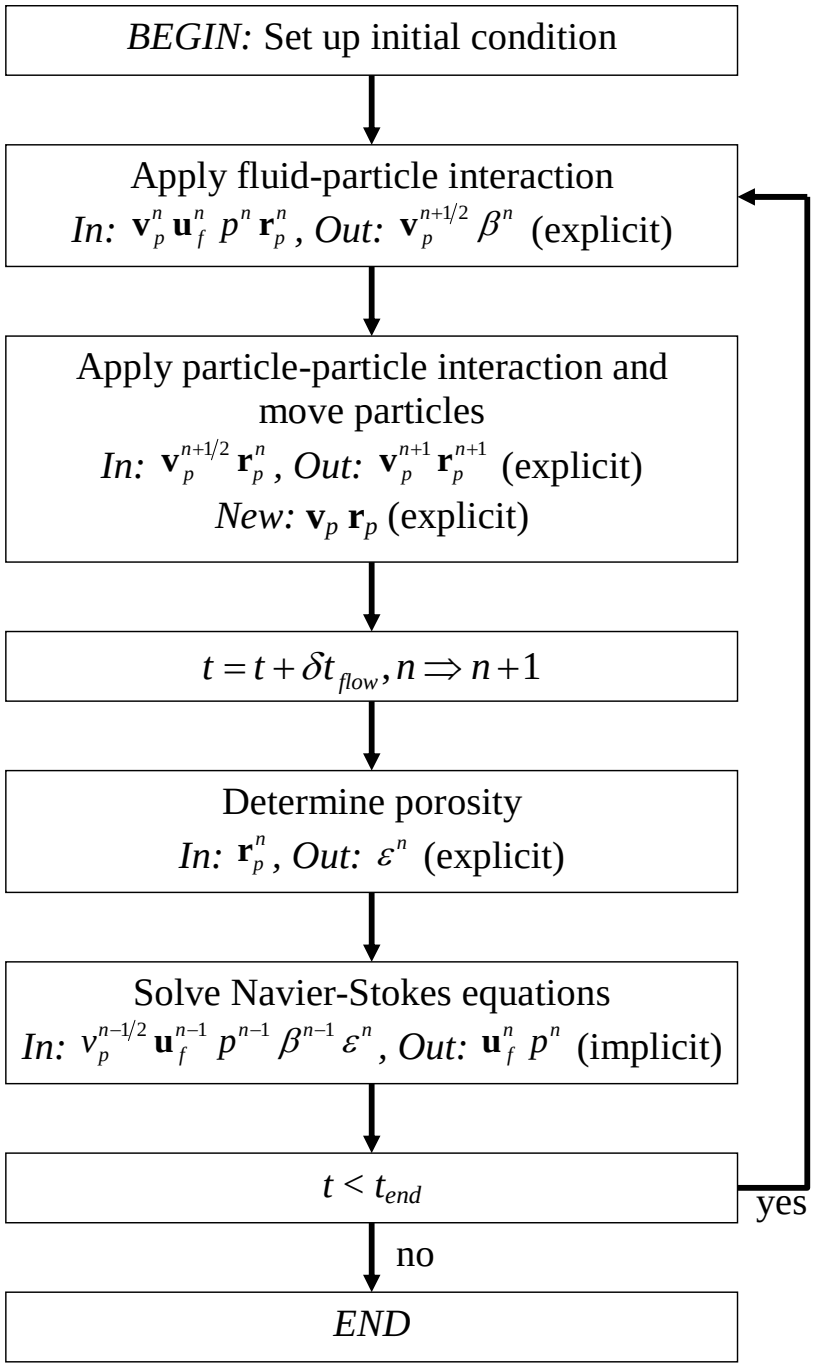

Figure 3.5 Flow diagram of the discrete particle model.

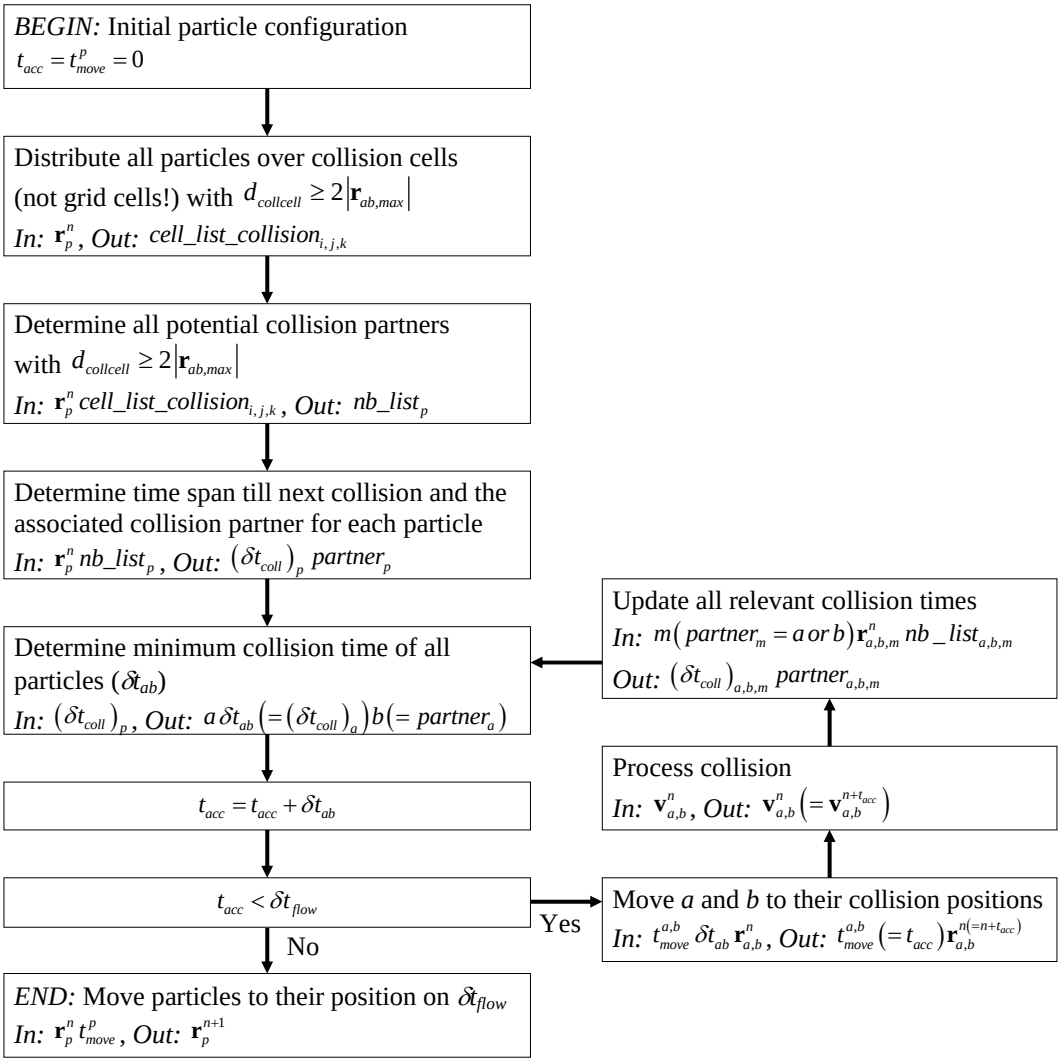

Figure 3.6 Hard sphere collision algorithm.

3.5.1 Hard sphere approach

The hard sphere approach is event driven, which means that the collision algorithm, illustrated in Figure 3.6, is searching for the next collision in the fluidized bed holding N_{part} particles with index $B = \{0, 1, .., N_{part} - 1\}$. In between subsequent collisions all particles are assumed to be in free flight.

To make the search for the next collision more efficient only collisions that can occur during one main time step are considered. This limits the maximum distance between particle a and potential collision partner b, which can also be a wall, to:

$$\left|\mathbf{r}_{ab}\right|_{max} = r_a + r_{max} + 2v_{max}\delta t_{flow} \tag{3.54}$$

where $\mathbf{r}_{ab} = \mathbf{r}_a - \mathbf{r}_b$

$$r_{max} = \max\left(r_a\right) \qquad \forall a \in B$$

and $$v_{max} = \max\left(\left|\mathbf{v}_a\right|\right) \qquad \forall a \in B$$

All particles (including walls) within this distance of particle *a* make up its neighbor list, $Nb_{list}(a)$. The time required for a particle *a* to collide with a collision partner $b \in Nb_{list}(a)$ from their current position can be determined by:

$$\delta t_{pair}(a,b) = \frac{-\mathbf{r}_{ab} \cdot \mathbf{v}_{ab} - \sqrt{(\mathbf{r}_{ab} \cdot \mathbf{v}_{ab})^2 - \mathbf{v}_{ab}^2 \left(-\mathbf{r}_{ab}^2 - (r_a + r_b)^2\right)}}{\mathbf{v}_{ab}^2} \tag{3.55}$$

where $\mathbf{v}_{ab} = \mathbf{v}_a - \mathbf{v}_b$.

Note that if $\mathbf{r}_{ab} \cdot \mathbf{v}_{ab} > 0$ the particles are moving away from each other. In this case no collision is possible and $\delta t_{pair}(a,b)$ is discarded.

The minimum of all $\delta t_{pair}(a,b)$ of particle *a* with partner $b \in Nb_{list}(a)$ is defined as the collision time of particle *a*:

$$\delta t_{coll}(a) = \min\left(\delta t_{pair}(a,b)\right) \quad \forall b \in Nb_{list}(a)$$

The time to the next collision in the whole domain is obtained by:

$$\delta t_{ab} = \min\left(\delta t_{coll}(a)\right) \quad \forall a \in B$$

This time step is added to the time at which the last collision occurred:

$$t_{acc} = t_{acc} + \delta t_{ab}$$

Only particle *a* and its partner *b* are moved to their position at time t_{acc} to minimize the number of computations (and accompanying computational errors). This can only be done when the time each particle has already moved, t_{move}, (which is taken into account for each subsequent calculation involving that particle) is stored.

Once the next collision is determined, momentum is exchanged between particle *a* and *b*, as described in section 3.3.1. Subsequently only the collision times affected by the collision are updated, i.e. the collision times of the colliding particles themselves and of the particles that prior to the collision regarded one of the colliding particles as their collision partner.

Once all collisions are processed (t_{acc} reaches δt_{flow}), all particles are moved to their position at δt_{flow}.

Chapter 4

Description and mapping of flow regimes

Abstract

Regime mapping in spout-fluid beds has been the subject of several studies, which are discussed in this chapter. Based on these studies six flow regimes observed in spout-fluid beds are identified and presented. The characteristic flow behavior of these flow regimes is described in detail, and illustrated using snapshots and frequency spectra of the pressure drop fluctuations.

By comparing the frequency spectra of different flow regimes, the distinguishing features of the flow regimes have been identified. It was found that the frequency spectra of the different flow regimes differ most significantly in the shape and frequency of the characteristic frequency peak(s).

This information was used to construct flow regime maps, which show the manner in which the flow regimes depend on the spout and background velocity, for different geometries, particle size distributions, and particle properties. Although the flow regimes are distributed in a similar manner for all cases, the geometry, particle properties and particle size distribution have a profound influence on the flow regime map, especially on the exact location of the boundaries between the flow regimes. It can therefore be concluded that the flow regime map of a spout-fluid bed is not only determined by the spout and background velocities.

4.1 Introduction

The successful application of spout-fluid beds sensitively depends on the operating conditions, like the background fluidization velocity (u_{bg}) and the spout velocity (u_{sp}). Insight in the influence of the operating conditions on the system behavior can be obtained through a flow regime map, i.e. a map that displays the manner in which the flow regimes depend on u_{bg} and u_{sp}. A flow regime is defined as a range of operating conditions, which display similar fluidization behavior.

The first flow regime map of a spout-fluid bed has been reported by Nagarkatti and Chatterjee (1974). Their flow regime map, like most flow regime maps that have been published since then (He *et al.*, 1992; Sutanto *et al.*, 1985; Vukovic *et al.*, 1984), was based on visual observation. Unfortunately, visual observation requires visual access to all relevant parts of the spout-fluid bed, like e.g. the spout channel. In a 3D spout-fluid bed, the spout channel is not necessarily near a wall, which only allows visual access with the use of an intrusive optical probe.

Zhang and Tang (2004) mapped the operating regimes based on frequency spectra resulting from spectral analysis of fluctuations in the bed pressure drop. The only requirement for measuring the bed pressure drop is access to the bed with a pressure sensor, which is usually much less difficult to obtain than visual access. Since the pressure drop fluctuations travel through the bed, they can be recorded at numerous locations in the bed, allowing the pressure sensor to be placed in a position, where it is not intrusive, which offers an advantage over optical probes. Another advantage of measuring the pressure drop fluctuations is that it, contrary to visual observation, produces quantitative results.

Zhang and Tang (2004) produced an overview of the operating regimes that have been distinguished in a spout-fluid bed by various authors. Most authors distinguished similar flow regimes, although the adopted nomenclature differed. In this thesis the nomenclature proposed by Zhang and Tang (2004) will be used, with one exception: the fixed bed regime will be split into a fixed bed regime and an internal spout regime. It should be noted that this distinction can only be made when there is visual access to the location of the spout. The following flow regimes were distinguished:

- fixed bed regime;
- internal spout regime;
- spouting with aeration regime;
- bubbling/slugging bed regime;
- spout-fluidization regime;
- jet in fluidized bed regime.

In this chapter, the experimental procedure used for the flow regime mapping will be presented followed by a discussion on the characteristic bed behavior of all observed flow regimes. Subsequently a method is presented to distinguish between the flow regimes based on both pressure signals and visual observations. Finally flow regime maps for all systems will be presented and discussed.

4.2 Experimental procedure

In this chapter experimental results obtained for both pseudo-2D and 3D spout-fluid beds will be reported. In this section the geometrical details will be presented together with the measuring equipment that was used to obtain the flow regime maps.

4.2.1 Measuring equipment

The measurements of the fluctuations in the bed pressure drop (excluding the gas distributor) that are required for the flow regime identification were recorded using a high frequency pressure probe (Kulite XT-190M-0.35BAR VG) at a frequency of 100 Hz.

In case visual access to the spout channel in the 3D set-up was possible, digital images were recorded with a 262 Hz CCD camera (Dalsa CA-D6) equipped with a 12.5 mm lens. The aperture of the camera was set to f4.0 and the exposure time was fixed at 3.8 ms. The recorded images consist of 532 x 516 8-bit pixels.

In the pseudo-2D set-up, digital images were recorded with a 636 Hz CMOS camera (PCO 1200 HS), which was positioned at a distance of 1.5 m from the bed. The camera was operated at a frequency of 62.5 Hz and the exposure time was fixed at 0.4275 ms. The recorded images consist of 933 x 420 8-bit pixels.

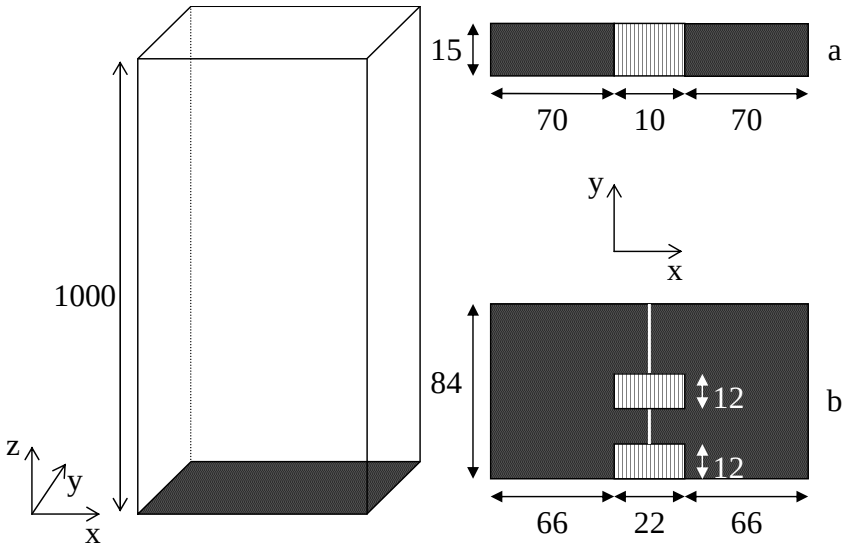

Figure 4.1 Schematic representation of the geometry of the pseudo-2D (a) and 3D bed (b), dimensions are given in mm.

Property	**Small particles**	**Large particles**	**Urea particles**	**Unit**
Material	Glass	Glass	Urea	-
d_p	2.49 ± 0.02	4.04 ± 0.02	3.7 ± 0.3	mm
ρ_p	2526 ± 6	2526 ± 1	1240	kg/m^3
u_{mf}	1.28 ± 0.02	1.77 ± 0.03	1.12 ± 0.05	m/s
$e_{n,\,p \leftrightarrow p}$	0.97 ± 0.01 [a]	0.97 [b]	0.3 [c]	-
$e_{n,\,p \leftrightarrow w,\,glass}$	0.97 ± 0.01 [a]	0.97 [b]	-	-
$e_{n,\,p \leftrightarrow w,\,polycarbonate}$	0.97 [b]	0.97 [b]	-	-
$e_{n,\,p \leftrightarrow w,\,aluminum}$	0.97 [b]	0.97 [b]	-	-
$\mu_{p \leftrightarrow p}$	0.10 ± 0.01 [a]	0.10 [b]	-	-
$\mu_{p \leftrightarrow w,\,glass}$	0.09 ± 0.01 [a]	0.10 [b]	-	-
$\mu_{p \leftrightarrow w,\,polycarbonate}$	0.10 [b]	0.10 [b]	-	-
$\mu_{p \leftrightarrow w,\,aluminum}$	0.10 [b]	0.10 [b]	-	-
$\beta_{0,\,p \leftrightarrow p}$	0.33 ± 0.05 [a]	0.33 [b]	-	-
$\beta_{0,\,p \leftrightarrow w,\,glass}$	0.33 ± 0.05 [a]	0.33 [b]	-	-
$\beta_{0,\,p \leftrightarrow w,\,polycarbonate}$	0.33 [b]	0.33 [b]	-	-
$\beta_{0,\,p \leftrightarrow w,\,aluminum}$	0.33 [b]	0.33 [b]	-	-

[a] measured through detailed collision measurements, see Kharaz et al. (1999)

[b] not measured, but estimated based on the properties of small particles and/or other wall materials

[c] estimated based on indicative impact experiments that measured the particle velocity before and after collision with a wall

Table 4.1 Particle properties.

4.2.2 Pseudo-2D set-up

The pseudo-2D gas-fluidized bed is schematically represented in Figure 4.1a. The bed is 15 mm deep, i.e. six particle diameters, to prevent bridge formation, i.e. stable particle configurations extending from wall to wall. The depth of the bed is assumed to be sufficiently small to display pseudo-2D behavior.

The front wall of the bed consists of a glass plate to permit visual observation of the particle motion inside the bed. The side walls of the bed are made of aluminum strips and the back wall is made of polycarbonate.

The set-up was filled with $2.45 \cdot 10^4$ small particles. The properties of the particles that were used in the experiments are given in Table 4.1.

Dry pressurized air from a tank, which was kept at a pressure of 5 bar, was fed to the bed through three separate sections. A 3 mm thick porous plate with an average pore size of 10 microns provided a homogeneous gas distribution over the two fluidization sections. A 0.5 mm metal gauze covered the spout mouth located in between the fluidization sections. The gas flow rate in each section was accurately controlled by mass flow controllers and rapidly responding magnetic valves. To prevent the build up of static electricity the humidity of the air in the fluidization sections was maintained at 60-70% by addition of steam.
The pressure probe was positioned in the back (polycarbonate) wall of the bed about 0.01 m above the porous plate and 0.04 m right of the left wall.

4.2.3 3D set-up

The 3D gas-fluidized bed is schematically represented in Figure 4.1b. The side walls of the bed are made of aluminum, while the front and back walls are made of polycarbonate.
The set-up was either filled with:

- a monodisperse particulate phase consisting of $4.48 \cdot 10^4$ large particles;
- a bidisperse particulate phase, with a minimum fluidization velocity (u_{mf}) of 1.46 m/s, consisting of $9.79 \cdot 10^4$ small particles and $2.29 \cdot 10^4$ large particles;
- a monodisperse particulate phase consisting of $5.9 \cdot 10^4$ urea particles.

The properties of the particles that were used are given in Table 4.1.
Ambient air pressure was increased by 0.35 bar using a blower. Subsequently the air was cooled to a temperature of approximately 40°C, and fed to the bed through four separate sections. A 2 mm thick porous plate with an average pore size of 100 µm provided a homogeneous gas distribution over the two fluidization sections. The two spout sections, which were located between the two fluidization sections at both the front wall and in the geometrical centre of the bed (see Figure 4.1b), were covered with a 0.5 mm metal gauze.
The flow rate of the gas in each section was controlled by control valves. During an experiment only one of the spout sections was operated as a spout. The gas velocity through the remaining spout section was set to be equal to the gas velocity in the fluidization sections. The gas flow rate was calibrated prior to the experiments using a turbine meter, which was connected to the bed exit.
The pressure probe was positioned in the middle of the back wall of the bed about 0.01 m above the porous plate.

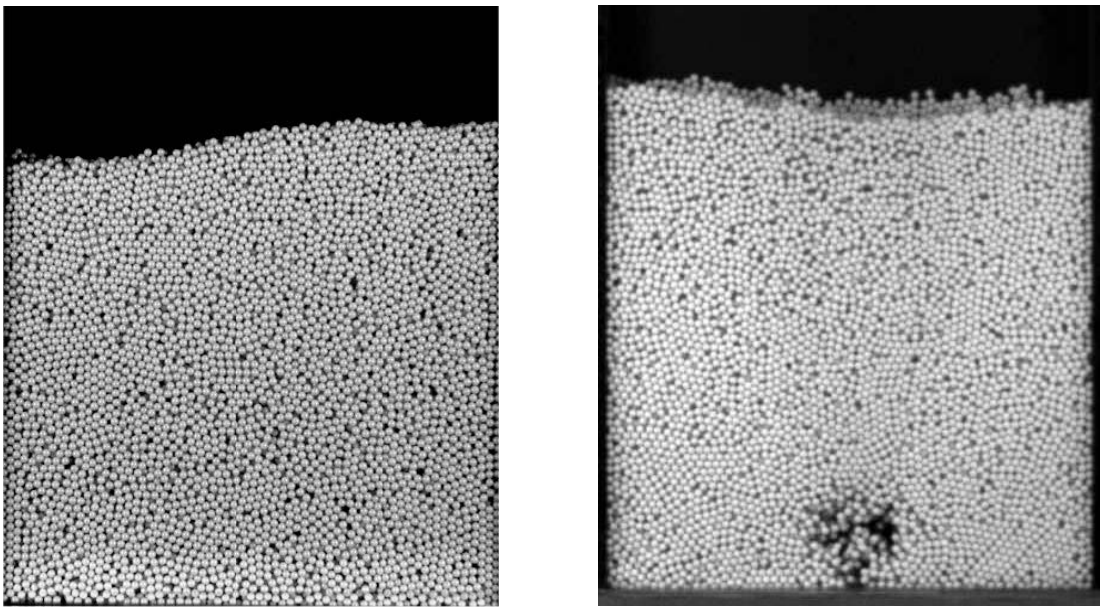

a b

Figure 4.2 Snapshot of (a) the fixed bed regime (u_{bg} = u_{sp} = 1.0 m/s) and (b) the internal spout regime (u_{bg} = 0.0 m/s, u_{sp} = 20 m/s).

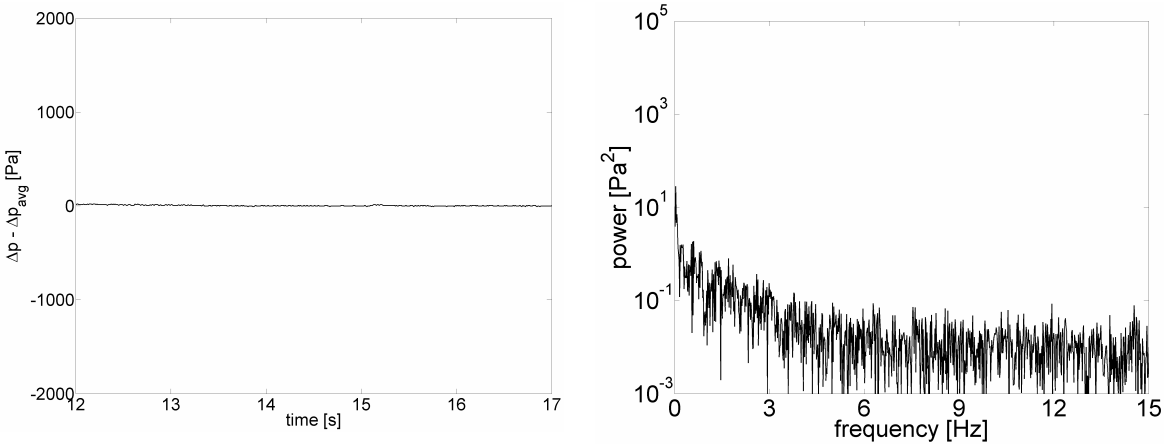

a b

Figure 4.3 Fluctuations of the bed pressure drop around the time-averaged value (a) for the fixed bed regime (u_{bg} = u_{sp} = 1.0 m/s) and the associated frequency spectrum (b).

4.3 Flow regimes

4.3.1 Fixed bed regime

In the fixed bed regime all particles have a fixed position, which is illustrated in Figure 4.2a. Since the particles do not move, the particle configuration does not change and consequently the bed pressure drop shown in Figure 4.3a is virtually constant. The fluctuations that are observed appear to be noise. Consequently the frequency spectrum of the pressure drop fluctuations presented in Figure 4.3b does

not display any peaks with significant power. The power is however slightly elevated at low frequencies, which is probably caused by external disturbances, like an adjustment of the position of the pressure control valve.

4.3.2 Internal spout regime

In the internal spout regime the spout only penetrates part of the bed, which is illustrated by the snapshot in Figure 4.2b. The particles in the stable spout channel move upward at relatively high velocities, while the particles adjacent to the spout channel move downward until they are dragged into the spout channel. The remaining large majority of the particles do not move at all.

Since most of the particles do not move and the particles that do move, move very regularly, the particle configuration itself does not change significantly. For this reason, the bed pressure drop in Figure 4.4a is virtually constant. Consequently the frequency spectrum of the pressure drop fluctuations in Figure 4.4b does not display any peaks with significant power. The power is however slightly elevated at low frequencies, which is probably caused by external disturbances, like an adjustment of the position of the pressure control valve.

Since the frequency spectrum of the internal spout regime in Figure 4.4b is very similar to the frequency spectrum of the fixed bed regime in Figure 4.3b, it is virtually impossible to distinguish between these flow regimes based solely on the frequency spectra. Although it needs to be noted that the powers in the internal spout regime are generally larger than the powers in the fixed bed regime.

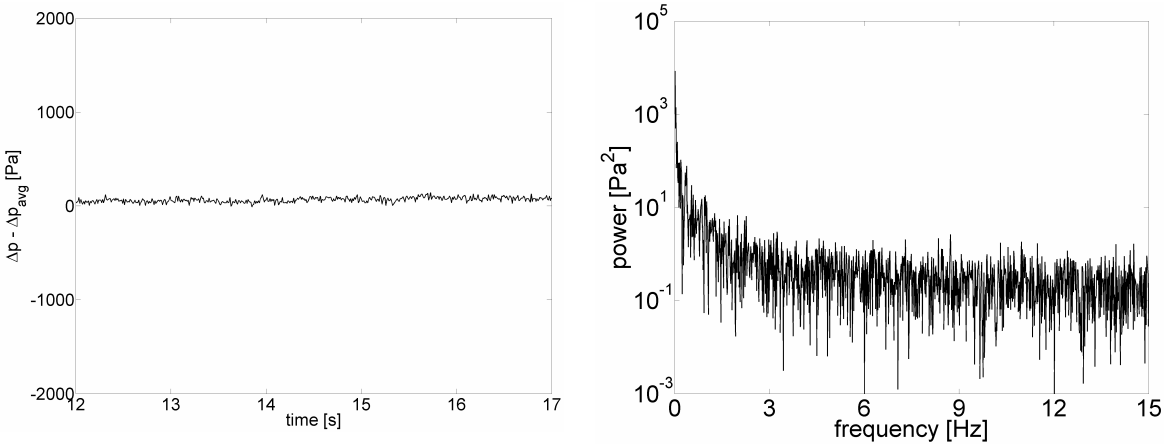

a b

Figure 4.4 Fluctuations of the bed pressure drop around the time-averaged value (a) for the internal spout regime (u_{bg} = 0.0 m/s, u_{sp} = 20 m/s) and the associated frequency spectrum (b).

4.3.3 Spouting with aeration regime

In the spouting with aeration regime, the spout channel is stable and continuously penetrates the entire bed as can be seen in the snapshot in Figure 4.5. In the spout channel, where the particle concentration is low, the particles move upward at relatively high velocities until they reach the fountain, where they lose their momentum and drop back onto the annulus. Most particles in the annulus move slowly towards the base of the spout channel until they are dragged into the spout channel. When u_{bg} is below the minimum fluidization velocity (u_{mf}), the particles in the lower corners of the bed do not move.

Figure 4.6a shows that, since the particle configuration itself does not change significantly, the movement of the particles hardly affects the bed pressure drop. Consequently the frequency spectrum in Figure 4.6b shows no characteristic frequency peak indicating that the particle behavior is not periodic.

Compared to the frequency spectrum of the internal spout regime in Figure 4.4b, the frequency spectrum of the spouting with aeration regime in Figure 4.6b displays a larger and much more uniform power, i.e. the power is not elevated at low frequencies like it was in the internal spout regime and the fixed bed regime. The power is larger because of the larger average amplitude of the pressure drop fluctuations in Figure 4.6a compared to Figure 4.4a.

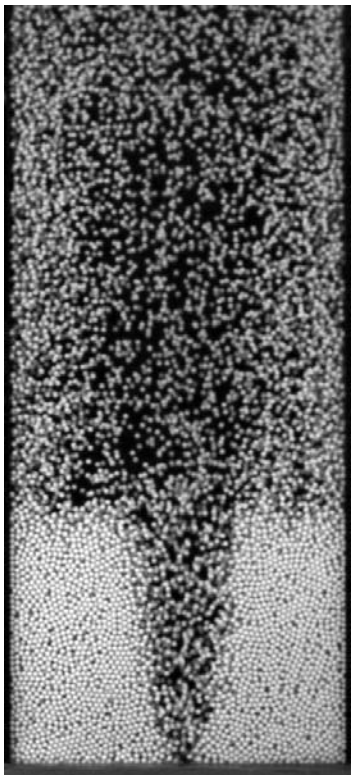

Figure 4.5 Snapshot of the spouting with aeration regime (u_{bg} = 1.0 m/s, u_{sp} = 65 m/s).

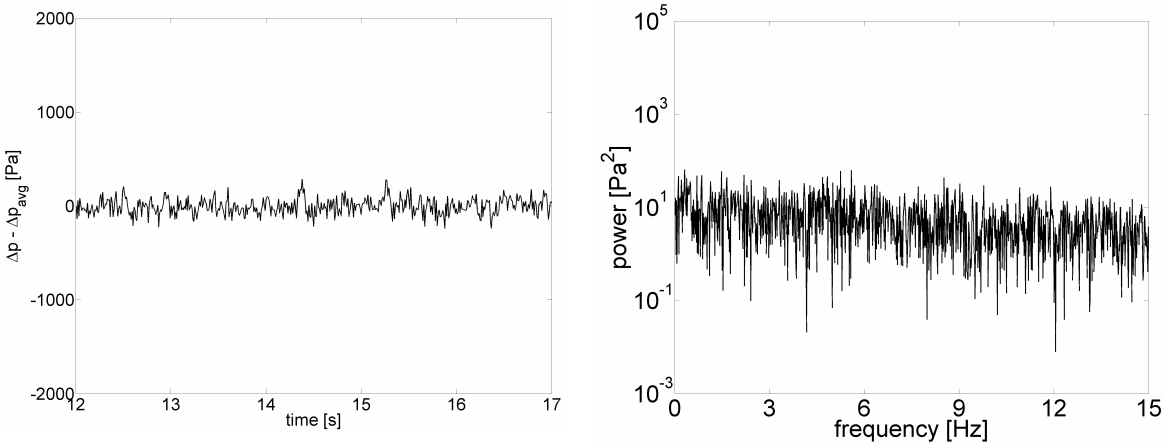

a b

Figure 4.6 Fluctuations of the bed pressure drop around the time-averaged value (a) for the spouting with aeration regime (u_{bg} = 1.0 m/s, u_{sp} = 65 m/s) and the associated frequency spectrum (b).

4.3.4 Bubbling/Slugging bed regime

The behavior of a bubbling/slugging bed is illustrated by the snapshots shown in Figure 4.7. In the bubbling/slugging bed regime, all particles are moving and gas bubbles are formed just above the bottom plate. The bubbles grow through coalescence resulting in bubbles with different sizes and shapes. When Geldart D powders are used, which is usually the case in spout-fluid beds, the diameter of some bubbles can reach a size up to the diameter of the bed. These bubbles are termed slugs.

When a bubble is formed, the gas in the bubble not only supports the weight of all the particles above the bubble, but even accelerates them. During the formation of a slug, this means that the added pressure of the weight of the entire bed above the slug is acting on the slug. When the slug rises, the configuration of the particles above the slug will become more dilute, eventually resulting in a situation where a large portion of the bed is almost uniformly filled with particles, resulting in a relatively dilute bed and consequently a relatively low drag force and related pressure drop. This allows gravity to bring the particles back to the bottom of the bed, trapping the gas and increasing the pressure, which initiates the formation of the next bubble or slug. Figure 4.8, which shows the fluctuations in the average height of the particles and the bed pressure drop as a function of time for a simulation of a bubbling/slugging 3D bed filled with glass particles with a diameter of 4 mm, illustrates the relation between the average height of the particles, which was not obtained experimentally, and the bed pressure drop, which can be obtained experimentally.

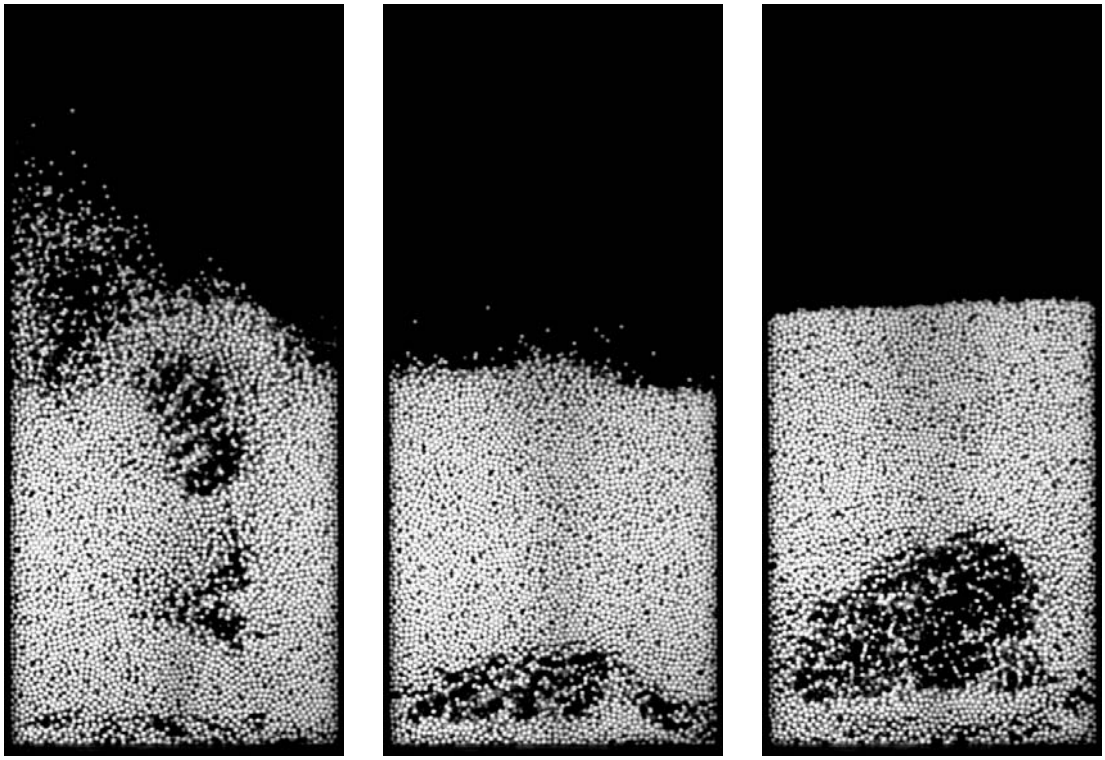

0.0 s 0.08 s 0.16 s

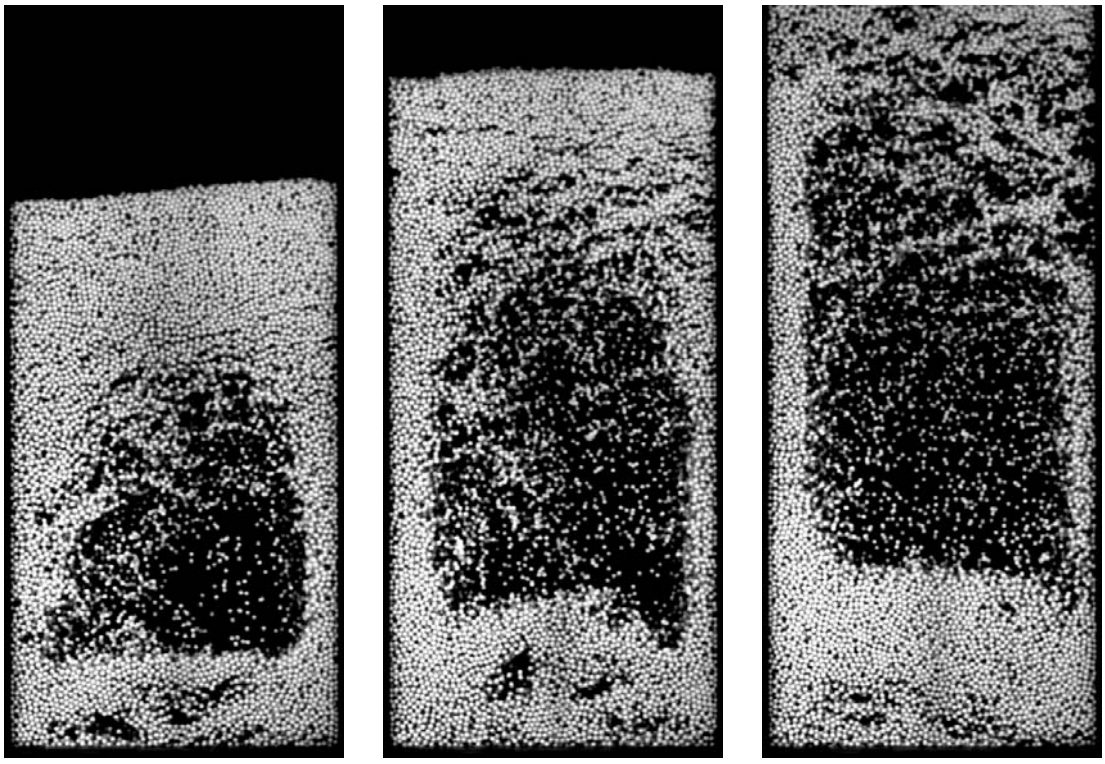

0.24 s 0.32 s 0.40 s

Figure 4.7 Snapshots at different time intervals of the bubbling/slugging bed regime ($u_{bg} = u_{sp} = 2.5$ m/s).

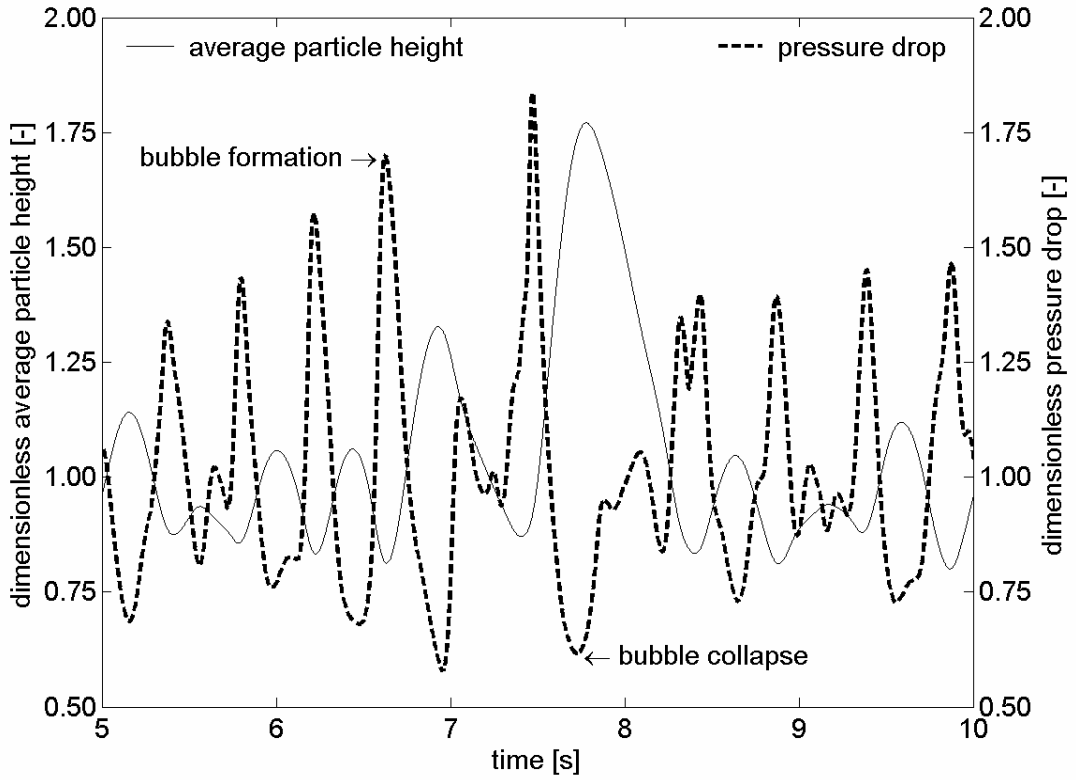

Figure 4.8 Computed fluctuations of the dimensionless average particle height and the dimensionless bed pressure drop for the bubbling/slugging bed regime ($u_{bg} = u_{sp} = 3.5$ m/s) in a 3D bed filled with glass particles with a diameter of 4 mm.

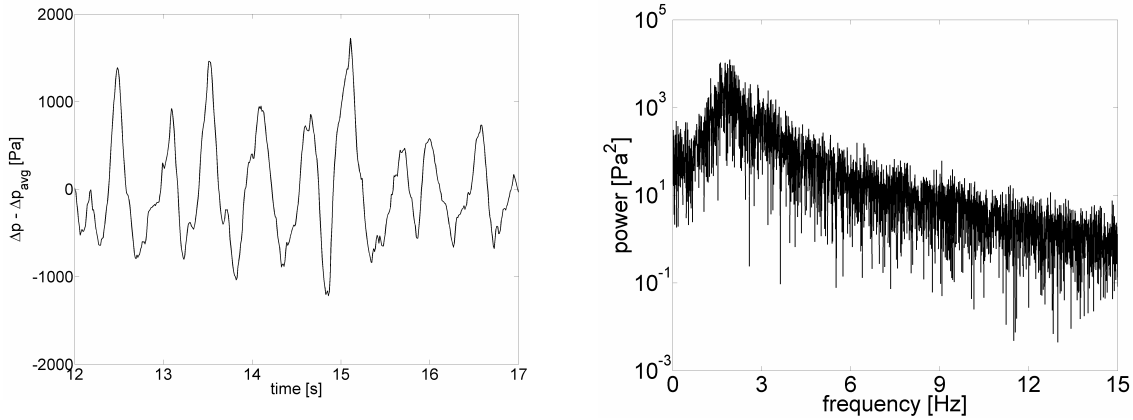

Figure 4.9 Fluctuations of the bed pressure drop around the time-averaged value (a) for the bubbling/slugging bed regime ($u_{bg} = u_{sp} = 2.5$ m/s) and the associated frequency spectrum (b).

The larger the pressure build-up, the larger the force by which the particles in the slug are launched, the higher the particles will rise and the longer the particles will take to return to the bottom of the bed to form the next bubble or slug. For this reason the frequency of the characteristic frequency peak in Figure 4.9b is low, but since bubbles

with many different sizes and shapes are formed, the peak is relatively wide. The substantial amplitude of the pressure drop fluctuations in Figure 4.9a causes the power of the frequency peak to be large, despite its large width.

4.3.5 Spout-fluidization regime

In the spout-fluidization regime, a spout channel is present, which is periodically blocked by particles from the annulus as illustrated by the snapshots in Figure 4.10. This behavior occurs, when u_{sp} is sufficiently high to enable the spout channel to reach the bed surface, but too low to prevent groups of particles from entering the spout channel. When a group of particles moves into the spout channel, the spout channel is blocked to some extent, causing an elevated pressure in the spout channel, which enables the gas in the spout channel to remove the blockage. After the blockage is removed the pressure in the spout channel drops, allowing the next group of particles from the annulus to move into the spout channel.

Since the groups of particles blocking the spout channel are of roughly the same size, the associated pressure drop fluctuations are very regular, which is illustrated in Figure 4.11a. The regularity and moderate amplitude of the pressure drop fluctuations results in a very narrow and powerful frequency peak in Figure 4.11b. The frequency of this peak is high, because it takes little time to form the small blockage and remove it from the spout channel.

Note that also the second and third harmonic frequency peak can be observed.

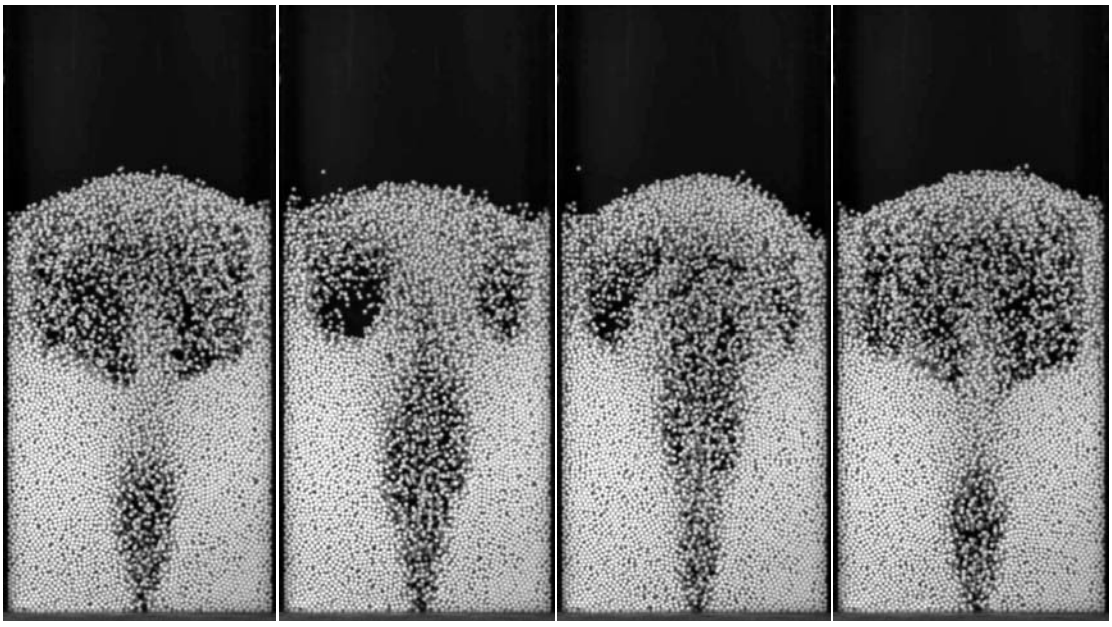

0.00 s 0.06 s 0.13 s 0.19 s

Figure 4.10 Snapshots at different time intervals of the spout-fluidization regime (u_{bg} = 1.0, u_{sp} = 35 m/s).

4.3.6 Jet in fluidized bed regime

In the jet in fluidized bed regime, the bed contains both a spout channel and bubbles that are interacting with one another. The interaction consists of bubbles that block the spout channel at the base or tilt it and a spout channel that attracts the bubbles, which hinders bubble growth in the horizontal plane, and consequently prohibits the formation of large bubbles and slugs.

The interaction between the spout channel and the bubbles can yield stable and unstable behavior. The more stable mode of the jet in fluidized bed regime is termed the single frequency mode. In this mode, every bubble that is formed leaves the bed through the spout channel. When the bubble collapses, the whole bed collapses blocking the spout channel and triggering the formation of the next bubble as is illustrated by the snapshots in Figure 4.12. The stability of this mode is illustrated by the rather periodic pressure signal and the single characteristic frequency peak observed in Figure 4.13.

Compared to the spout-fluidization regime the blockage of the spout channel in the single frequency mode of the jet in fluidized bed regime occurs at a lower position in the bed and consequently involves a larger number of particles. Since the extent of blockage is larger, removal of the particles in the spout channel consumes more time and causes the frequency of the characteristic frequency peak to be lower. Furthermore the pressure drop fluctuations in the jet in fluidized bed regime are less regular, resulting in a wider frequency peak.

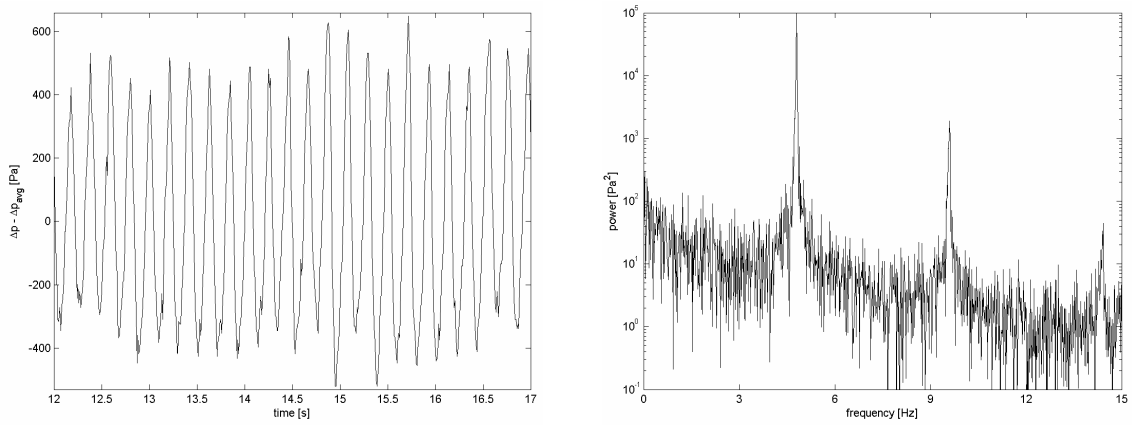

a b

Figure 4.11 Fluctuations of the bed pressure drop around the time-averaged value (a) for the spout-fluidization regime (u_{bg} = 1.0, u_{sp} = 35 m/s) and the associated frequency spectrum (b).

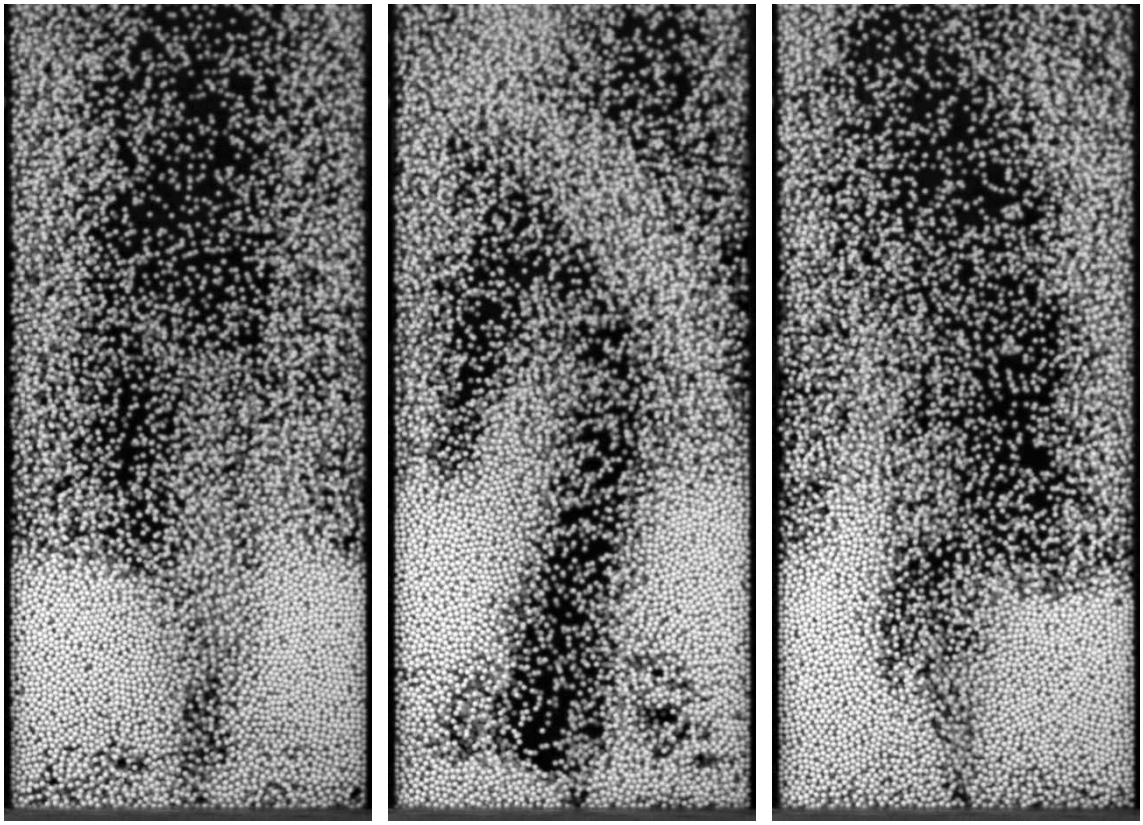

0.00 s 0.13 s 0.24 s

Figure 4.12 Snapshots at different time intervals of the single frequency mode of the jet in fluidized bed regime (u_{bg} = 3.0, u_{sp} = 40 m/s).

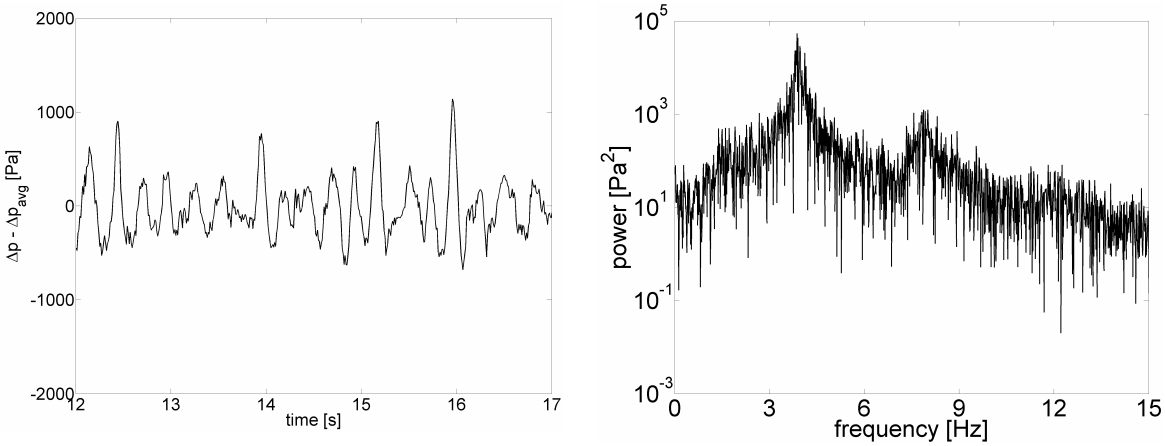

a b

Figure 4.13 Fluctuations of the bed pressure drop around the time-averaged value (a) for the single frequency mode of the jet in fluidized bed regime (u_{bg} = 3.0, u_{sp} = 40 m/s) and the associated frequency spectrum (b).

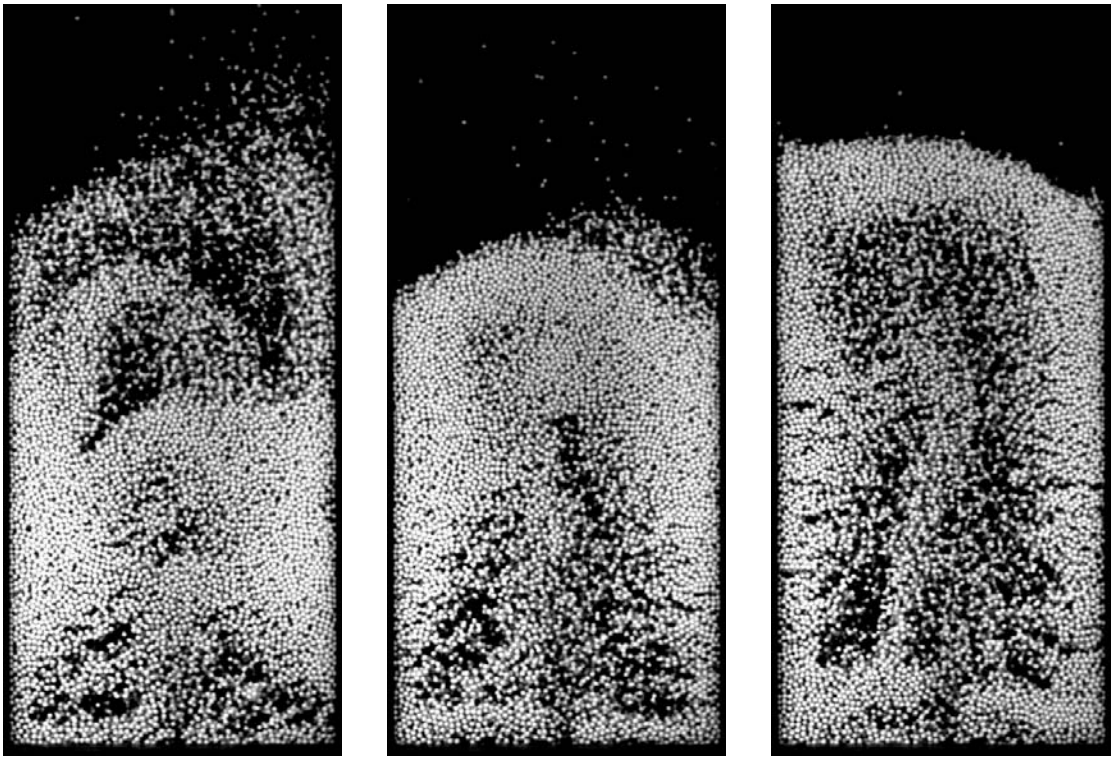

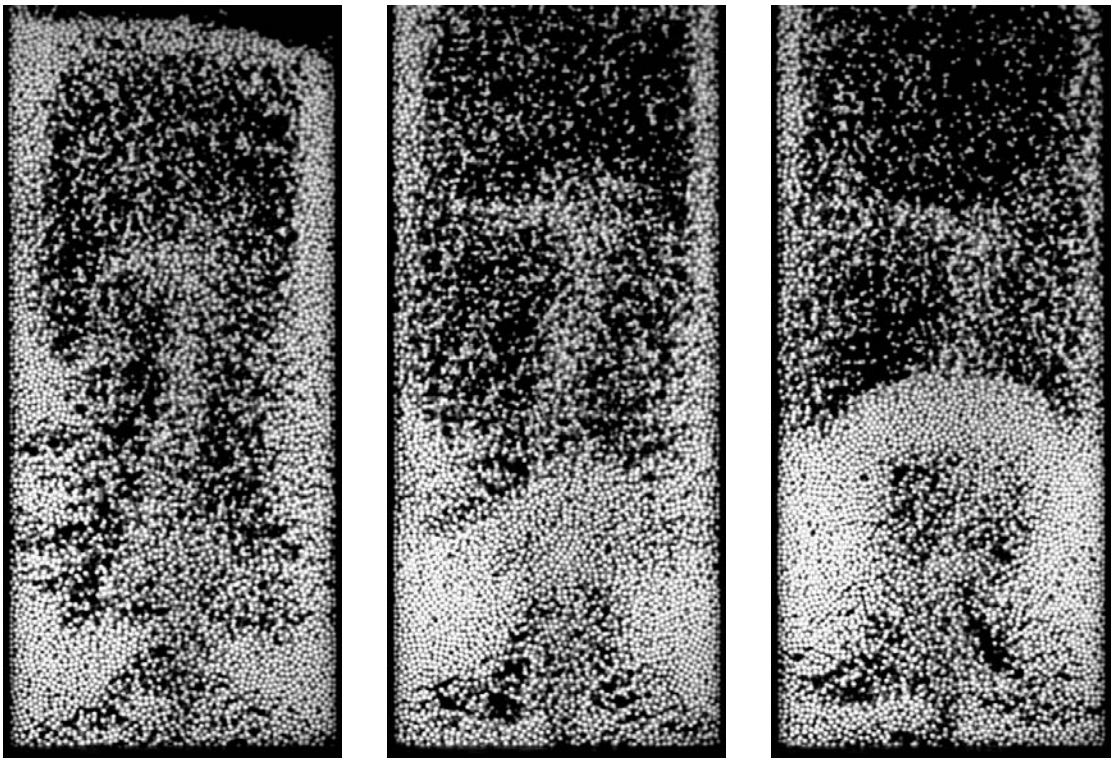

Figure 4.14 Snapshots at different time intervals of the multiple frequency mode of the jet in fluidized bed regime (u_{bg} = 3.0, u_{sp} = 15 m/s).

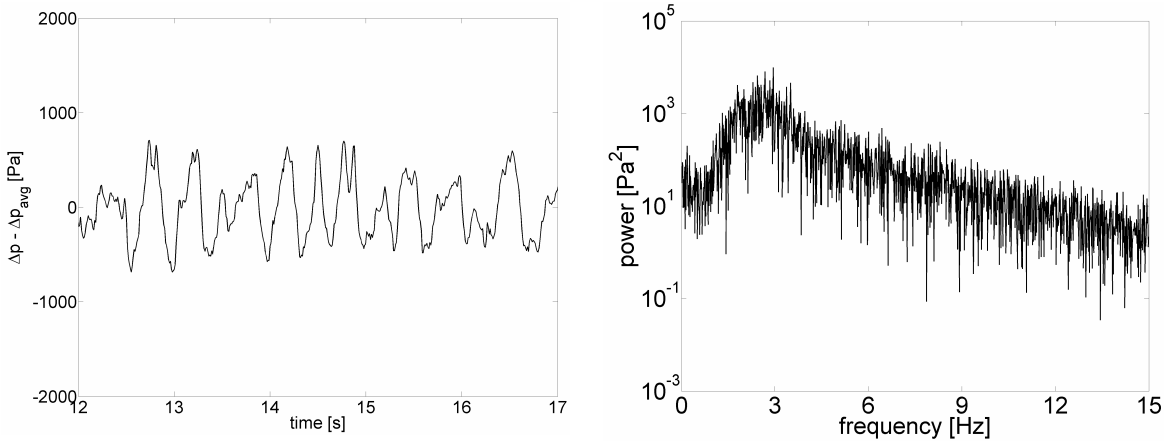

a b

Figure 4.15 Fluctuations of the bed pressure drop around the time-averaged value (a) for the multiple frequency mode of the jet in fluidized bed regime (u_{bg} = 3.0, u_{sp} = 15 m/s) and the associated frequency spectrum (b).

The less stable mode of the jet in fluidized bed regime is termed the multiple frequency mode and is illustrated by the snapshots in Figure 4.14. The bubbles dominate the particle behavior in this mode, and the spout only influences the direction in which the bubbles move. Because of the mutual influence of the spout channel and the bubbles, the direction in which the bubbles move changes continuously. Since the bubbles dominate the behavior of the bed, the pressure drop fluctuations in Figure 4.15a resemble the pressure drop fluctuations of the bubbling/slugging bed in Figure 4.9a. Nevertheless, since the spout channel prevents the formation of large bubbles and slugs, the frequency of the pressure drop fluctuations is significantly higher as is evident from inspection of the frequency spectrum in Figure 4.15b. The frequency peak is wide, since bubbles with different shapes and sizes are being formed.

Flow regime	Characteristic frequency peak	
	Frequency	Shape
Internal spout / Fixed bed	Low	Intermediate width and low power
Spouting with aeration	No peak, comparable and small power for all frequencies	
Bubbling/Slugging bed	Low	Broad and high power
Spout-fluidization	High	Narrow and high power
Jet in fluidized bed	Intermediate	Intermediate width and high power

Table 4.2 Characteristics of the flow regimes.

4.4 Flow regime identification

High frequency pressure drop measurements and high frequency video capture are employed to identify the flow regime. The pressure drop fluctuations are transformed into a frequency spectrum using a Fourier transformation using the procedure described in section 2.4. The frequency spectrum shows the shape and frequency of the characteristic frequency peak(s) for each operating condition. By comparing these characteristics with the characteristics of the flow regimes described above and summarized in Table 4.2, the flow regime can be identified.
When the system is accessible with a digital camera, that is when the spout is positioned at the wall, digital images can be used to confirm the flow regime. The digital images are also used to explain the pressure drop fluctuations based on the phenomena observed in the spout-fluid bed.

Information about the operating conditions can also be used to facilitate the identification of the flow regime. It is for example very unlikely that the jet in fluidized bed regime occurs, when u_{bg} is below u_{mf}. Furthermore, the flow regimes observed for comparable operating conditions can also be of assistance to determine the flow regime.
There is no clear boundary between the flow regimes, which implies that some of the operating conditions are in between flow regimes. The frequency spectra associated with these operating conditions generally show characteristics of the surrounding flow regimes.
Some flow regimes are difficult to distinguish based solely on pressure drop fluctuations. For instance in both the fixed bed regime, the internal spout regime and the spouting with aeration regime virtually no significant fluctuations are present. However, the spectrum for the spouting with aeration regime differs significantly from the other two flow regimes. In the spouting with aeration regime all frequencies display comparable power, while the power spectrum of the other flow regimes shows a slightly increasing value towards lower frequencies. It is however virtually impossible to discriminate between the fixed bed regime and the internal spout regime based solely on frequency spectra. In that case additional information, e.g. visual observation, is required.

4.5 Flow regime maps

In order to obtain comprehensive flow regime maps, the pressure drop fluctuations were measured over a wide range of operating conditions. In the 3D set-up the background velocity was varied from 0 to 3.5 m/s with increments of 0.5 m/s and the spout velocity was varied from 40 to 95 m/s with increments of 5 m/s. Due to

limitations of the set-up, it was not possible to use spout velocities below 40 m/s. Consequently the only spout velocity below 40 m/s was 0 m/s. In the pseudo-2D set-up the background velocity was varied from 0 to 3.0 m/s with increments of 0.5 m/s and the spout velocity was varied from 0 to 70 m/s with increments of 5 m/s. In both set-ups the pressure drop fluctuations were recorded over a period of one minute.
Using the method described in the previous section, flow regime maps for different geometries and particle size distributions (PSD) have been recorded, which are presented in Figure 4.16 and Figure 4.17. The following systems were studied:

A. Monodisperse (4.0 mm glass) particulate phase in a three-dimensional bed with the spout channel positioned in the geometrical centre of the bed;
B. Bidisperse (2.5/4.0 mm glass) particulate phase in a three-dimensional bed with the spout channel positioned in the geometrical centre of the bed;
C. Monodisperse (4.0 mm glass) particulate phase in a three-dimensional bed with the spout channel positioned at the wall;
D. Monodisperse (2.5 mm glass) particulate phase in a pseudo-2D bed;
E. Monodisperse (3.8 mm urea) particulate phase in a three-dimensional bed with the spout channel positioned in the geometrical centre of the bed.

In the flow regime maps for all these systems, the flow regimes are distributed over the operating conditions in approximately the same manner:

- Spouting with aeration regime at low u_{bg} and high u_{sp};
- Internal spout and fixed bed regime at low u_{bg} and intermediate u_{sp};
- Slugging bed regime at high u_{bg} and low u_{sp};
- Jet in fluidized bed regime at high u_{bg} and intermediate to high u_{sp};
- Spout-fluidization regime at intermediate u_{bg} (around u_{mf}) and intermediate u_{sp}.

System A consists of a particulate phase with almost “ideal” properties. The glass beads are almost perfectly spherical, have close to ideal collision properties, i.e. the amount of energy that is dissipated during a collision is relatively small, and are of almost the same size. Furthermore the spout channel is positioned in the geometrical centre of the 3D bed, which prevents the walls from influencing the spout behavior. This near-ideal situation entails that there is little resistance to changes in the fluidization regime. A comparison between the flow regime map of system A and that of the other regimes indeed shows that the transitions between the regimes are sharper in system A.

The PSD in system B differs from system A in the sense that it consists of two types of particles instead of one. In system B the range of operating conditions displaying

spouting with aeration behavior is reduced. This phenomenon is probably caused by the presence of particles with two different sizes. The larger particles will disturb the spout channel up to larger spout velocities than the smaller particles. The spout channel will therefore be less stable and consequently the spouting with aeration regime is less likely to occur.

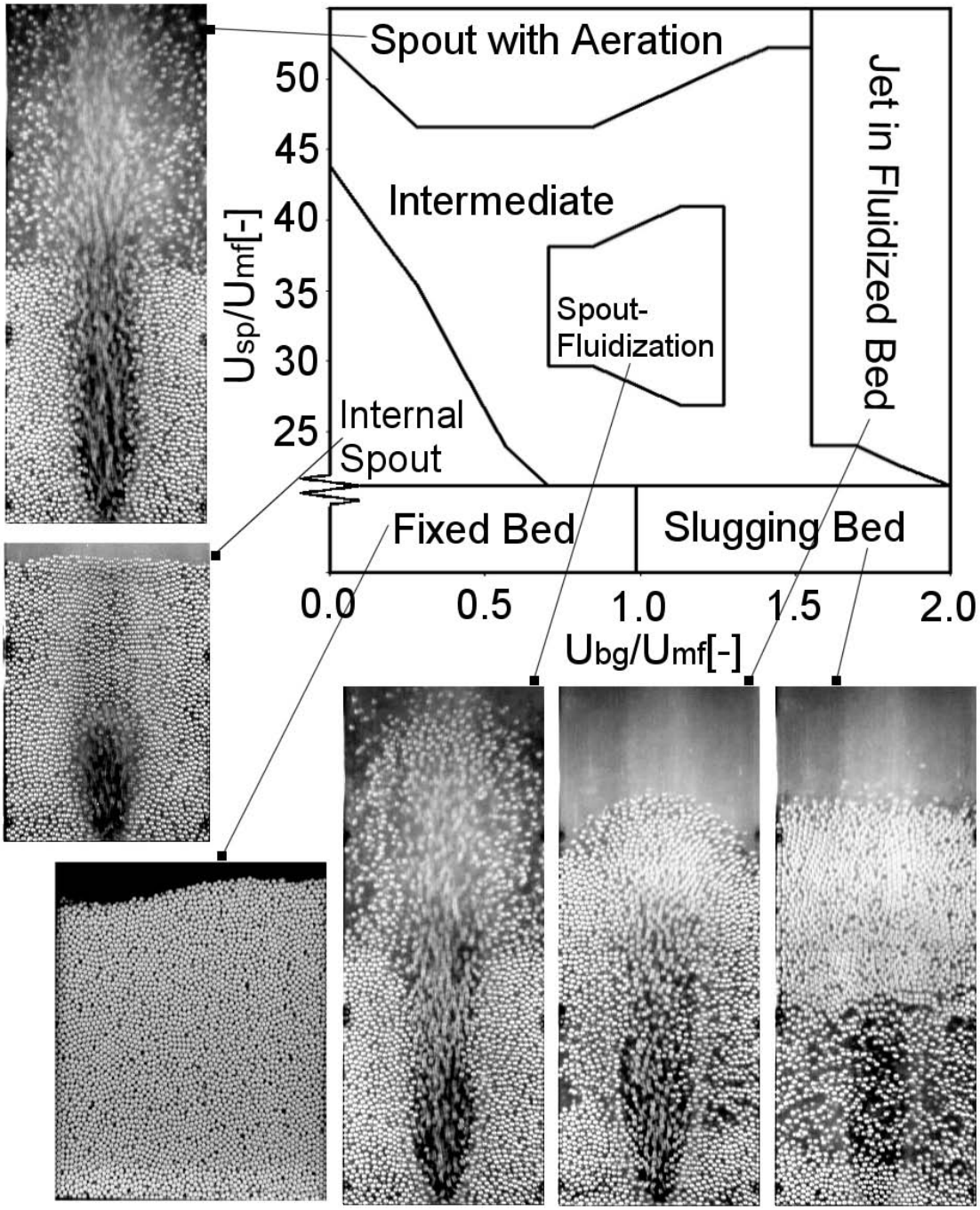

Figure 4.16 Flow regime map with example snapshots for system C, monodisperse particle size distribution in a 3D spout-fluid bed with a spout at the wall.

The difference between systems A and C is the position of the spout. The spout channel in system C is positioned near the wall, therefore the particles can only enter the spout channel from three directions instead of four. Consequently, it is less likely that the particles block the spout channel. As a result, the range of operating conditions displaying spout-fluidization behavior is reduced. Since spout-fluidization can occur at much lower background velocities in system A, it can also produce pressure drop fluctuations with a much lower frequency. Frequencies as low as 2 Hz have been observed in system A.

In system D, both the bed geometry, pseudo-2D, and the size of the particles differ from system A. In system D, the spout channel is only accessible from two directions instead of four. Therefore the range of operating conditions displaying spout-fluidization behavior in system D is relatively small, similar to system C. Another noticeable difference is that the internal spout regime is observed over a smaller range of operating conditions. This can be attributed to the ratio between the background area and the spout area, which is relatively small in the pseudo-2D geometry (14) compared to the 3D geometry (48). All flow regime maps show that the internal spout regime is roughly bounded by the spout velocity at which the superficial gas velocity equals the minimum fluidization velocity.

The particles in system E consist of another material, urea, and are slightly smaller than the particles in system A. This results in a flow regime map, where the spout-fluidization regime even occurs at high spout velocities. The more pronounced departure from the spherical shape and the strongly non-ideal collision properties of the urea particles, i.e. considerable energy dissipation during collisions, are responsible for this behavior. Both of these properties will keep the particles closer together and consequently the particles move in groups instead of individually. It is therefore more likely that a group of particles enters and blocks the spout channel resulting in spout-fluidization behavior, even at high spout velocities.

It can be concluded, that the flow regime map of a spout-fluid bed is not only determined by the spout and background velocities. The geometry, particle properties and particle size distribution also have a profound influence on the flow regime map. These parameters especially influence the exact location of the boundaries between the flow regimes.

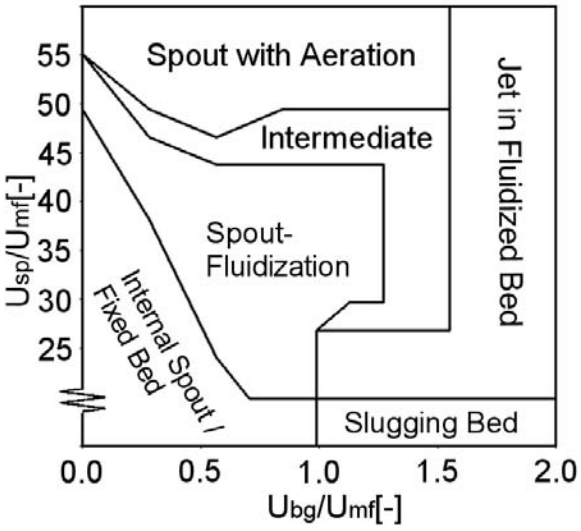

System A: monodisperse 3D centre spout

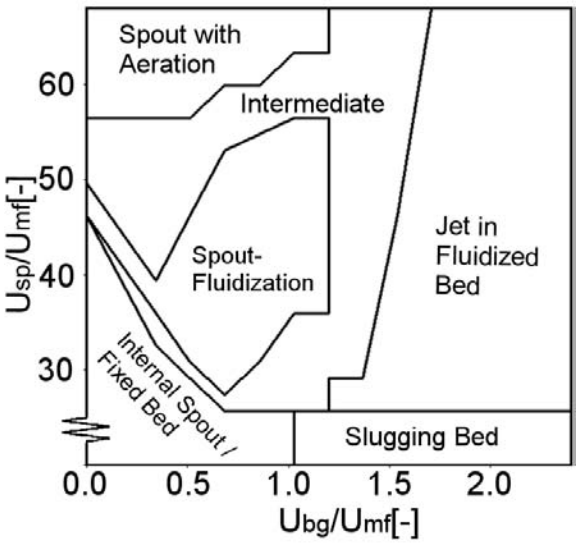

System B: bidisperse 3D centre spout

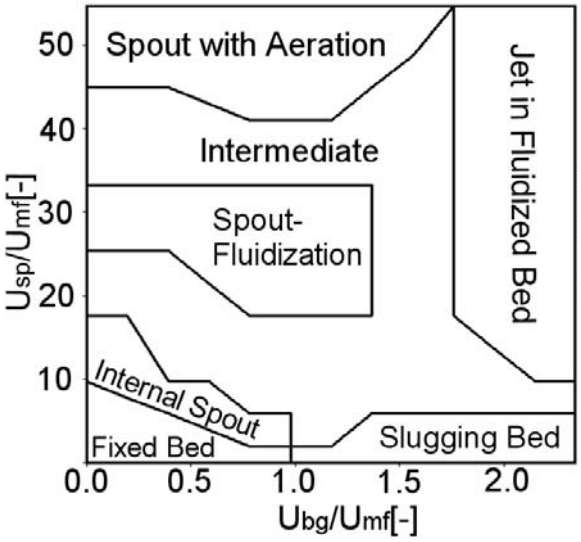

System D: monodisperse 2D

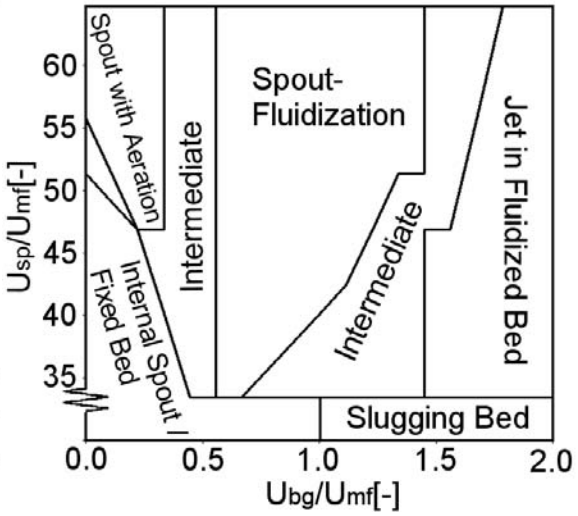

System E: monodisperse urea 3D centre spout

Figure 4.17 Flow regime maps for particles with varying properties in three different spout-fluid beds.

Chapter 5

Verification and validation of a DPM for a pseudo-2D spout-fluid bed

Abstract

In this chapter the discrete particle model described in chapter 3 is verified and validated in a pseudo-2D set-up.
The time-averaged particle flux and the pressure drop fluctuations for simulations started from slightly different initial conditions have been compared for different operating regimes. Based on the simulation results, it can be concluded that the instantaneous model results are affected by the initial conditions. The time-averaged results are however virtually independent of the initial conditions provided that the averaging period is sufficiently large.
The time-averaged particle flux and the pressure drop fluctuations obtained with both particle-particle interaction models presented in chapter 3 have been compared for different operating regimes. It proved that the chosen spring stiffness was sufficiently large to prevent it from affecting the simulation results of the soft-sphere model. Furthermore, for this value of the spring stiffness the results obtained with the hard and soft sphere model are virtually identical, indicating that the models are interchangeable.

In order to facilitate a sufficiently fine grid to resolve all details of the flow, a new method for the implementation of the two-way coupling is proposed. This method, which is referred to as the “cube method”, produces grid independent results for both the drag force exerted on a single particle and the pressure drop over a packed bed.
The results of the cube method display slight offsets from the analytical solutions for small grid sizes. These offsets are however significantly smaller than the offsets observed with the conventional method.

Based on the simulation results, a value of 5 is proposed for the ratio between the cube and particle diameter. This value is considered to be sufficiently small to capture the details of the flow. Furthermore the value is sufficiently large to reduce the offset to an acceptable level.
The pressure drop fluctuations, the time-averaged particle flux and the time-averaged gas velocity for different operating regimes show that even in a system where the width of the spout channel is 10 mm, a numerical grid size of 10mm (i.e. 4 times the particle diameter) is sufficiently small to obtain grid independent results.

Several drag closures were tested in the DPM to assess their suitability regarding spout-fluid beds. The time-averaged particle flux and the pressure drop fluctuations for all drag closures presented in chapter 3 have been compared for different operating regimes. It was found that the most frequently used drag model (i.e. the Ergun equation (1952) for low porosities, and the Wen and Yu relation (1966) for high porosities) produces unsatisfactory results for fluid beds with stable high velocity jets, as encountered in spout(-fluid) beds. The usage of the minimum of the drag given by the relations of Ergun (1952), and Wen and Yu (1966), as well as the relation proposed by Koch and Hill (2001) improves the predictions of the DPM, although the computed frequency of the pressure drop fluctuations is still somewhat too high. Because of its more fundamental nature the use of the Koch and Hill relation (2001) is to be preferred.

Part of this chapter was published as:

Link, J.M., Deen, N.G., and Kuipers, J.A.M., 2004. Discrete Particle Simulation of a Spout-Fluid Bed: Treatment of two-way Coupling and Effect of Drag Closure, Proceedings 5th International Conference on Multiphase Flow, ICMF'04, Yokohama, Japan, May 30-June 4, 2004, Paper No. 457.

J.M. Link, L.A. Cuypers, N.G. Deen, and J.A.M. Kuipers, Flow regimes in a spout–fluid bed: A combined experimental and simulation study, Chemical Engineering Science, 60-13, 3425-3442

5.1 Introduction

The spout-fluid bed poses some challenges for the DPM: a steep velocity gradient in the gas phase is present near the spout region and the particle Reynolds numbers are much higher than those encountered in regular (bubbling) fluidized beds, especially near the spout mouth. For this reason the effects of various numerical settings on the simulation results will be assessed in this chapter in order to determine the proper settings for simulating spout-fluid beds.
In order to resolve the large velocity gradients in the spout region, a sufficiently fine computational mesh is required. This requirement complicates the two-way coupling, since in DPM simulations computational cells are used, which are typically large in comparison with the particle size. In order to overcome these contradictory demands, a new method was introduced in chapter 3 to calculate the porosity and the forces acting on a particle in a grid-independent manner while assuring a sufficiently fine solution of the gas flow field. In this chapter, the grid dependency of the new method is assessed, in comparison with the conventional method, by investigating the computed gas phase flow field for two operating regimes.
In addition several drag relations are tested regarding their suitability to describe the effective drag force acting on particles in spout-fluid beds by comparing the simulation results with experimentally determined pressure drop fluctuations and particle flux profiles.

The organization of this chapter is as follows. In section 5.2 the experimental procedure will be explained, followed by a presentation of the test cases that are used in this chapter in section 5.3. Subsequently the reproducibility of the simulations is investigated in section 5.4, by considering different initial conditions. In section 5.5 the results obtained with different collision models are compared. The grid dependency of the new and the conventional mapping methods are assessed in section 5.6. Finally, the results obtained with several drag relations are compared in section 5.7.

5.2 Experimental procedure

The objective of the experiments presented in this chapter is to select a proper drag closure and numerical settings. For this purpose, a pseudo-2D geometry is preferred over a 3D geometry, because it is more accessible to experimental techniques, which allows a more detailed experimental study, and requires less computational time for the simulations. To ensure that all characteristic behavior in a pseudo-2D spout-fluid

bed is captured, suitable operating conditions were selected from the flow regime map presented in chapter 4.

The set-up consists of a pseudo-2D gas-fluidized bed, schematically represented in Figure 5.1, and an air supply system. The depth of the bed is 6 times the particle diameter (i.e. 15 mm) to prevent bridge formation, i.e. stable particle configurations extending from wall to wall. The depth of the bed is assumed to be sufficiently small for the bed to display pseudo-2D behavior, which is necessary to enable the use of digital image analysis as a whole field measuring technique.
The front wall of the bed consists of a glass plate to permit visual observation of the particle motion inside the bed. The side walls of the bed are made of aluminum strips and the back wall is made of polycarbonate.
The set-up was filled with $2.45 \cdot 10^4$ small particles. The properties of the particles that were used are given in Table 5.1.
Dry pressurized air from a tank, which was kept at a pressure of 5 bar, was fed to the bed through three separate sections. A 3 mm thick porous plate with an average pore size of 10 microns provided a homogeneous gas distribution over the two fluidization sections. A 0.5 mm metal gauze covered the spout mouth located in between the fluidization sections. The gas flow rate in each section was accurately controlled by mass flow controllers and rapidly responding magnetic valves. To prevent the build-up of static electricity the humidity of the air in the fluidization sections was maintained at 60-70% by addition of steam.

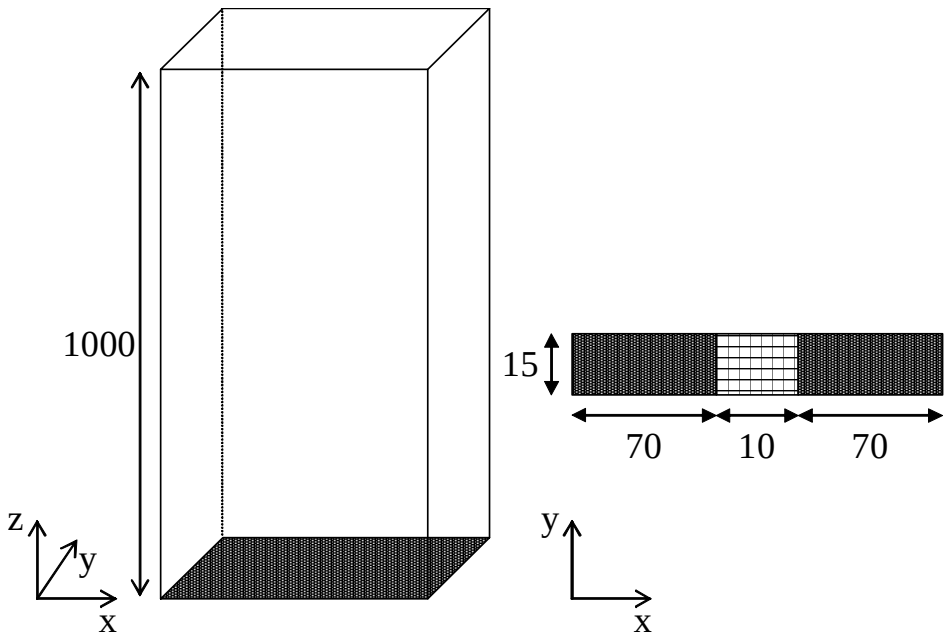

Figure 5.1 Schematic representation of the geometry of the pseudo-2D bed, dimensions are given in mm.

Property	**Particles**	**Unit**
Material	Glass	-
d_p	2.49 ± 0.02	mm
ρ_p	2526 ± 6	kg/m^3
u_{mf}	1.28 ± 0.02	m/s
$e_{n,\, p \leftrightarrow p}$	0.97 ± 0.01 [a]	-
$e_{n,\, p \leftrightarrow w,\, glass}$	0.97 ± 0.01 [a]	-
$e_{n,\, p \leftrightarrow w,\, polycarbonate}$	0.97 [b]	-
$e_{n,\, p \leftrightarrow w,\, aluminum}$	0.97 [b]	-
$\mu_{p \leftrightarrow p}$	0.10 ± 0.01 [a]	-
$\mu_{p \leftrightarrow w,\, glass}$	0.09 ± 0.01 [a]	-
$\mu_{p \leftrightarrow w,\, polycarbonate}$	0.10 [b]	-
$\mu_{p \leftrightarrow w,\, aluminum}$	0.10 [b]	-
$\beta_{0,\, p \leftrightarrow p}$	0.33 ± 0.05 [a]	-
$\beta_{0,\, p \leftrightarrow w,\, glass}$	0.33 ± 0.05 [a]	-
$\beta_{0,\, p \leftrightarrow w,\, polycarbonate}$	0.33 [b]	-
$\beta_{0,\, p \leftrightarrow w,\, aluminum}$	0.33 [b]	-
[a] measured through detailed collision measurements, see Kharaz et al. (1999) [b] not measured, but estimated based on the properties of other wall materials		

Table 5.1 Particle properties.

During the experiments, the fluctuations in the bed pressure drop (excluding the gas distributor) are recorded using a high frequency pressure probe (Kulite XT-190M-0.35BAR VG) at a frequency of 100 Hz. The pressure probe was positioned in the back (polycarbonate) wall of the bed about 0.01 m above the porous plate and 0.04 m right of the left wall. The pressure drop fluctuations were recorded during a period of one minute.

Digital images were recorded with a 262 Hz CCD camera (Dalsa CA-D6) equipped with a 12.5 mm lens. The aperture of the camera was set to f4 and the exposure time was fixed at 3.8 ms. The recorded images consist of 532 x 516 8-bit pixels. The image quality depends on the illumination conditions of the bed, which were set to be strong and continuous. This was accomplished with the use of two 500 W halogen lamps positioned along each side of the camera, which were illuminating the bed under a small angle (< 45°) in order to prevent undesirable reflections. The digital images were recorded over a period of 20 s.

5.3 Flow regime map and case selection

The flow regime map that was constructed in chapter 4 is reproduced in Figure 5.2. From this regime map two test cases were selected using the following selection criteria:

1. The selected regimes are representative for most of the behavior encountered in a spout-fluid bed.
2. The selected regimes display dynamic behavior.
   The presence of dynamic behavior allows both a qualitative and a quantitative comparison between the results of the experiments and the simulations.
3. The selected operating conditions are well within the regime limits.
   When the operating condition is on the border between two regimes, small deviations in the simulation results can cause large deviations in the predicted regime.

Based on these criteria, two test cases were selected. These are marked in the flow regime map and are presented in Table 5.2.

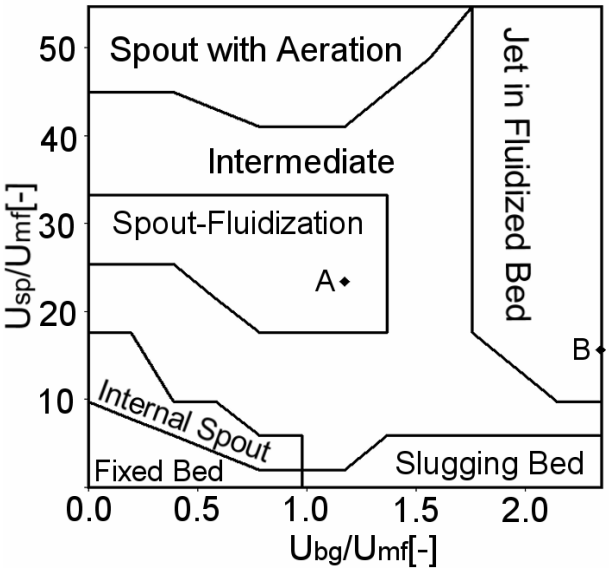

Figure 5.2 Regime map for a monodisperse particle size distribution in a pseudo-2D spout-fluid bed (system D, see chapter 4), indicating the operating conditions for the selected cases A and B.

Case	Flow regime	u_{bg} (m/s)	u_{bg} /u_{mf} (-)	u_{sp} (m/s)	u_{sp} /u_{mf} (-)
A	Spout-fluidization	1.5	1.2	30	23
B	Jet-in-fluidized-bed	3.0	2.3	20	16

Table 5.2 Test cases for the pseudo-2D spout-fluid bed.

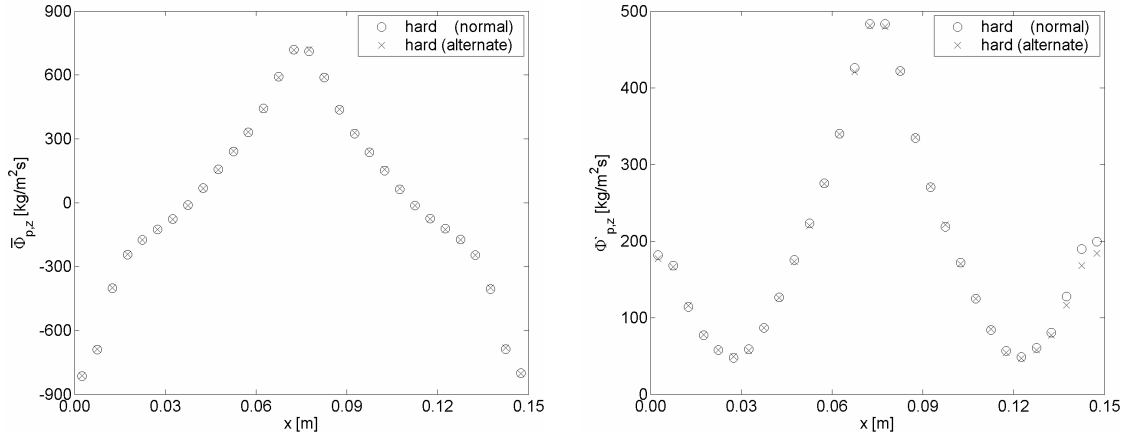

case A, spout-fluidization

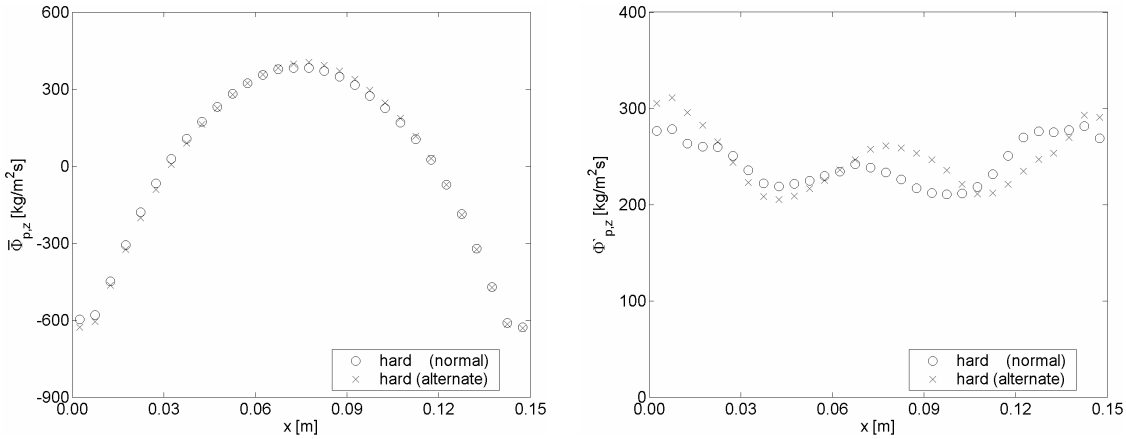

case B, jet in fluidized bed

Figure 5.3 Profiles of the vertical time-averaged particle flux and associated fluctuations at a height of 0.15 m for two different initial conditions (the base case, i.e. normal, and the altered case, i.e. alternate) and for two different regimes.

5.4 Reproducibility

The behavior of a spout-fluid bed can be considered as chaotic, especially in the regimes with a relatively large background velocity. Therefore the simulation results for two different initial conditions were compared. The only difference between the initial conditions was the sign of the velocity of one particle (out of ~25,000). The simulations were performed for both test cases for a period of 20 s (see also Table 5.2).

The particle dynamics can be characterized by the time-averaged particle fluxes, which are displayed in Figure 5.3 for both cases. For case A, the spout-fluidization regime, both the time-averaged result and the associated RMS are virtually identical. This indicates that the run-time of the simulation was sufficiently long to eliminate

the influence of the initial conditions. This observation agrees with the regular, high frequency behavior observed in the spout-fluidization regime.

The time-averaged particle flux for case B, the jet in fluidized bed regime, is also hardly affected by the initial conditions. The associated RMS however shows a variation of approximately 10%. Further analysis showed that this variation increased with decreasing length of the simulation and will most likely decrease for longer simulations. It is concluded that case B requires a longer simulation period than case A because of the more irregular, low frequency behavior observed in the jet-in-fluidized-bed regime.

Subsequently, the dynamic behavior of the case that proved to be most difficult (i.e. case B) was assessed in more detail by spectral analysis of the pressure drop fluctuations. The pressure drop fluctuations, displayed in Figure 5.4, are found to be very irregular.

However, the frequency spectra of these fluctuations, displayed in Figure 5.5, show that the overall behavior starting from different initial conditions is similar.

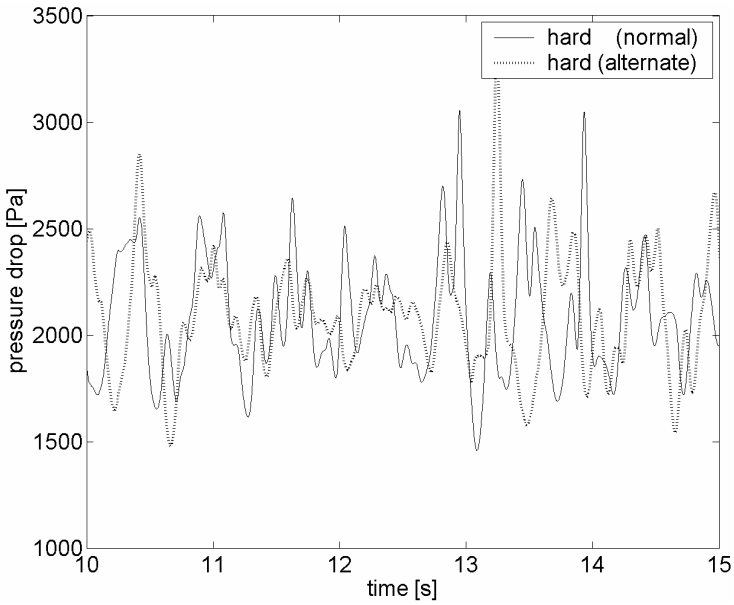

Figure 5.4 Computed pressure drop fluctuations over the entire bed for case B, the jet in fluidized bed regime, with two different initial conditions (the base case, i.e. normal, and the altered case, i.e. alternate).

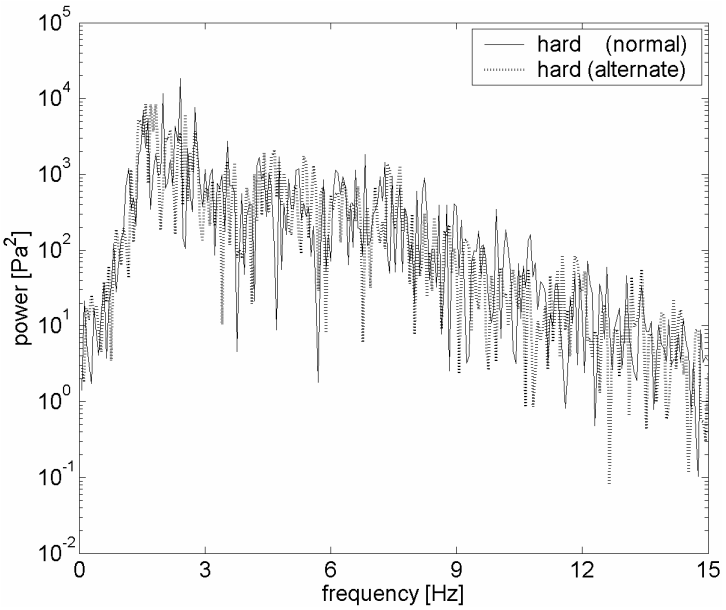

Figure 5.5 Frequency spectra of computed pressure drop fluctuations over the entire bed for case B, the jet in fluidized bed regime, with two different initial conditions (the base case, i.e. normal, and the altered case, i.e. alternate).

5.5 Collision model

In this study two collision models are used to determine the particle-particle interaction; the hard sphere model and the soft sphere model. The influence of the collision model on the simulation results is assessed in this section.

In the soft sphere collision model the spring stiffness is used as an input parameter. In this study a relatively large value of 10,000 N/m was used for the spring stiffness because of the large particle velocity differences that can be encountered in a spout-fluid bed. To test whether this value was sufficiently large the results of a simulation were compared with the results of a similar simulation with a spring stiffness of 100,000 N/m. The latter value was considered to be sufficiently large, since when this value was used to calculate the maximum overlap, using Ye (2005) and assuming a relatively large impact velocity (2.5 m/s), an overlap of just 1% was found.
Furthermore, the results of the simulations using the soft sphere model are compared with those of the hard sphere model.
The simulations with a duration of 20 s were performed for both test cases described in Table 5.2.

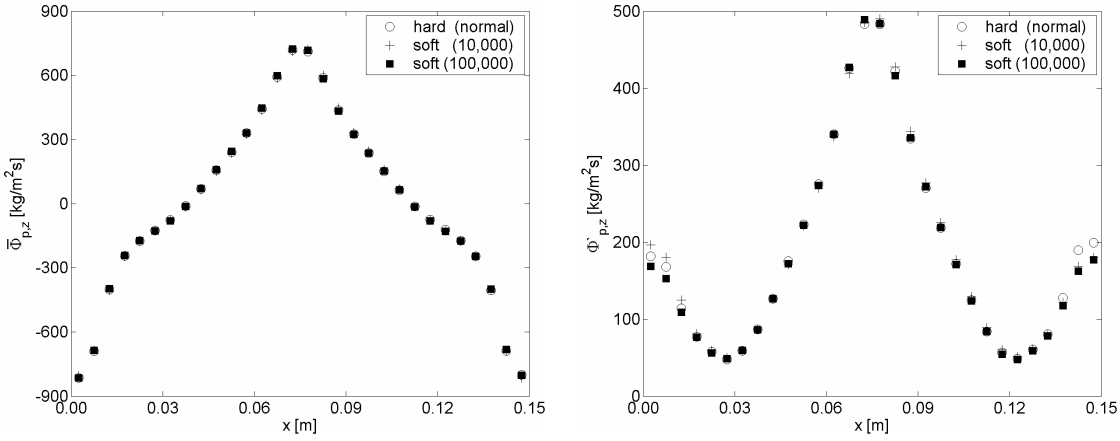

case A, spout-fluidization

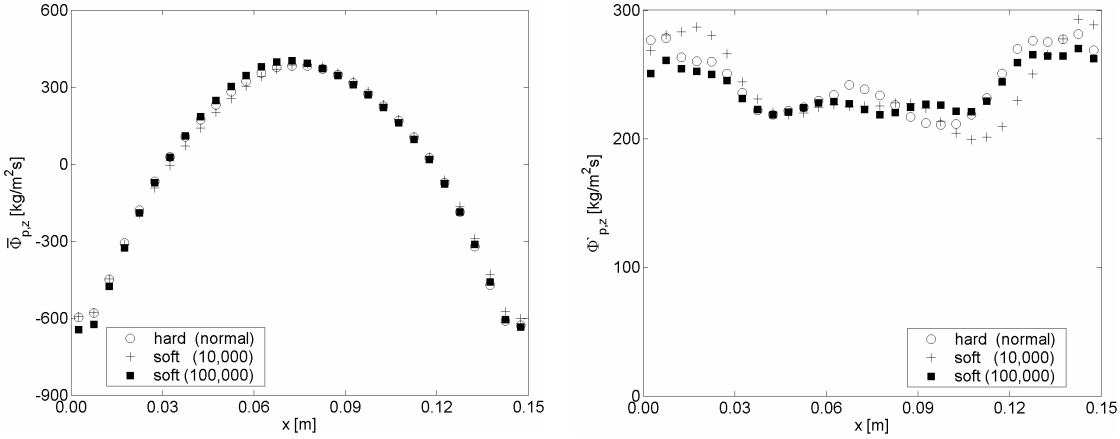

case B, jet in fluidized bed

Figure 5.6 Profiles of the vertical time-averaged particle flux and associated fluctuations at a height of 0.15 m for three different collision models and for two different regimes.

Figure 5.6 shows the time-averaged particle flux and the associated RMS. The time-averaged results are very similar, as is the RMS of case A. The RMS of case B is not exactly the same for the three collision models, but the trends are similar.
The pressure drop fluctuations in Figure 5.7 show that the fluctuations differ significantly, but that the patterns of the fluctuations are comparable. This is confirmed by the associated frequency spectra that are shown in Figure 5.8, which are very similar for all collision models.

The uncertainty in the RMS of the particle flux for case B can be attributed to the finite run-time of the simulation, as was shown in the previous section. Since all other investigated properties are similar for both values of the spring stiffness, it can be concluded that a spring stiffness of 10,000 N/m is sufficiently large to obtain results that are independent of the spring stiffness.

The results for the hard sphere model and the soft sphere models show similar trends as observed for the influence of the spring stiffness and the initial conditions. Therefore it can be concluded that the results using both collision models are comparable.

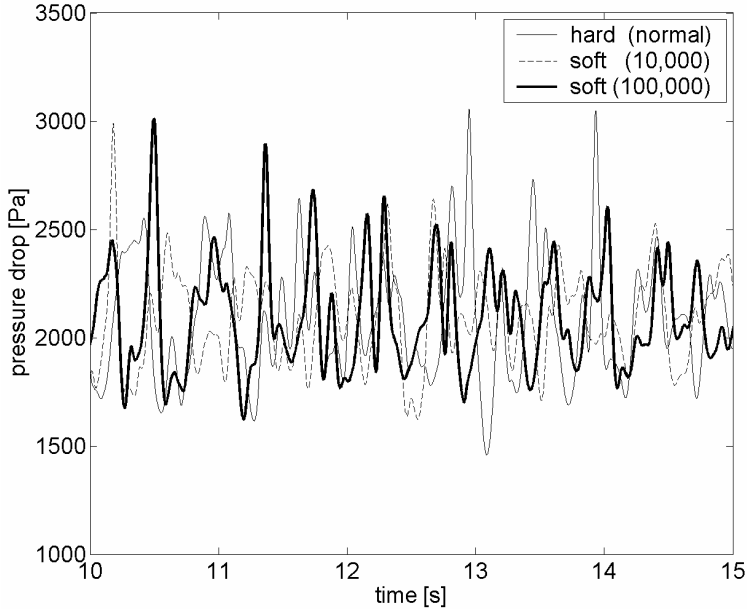

Figure 5.7 Computed pressure drop fluctuations over the entire bed for case B, the jet in fluidized bed regime, with three different collision models.

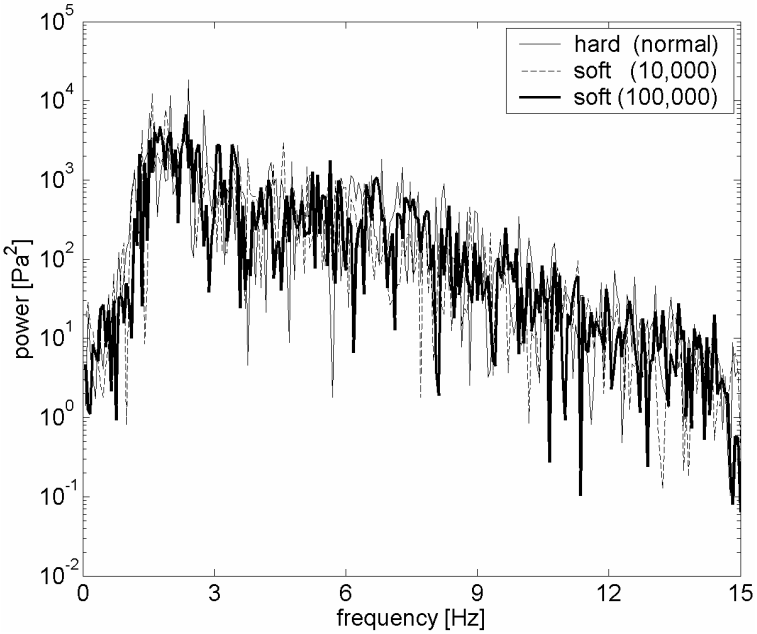

Figure 5.8 Frequency spectra of computed pressure drop fluctuations over the entire bed for case B, the jet in fluidized bed regime, with three different collision models.

5.6 Grid resolution

A new method, which will be referred to as the "cube method", was proposed in chapter 3 to exchange properties between the gas phase at the Eulerian grid points and the particles at the Langrangian positions. This method is verified in the first part of this section and compared with the results obtained with the method proposed by Hoomans *et al.* (1996), which will be referred to as "Hoomans method". In the second part of this section the grid dependency of the spout-fluid bed simulations will be assessed.

5.6.1 Model verification

The main objective of the verification is to determine the grid dependency of the cube method.

For this purpose two test cases were selected:

1. a dense packed bed to determine the performance of the cube method for dense systems.
2. a large bed containing a single particle to determine the performance of the cube method for dilute systems.

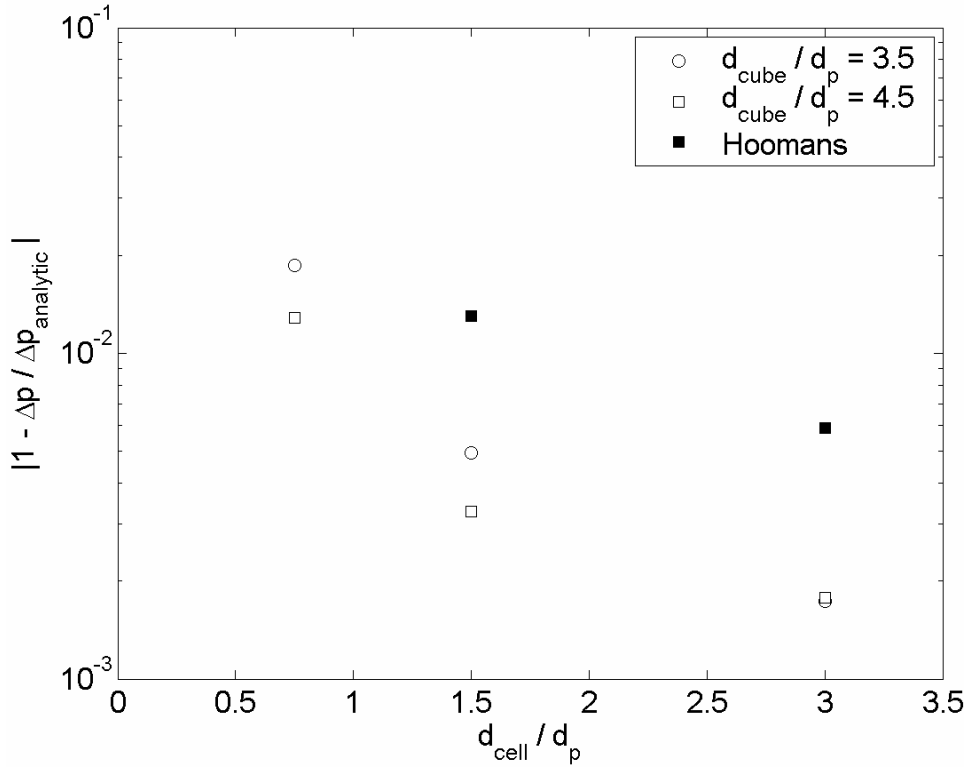

Figure 5.9 Deviation from the analytical pressure drop over a packed bed as a function of the grid cell size calculated using the cube method (with different cube sizes) and the method used by Hoomans *et al.* (1996).

In the packed bed case, a cubic bed assuming free-slip boundaries is completely filled with particles at an equidistant spacing of exactly one particle diameter (4 mm) in all directions, i.e. the particles are touching each other. This spacing produces a uniform porosity of:

$$\varepsilon_f = 1 - \frac{(\pi/6) d_p^3}{d_p^3} = 1 - \frac{\pi}{6} = 0.48 \tag{5.1}$$

Gas flows through the bed at a constant superficial velocity of 0.5 m/s. The gas-particle drag was modeled with the Ergun equation (1952). The computed pressure drop over the bed was compared to the analytical pressure drop obtained from the Ergun equation.

Three different grid sizes and two different cube sizes were used. The relative deviation from the analytical pressure drop is displayed in Figure 5.9 for all simulations that were conducted. It turned out that Hoomans' method could no longer be applied, when the grid size was smaller than the particle size. This is due to the assumption that a particle is distributed over a maximum of two grid cells in each direction.
Figure 5.9 shows that the deviation from the analytical pressure drop is larger for Hoomans' method than for the cube method, while the deviation decreases with increasing cube size. Unfortunately the deviation from the analytical solution increases with decreasing grid size for both methods and cube sizes.
The origin of this deviation lies in the cubic nature of the distribution, which causes discrete local fluctuations in the porosity. Consequently, the cube method does not produce the analytical pressure drop and is therefore not completely accurate. When the grid size is further decreased, the solution using the cube method will, contrary to the Hoomans' method, in theory converge to a single value, because of the grid independent size of the cubes around the particles. Therefore the cube method is in theory grid independent. Furthermore, the discrete fluctuations decrease with increasing cube size because of the smaller average particle volume fraction of larger cubes.

In the other test, a single particle with a diameter of 4 mm was kept at a constant position in the center of a bed with free-slip boundary conditions. The superficial gas velocity is set to 16.28 m/s, which is the analytical terminal velocity at a porosity of 1. The DPM was used to calculate the net vertical force exerted on the particle by the gas phase using both the cube method and Hoomans' method, employing several grid and cube sizes.

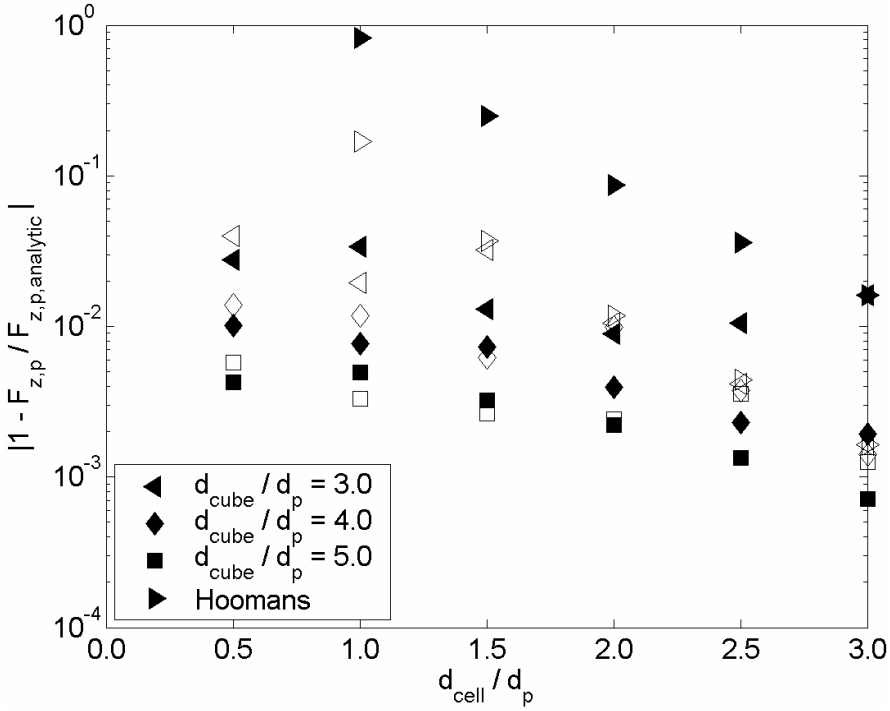

Figure 5.10 Deviation from the analytical drag force on a single particle as a function of the grid cell size calculated using the cube method (with different cube sizes) and the method used by Hoomans *et al.* (1996). The cases for which the center of mass of the particle is positioned in the corner point of eight Eulerian cells are represented by open dots, while filled dots represent the cases for which the center of mass of the particle is positioned in the center of an Eulerian cell.

Additionally, the position of the particle relative to the Eulerian cells was varied to assess the influence of the resulting average gas properties on the force experienced by the particle. For all simulations, the center of mass of the particle was either positioned in a cell center or at the corner point of a cell.
The relative deviation from the analytical force is displayed in Figure 5.10 for all simulations that were conducted. It is found that Hoomans' method can no longer be applied, when the grid size is smaller than the particle diameter, which is due to the assumption that a particle is distributed over a maximum of two grid cells in each direction.

Figure 5.10 shows that the accuracy of Hoomans' method rapidly decreases when the grid is refined. This is caused by the decreasing porosity of the cell(s) containing the particle. This effect is also observed for the new method, but to a much lesser extent. The deviation appears to reach a stable value when the grid size is smaller than the particle diameter. This can be explained, since the deviation originates from

comparison to the analytical porosity, which is assumed to be unity, and can therefore not be reached by the simulation. The simulation does however reach a point where a further decrease of the cell size does no longer affect the porosity.
Since the average porosity increases with cube size, the results obtained with larger cubes are more accurate.
Apart from improving the accuracy, the cube method also decreases the influence of the particle position within a cell.

The cube method presented in this study produces better results than the method that was originally used by Hoomans *et al.* (1996) for both dense and dilute beds. A drawback of the cube method is that its results are not completely accurate under most circumstances. The inaccuracy of the cube method can however be diminished and probably even removed by using weight factors that decrease with increasing distance from the particle, e.g. triangular, Gaussian or sine functions (see for example Zhu & Yu, 2002). A drawback of such functions is that they will (significantly) increase the required computational time to remove rather small inaccuracies, which will only be noticeable for very fine grids.
The improvement of the accuracy compared to Hoomans' method along with the grid independency were considered to be sufficient reason to use the cube method for the simulations presented in this thesis. It was decided not to use the alternative, more accurate functions in this work, since the inaccuracies for the simulations presented in this thesis will be small given the relatively large grid size that was used in the simulations. The inaccuracy was reduced by setting the cube diameter to 5 times the particle diameter. A larger value was not considered to be desirable, since it would impair the representation of the local particle configuration.
In order to examine whether the new method for the two-way coupling is effective, the porosity based on a random particle configuration was determined using the new method and Hoomans' method. The results of the calculation are presented in Figure 5.11, which shows that the results of the new method are consistent, although minor scattering near the walls can be observed, when a fine computational grid is used. The method used by Hoomans *et al.* (1996) exhibits significant scattering over the entire width of the bed, when the computational grid is refined. For coarse grids, both methods produce similar results.

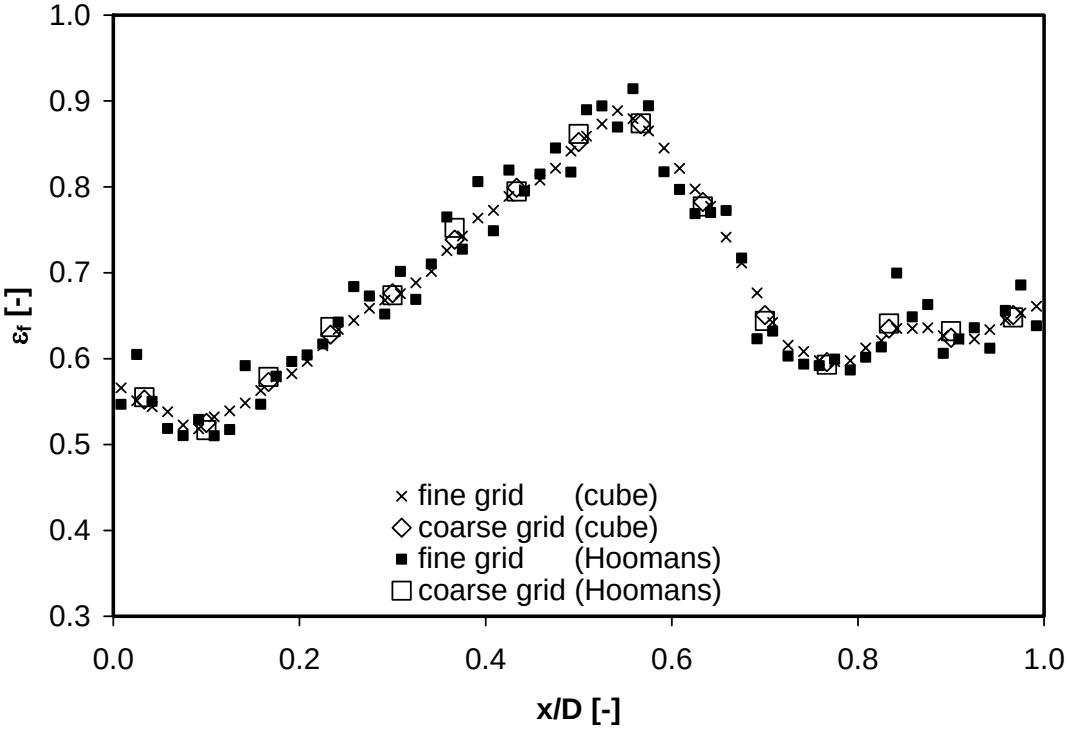

Figure 5.11 Porosity profile of a random particle configuration determined with the cube method and the method used by Hoomans *et al.* (1996) for a fine grid (d_{cell}/d_p = 1.0) and a coarse grid (d_{cell}/d_p = 4.0).

5.6.2 Grid selection

The cube method was used to assess the influence of the computational grid on the results of the simulations. The DPM, described in chapter 3, was used to simulate the flow in the pseudo-2D spout-fluid bed, described in section 5.2, on a fine (5 mm) and a coarse (10 mm) computational grid. Two test cases (A and B), corresponding to different regimes, were investigated (see Table 5.2). A period of 20 s was simulated from identical initial conditions using the Koch and Hill (2001) drag relation. In the analysis the first 4 s were omitted to eliminate start-up effects.

The pressure drop over the bed was recorded at a frequency of 1000 Hz for all test cases. The results are displayed in Figure 5.12. In order to enable a quantitative comparison, a frequency spectrum, displayed in Figure 5.13, was determined by applying the SAPDF technique, described in chapter 2, to the dynamic pressure drop signals.

The pressure drop signals displayed in Figure 5.12 show small differences between the two computational grids. Consequently, the resulting frequency spectra, which are displayed in Figure 5.13, show only minor differences in the dominant frequencies that were obtained. It is concluded that the coarse grid yields a sufficiently accurate resolution to capture the dynamics of the pseudo-2D spout-fluid bed.

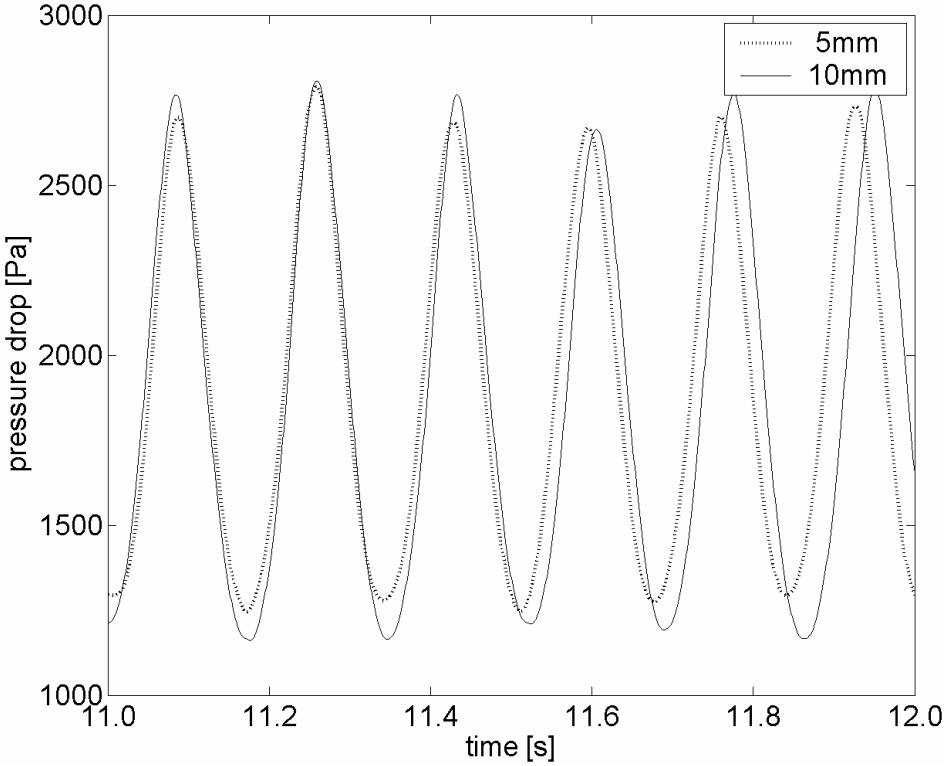

Case A, spout-fluidization

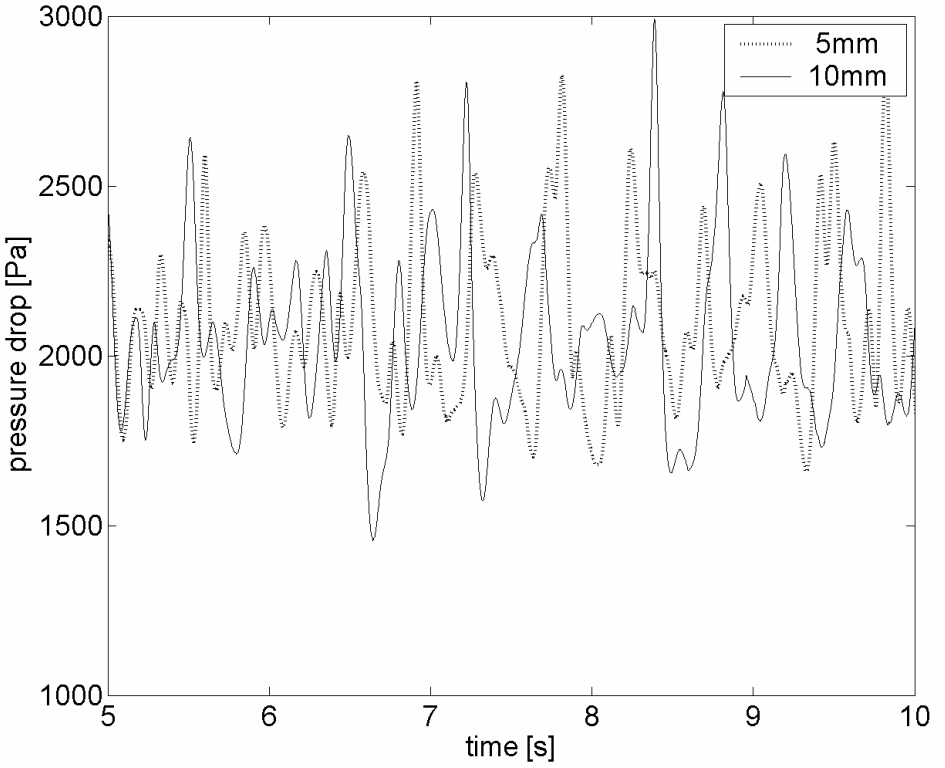

Case B, jet in fluidized bed

Figure 5.12 Computed pressure drop fluctuations over the entire bed for two different regimes on two computational grids.

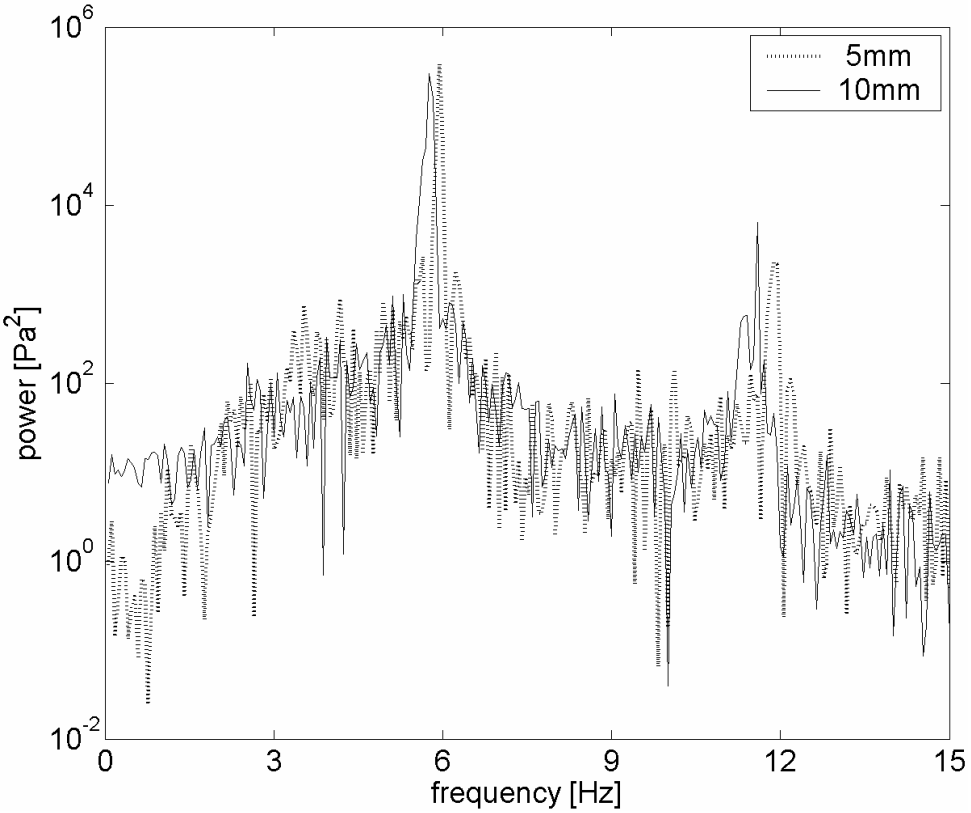

Case A, spout-fluidization

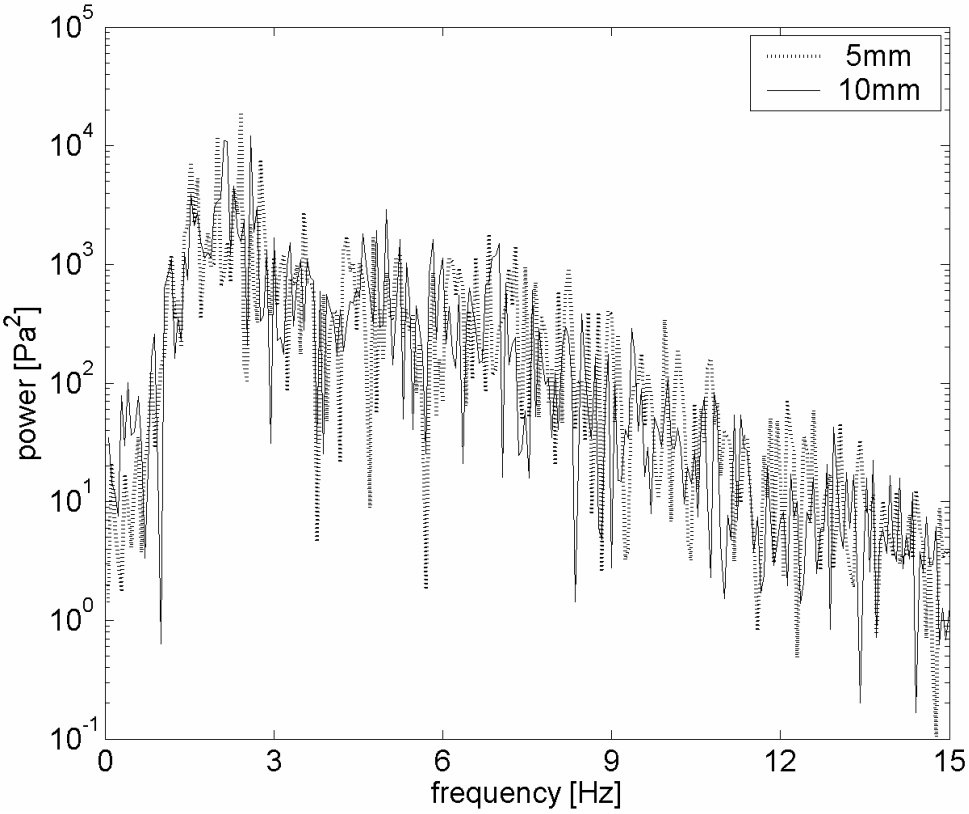

Case B, jet in fluidized bed

Figure 5.13 Frequency spectra of computed pressure drop fluctuations over the entire bed for two different regimes on two computational grids.

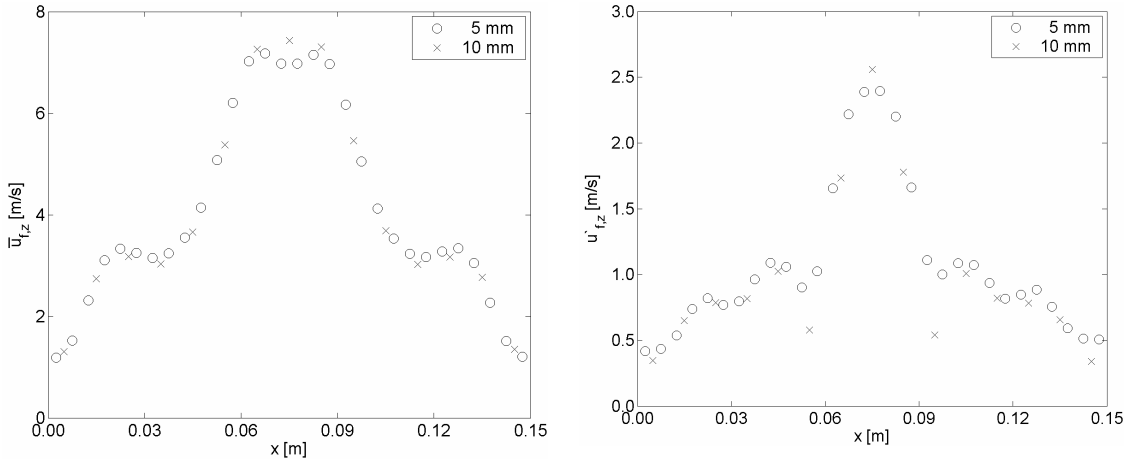

Case A, spout-fluidization

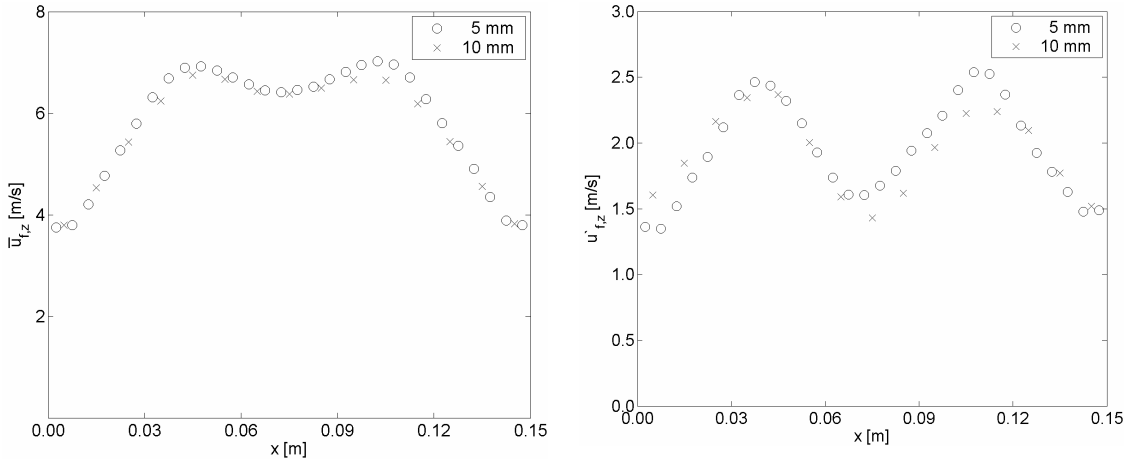

Case B, jet in fluidized bed

Figure 5.14 Profiles of the time-averaged gas velocity and associated fluctuations at a height of 0.15 m for two different regimes on two computational grids.

The computed gas velocity and the particle flux fields were stored at a frequency of 250 Hz. From these quantities time-averaged and root mean square values were derived, which are presented in Figure 5.14 and Figure 5.15 respectively.

Figure 5.14 shows that the vertical time-averaged gas velocity and its fluctuations are slightly influenced by the choice of the computational grid for both cases. As can be expected, the vertical time-averaged particle fluxes in Figure 5.15 display less sensitivity with respect to the size of the computational grid.

Since the differences between the results for both grids are of the same order of magnitude as the reproducibility, a grid size of 10 mm is considered to be sufficiently fine for the simulations reported here. It is noted that larger grid cells were not considered because of the limited size of the spout channel.

5.7 Drag closure

A proper description of the fluid-particle interaction (drag) in spout-fluid beds is vital to obtain realistic simulation results. The drag is described using the inter-phase momentum transfer coefficient, β, which can be calculated using several drag relations. Three different drag relations were presented in chapter 3 and are summarized in Table 5.3.

In order to identify a suitable drag closure for the DPM simulations of spout-fluid beds, the fluid-particle interaction is characterized by recording the distribution of the particle Reynolds number, Re_p, for both cases summarized in Table 5.2, employing the drag model of Koch and Hill (2001).

The Re_p that were observed during DPM simulations were recorded for a period of 1 s. Figure 5.16 shows the resulting distribution of Re_p. It can be seen that for both cases most particles (97%) have a relatively high Reynolds number, i.e. between 200 and 10,000.

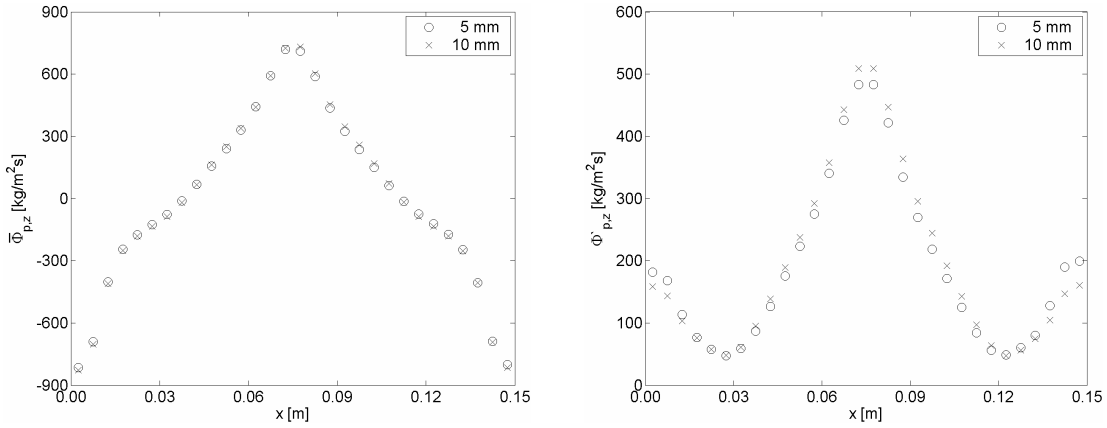

Figure 5.15 Profiles of the vertical time-averaged particle flux and associated fluctuations at a height of 0.15 m for two different regimes on two computational grids.

Drag relation	**Reference**
$\beta_{Ergun} = 150\frac{\varepsilon_p^2}{\varepsilon_f}\frac{\mu_f}{d_p^2} + 1.75\varepsilon_p\frac{\rho_f}{d_p}\left\|\mathbf{u}_f - \mathbf{v}_p\right\|$	Ergun (1952)
$\beta_{Wen\&Yu} = \frac{3}{4}C_D\varepsilon_p\frac{\rho_f}{d_p}\left\|\mathbf{u}_f - \mathbf{v}_p\right\|\varepsilon_f^{-1.65}$	Wen and Yu (1966)
$\beta_{Koch\&Hill} = \frac{18\mu_f\varepsilon_f^2\varepsilon_p}{d_p^2}\left(F_0(\varepsilon_p) + \frac{1}{2}F_3(\varepsilon_p)\,\mathrm{Re}_p\right)$ if $\mathrm{Re}_p > 40$	Koch and Hill (2001)
with	
$C_D = \begin{cases} \frac{24}{\mathrm{Re}_p}(1 + 0.15\,\mathrm{Re}_p^{0.687}) & \text{if } \mathrm{Re}_p < 1000 \\ 0.44 & \text{if } \mathrm{Re}_p \geq 1000 \end{cases}$	Schiller and Naumann (1933)
$\mathrm{Re}_p = \frac{\varepsilon_f\rho_f\left\|\mathbf{u}_f - \mathbf{v}_p\right\|d_p}{\mu_f}$	
$F_0(\varepsilon_p) = \begin{cases} \frac{1 + 3\sqrt{\frac{\varepsilon_p}{2}} + \frac{135}{64}\varepsilon_p\ln(\varepsilon_p) + 16.14\varepsilon_p}{1 + 0.681\varepsilon_p - 8.48\varepsilon_p^2 + 8.16\varepsilon_p^3} & \text{if } \varepsilon_p < 0.4 \\ \frac{10\varepsilon_p}{\varepsilon_f^3} & \text{if } \varepsilon_p \geq 0.4 \end{cases}$	
$F_3(\varepsilon_p) = 0.0673 + 0.212\varepsilon_p + \frac{0.0232}{\varepsilon_f^5}$	

Table 5.3 Drag closures for the inter-phase momentum transfer coefficient, β.

Subsequently the dimensionless drag force was determined. The dimension of the drag force was removed in such a way that a function, which depends exclusively on Re_p and ε_p, is obtained. Figure 5.17 shows the dimensionless drag force resulting from the three drag relations for the previously determined range of Re_p, and $\varepsilon_p = 0.2$. The figure shows that the Ergun (1952), and Wen and Yu (1966) relations predict differences in drag forces up to a factor of four for larger Re_p. Therefore the conventional drag model, which switches between these relations at $\varepsilon_p = 0.2$ will result in a large discontinuity in the drag force at high Re_p, which has no physical background and may cause numerical instabilities.

The Koch and Hill relation (2001) predicts values in between the Ergun (1952), and Wen and Yu (1966) relations and can therefore be considered as an alternative. Another way to overcome the discontinuity is to use the minimum of the Ergun (1952), and Wen and Yu (1966) relations.

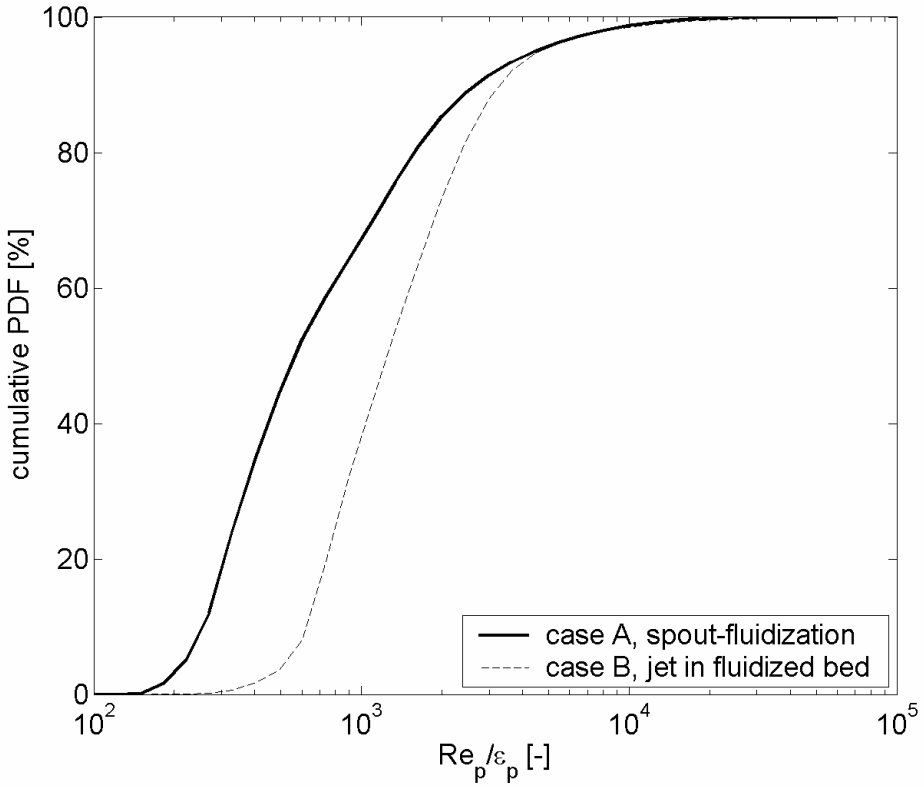

Figure 5.16 Cumulative distribution of particle Reynolds numbers for two different regimes in a spout-fluid bed.

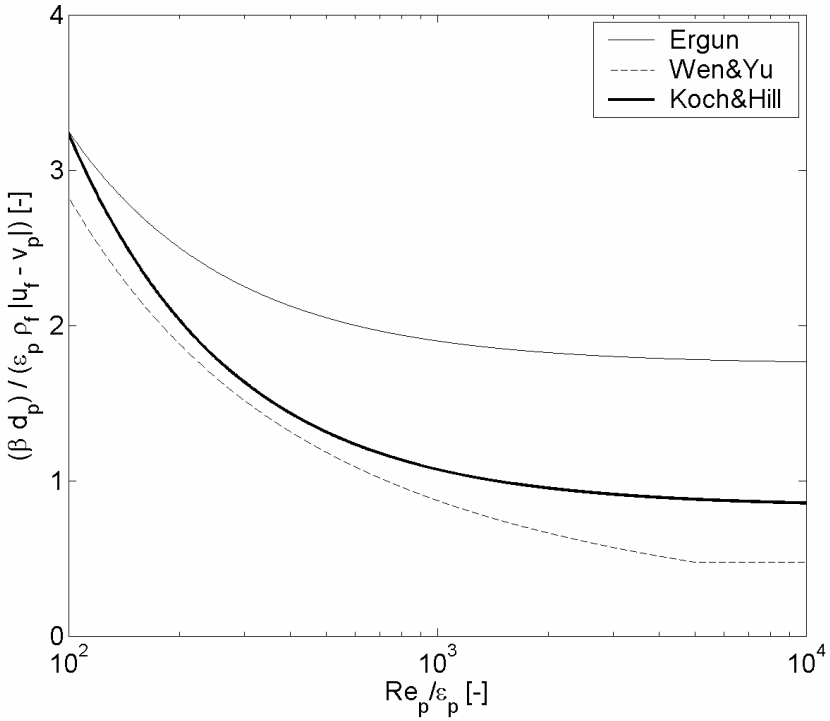

Figure 5.17 Dimensionless drag force calculated using several drag closures with $\varepsilon_p = 0.2$.

Test cases A and B were used to compare the DPM results for the pseudo-2D spout-fluid bed using the following three drag models:

1. The conventional drag model;
   if $\varepsilon_p > 0.2$ the Ergun equation (1952) is used, otherwise the Wen and Yu relation (1966) is used.
2. The Koch & Hill drag model;
   the relation of Koch and Hill (2001) is used.
3. The minimum drag model;
   the minimum of the Ergun equation (1952), and the Wen and Yu relation (1966) is used.

A period of 20 s was simulated from identical initial conditions using a fine (5 mm) computational grid. For the last 16 s of the simulation, the computed pressure drop fluctuations, which were recorded at a frequency of 1000 Hz, were compared with dynamic pressure drop measurements. Furthermore, the computed particle flux was compared with experimental data resulting from combined particle image velocimetry and particle volume fraction measurements. To facilitate a quantitative comparison of the results, the pressure drop fluctuations, which are presented in Figure 5.18, were converted into frequency spectra. The frequency spectra were obtained using the SAPDF technique (see chapter 2) and are displayed in Figure 5.19.
For spout-fluidization (case A in Figure 5.18) a periodically fluctuating pressure drop is obtained for the Koch & Hill model, the minimum model and the experiments, while the conventional model displays a less regular pattern. These results are also reflected in the power spectra for case A presented in Figure 5.19. That is to say that, except for the conventional model, a dominant frequency between 5 and 6 Hz is found. The jet in fluidized bed case (case B in Figure 5.18) shows that the differences between the drag models are less pronounced resulting in similar frequency spectra for case B, which are displayed in Figure 5.19. Each of the drag closures predicts a randomly meandering spout, which leads to an irregular pressure drop signal corresponding to a wide frequency peak.

Besides the pressure drop measurements, digital images were recorded. These images were analyzed using the particle detection and PIV technique described in chapter 2. The results of these techniques were combined to obtain the particle flux:

$$\mathbf{\Phi}_s = \varepsilon_s \rho_s \mathbf{v}_s \tag{5.2}$$

The measured vertical time-averaged particle flux is presented in Figure 5.20 together with the vertical time-averaged particle fluxes predicted by the different drag models.

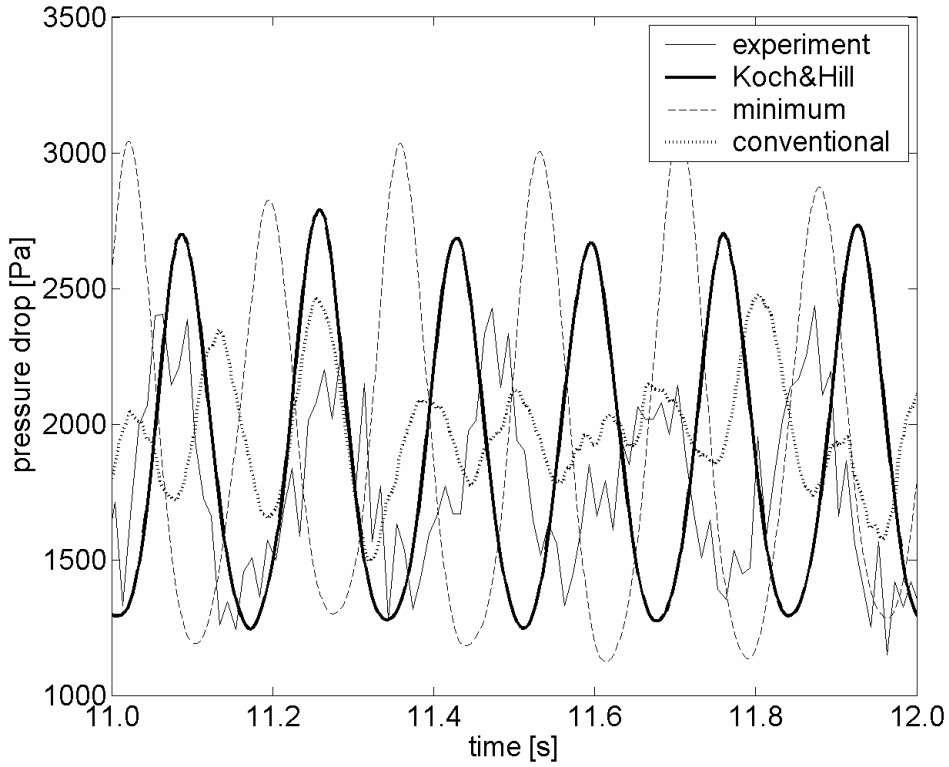

Case A, spout-fluidization

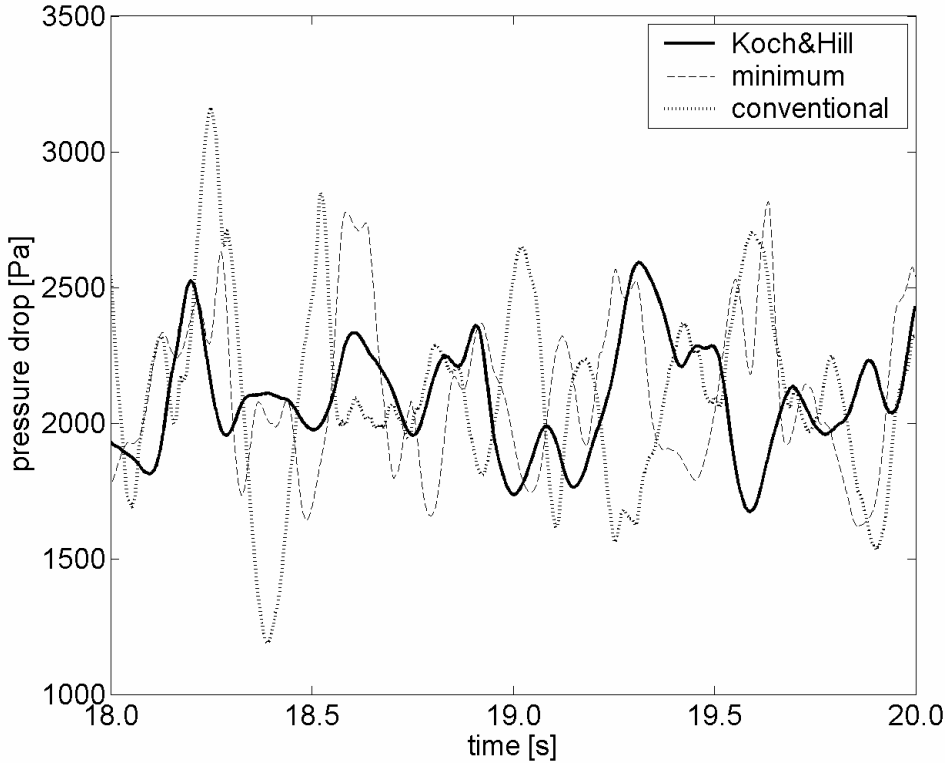

Case B, jet in fluidized bed

Figure 5.18 Measured and computed pressure drop fluctuations over the entire bed for two different regimes using several drag closures.

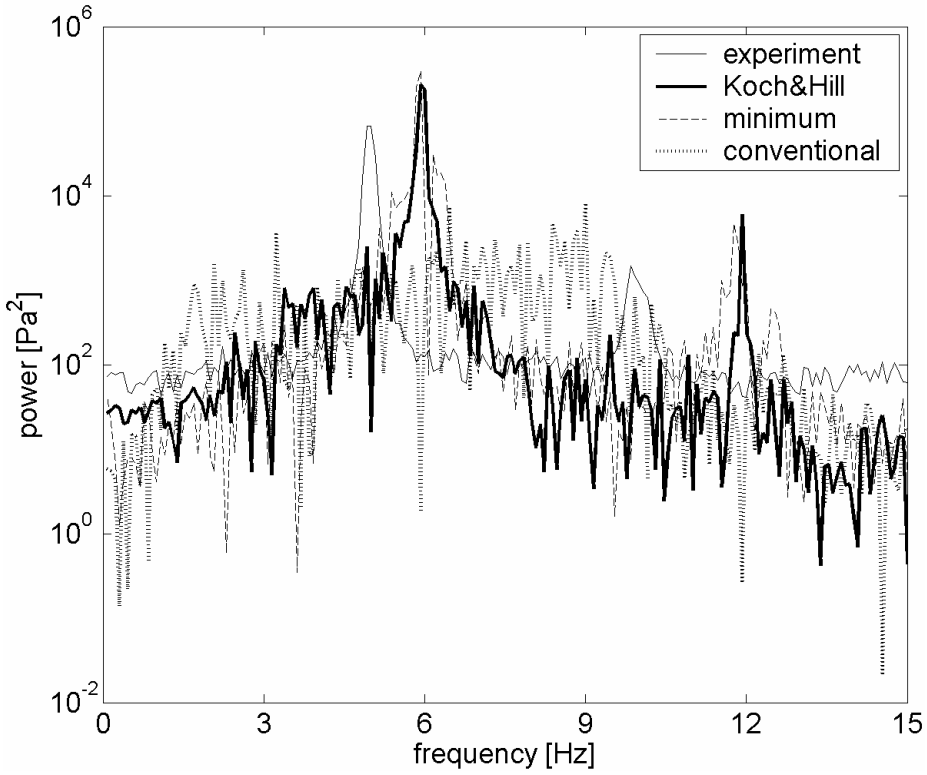

Case A, spout-fluidization

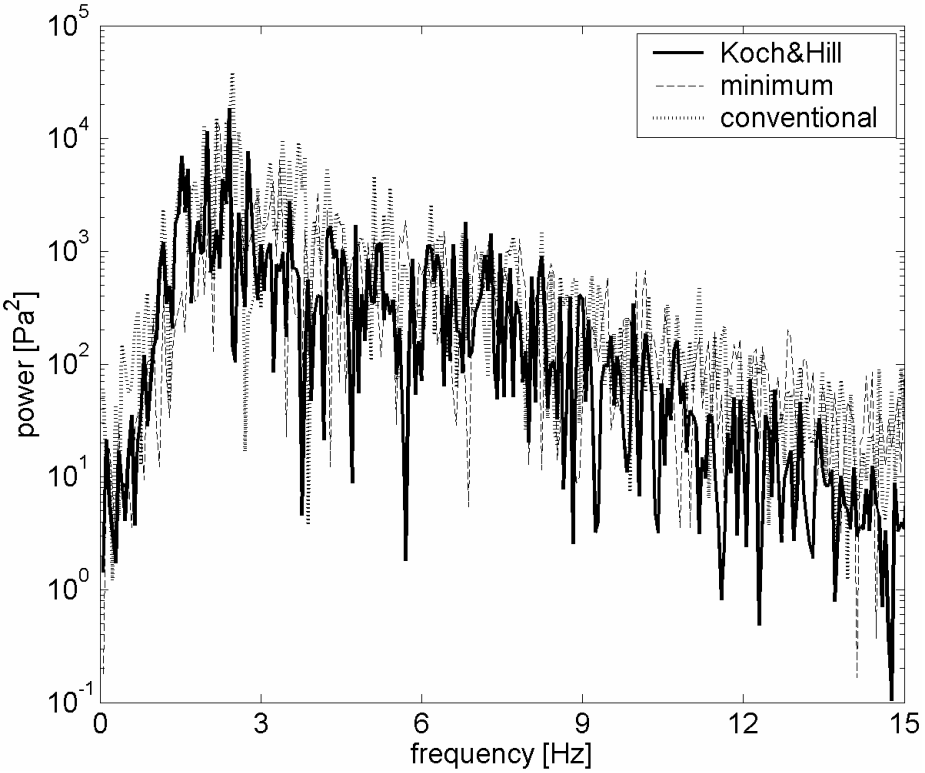

Case B, jet in fluidized bed

Figure 5.19 Frequency spectra of the measured and computed pressure drop fluctuations over the entire bed for two different regimes using several drag closures.

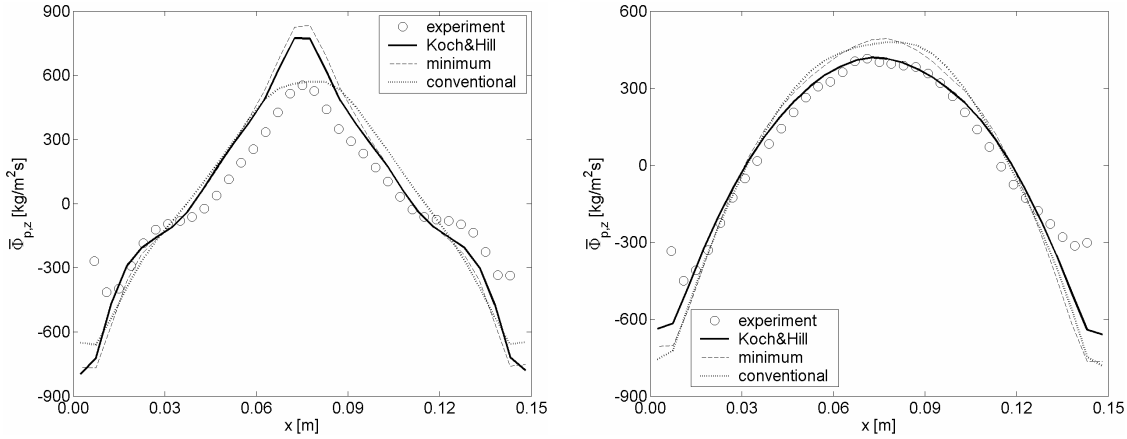

Case A, spout-fluidization Case B, jet in fluidized bed

Figure 5.20 Measured and computed vertical time-averaged particle flux profiles at a height of 0.13 m for two different regimes using several drag closures.

In Figure 5.20, case A displays a relatively narrow peak in the vertical time-averaged particle flux profile, which is captured reasonably well by both the Koch & Hill model and the minimum model. The conventional model however, produces a broader peak. The deviating results obtained from the conventional model can be explained by considering Figure 5.17. The conventional model predicts very large drag forces in the annulus, where $\varepsilon_p > 0.2$, and small drag forces in the spout, where $\varepsilon_p < 0.2$. The system will therefore display behavior, which is similar to a situation with a higher background velocity and a lower spout velocity, and will consequently resemble the results for case B. The particle flux profiles for case B are similar with all drag models and the agreement with the experimental results is very good.

The conventional drag model, which is used most frequently (i.e. the Ergun equation (1952) for low porosities, and the Wen and Yu relation (1966) for high porosities), is less suitable for modeling fluid beds with stable high velocity jets, as encountered in spout(-fluid) beds. The minimum of the relations of Ergun (1952), and Wen and Yu (1966), as well as the relation proposed by Koch and Hill (2001) are more suitable, although the computed frequency of the pressure drop fluctuations is somewhat too high. Because of the similarity between the results of these models and the large differences between the drag forces predicted by these models it is unlikely that the results can be improved by using yet another drag model. Because of its more fundamental basis the use of the Koch and Hill relation (2001) is to be preferred and is therefore used in the remaining simulations reported in this thesis.

5.8 Conclusions

Based on the simulation results presented in this chapter, it can be concluded that the instantaneous model results are affected by the initial conditions. The time-averaged results are however virtually independent of the initial conditions provided that the averaging period is sufficiently large.

The spring stiffness was chosen sufficiently large to prevent it from affecting the simulation results.
Furthermore, for this value of the spring stiffness the results obtained with the hard and soft sphere model are virtually identical.

In order to facilitate a sufficiently fine grid to resolve all details of the flow, a new method for the implementation of the two-way coupling is proposed. This method, which is referred to as the "cube method", produces grid independent results for both the drag force exerted on a single particle and the pressure drop over a packed bed.
The results of the cube method display slight offsets from the analytical solutions for small grid sizes. These offsets are however significantly smaller than the offsets observed with the conventional method.
Based on the simulation results, a value of 5 is proposed for the ratio between the cube and particle diameter. This value is considered to be sufficiently small to capture the details of the flow. Furthermore the value is sufficiently large to reduce the offset to an acceptable level.
The offset can most probably be resolved by applying particular weight kernels to the cube method.
Even in a system where the width of the spout channel is 10 mm, a numerical grid size of 10mm (i.e. 4 times the particle diameter) is sufficiently small to obtain grid independent results.

Several drag closures were tested in the DPM to assess their suitability regarding spout-fluid beds. It was found that the most frequently used drag model (i.e. the Ergun equation (1952) for low porosities, and the Wen and Yu relation (1966) for high porosities) produces unsatisfactory results for fluid beds with stable high velocity jets, as encountered in spout(-fluid) beds. The usage of the minimum of the drag given by the relations of Ergun (1952), and Wen and Yu (1966), as well as the relation proposed by Koch and Hill (2001) improves the predictions of the DPM, although the computed frequency of the pressure drop fluctuations is still somewhat too high. Because of its more fundamental nature the use of the Koch and Hill relation (2001) is to be preferred.

Chapter 6

Experimental and computational study of a 3D spout-fluid bed

Abstract

In this chapter, results are reported of a combined experimental and simulation study on the various regimes, which can be encountered during spout-fluid bed operation.
A regime map for a 3D spout-fluid bed was composed employing spectral analysis of pressure drop fluctuations and fast video recordings. In addition 3D Euler-Lagrange computations were performed to assess the capability of the model to reproduce the experimentally observed flow regimes.
Spectral analysis of pressure drop fluctuations revealed that for most investigated regimes the model is able to predict the appropriate regime. The frequency, at which the largest power is found, is overpredicted by the model in most cases. Contrary to the experimental observations, the model did not predict any large slugs in the slugging bed regime.
The remaining differences between the simulated and experimentally observed bed behavior is most likely related to the representation of the effective fluid-particle interaction in the model, which relies on a homogeneous distribution of the particles on the length scale that is used to calculate the fluid-particle drag.

The computations were also used to study the particle motion in a 3D spout-fluid bed. Both mono-disperse and bi-disperse systems were investigated. The simulation results were compared with velocity maps determined from particle trajectories acquired using positron emission particle tracking.
The model accurately reproduces measured particle velocities, including their root mean square, for all investigated conditions and is therefore able to capture the details of the particle flow in various flow regimes.

Detailed analysis of the results shows that the model has difficulty predicting the exact shape of the spout channel, which is probably related to the heterogeneity in the solids volume fraction, which was already observed in relation with the pressure drop fluctuations.

The bi-disperse system revealed no difference between the time-averaged particle velocities of the small and large particles, despite the fact that the net force on, and consequently the acceleration of, the small particles is relatively larger. The computed root mean square was generally larger for the small particles, which was not as clearly observed in the experiments, which is probably related to the post-processing method of the experimental results.
The DPM results for a mixture of large and small particles revealed some differences between the concentration and flux of large and small particles, although most differences in the particle concentrations disappeared at higher background velocities.

The experimental study of the particle circulation time distribution revealed that it correlates well with the mobility of the particles. Since the jet-in-fluidized-bed regime displays the highest number of particle circulations within a fixed period of time and shows the most narrow particle circulation time distribution, this regime will probably provide the most (homogeneously distributed) growth opportunities in a granulator.

Part of this chapter is in preparation for publication in AIChE Journal and part of it was published as:

J.M. Link, L.A. Cuypers, N.G. Deen, and J.A.M. Kuipers, Flow regimes in a spout–fluid bed: A combined experimental and simulation study, Chemical Engineering Science, 60-13, 3425-3442

Link, J.M., Fan, X., Wood, J., Deen, N.G., Ingram, A., Parker, D.J. and Kuipers, J.A.M., 2005. Comparison of PEPT measurements and discrete particle simulations in a rectangular 3D spout-fluid bed, Proceedings 7th World Congress of Chemical Engineering, 10-14 July 2005, Glasgow, Scotland.

6.1 Introduction

In this chapter the combined results of experiments and simulations are presented that were obtained for a 3D spout-fluid bed. The experiments were performed to obtain insight in the behavior of a spout-fluid bed and to validate the computational model that was discussed in chapter 3 over a wide range of conditions.

This chapter is organized as follows. In section 6.2 the experimental procedure is presented. The different flow regime maps that have been obtained for a 3D spout-fluid bed are presented in section 6.3. For more information on flow regimes and flow regime maps the reader is referred to chapter 4. The flow regime maps have been used to select operating conditions that facilitate the validation of the model for different regimes. These conditions have been marked in the flow regime map. The details of the measurements performed for these cases are also presented in this section.

Section 6.4 discusses the results of the pressure drop fluctuation measurements that have been performed for all cases. In this section the capability of the model to predict the dynamic behavior for various flow regimes and configurations is assessed. To illustrate the origin of the pressure drop fluctuations, the associated behavior of the gas bubbles is visualized for a number of cases by means of iso-surface plots of the solids volume fraction. The theory that is needed for the spectral analysis of the pressure drop fluctuations is explained in section 2.4.

This section also discusses the particle velocity profiles that have been obtained using positron emission particle tracking (PEPT), which was presented in section 2.5. These results were only obtained for a limited number of cases, through which the capability of the model to quantitatively predict the particle motion in various flow regimes has been assessed.

In section 6.5 the numerical results are used to determine solids volume fractions, which could not be obtained from the experimental techniques that were employed. The particle fluxes are examined and the difference in the behavior of particles with different sizes is assessed.

In section 06.6 the particle circulation time distributions obtained for several cases are presented and mutually compared. The particle circulation time, which is defined in section 2.5.1, has been obtained from the PEPT measurement data.

The conclusions of this chapter are given in section 6.7.

6.2 Experimental procedure

In this section the experimental set-up and the measuring equipment that was used are presented.

6.2.1 3D gas-fluidized bed set-up

The 3D set-up consists of a gas-fluidized bed and an air supply system, which are schematically represented in Figure 6.1. The side walls of the bed are made of aluminum, while the front and back walls are made of polycarbonate.

Air was fed to the bed through four separate sections. A 2 mm thick porous plate with an average pore size of 100 μm provided a homogeneous gas distribution over the two fluidization sections. Figure 6.1 shows that the bed contains two spout sections, which were covered by a 0.5 mm metal gauze and located on the border between the two fluidization sections at both the front wall (configuration A) and the geometrical centre of the bottom plate (configuration B).

The flow rate of the gas in each section was controlled by control valves. During an experiment only one of the spout sections was operated as a spout. The gas velocity through the other spout section was set to be equal to the gas velocity in the fluidization sections. The gas flow rate was calibrated prior to the experiments using a turbine meter, which was connected to the bed exit.

The following particle mixtures were used:

- a mono-disperse size distribution consisting of $4.48 \cdot 10^4$ large particles;
- a bi-disperse size distribution consisting of $9.79 \cdot 10^4$ small particles, i.e. 50 w%, and $2.29 \cdot 10^4$ large particles, i.e. 50 w%, with a minimum fluidization velocity (u_{mf}) of 1.46 m/s.

The properties of the particles that were used are given in Table 6.1.

Experiments with both configuration A and B were performed in the laboratory of the Fundamentals of Chemical Reaction Engineering group at the University of Twente, the Netherlands. In these configurations, the air was supplied by a blower, which elevated the ambient air pressure before the control valves by 0.35 bar. The air coming from the blower was cooled to a temperature of approximately 40°C.

The experiments with configuration B were also performed in the laboratory of the Positron Imaging Centre at the University of Birmingham, United Kingdom. In this configuration, the air was supplied by a blower, which elevated the ambient air pressure before the control valves by 0.35 bar. Unfortunately, the air coming from the blower could not be cooled. Depending on the flow rate, the temperatures ranged from 40°C to 50°C.

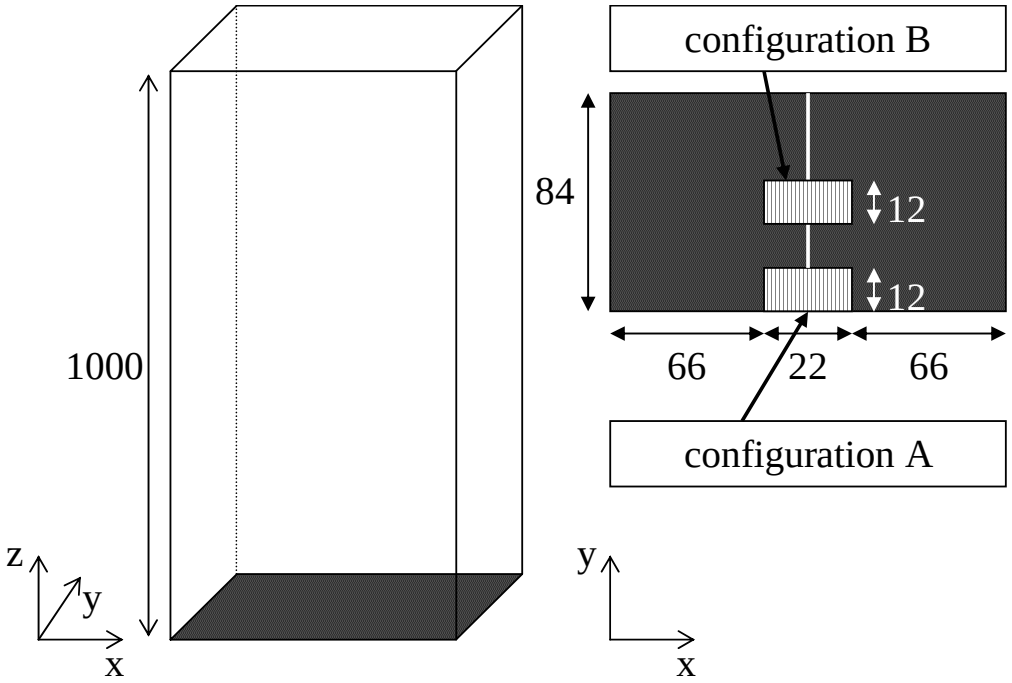

Figure 6.1 Schematic representation of the geometry of the 3D bed, dimensions are given in mm.

Property	**Small particles**	**Large particles**	**Unit**
Material	Glass	Glass	-
d_p	2.49 ± 0.02	4.04 ± 0.02	mm
ρ_p	2526 ± 6	2526 ± 1	kg/m^3
u_{mf}	1.28 ± 0.02	1.77 ± 0.03	m/s
$e_{n,\,p \leftrightarrow p}$	0.97 ± 0.01[a]	0.97[b]	-
$e_{n,\,p \leftrightarrow w,\,glass}$	0.97 ± 0.01[a]	0.97[b]	-
$e_{n,\,p \leftrightarrow w,\,polycarbonate}$	0.97[b]	0.97[b]	-
$e_{n,\,p \leftrightarrow w,\,aluminum}$	0.97[b]	0.97[b]	-
$\mu_{p \leftrightarrow p}$	0.10 ± 0.01[a]	0.10[b]	-
$\mu_{p \leftrightarrow w,\,glass}$	0.09 ± 0.01[a]	0.10[b]	-
$\mu_{p \leftrightarrow w,\,polycarbonate}$	0.10[b]	0.10[b]	-
$\mu_{p \leftrightarrow w,\,aluminum}$	0.10[b]	0.10[b]	-
$\beta_{0,\,p \leftrightarrow p}$	0.33 ± 0.05[a]	0.33[b]	-
$\beta_{0,\,p \leftrightarrow w,\,glass}$	0.33 ± 0.05[a]	0.33[b]	-
$\beta_{0,\,p \leftrightarrow w,\,polycarbonate}$	0.33[b]	0.33[b]	-
$\beta_{0,\,p \leftrightarrow w,\,aluminum}$	0.33[b]	0.33[b]	-

[a] measured through detailed collision measurements, see Kharaz et al. (1999)

[b] not measured, but estimated based on the properties of other wall materials

Table 6.1 Particle properties.

6.2.2 Measuring equipment

During all experiments, the fluctuations in the bed pressure drop (excluding the gas distributor) were recorded using a high frequency pressure probe (Kulite XT-190M-0.35BAR VG) at a frequency of 100 Hz. The pressure probe was positioned in the middle of the back wall of the bed about 0.01 m above the porous plate. The pressure drop fluctuations were recorded over a period of at least one minute.

During the PEPT measurements, the bed was operated in configuration B, and placed between the detectors, covering a height of 0.47 m. Depending on the amount of radiation emitted by the single tracer particle, the space between the detectors and the bed was varied. The tracer particle was produced by exposing one of the particles used in the experiments to a ^{3}He beam generated by a cyclotron to produce the positron emitter ^{18}F from reactions involving ^{16}O in the glass. The position of the tracer particle was recorded over a period of one hour at a frequency ranging from 100 to 300 Hz depending on the amount of radiation emitted by the single tracer particle and the location of the detectors. Furthermore, the total flow rate through the bed was measured at the bed exit through a turbine meter.

6.3 Flow regime map and case selection

The experiments presented in this chapter were performed to study the behavior of a three dimensional spout-fluid bed and assess the capability of the model to predict this behavior. To ensure that the main flow regimes encountered in a spout-fluid bed were considered, a flow regime map has been recorded from which suitable operating conditions were selected. More information about flow regimes and flow regime maps is given in chapter 4.

In order to obtain a comprehensive flow regime map for the three dimensional spout-fluid bed, pressure drop fluctuations were measured over a wide range of operating conditions. The background velocity was varied from 0 to 3.5 m/s with increments of 0.5 m/s and the spout velocity was varied from 40 to 95 m/s with increments of 5 m/s. Due to limitations of the set-up, it was not possible to use spout velocities below 40 m/s. Consequently the only spout velocity that was used below 40 m/s was 0 m/s.

Figure 6.2 shows the flow regime map that was recorded for the mono-disperse size distribution in configuration A, i.e. spout at the wall. The operating conditions that were selected are marked in the flow regime map and presented in Table 6.2, which also includes the details of the experiments and simulations. All simulations were carried out on a computational grid consisting of 21 x 14 x 100 cells (W x D x H). Although all studied cases correspond to different flow regimes, the superficial gas velocity is the same for all cases.

Figure 6.3 shows the flow regime map that was recorded for the mono-disperse size distribution in configuration B, i.e. spout in the center. The operating conditions that were selected are marked in the flow regime map and presented in Table 6.3, along with the details of the experiments and simulations. For the simulations, the hard sphere model was used in all cases.

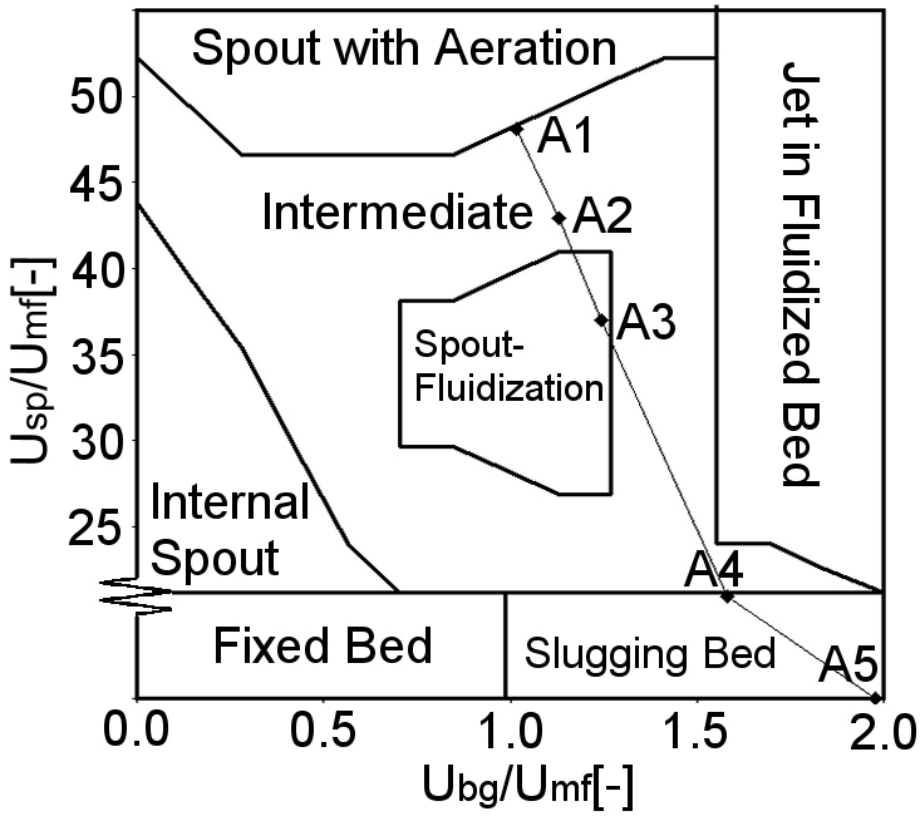

Figure 6.2 Flow regime map of a 3D spout-fluid bed with configuration A containing a mono-disperse size distribution (system C, see chapter 4).

Case	Flow regime	u_{bg}		u_{sp}		u_{sup}		t_{sim}	t_{exp}	Collision model
		[m/s]	[u_{mf}]	[m/s]	[u_{mf}]	[m/s]	[u_{mf}]	[s]	[s]	
A1	Intermediate/ Spouting-with-aeration	1.8	1.0	85	48	3.5	2.0	20	70	Soft sphere
A2	Intermediate	2.0	1.1	76	43	3.5	2.0	20	73	Hard sphere
A3	Spout-fluidization	2.2	1.2	66	37	3.5	2.0	20	76	Hard sphere
A4	Jet-in-fluidized-bed	2.8	1.6	37	21	3.5	2.0	20	70	Hard sphere
A5	Slugging-bed	3.5	2.0	3.5	2.0	3.5	2.0	66	75	Hard sphere

Table 6.2 Test cases for a 3D spout-fluid bed with configuration A, spout at the wall.

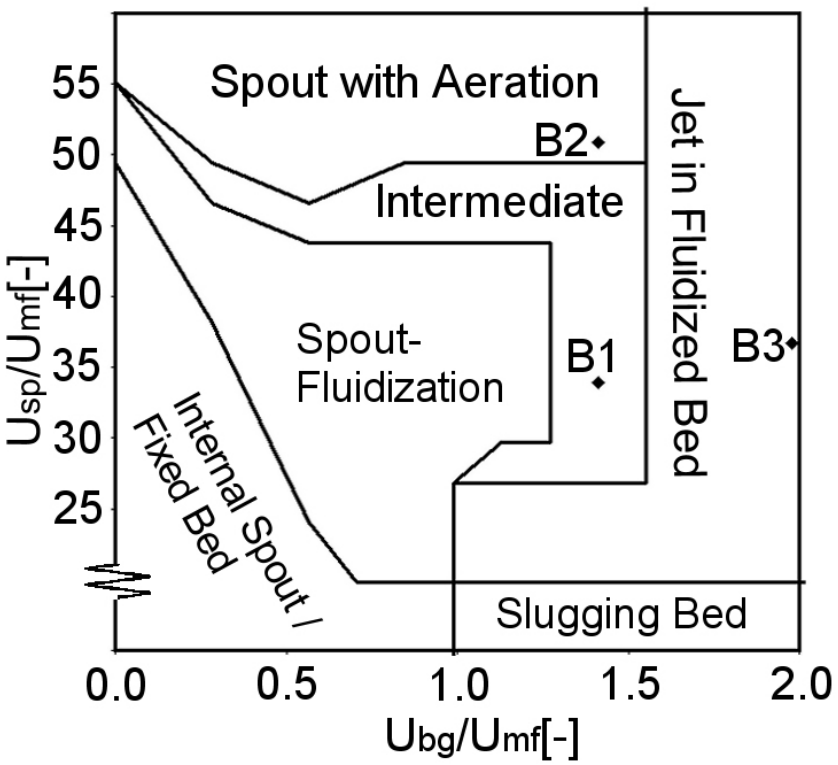

Figure 6.3 Flow regime map of a 3D spout-fluid bed with configuration B, spout in the center, containing a mono-disperse size distribution (system A, see chapter 4).

Case	Flow regime	System	u_{bg}		u_{sp}		u_{sup}		t_{sim}	t_{PEPT}	t_{pdf} [s]	
			[m/s]	[u_{mf}]	[m/s]	[u_{mf}]	[m/s]	[u_{mf}]	[s]	[s]	UK	NL
B1	Intermediate / Spout-fluidization	Mono-disperse	2.5	1.4	60	34	3.7	2.1	20	3600	119	51
B2	Spouting-with-aeration	Mono-disperse	2.5	1.4	90	51	4.3	2.4	20	3600	119	68
B3	Jet-in-fluidized-bed	Mono-disperse	3.5	2.0	65	37	4.8	2.7	20	3600	120	60
B4	Intermediate / Spout-fluidization	Bi-disperse	1.8	1.2	60	41	3.0	2.0	20	3600	3553	68
B5	Intermediate / Spouting-with-aeration	Bi-disperse	2.0	1.4	95	65	3.9	2.7	20	3600	-	68
B6	Jet-in-fluidized-bed (single)	Bi-disperse	2.5	1.7	95	65	4.4	3.0	20	3600	3564	54
B7	Jet-in-fluidized-bed (multi)	Bi-disperse	3.0	2.1	40	27	3.8	2.6	20	3600	3604	68

Table 6.3 Test cases for a 3D spout-fluid bed with configuration B, spout in the centre.

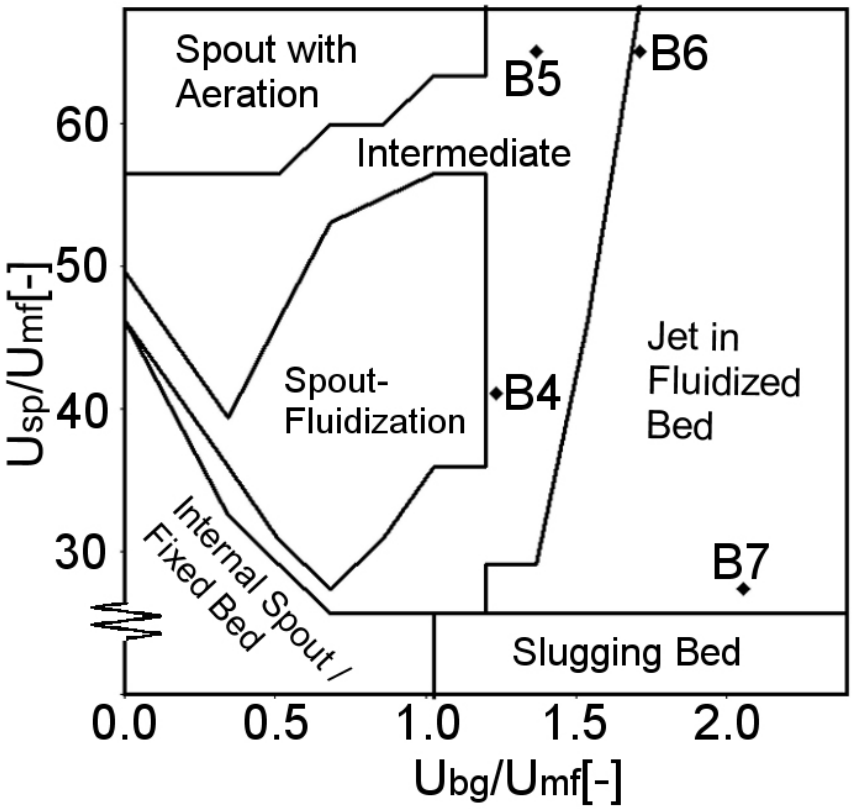

Figure 6.4 Flow regime map of a 3D spout-fluid bed with configuration B, spout in the center, containing a bi-disperse size distribution (system B, see chapter 4).

Figure 6.4 shows the flow regime map that was recorded for the bi-disperse size distribution in configuration B. The operating conditions that were selected are marked in the flow regime map and presented in Table 6.3, along with the details of the experiments and simulations. For the simulations, the hard sphere model was used in all cases.

6.4 Validation

Pressure drop fluctuations reflect the dynamic behavior of the bed, and were therefore measured in all the selected cases, described in the previous section, for both configuration A and B.

The main objective of the pressure drop measurements in configuration A was to examine whether the discrete particle model, described in chapter 3, was able to predict the dynamic behavior observed in the most relevant flow regimes, i.e. flow regimes, which display no defluidization. For this purpose, the frequency spectra of the pressure drop fluctuations predicted by the model were compared with their experimental counterparts. This comparison was also made for the amplitude of the pressure drop fluctuations.

In configuration B the measured pressure drop fluctuations were not only used for model validation, but also to check whether the experiments conducted at the University of Birmingham (UK) were in agreement with the results obtained at the University of Twente (NL). The bubble behavior associated with the pressure drop fluctuations for the cases in configuration B was visualized using iso-surface plots at a solids volume fraction of 0.3. This value was used, since it is inbetween the solids volume fraction for the dense (~ 0.6) and dilute areas (~ 0.0).

The background fluidization velocity exceeded the minimum fluidization velocity for all cases to avoid stagnant areas, which cannot be simulated efficiently with the hard sphere DPM. Stagnant areas were nevertheless formed in case A1 and this case was therefore simulated using the soft sphere approach. All other cases were simulated using the hard sphere approach, which requires less CPU time provided that no stagnant areas are present.
The experimental pressure drop was recorded at a frequency of 100 Hz. The experiments in Twente were conducted for about one minute, while most of the experiments in Birmingham lasted one hour, the exact periods can be found in Table 6.2 and Table 6.3. These tables also show that most computed pressure drop fluctuations were calculated for a period of 20 s. A few cases required a longer time interval to obtain statistically reliable results, because of the low frequency of the pressure drop fluctuations. The first 3 s of the simulations were excluded from the spectral analysis to prevent start-up effects from influencing the results. The computed results for configuration A were obtained at a frequency of 125 Hz, while the results for configuration B were available at a frequency of 1000 Hz.
The amplitude of the pressure drop fluctuations is represented in terms of the root mean square and is given in Table 6.4.

Case	**A1**	**A2**	**A3**	**A4**	**A5**	**B1**	**B2**	**B3**	**B4**	**B5**	**B6**	**B7**
Experiment-NL	48	61	205	619	877	209	166	795	-	103	550	752
Experiment-UK	-	-	-	-	-	241	84	763	181	-	495	750
Simulation	43	73	325	742	617	226	34	463	404	64	261	533

Table 6.4 Root mean square of the measured and computed pressure drop fluctuations [Pa].

6.4.1 Configuration A

The frequency spectra of the measured and computed pressure drop fluctuations for case A1, the intermediate/spouting-with-aeration regime, are shown in Figure 6.5. In both frequency spectra, a broad peak with low power (~100 Pa^2) is found at a relatively high frequency (5-7 Hz), which corresponds with an intermediate regime.

Since the power is very small, the flow regime is much closer to the spouting-with-aeration regime than to the spout-fluidization regime. The trends in the frequency spectra are similar, although the model predicts the largest power at a somewhat higher frequency.
Table 6.4 shows that the amplitude of the pressure drop fluctuations predicted by the DPM is close to the measured value. The power of the pressure drop fluctuations however is slightly overpredicted by our model, which indicates that the pressure drop fluctuations predicted by the model were a little more regular.

The frequency spectra of the measured and computed pressure drop fluctuations for case A2, the intermediate regime between spouting-with-aeration and spout-fluidization, are displayed in Figure 6.6. In both frequency spectra a broad peak with low power (~1,000 Pa^2) is found at a relatively high frequency (5-7 Hz), which is typical for this flow regime. The trends in the frequency spectra are similar, although the model predicts the largest power at a higher frequency.
The power in both frequency spectra is approximately an order of magnitude larger compared to case A1, the intermediate/spouting-with-aeration regime, which indicates that the flow regime is closer to the spout-fluidization regime compared to case A1.
Table 6.4 shows that the amplitude of the pressure drop fluctuations predicted by the DPM is approximately 20% larger than the measured value. The power of the pressure drop fluctuations however is overpredicted to a larger extent.

The frequency spectra of the measured and computed pressure drop fluctuations for case A3, the spout-fluidization regime, are given in Figure 6.7. Both frequency spectra display a narrow peak with large power (~10^5 Pa^2) at a relatively high frequency (5-6 Hz), which is representative for this flow regime. The trends in the frequency spectra are very similar, although the model predicts the largest power at a higher frequency.
Table 6.4 shows that the amplitude of the pressure drop fluctuations predicted by the simulations is approximately 60% larger than the measured value. Since the power of the pressure drop fluctuations is a quadratic function of the amplitude, the difference in the magnitude of the power observed in the experiment and in the simulation can be largely attributed to the difference in the amplitude.

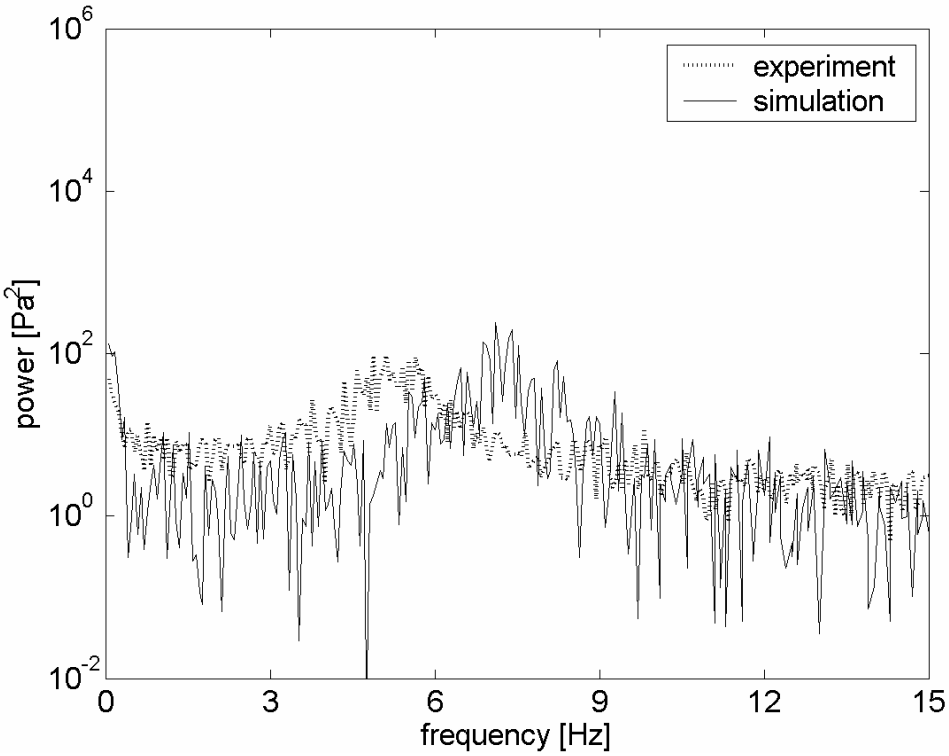

Figure 6.5 Frequency spectra of the measured and computed pressure drop fluctuations of case A1, the intermediate/spouting-with-aeration regime.

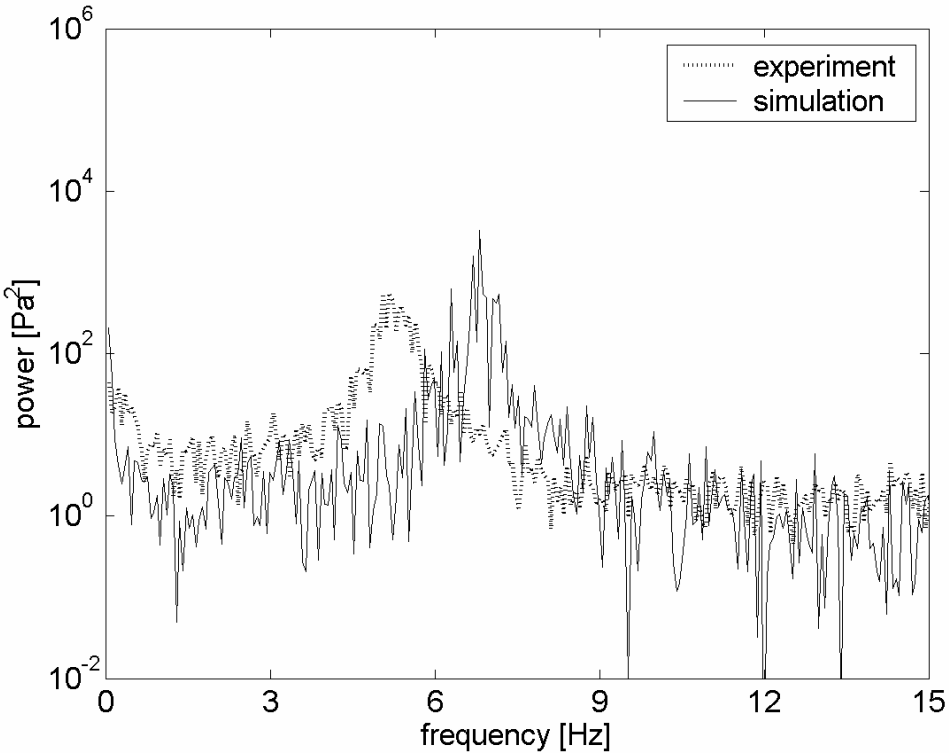

Figure 6.6 Frequency spectra of the measured and computed pressure drop fluctuations of case A2, the intermediate regime between spouting-with-aeration and spout-fluidization.

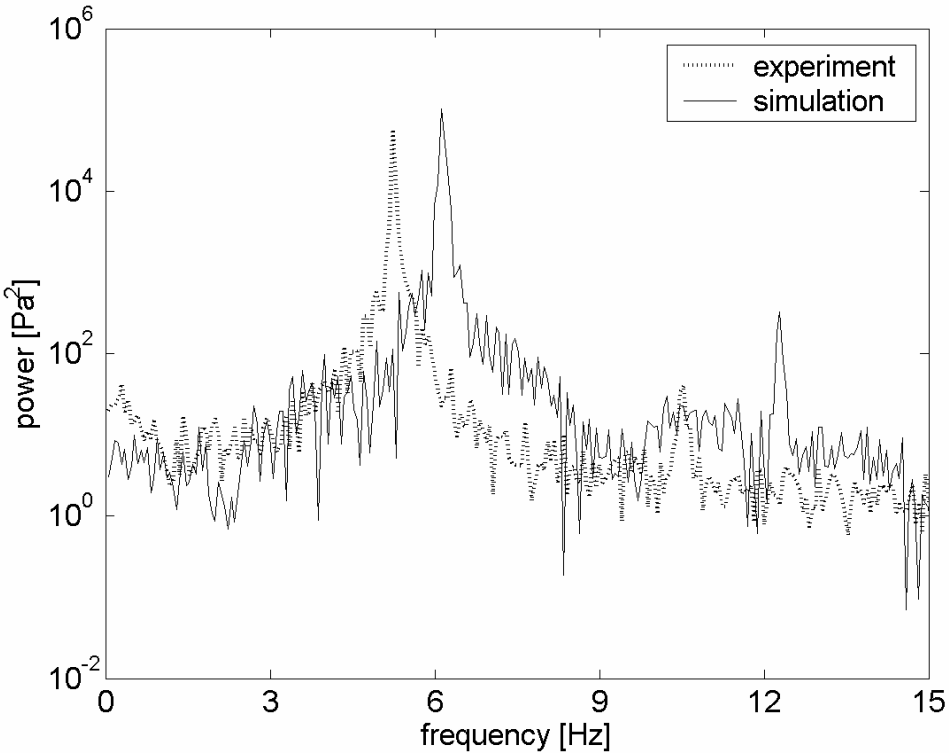

Figure 6.7 Frequency spectra of the measured and computed pressure drop fluctuations of case A3, the spout-fluidization regime.

Figure 6.8 shows the frequency spectra of the measured and computed pressure drop fluctuations for case A4, the jet-in-fluidized-bed regime. The frequency spectra show that the simulation and the experiment display different behavior. The frequency spectrum of the measured pressure drop fluctuations displays a broad peak with large power (~$5 \cdot 10^4$ Pa^2) at low frequency (1-4 Hz), which is indicative for the multiple frequency mode of this flow regime, while the simulation results exhibit a relatively narrow peak with very large power (~$5 \cdot 10^5$ Pa^2) at an intermediate frequency (~3.5 Hz), which is typical for the single frequency mode of this flow regime.

Although the flow regime predicted by the model is the same as the experimentally observed flow regime, the mode is clearly different. Since the mode is rather sensitive to a relatively small change in the operating conditions, it is difficult to predict it exactly.

Table 6.4 shows that the amplitude of the pressure drop fluctuations obtained from the simulations is approximately 20% larger than the measured value. The power of the pressure drop fluctuations predicted by the model however is about an order of magnitude larger than the experimental result. This implies that the pressure drop fluctuations predicted by the model were much more regular.

The frequency spectra of the measured and computed pressure drop fluctuations for case A5, the bubbling-/slugging-bed regime, are shown in Figure 6.9. The frequency spectra show that the simulation and the experiment display different behavior. The frequency spectrum of the measured pressure drop fluctuations displays a relatively narrow peak with large power (~$3 \cdot 10^5$ Pa^2) at a low frequency (~1.5 Hz), which is typical for this flow regime, while the numerical results exhibit a broad peak with large power (~$6 \cdot 10^4$ Pa^2) at a low frequency (1-3 Hz), which is representative for the multiple frequency mode of the jet-in-fluidized-bed regime, and therefore resembles the experimental result for case A4, which is in the jet-in-fluidized-bed regime.
Table 6.4 shows that the amplitude of the pressure drop fluctuations predicted by the simulations is approximately 30% lower than the measured value. The power of the measured pressure drop fluctuations was approximately five times as large as the power predicted by the model, i.e. the pressure drop fluctuations in the experiment were more regular.

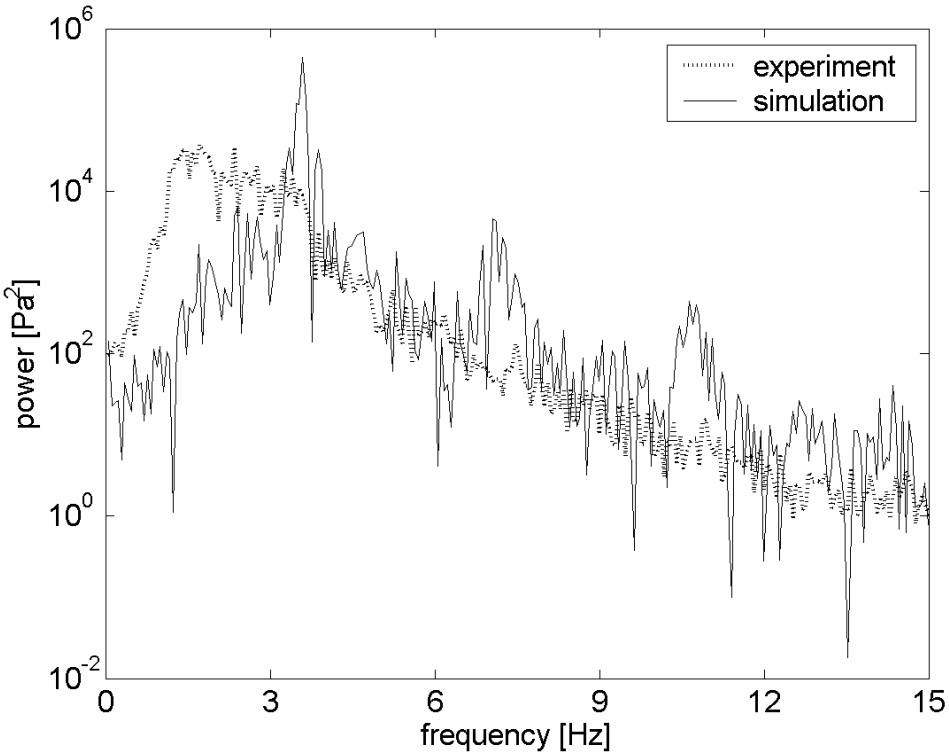

Figure 6.8 Frequency spectra of the measured and computed pressure drop fluctuations of case A4, the jet-in-fluidized-bed regime.

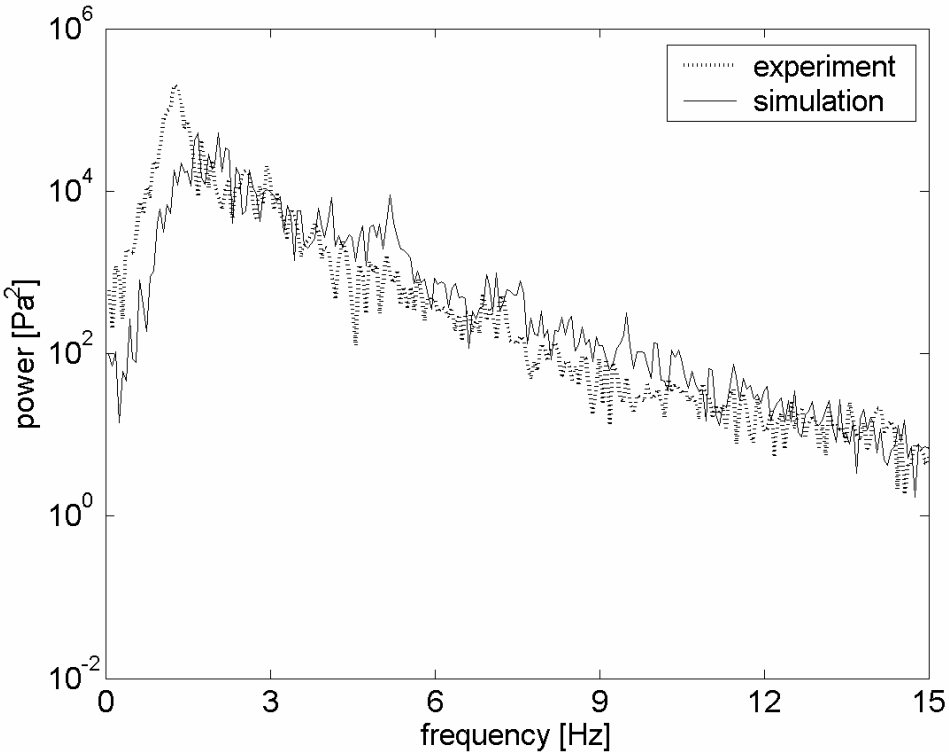

Figure 6.9 Frequency spectra of the measured and computed pressure drop fluctuations of case A5, the bubbling-/slugging-bed regime.

6.4.2 Configuration B

In this section the combined computed and experimental results for configuration B are presented. These results consist of frequency spectra of pressure drop fluctuations and particle velocity fields.

The results of the PEPT measurements consisted of a particle trajectory from which a particle velocity history was derived. Consequently for each time step the particle velocity was only known at a single location. To obtain a time-averaged velocity field the results from a measurement over a longer period of time were combined. Since information about the particle velocity in a certain area, or cell, can only be obtained when a particle is present, the time-average was obtained by averaging all particle velocities that were obtained within each cell:

$$\left\langle \mathbf{v}_{i,j,k} \right\rangle = \frac{\sum_{i=1}^{N_t} \mathbf{v}_p \delta}{\sum_{i=1}^{N_t} \delta} \qquad \text{, where } \begin{cases} \delta = 1 & \forall p \in i,j,k \\ \delta = 0 & \forall p \notin i,j,k \end{cases} \tag{6.1}$$

where p represents a particle in cell i, j, k and N_t is the number of time steps.

The measured and computed time-averaged particle velocities are presented through several types of charts. The overall flow field is represented by the particle velocity field in the central xz-plane, i.e. $0.036 < y \leq 0.048$ m, which is illustrated in Figure 6.10. Two particle velocity profiles in the central xz-plane are shown; one to illustrate the particle velocities in the annulus and the spout channel, at $z = 0.15$ m, and one to illustrate the particle velocities in the fountain, at $z = 0.25$ m. At these same levels a profile of the root mean square (RMS) of the particle velocity in both the horizontal and vertical direction is displayed. Finally, a surface plot of the velocity field in the xy-plane at $z = 0.15$ m is presented. Since the experimental surface plots are difficult to combine, they are only displayed for the large particles, while the model results are based on both types of particles. This will hardly affect the results, since the velocities of the large and small particles are very similar at this height.

Spouting-with-aeration regime

Cases B2 (mono-disperse) and B5 (bi-disperse) are in the spouting-with-aeration regime, which means that the shape of the spout channel is virtually constant (see Figure 6.11).

Consequently, the frequency spectra of the measured and computed pressure drop fluctuations, which are given in Figures 6.12 and 6.13, do not contain any significant peaks. The computed spectrum does however display a broad peak with very low power (~100 Pa^2) at a relatively high frequency (6 Hz, respectively 7 Hz), which corresponds to the intermediate regime. Since the power is very small, the flow regime is much closer to the spouting-with-aeration regime than to the spout-fluidization regime. Apart from that, the trends in the frequency spectra are similar.
Table 6.4 shows that the amplitude of the pressure drop fluctuations predicted by the DPM is smaller than the measured value for both cases (for case B2 the difference was considerable), although it is noted that both are very small. The magnitude of the maximum power of the pressure drop fluctuations however is comparable, which indicates that the pressure drop fluctuations predicted by the model were a little more regular.

The experimental results for case B2 are comparable, while the experimental results for case B5 could not be compared, since the measurements performed in Birmingham could not be conducted due to equipment failure.

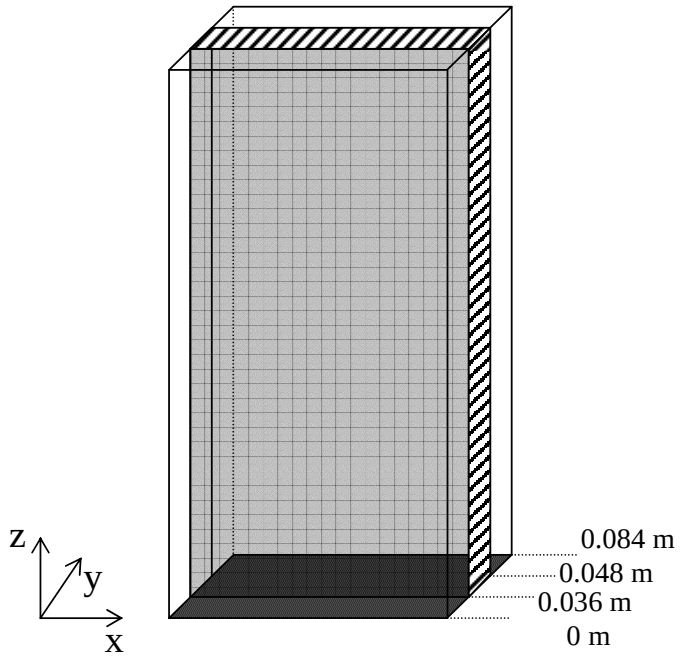

Figure 6.10 Schematic representation of central xz-plane in the geometry of the 3D bed.

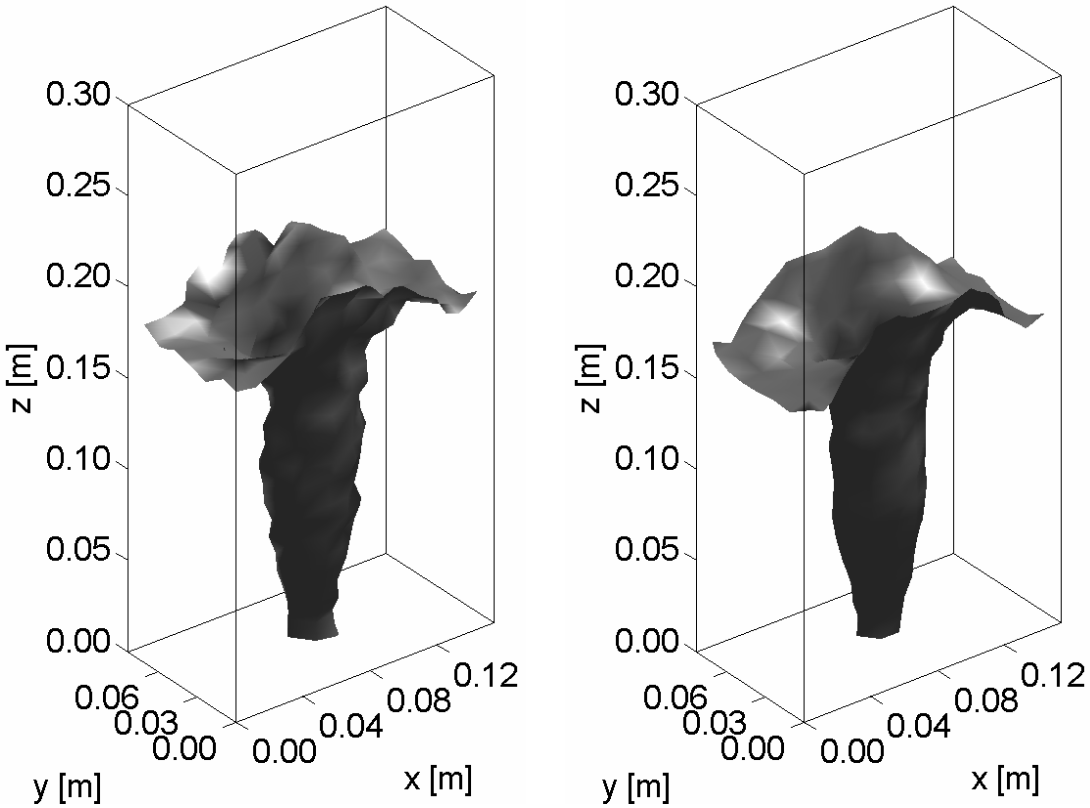

case B2 case B5

Figure 6.11 Plot of the iso-surface at a solids volume fraction of 0.3 for case B2, the spouting-with-aeration regime (mono-disperse), and case B5, the intermediate / spouting-with-aeration regime (bi-disperse).

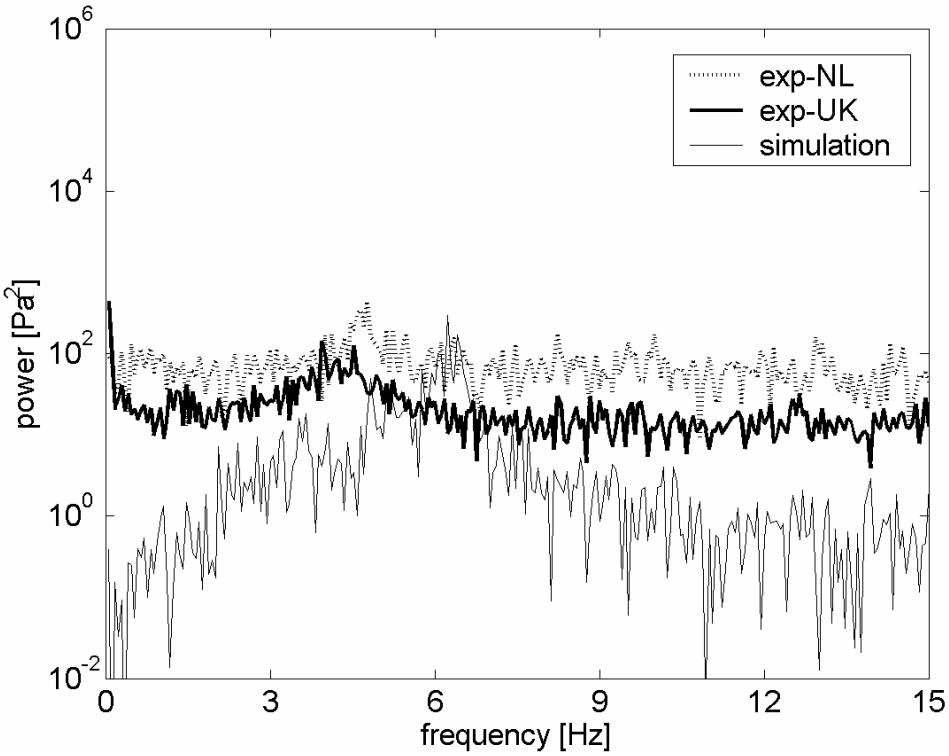

Figure 6.12 Frequency spectra of the measured and computed pressure drop fluctuations of case B2, the spouting-with-aeration regime (mono-disperse).

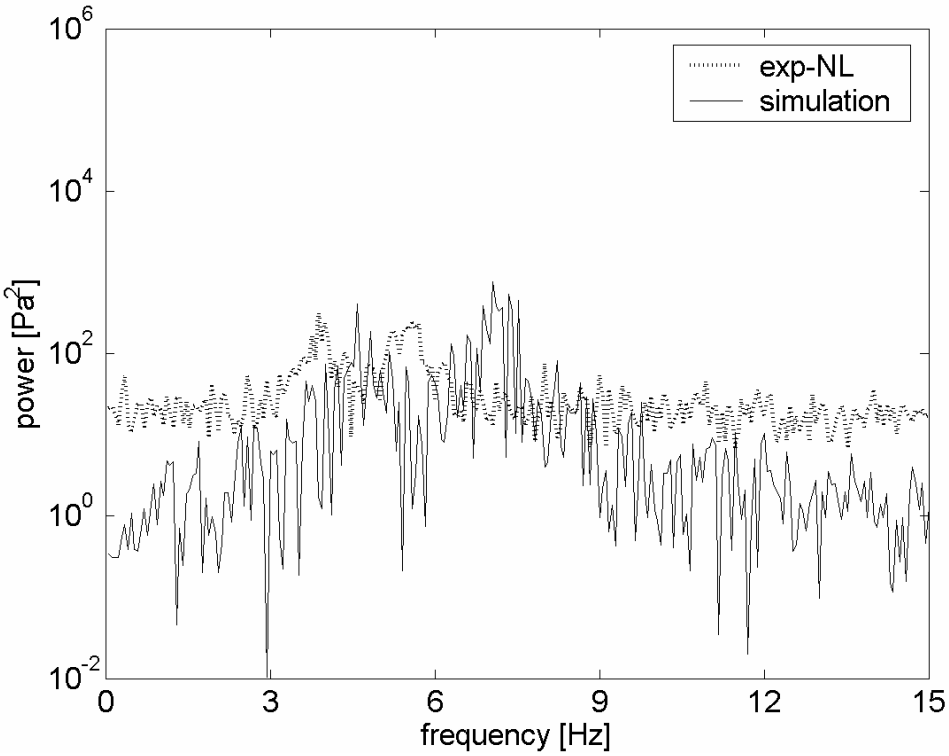

Figure 6.13 Frequency spectra of the measured and computed pressure drop fluctuations of case B5, the intermediate / spouting-with-aeration regime (bi-disperse).

Figures 6.14, 6.15, 6.16 and 6.17 show that the spouting-with-aeration regime displays a narrow spout channel with high time-averaged particle velocities due to the high gas velocity.

The profiles at a height of 0.15 m show that the RMS and the time-average of the particle velocities in the annulus are very small, which corresponds to the slow, but continuous movement of the particles through the annulus towards the spout channel, which occurs in the spouting-with-aeration regime. The RMS in the spout channel is much larger. Its value in the z-direction is approximately constant over the entire width of the channel, especially for the mono-disperse particles. The RMS in the fountain is comparable with the RMS in the spout channel and approximately constant over the entire width of the bed.

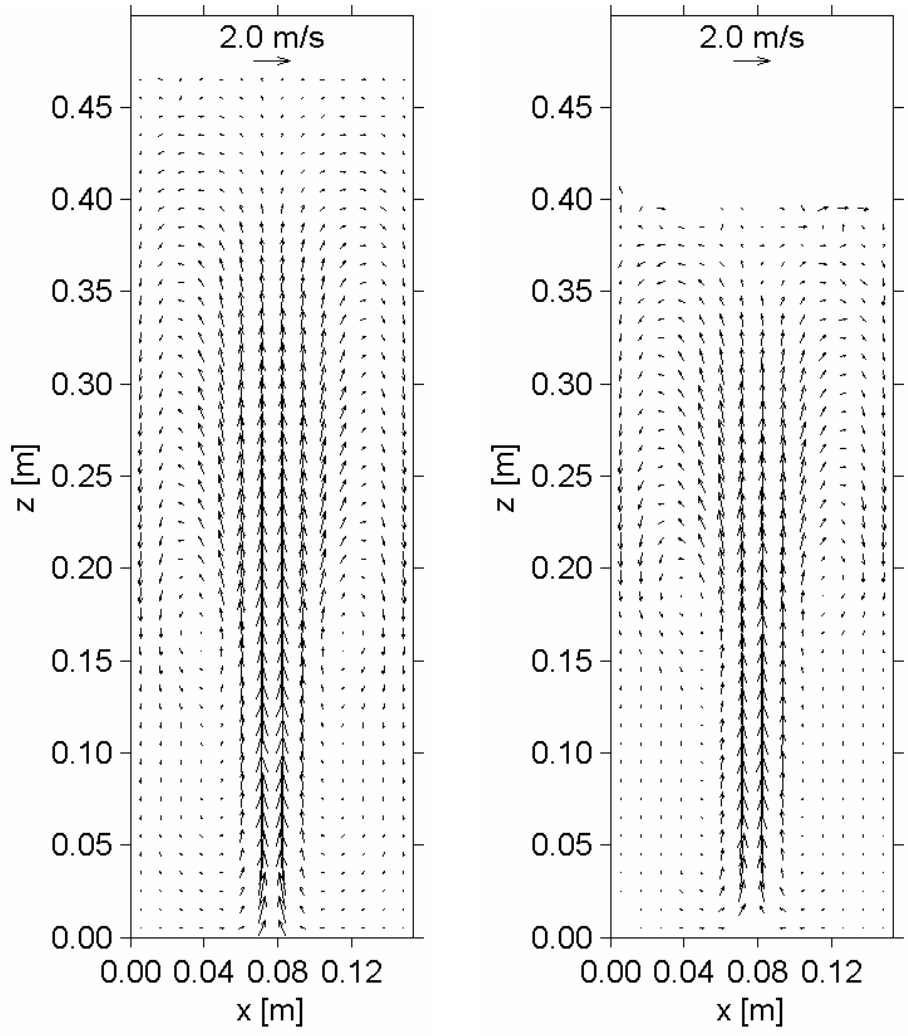

Computed field Measured field

Figure 6.14 Time-averaged particle velocity fields in the central xz-plane for case B2, the spouting-with-aeration regime (mono-disperse).

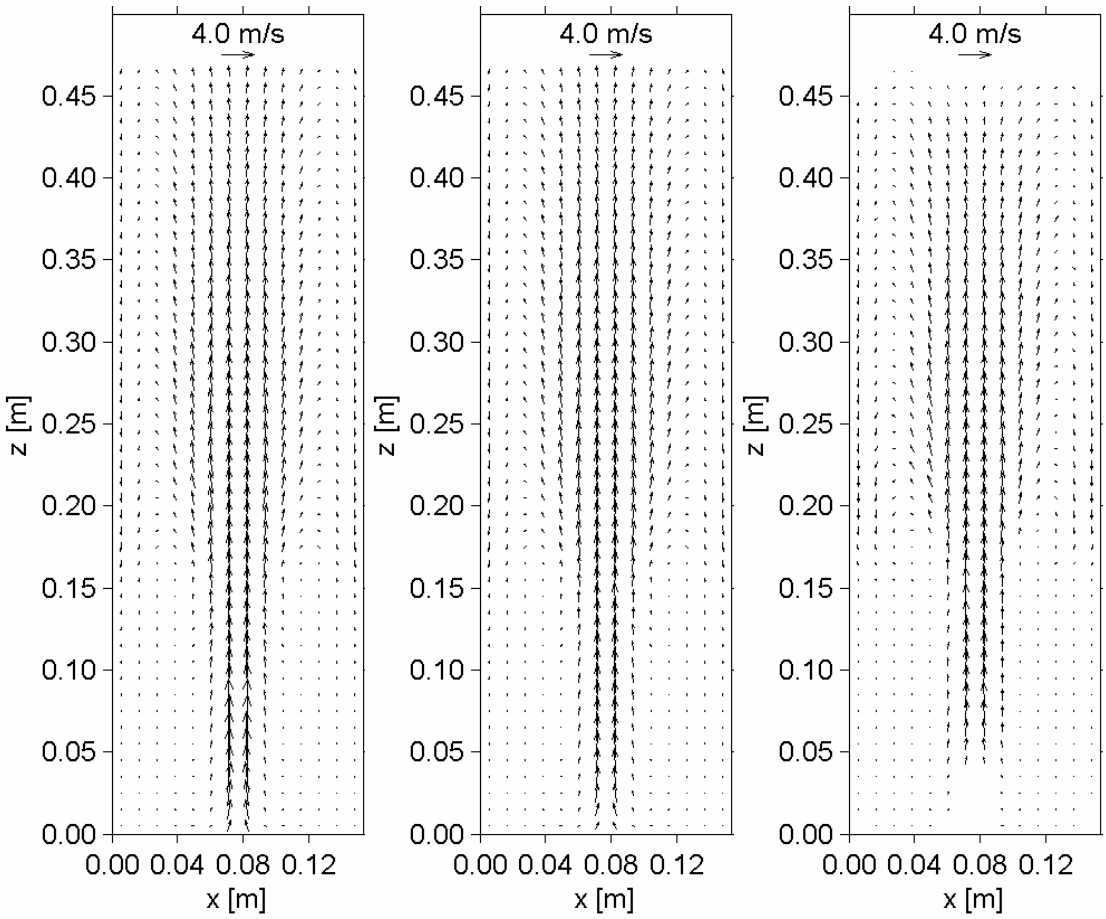

Computed field small particles | Computed field large particles | Measured field large particles

Figure 6.15 Time-averaged particle velocity fields in the central xz-plane for case B5, the intermediate / spouting-with-aeration regime (bi-disperse).

The computed time-averaged particle velocities in the spout channel are virtually the same for both particle sizes. The computed RMS of the velocity of the small particles however is almost twice as large as that of the large particles for case B5, the intermediate / spouting-with-aeration regime (bi-disperse). Since the velocity of the small particles has not been measured, this observation cannot be supported with the experiments.

The surface plots at z = 0.15 m show that the region with upward flow is much larger in the simulation, although the shape of the profile is quite similar. The downward velocity is much more homogeneous in the experimental result.

A comparison between the velocity fields and the iso-surface plots shows that the positive vertical velocities generally occur in the dilute regions of the bed.

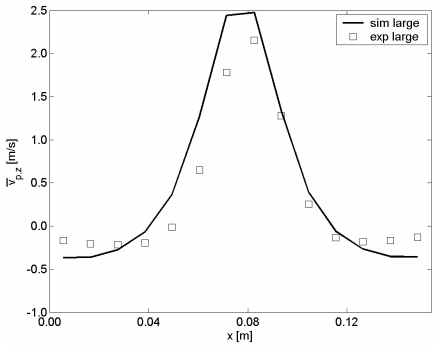

$\overline{v_{p,z}}$ -profile at z = 0.15 m

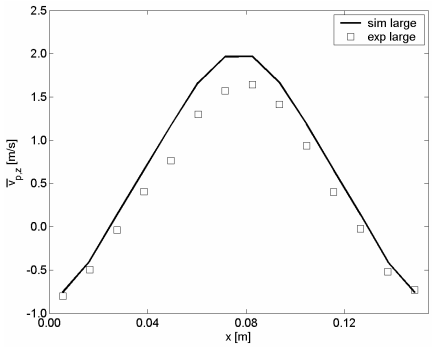

$\overline{v_{p,z}}$ -profile at z = 0.25 m

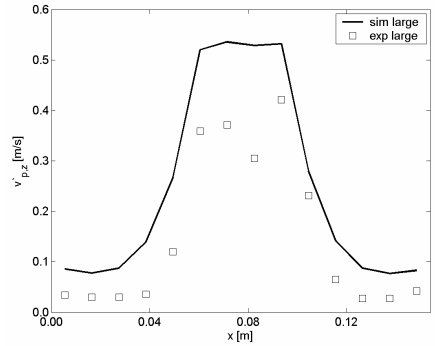

$v'_{p,z}$ -profile at z = 0.15 m

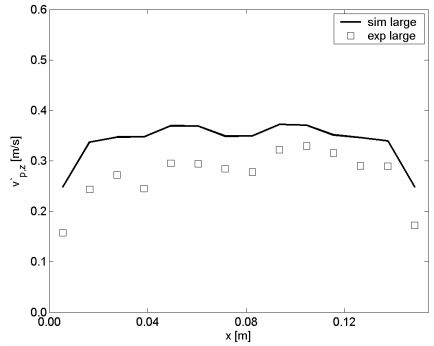

$v'_{p,z}$ -profile at z = 0.25 m

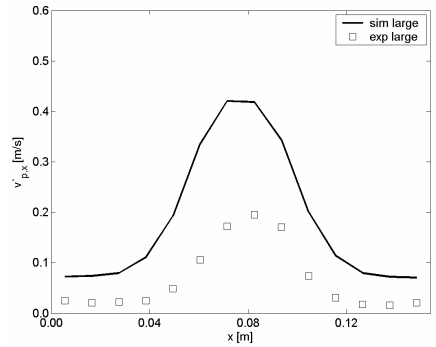

$v'_{p,x}$ -profile at z = 0.15 m

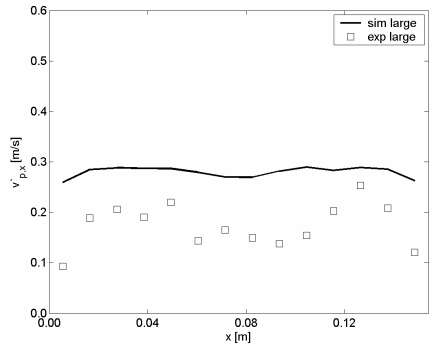

$v'_{p,x}$ -profile at z = 0.25 m

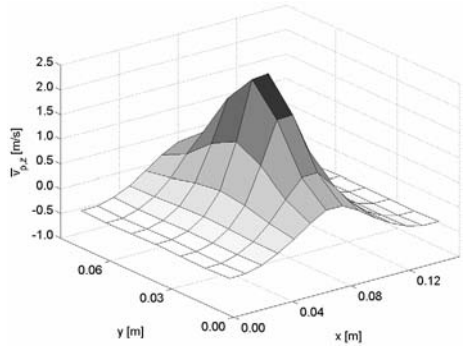

Computed $\overline{v_{p,z}}$ -surface plot at z = 0.15 m

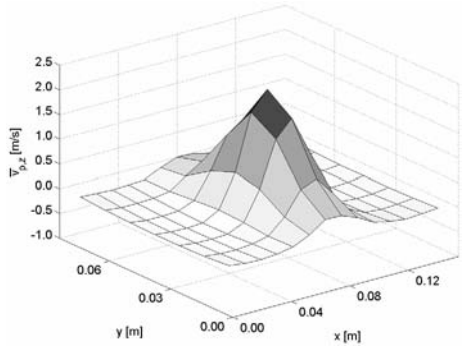

Measured $\overline{v_{p,z}}$ -surface plot at z = 0.15 m

Figure 6.16 Profiles of the time-averaged vertical particle velocity including the RMS in the central xz-plane and a surface plot at z = 0.15 m for case B2, the spouting-with-aeration regime (mono-disperse).

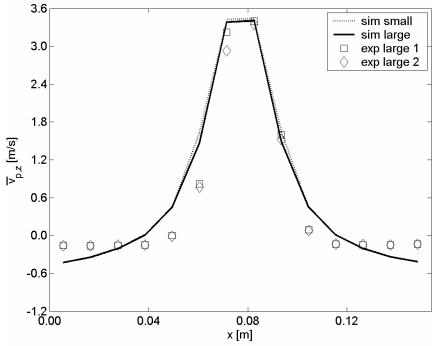

$\overline{v_{p,z}}$ -profile at z = 0.15 m

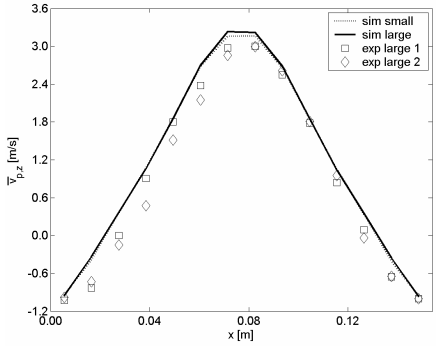

$\overline{v_{p,z}}$ -profile at z = 0.25 m

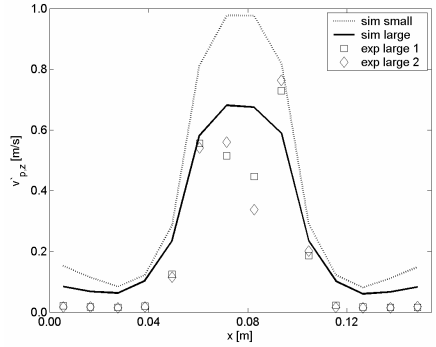

$v'_{p,z}$ -profile at z = 0.15 m

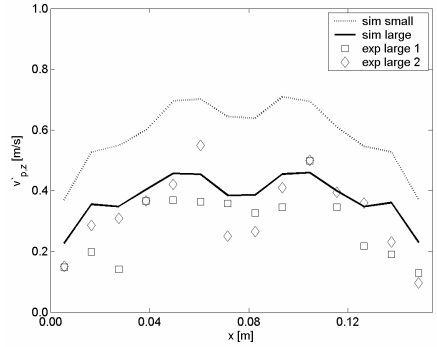

$v'_{p,z}$ -profile at z = 0.25 m

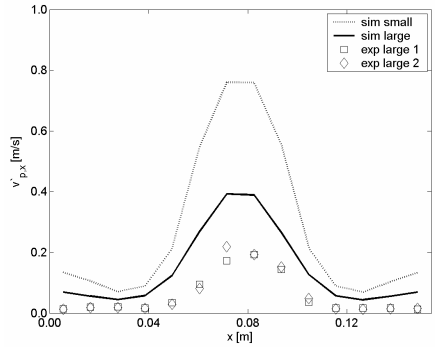

$v'_{p,x}$ -profile at z = 0.15 m

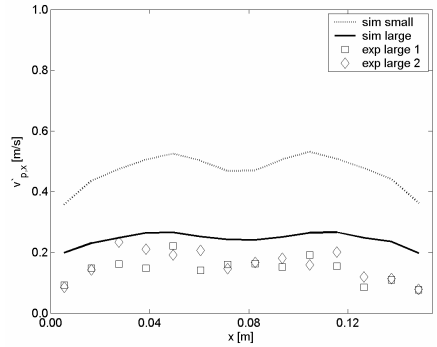

$v'_{p,x}$ -profile at z = 0.25 m

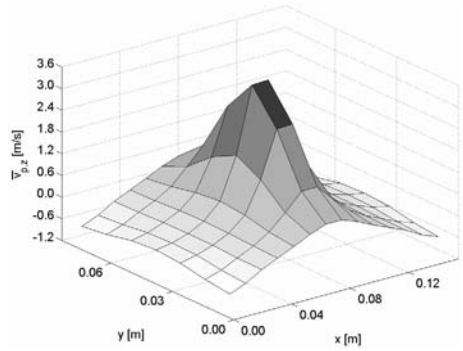

Computed $\overline{v_{p,z}}$ -surface plot at z = 0.15 m

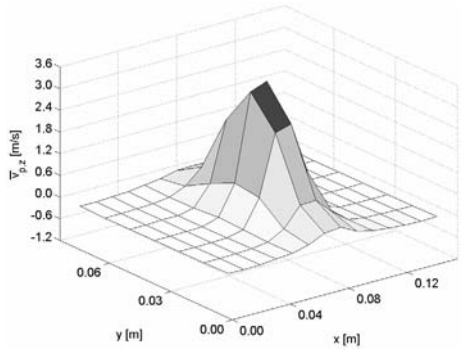

Measured $\overline{v_{p,z}}$ -surface plot at z = 0.15 m

Figure 6.17 Profiles of the time-averaged vertical particle velocity including the RMS in the central xz-plane and a surface plot at z = 0.15 m for case B5, the intermediate / spouting-with-aeration regime (bi-disperse).

Spout-fluidization regime

The series of solids volume fraction iso-surface plots for the cases operating in the intermediate / spout-fluidization regime, case B1 (mono-disperse) and B4 (bi-disperse), are shown in Figures 6.18 and 6.19. The plots for both cases illustrate how the spout channel grows in the vertical direction until it reaches the bed surface. Subsequently, a fountain is formed and the spout channel is closed halfway. The bottom half of the spout channel will then form the next bubble. The only difference between the plots is that case B1 takes approximately 0.2 s to complete one cycle, which corresponds to the frequency of ~5 Hz, while case B4 requires approximately 0.16 s, resulting in a somewhat higher frequency of ~6 Hz.

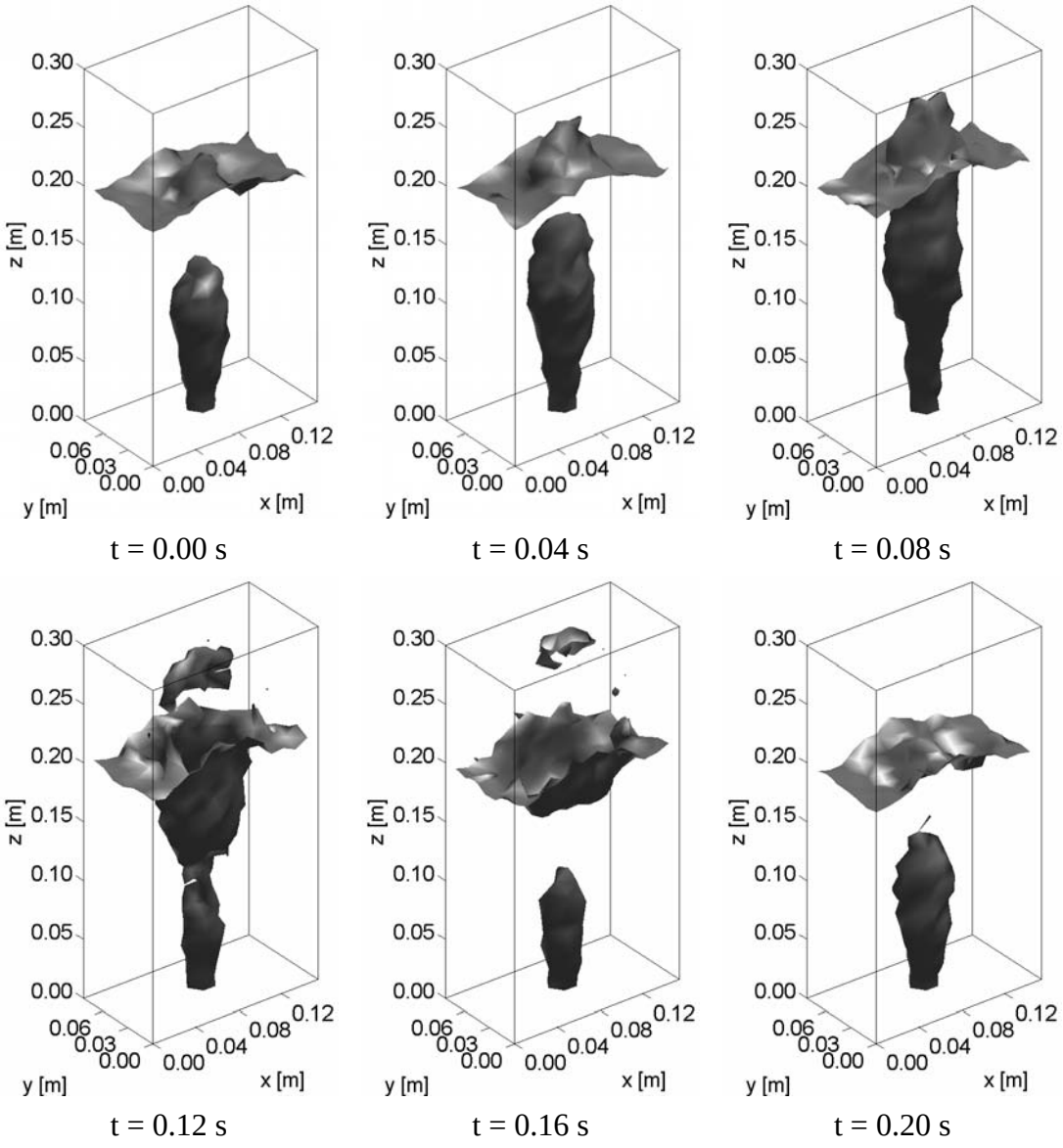

Figure 6.18 Plots of the iso-surface at a solids volume fraction of 0.3 for case B1, the intermediate / spout-fluidization regime (mono-disperse).

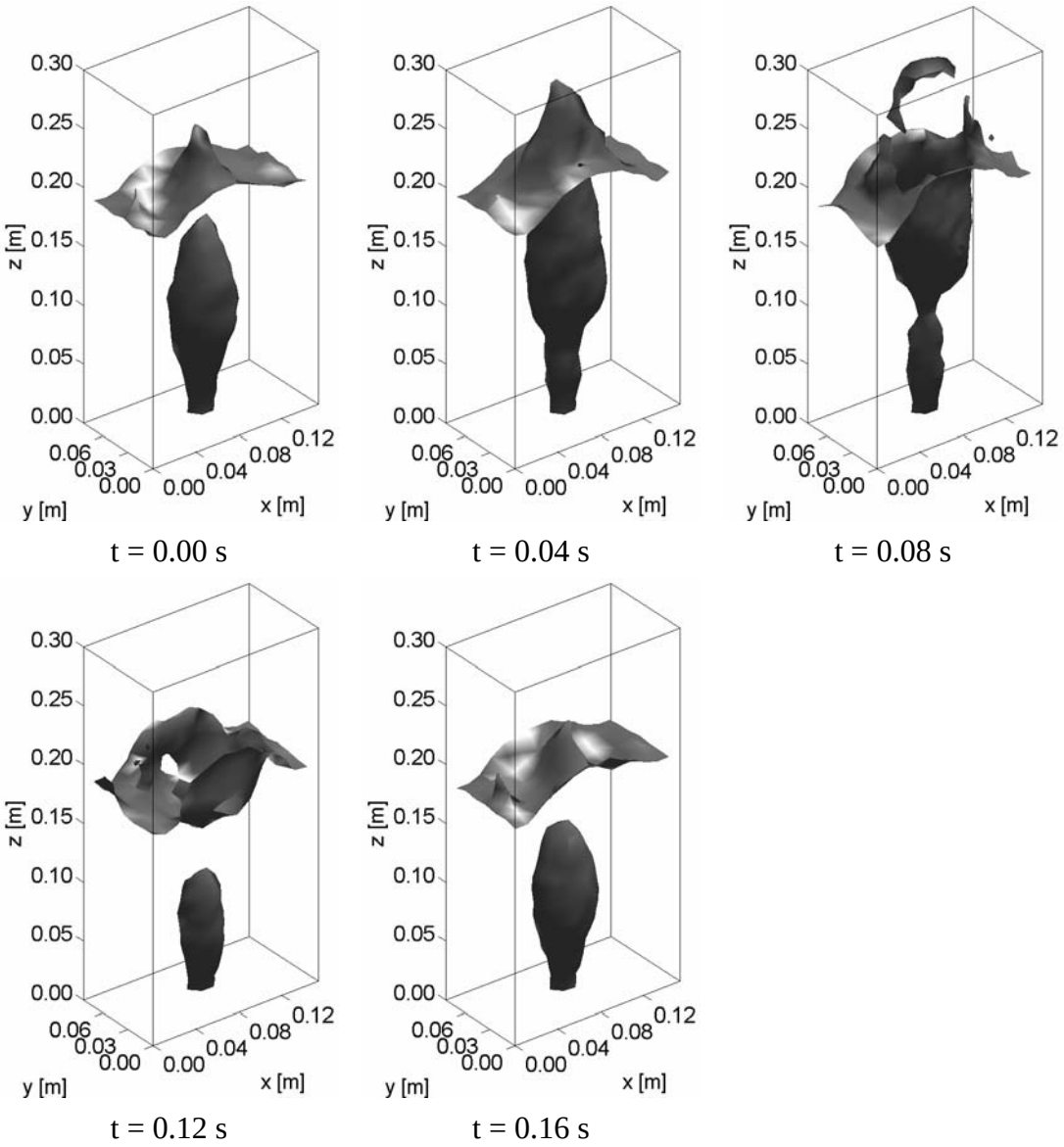

Figure 6.19 Plots of the iso-surface at a solids volume fraction of 0.3 for case B4, the intermediate / spout-fluidization regime (bi-disperse).

These same frequencies can also be observed in the frequency spectra of the computed pressure drop fluctuations given in Figures 6.20 and 6.21. In both cases, both the frequency spectra of the measured and computed pressure drop fluctuations display a narrow peak with large power (~$1 \cdot 10^5$ Pa^2) at a relatively high frequency (4 - 6 Hz), which is representative for the spout-fluidization regime. The trends in the frequency spectra are very similar, although the model predicts the largest power at a higher frequency.

Table 6.4 shows that, for case B1, the amplitude of the pressure drop fluctuations predicted by the simulations is in good agreement with the measured value, as is the magnitude of the power.

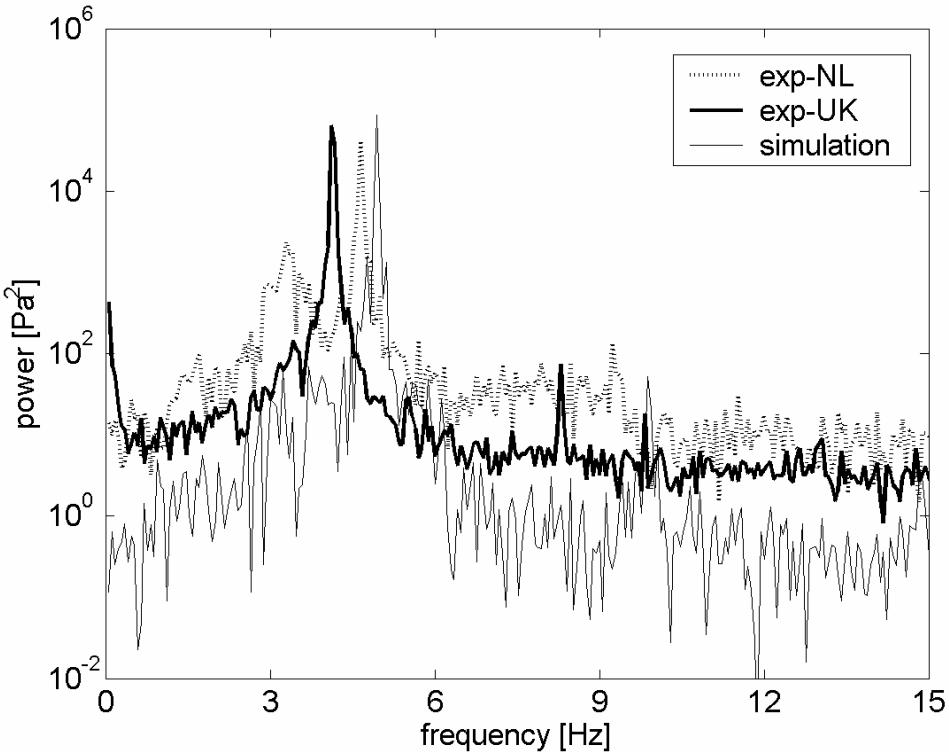

Figure 6.20 Frequency spectra of the measured and computed pressure drop fluctuations of case B1, the intermediate / spout-fluidization regime (mono-disperse).

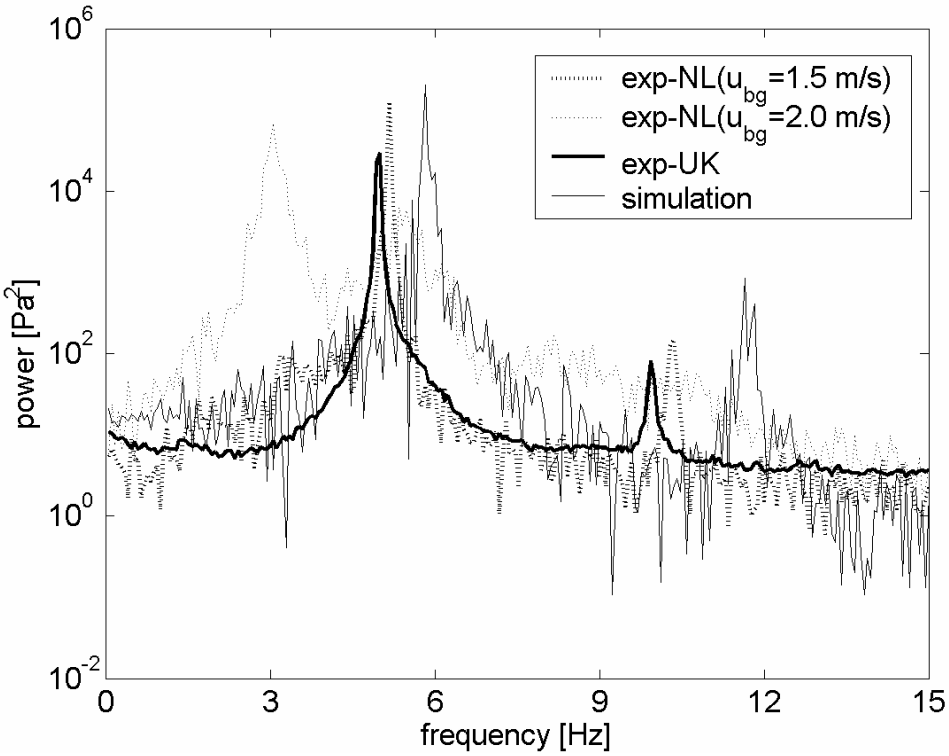

Figure 6.21 Frequency spectra of the measured and computed pressure drop fluctuations of case B4, the intermediate / spout-fluidization regime (bi-disperse).

For case B4, the amplitude of the pressure drop fluctuations obtained from the simulations is significantly larger than the measured value, as is the magnitude of the power. Since the magnitude of the power is severely reduced when the flow regime moves away from the spout-fluidization regime into the intermediate regime, the difference in power can be explained by a small difference in the flow regime.

Comparison of the experimental results for case B1 reveals some differences between the results obtained at the University of Twente and at the University of Birmingham. The experimental results for case B4 however are unfortunately difficult to compare, since the experiments at the University of Twente were not performed for exactly the same operating conditions. To be able to compare the results, the frequency spectra for the operating conditions closest to the desired one have been included in the figure. These frequency spectra show that the flow regime shifts from the spout-fluidization regime at a background velocity of 1.5 m/s to the intermediate regime at 2.0 m/s.
Consequently, a transition of the flow regime occurs between 1.5 m/s and 2.0 m/s, which will most likely result in a less profound frequency peak compared to the extremely regular spout-fluidization regime. This can be observed in the frequency spectrum recorded at the University of Birmingham, which shows a reduced magnitude of the power.

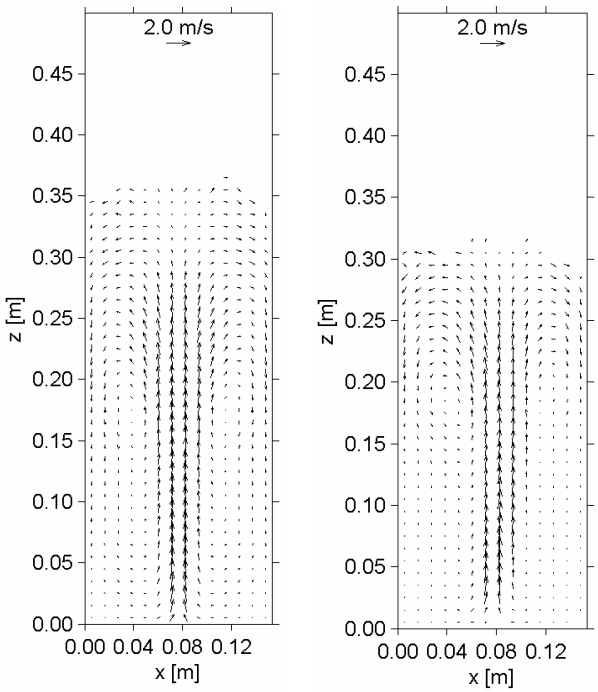

Computed field Measured field

Figure 6.22 Time-averaged particle velocity fields in the central xz-plane for case B1, the intermediate / spout-fluidization regime (mono-disperse).

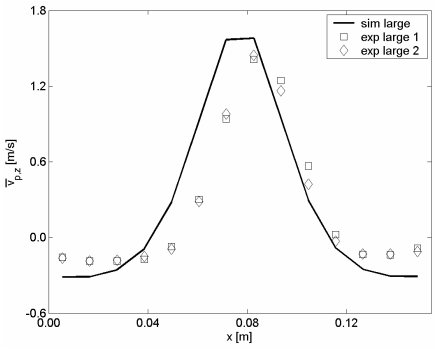

$\overline{v_{p,z}}$ -profile at z = 0.15 m

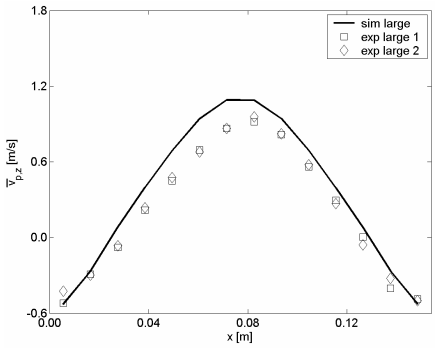

$\overline{v_{p,z}}$ -profile at z = 0.25 m

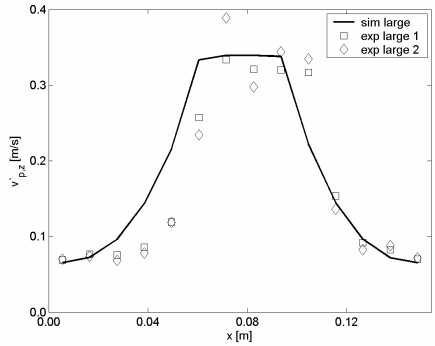

$v'_{p,z}$ -profile at z = 0.15 m

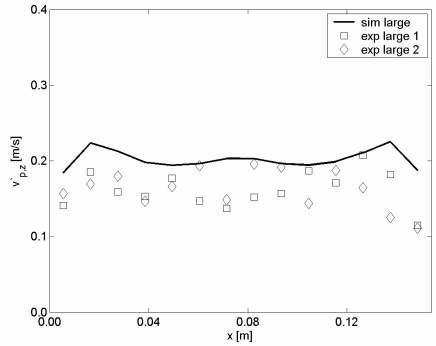

$v'_{p,z}$ -profile at z = 0.25 m

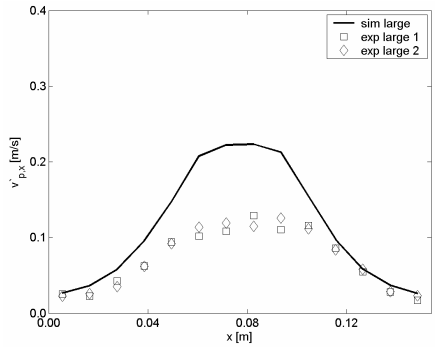

$v'_{p,x}$ -profile at z = 0.15 m

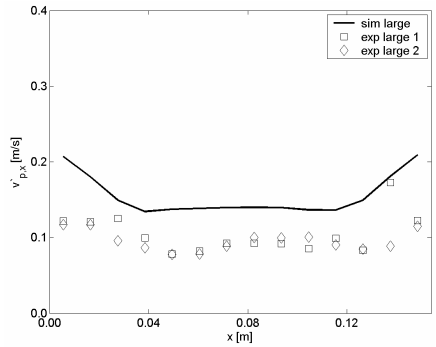

$v'_{p,x}$ -profile at z = 0.25 m

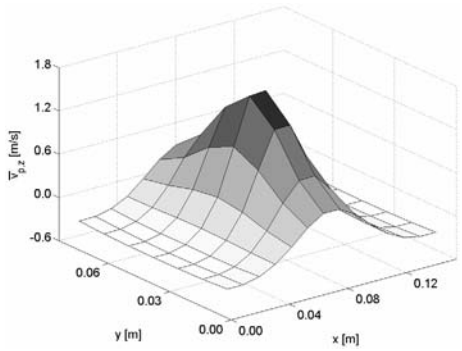

Computed $\overline{v_{p,z}}$ -surface plot at z = 0.15 m

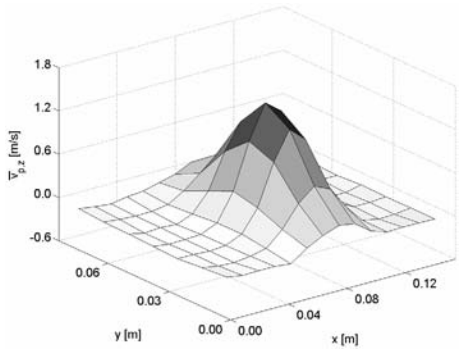

Measured $\overline{v_{p,z}}$ -surface plot at z = 0.15 m

Figure 6.23 Profiles of the time-averaged vertical particle velocity including the RMS in the central xz-plane and a surface plot at z = 0.15 m for case B1, the intermediate / spout-fluidization regime (mono-disperse).

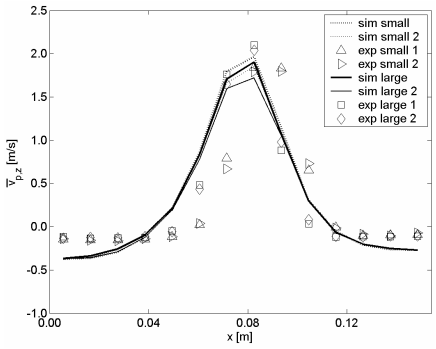

$\overline{v_{p,z}}$ -profile at z = 0.15 m

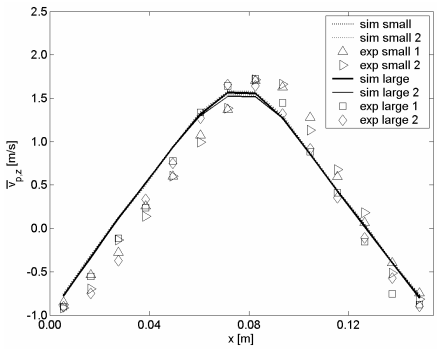

$\overline{v_{p,z}}$ -profile at z = 0.25 m

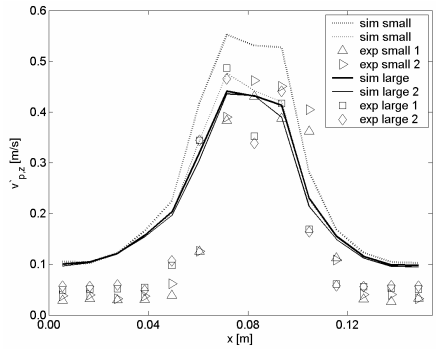

$v'_{p,z}$ -profile at z = 0.15 m

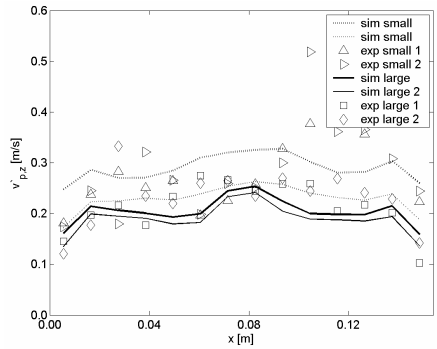

$v'_{p,z}$ -profile at z = 0.25 m

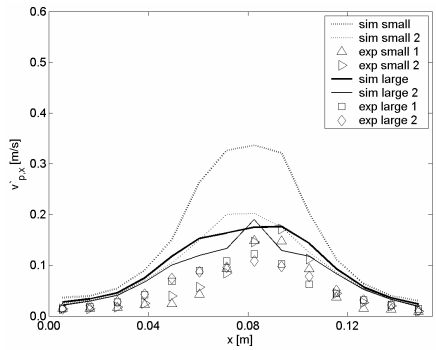

$v'_{p,x}$ -profile at z = 0.15 m

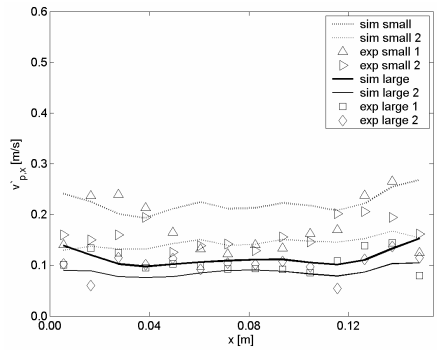

$v'_{p,x}$ -profile at z = 0.25 m

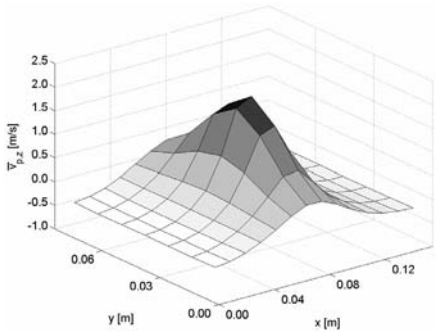

Computed $\overline{v_{p,z}}$ -surface plot at z = 0.15 m

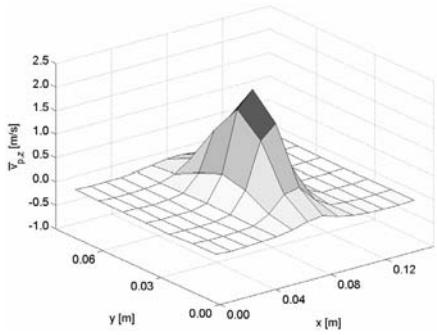

Measured $\overline{v_{p,z}}$ -surface plot at z = 0.15 m

Figure 6.24 Profiles of the time-averaged vertical particle velocity including the RMS in the central xz-plane and a surface plot at z = 0.15 m for case B4, the intermediate / spout-fluidization regime (bi-disperse). The

addition “1” represents the results obtained with instantaneous particle velocities, while the addition “2” represents the results calculated using the displacement during a period equivalent to the period used in the experiments.

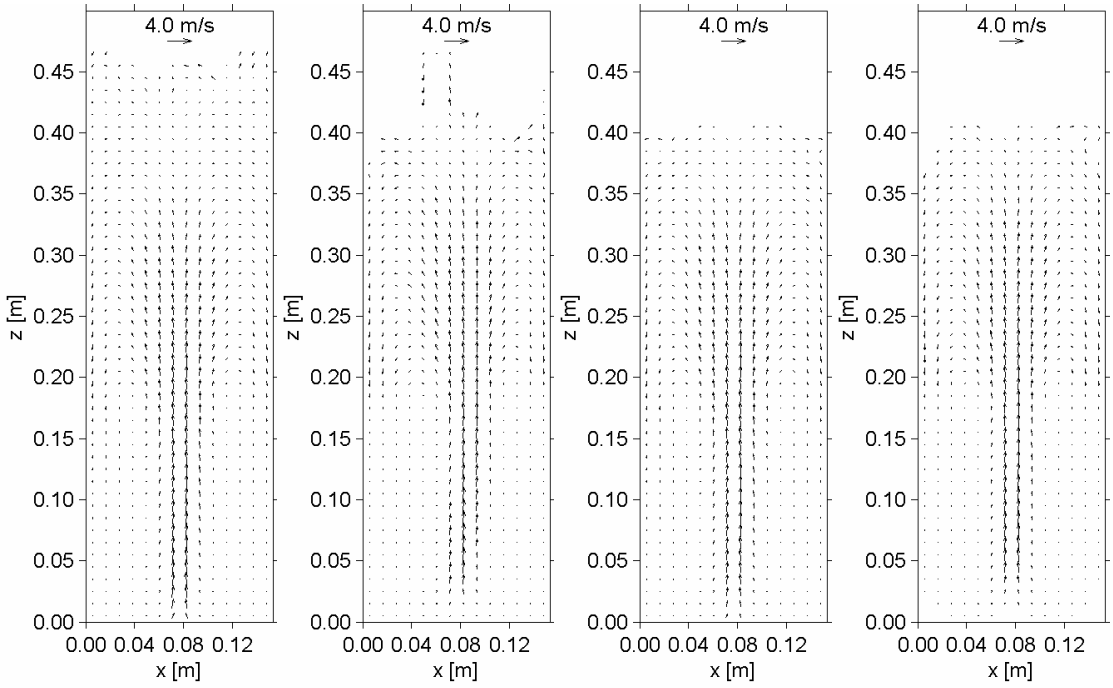

Computed field small particles | Measured field small particles | Computed field large particles | Measured field large particles

Figure 6.25 Time-averaged particle velocity fields in the central xz-plane for case B4, the intermediate / spout-fluidization regime (bi-disperse).

Figures 6.22, 6.23, 6.24 and 6.25 show that the spout channel in the spout-fluidization regime is somewhat wider than the spout channel in the spouting-with-aeration regime.

The spout-fluidization regime shows similar trends for the time-averaged particle velocity profiles and their RMS as compared with the spouting-with-aeration regime. The main difference is that the time-averaged particle velocities and their RMS are generally lower for the spout-fluidization regime than those encountered in the spouting-with-aeration regime.

The computed time-averaged particle velocities in the spout channel are virtually the same for both particle sizes. The computed RMS of the velocity of the small particles however is somewhat larger than the RMS of the velocity of the large particles. This effect cannot be observed as clearly in the experimental results.

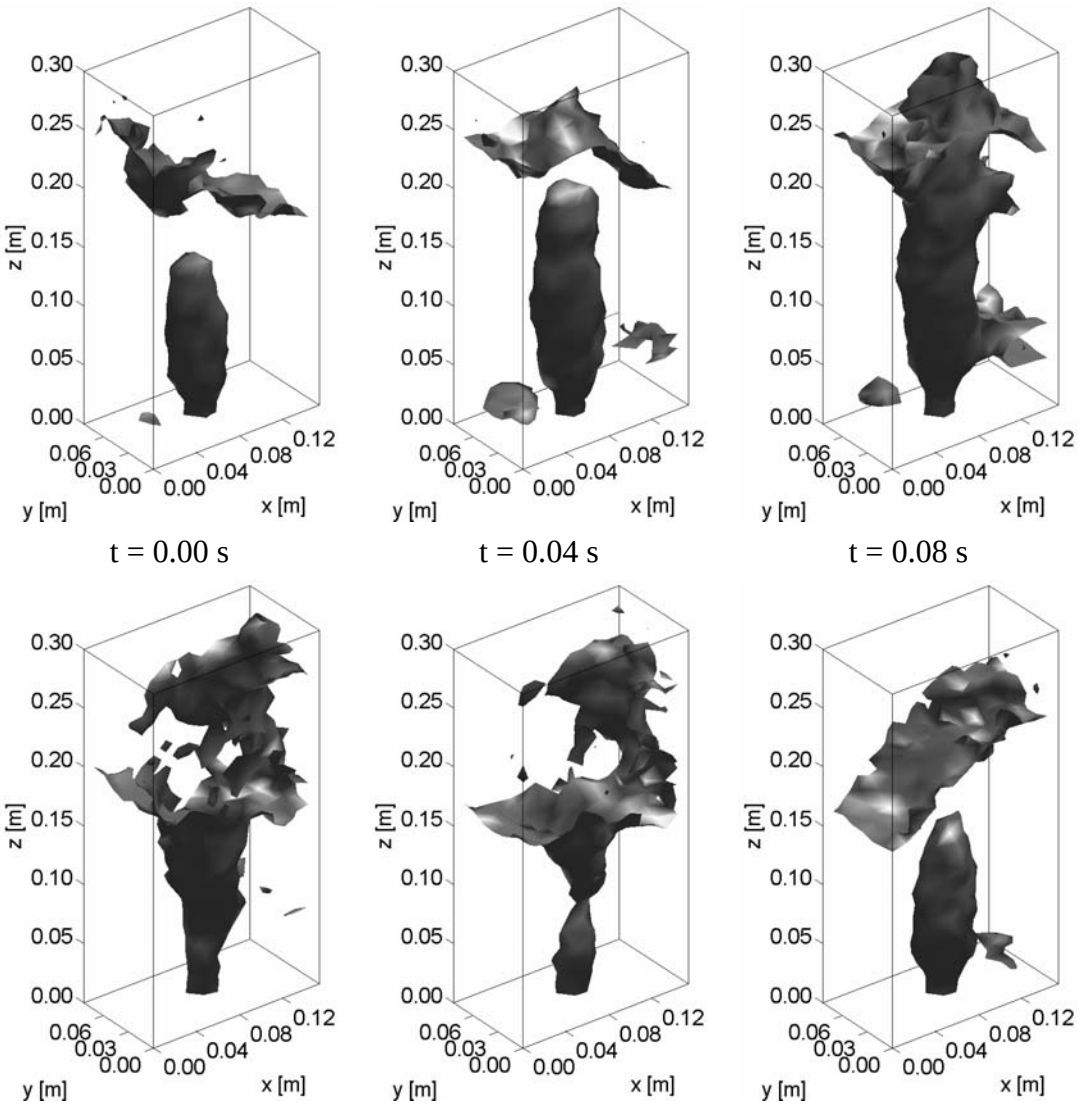

Figure 6.26 Plots of the iso-surface at a solids volume fraction of 0.3 for case B3, the jet-in-fluidized-bed regime (mono-disperse).

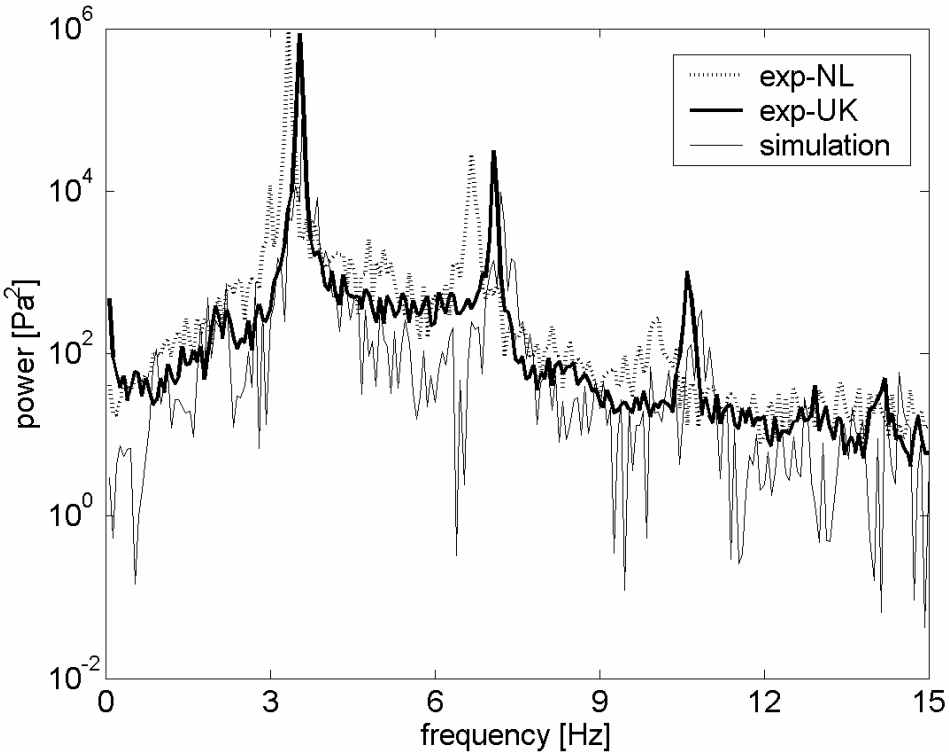

Figure 6.27 Frequency spectra of the measured and computed pressure drop fluctuations of case B3, the jet-in-fluidized-bed regime (mono-disperse).

Jet-in-fluidized-bed regime

The solids volume fraction iso-surface plots for the mono-disperse case in the jet-in-fluidized-bed regime (B3), displayed in Figure 6.26, show that the spout channel grows in the vertical direction until it reaches the bed surface. Small bubbles are present next to the spout channel, i.e. in the annulus, that merge with the spout channel. Subsequently, a fountain is formed and the spout channel is closed halfway. Finally, a new bubble is formed in the lower half of the spout channel.

This process consumes approximately 0.3 s, which corresponds to the frequency of ~3.5 Hz, which can be observed in the frequency spectra of the computed pressure drop fluctuations given in Figure 6.27. The frequency spectra of the measured and computed pressure drop fluctuations are in very good agreement. Both display a relatively narrow peak with very large power ($>1 \cdot 10^5$ Pa^2) at an intermediate frequency (~3.5 Hz), which is typical for the single frequency mode of this flow regime.

Table 6.4 shows that the amplitude of the pressure drop fluctuations predicted by the DPM is considerably smaller (40%) than the measured value, which results in a lower magnitude of the power of the pressure drop fluctuations.

The solids volume fraction iso-surface plots for the bi-disperse case in the jet-in-fluidized-bed regime (B6), given in Figure 6.28, show a stable spout channel, which appears to meander, since it bends in several directions. Bubbles can sometimes be discerned in the lower part of the bed next to the spout channel. This behavior clearly differs from the behavior for case B3 (see Figure 6.26), although the frequency of the fluctuations is similar, as is the flow regime.

The stability of the spout channel suggests that the pressure drop fluctuations are most likely caused by the bubbles in the annulus. Therefore this case can also be considered as an intermediate regime between spouting-with-aeration and jet-in-fluidized-bed, which is supported by the regime map in Figure 6.4.

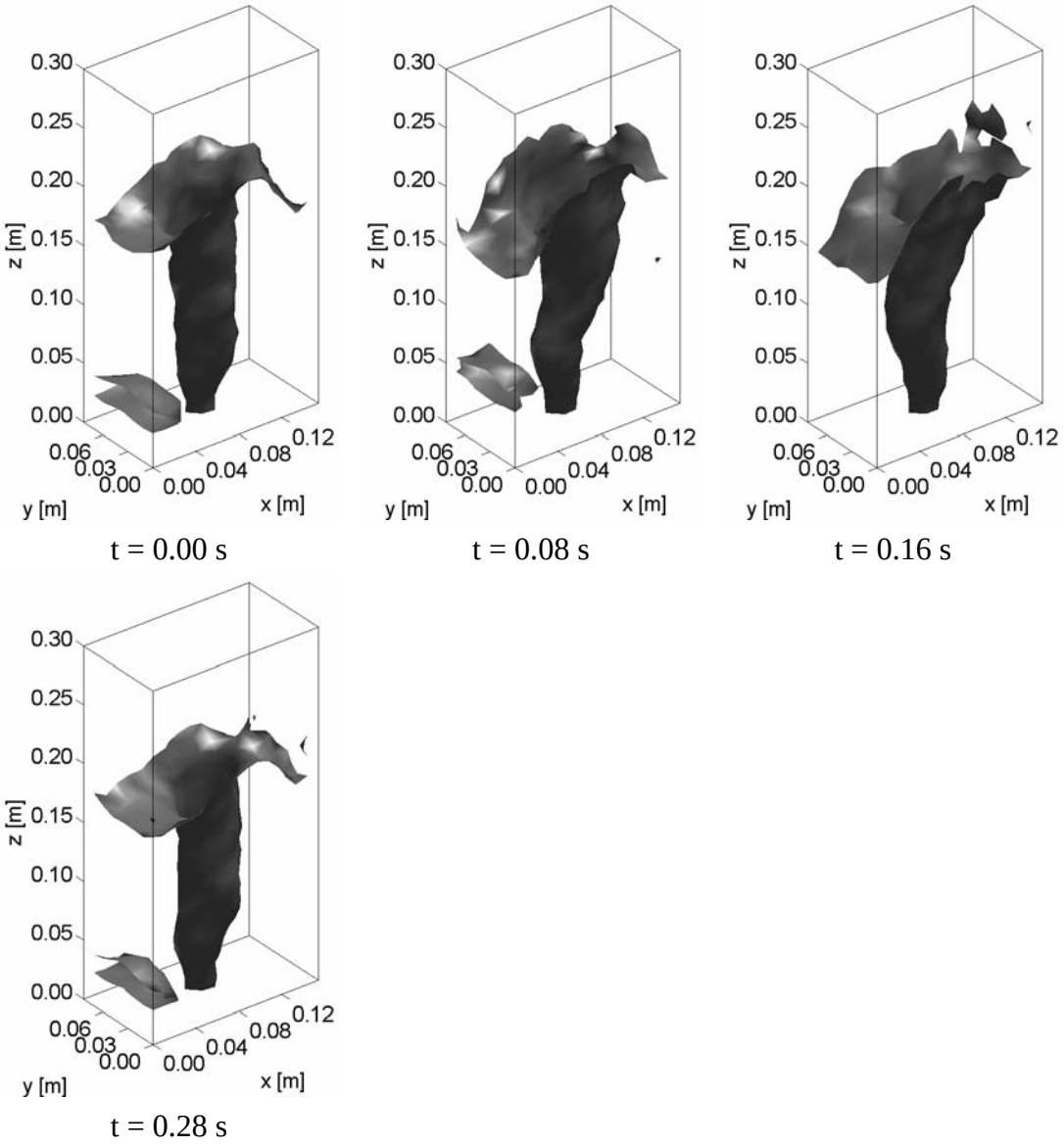

Figure 6.28 Plots of the iso-surface at a solids volume fraction of 0.3 for case B6, the jet-in-fluidized-bed regime (bi-disperse).

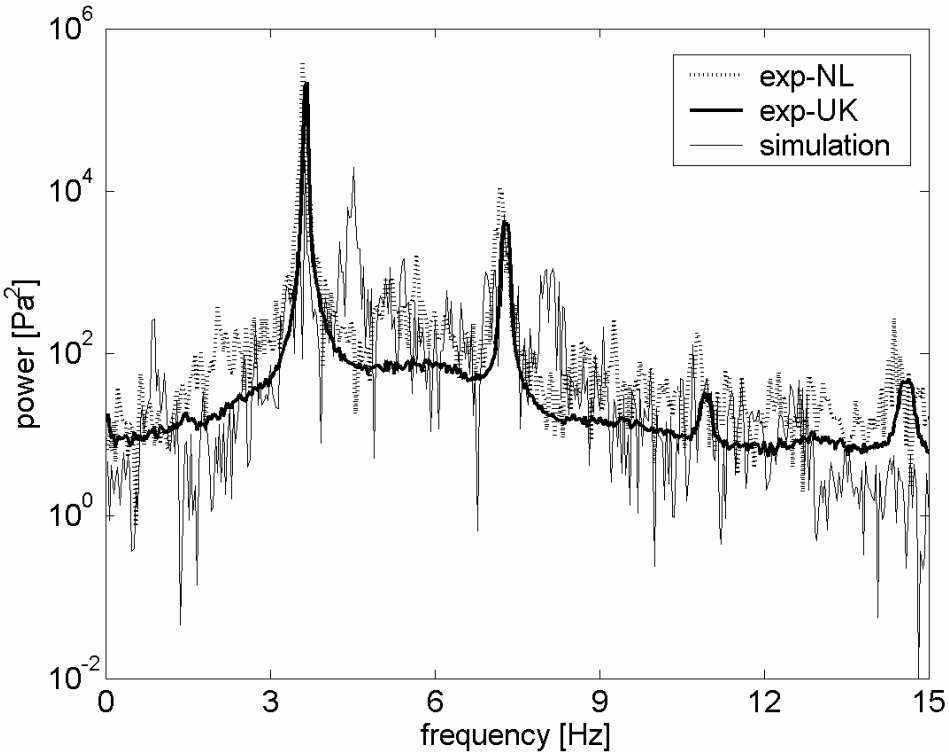

Figure 6.29 Frequency spectra of the measured and computed pressure drop fluctuations of case B6, the jet-in-fluidized-bed regime (bi-disperse).

Figure 6.29 shows the frequency spectra of the measured and computed pressure drop fluctuations which are in reasonable agreement. Both display a relatively narrow peak with large power (>$1 \cdot 10^4$ Pa^2) at an intermediate frequency (~3.5 Hz), which is typical for the single frequency mode of this flow regime. The model however also predicts a peak with a similar magnitude at 4.5 Hz.
Table 6.4 shows that the amplitude of the pressure drop fluctuations predicted by the DPM is considerably smaller (50%) than the measured value, which also results in a lower magnitude of the power of the pressure drop fluctuations.

Since case B7 is in the multi-frequency mode of the jet-in-fluidized-bed regime (bi-disperse), the flow behavior is not regular, which is illustrated by the iso-surface plots in Figure 6.30. The spout and the bubbles merge and erupt at the bed surface after which the spout is significantly tilted when it merges with the next bubble. The merging of the spouting channel and the surrounding bubbles was also observed in case B3 in Figure 6.26, which is also in the jet-in-fluidized-bed regime (mono-disperse), but to a far lesser extent.
Consequently, the frequency spectra of the measured and computed pressure drop fluctuation, given in Figure 6.31 display a relatively broad peak with large power (~$1 \cdot 10^4$ Pa^2) at a relatively low frequency (~2-4 Hz), which is typical for the multiple

frequency mode of this flow regime. The frequency spectra are in reasonable agreement, although the experiments display a small additional peak at 3 Hz, which the model does not predict.

Table 6.4 shows that the amplitude of the pressure drop fluctuations predicted by the DPM is smaller (30%) than the measured value. Apart from the additional peak at 3 Hz, the magnitude of the power of the pressure drop fluctuations is in good agreement.

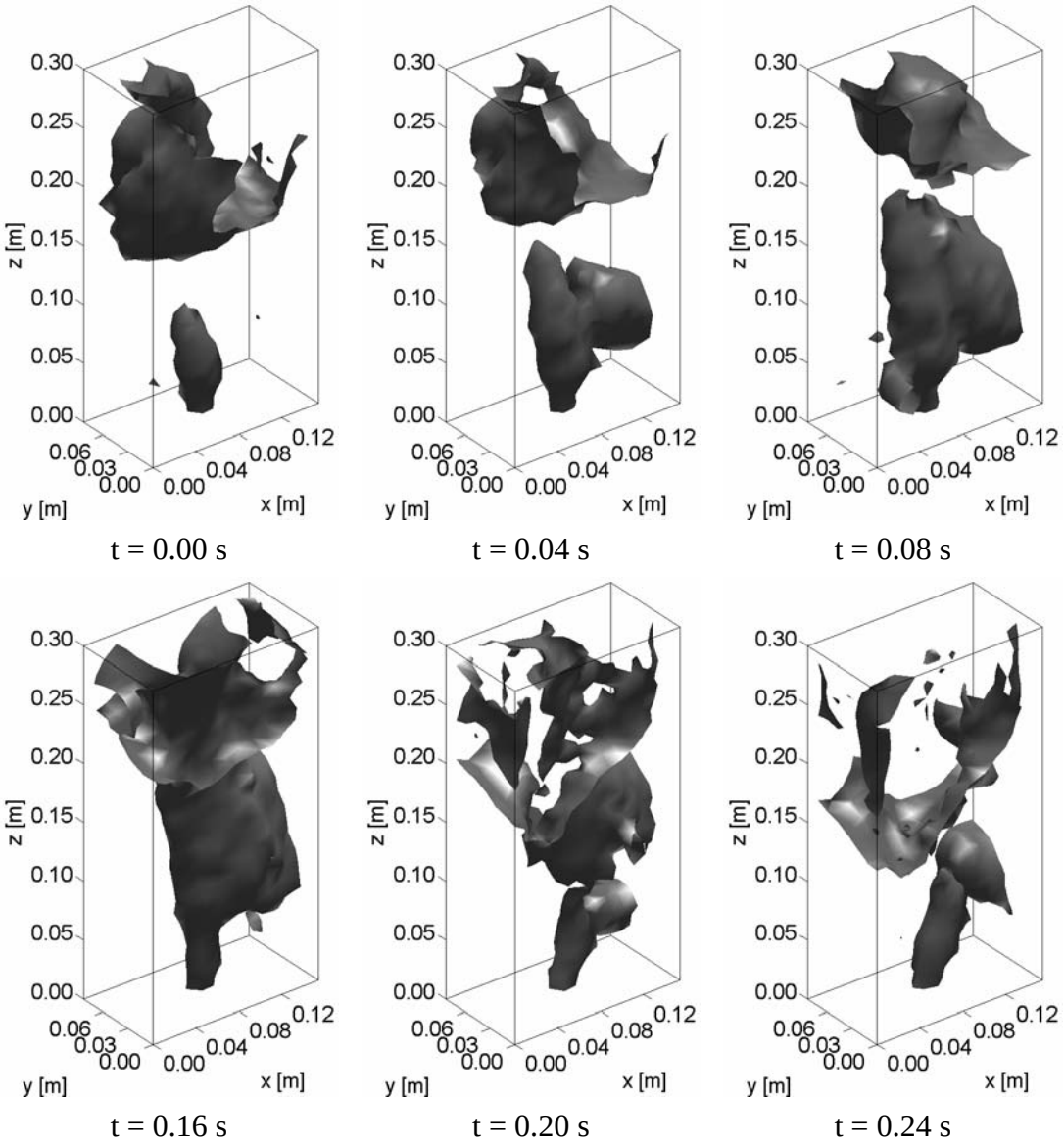

Figure 6.30 Plots of the iso-surface at a solids volume fraction of 0.3 for case B7, the jet-in-fluidized-bed regime (bi-disperse).

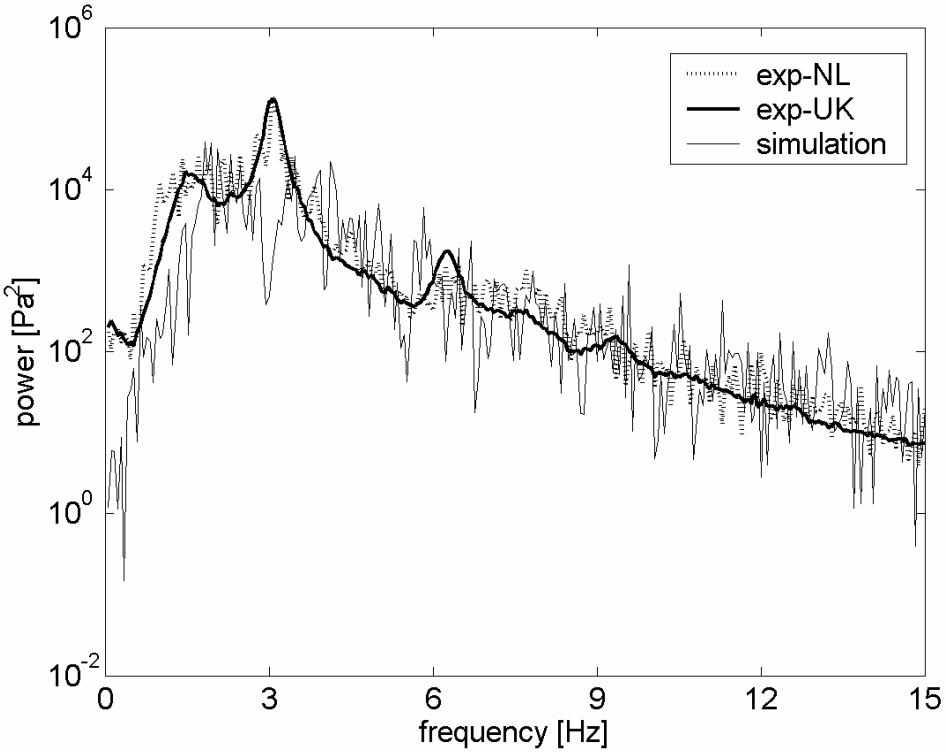

Figure 6.31 Frequency spectra of the measured and computed pressure drop fluctuations of case B7, the jet-in-fluidized-bed regime (bi-disperse).

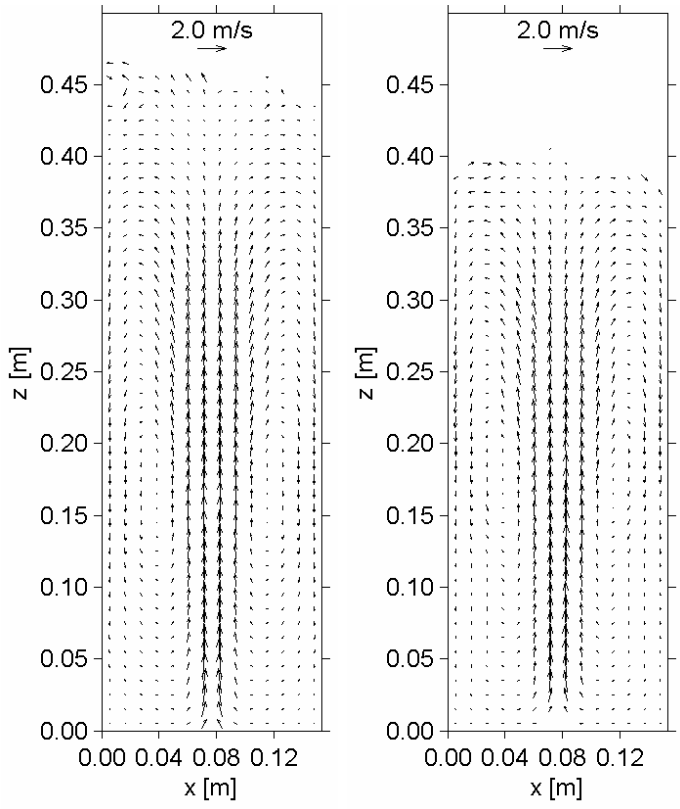

Figure 6.32 Time-averaged particle velocity fields in the central xz-plane for case B3, the jet-in-fluidized-bed regime (mono-disperse).

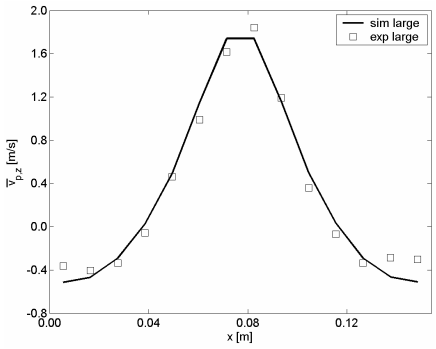

$\overline{v_{p,z}}$ -profile at z = 0.15 m

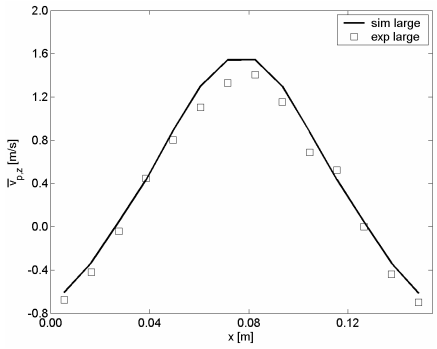

$\overline{v_{p,z}}$ -profile at z = 0.25 m

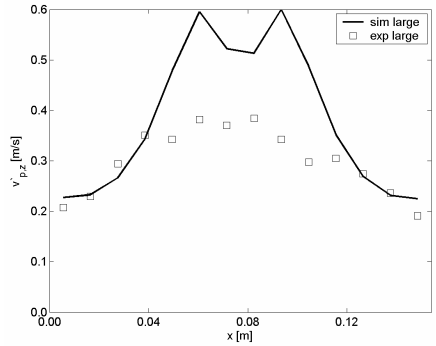

$v'_{p,z}$ -profile at z = 0.15 m

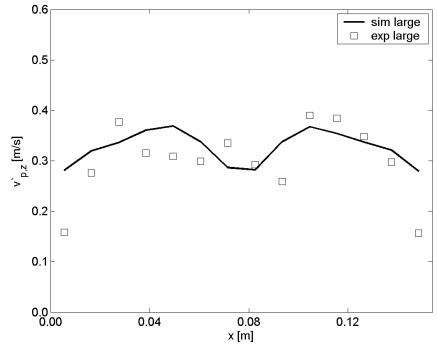

$v'_{p,z}$ -profile at z = 0.25 m

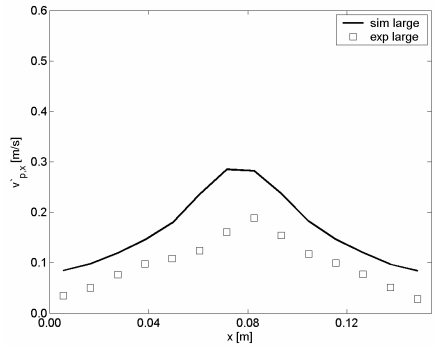

$v'_{p,x}$ -profile at z = 0.15 m

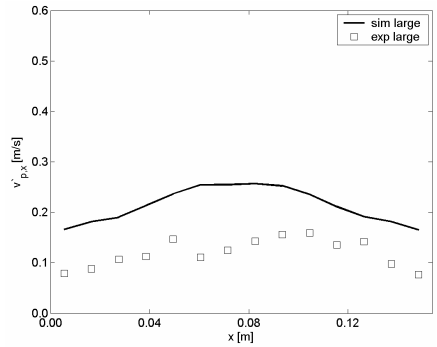

$v'_{p,x}$ -profile at z = 0.25 m

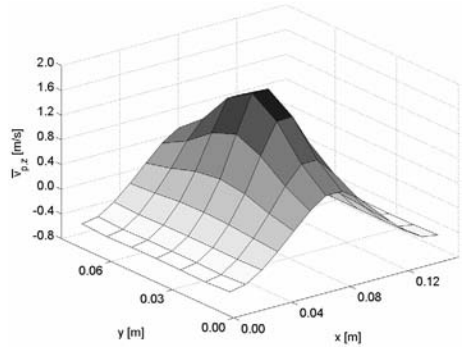

Computed $\overline{v_{p,z}}$ -surface plot at z = 0.15 m

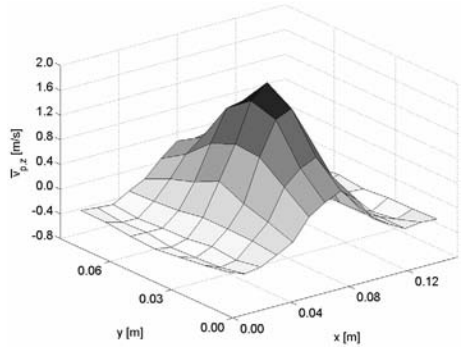

Measured $\overline{v_{p,z}}$ -surface plot at z = 0.15 m

Figure 6.33 Profiles of the time-averaged vertical particle velocity including the RMS in the central xz-plane and a surface plot at z = 0.15 m for case B3, the jet-in-fluidized-bed regime (mono-disperse).

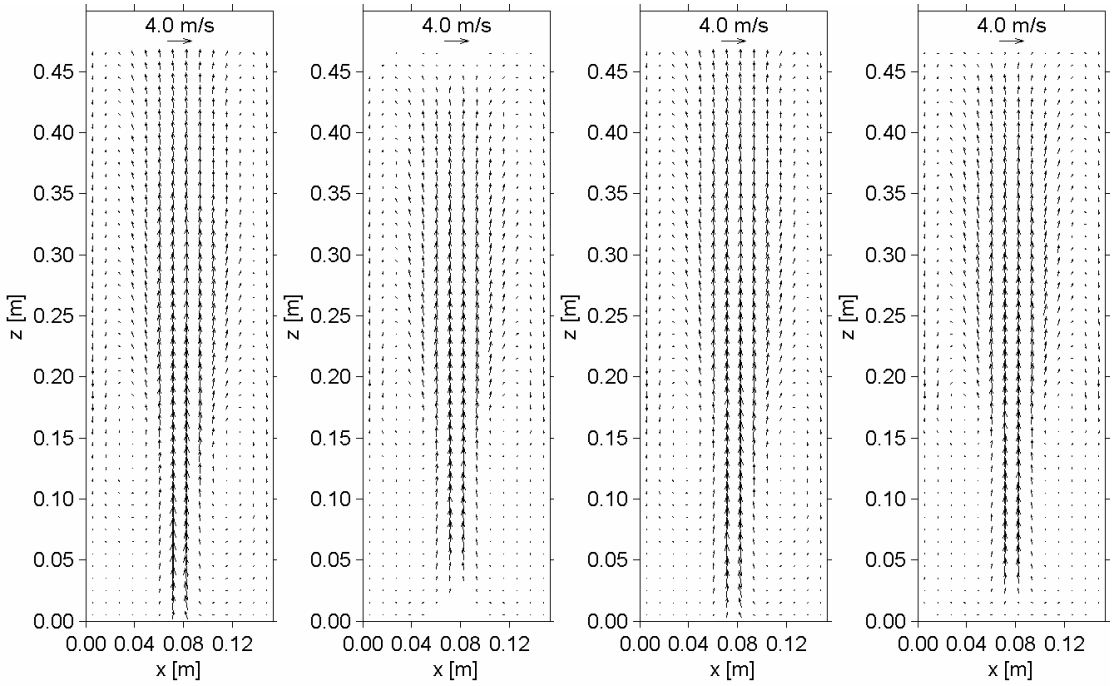

Computed field small particles | Measured field small particles | Computed field large particles | Measured field large particles

Figure 6.34 Time-averaged particle velocity fields in the central xz-plane for case B6, the jet-in-fluidized-bed regime (bi-disperse).

Figures 6.32, 6.33, 6.34 and 6.35 show that the single frequency mode of the jet-in-fluidized-bed regime resembles the spout-fluidization regime. The time-averaged particle velocities and the RMS are however much larger.

Both profiles at a height of 0.15 m show that the RMS and the time-average of the particle velocities in the annulus are smaller than those encountered in the spout channel. The RMS in the fountain is comparable with the RMS in the spout channel and is smaller near the walls than in the center of the bed. Contrary to the model result, the measured RMS in the z-direction of case B6, the jet-in-fluidized-bed regime (bi-disperse), is approximately constant in the spout channel.

The computed time-averaged particle velocities in the spout channel are virtually the same for both particle sizes. The computed RMS of the velocity of the small particles however, is somewhat larger than the RMS of the velocity of the large particles. The experimental result at a height of 0.25 m also shows this effect, but far less pronounced.

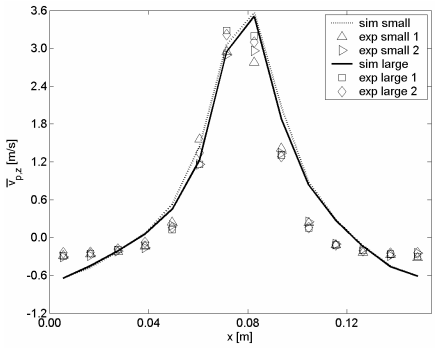

$\overline{v_{p,z}}$ -profile at z = 0.15 m

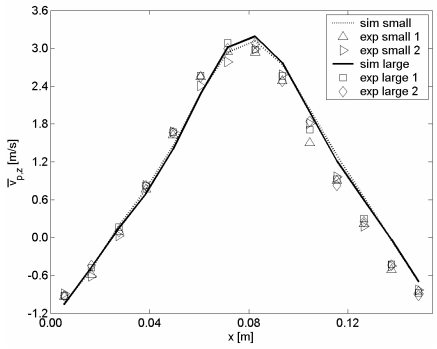

$\overline{v_{p,z}}$ -profile at z = 0.25 m

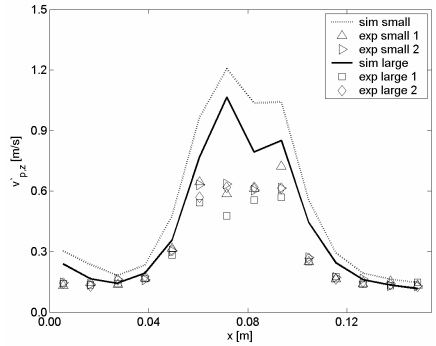

$v'_{p,z}$ -profile at z = 0.15 m

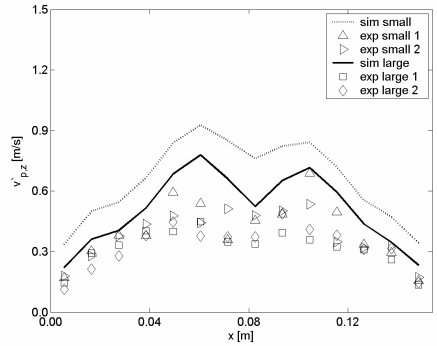

$v'_{p,z}$ -profile at z = 0.25 m

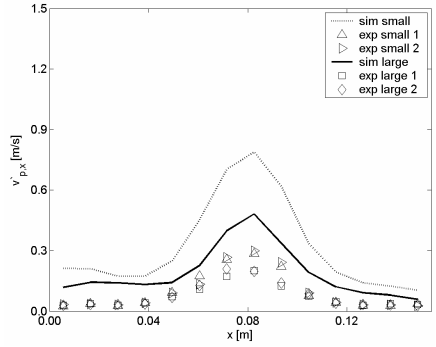

$v'_{p,x}$ -profile at z = 0.15 m

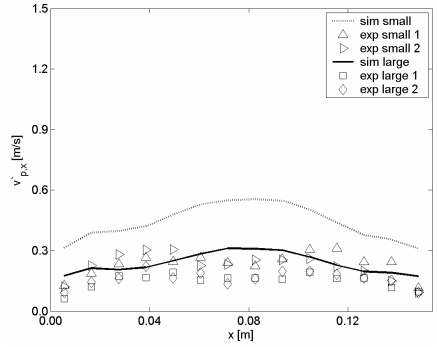

$v'_{p,x}$ -profile at z = 0.25 m

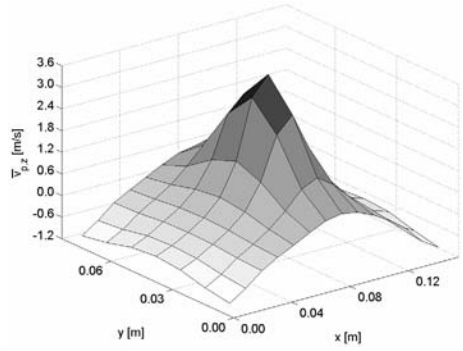

Computed $\overline{v_{p,z}}$ -surface plot at z = 0.15 m

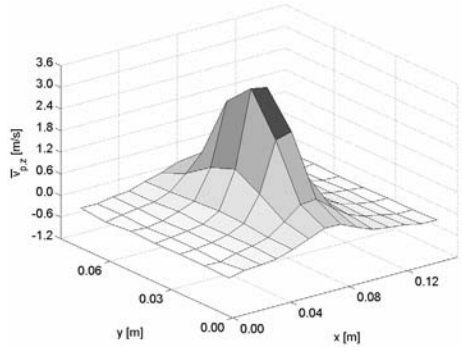

Measured $\overline{v_{p,z}}$ -surface plot at z = 0.15 m

Figure 6.35 Profiles of the time-averaged vertical particle velocity including the RMS in the central xz-plane and a surface plot at z = 0.15 m for case B6, the jet-in-fluidized-bed regime (bi-disperse).

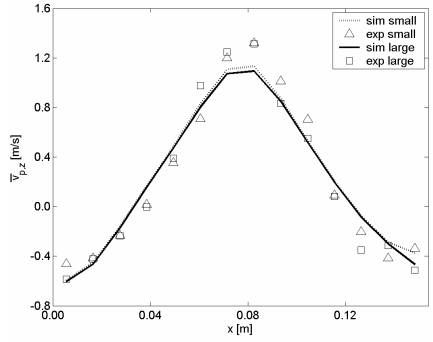

$\overline{v_{p,z}}$ -profile at z = 0.15 m

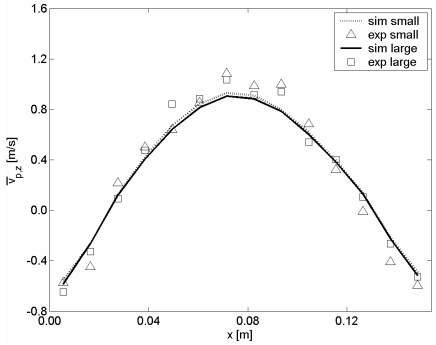

$\overline{v_{p,z}}$ -profile at z = 0.25 m

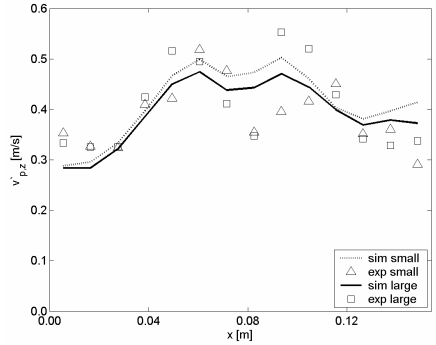

$v'_{p,z}$ -profile at z = 0.15 m

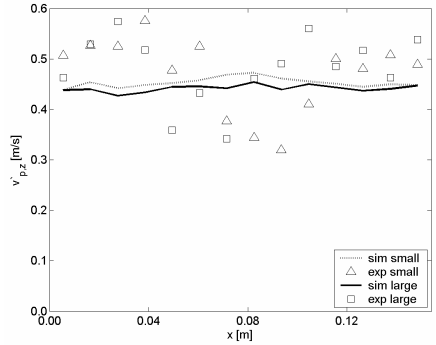

$v'_{p,z}$ -profile at z = 0.25 m

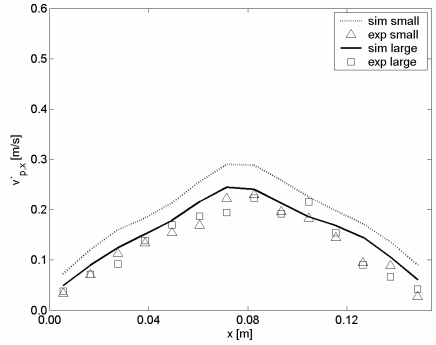

$v'_{p,x}$ -profile at z = 0.15 m

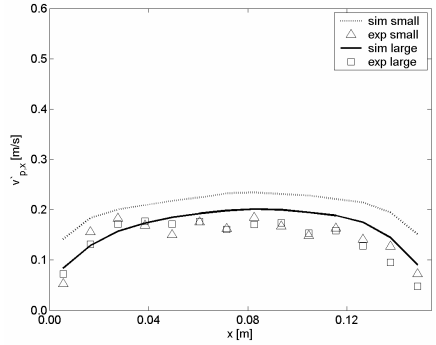

$v'_{p,x}$ -profile at z = 0.25 m

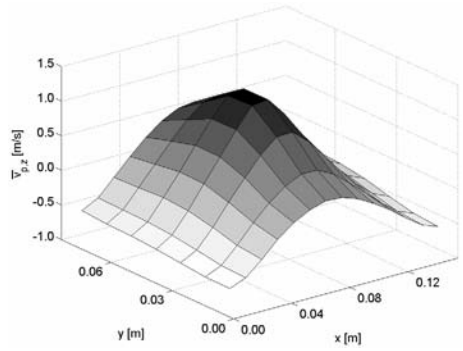

Computed $\overline{v_{p,z}}$ -surface plot at z = 0.15 m

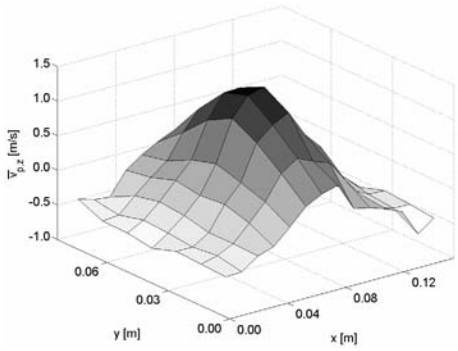

Measured $\overline{v_{p,z}}$ -surface plot at z = 0.15 m

Figure 6.36 Profiles of the time-averaged vertical particle velocity including the RMS in the central xz-plane and a surface plot at z = 0.15 m for case B7, the jet-in-fluidized-bed regime (bi-disperse).

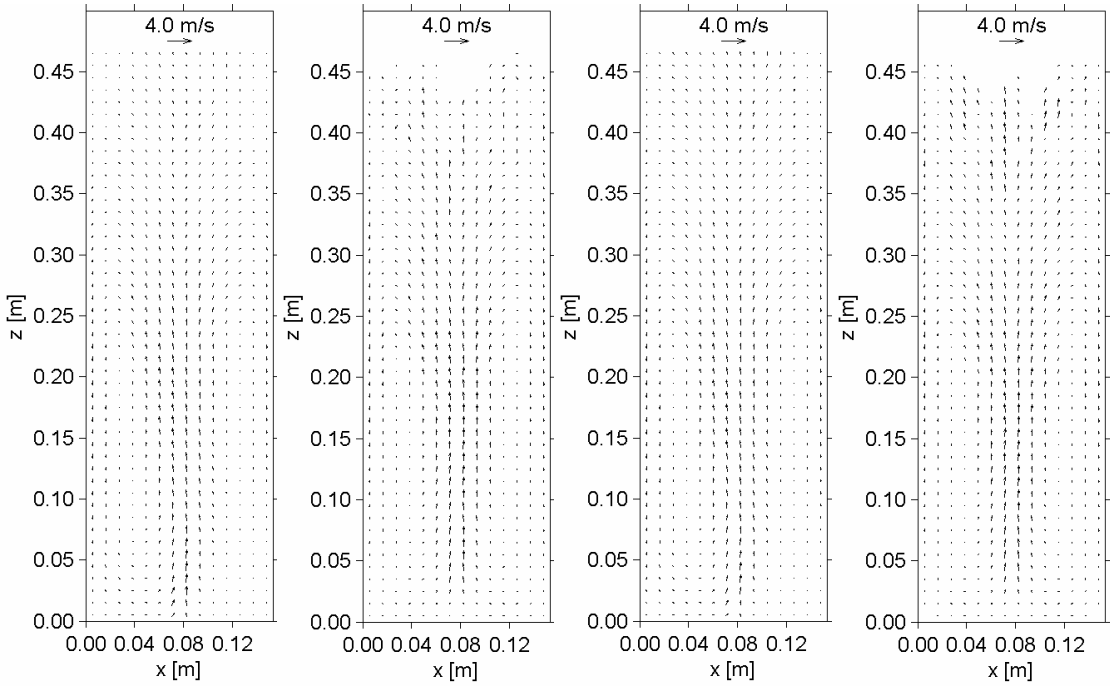

Computed field small particles | Measured field small particles | Computed field large particles | Measured field large particles

Figure 6.37 Time-averaged particle velocity fields in the central xz-plane for case B7, the jet-in-fluidized-bed regime (bi-disperse).

Figures 6.36 and 6.37 show that the spout channel in the multi frequency mode of the jet-in-fluidized-bed is very wide. This is caused by the large bubbles that are already formed near the bottom of the bed and move through the center of the bed. The time-averaged particle velocities are comparable with the spout-fluidization regime, although the superficial gas velocity is larger. The relatively large RMS of the vertical particle velocity is approximately the same in the annulus, the spout and the fountain. The RMS of the horizontal particle velocity shows the same profiles in the spout and in the fountain with lower values near the walls. The difference between the RMS of the velocity of the small particles and that of the large particles is negligible.

In the multi frequency mode of the jet-in-fluidized-bed regime, bubbles dominate the behavior of the bed. The particles are therefore not accelerated in the dilute spout channel but rather in the dense areas around the bubbles. Consequently the behavior of the small and large particles needs to be very similar. The bubbles also reverse the direction of movement in the annulus, which causes the time-averaged particle velocities to be smaller and which increases the RMS in the vertical direction in the annulus compared to the spout-fluidization regime.

Contrary to the other cases, the computed and measured surface plot at z = 0.15 m resemble each other closely.

6.4.3 Discussion

Frequency spectra

In most cases in both configuration A and B the model was able to predict the appropriate flow regime. Furthermore, the amplitude of the pressure drop fluctuations predicted by the model was of the same order as the experimental result, although some differences were observed. The frequency, at which the largest power was found, was generally overpredicted by the model. For a number of cases, the fluctuations predicted by the model were more regular than the measured fluctuations.

When the predictive capabilities of the model are evaluated, it can be concluded that the model accurately predicts the flow regimes at relatively low background velocities.

The flow regimes at higher background velocities, which are characterized by more bubbles and more types of bubbles, are more difficult to predict although satisfactory results were still obtained in most cases. A specific type of bubble, the large slug, was rarely encountered in the model although it did appear in the experiments on a regular basis in case A5, the bubbling-/slugging-bed regime. The transition between flow regimes proved to be difficult to predict, since the dynamics at the transition are very sensitive to minor changes in the operating conditions. Since the frequency is either low or indefinite in the cases described above, the quality of the results can be improved by running simulations over a longer period of time. This was not done because of limitations in the computational capacity.

The differences that were observed between the measured and simulated bed behavior, especially at low spout velocities, can in principle be attributed to the representation of gas-particle and/or particle-particle interaction.

A sensitivity study with respect to the values of the collision parameters for both particle-particle and particle-wall interaction revealed that the observed differences could not be reduced significantly by using different values for these parameters.

This leaves the representation of the fluid-particle interaction as a probable cause for most of the observed discrepancies. Although the fluid-particle drag obtained from lattice Boltzmann simulations is believed to be reasonably accurate, it is obtained for systems, in which the particles are homogeneously distributed in space. Heterogeneity is known to exist in dense gas-particle flows, especially around gas bubbles. The effect of this heterogeneity on effective fluid-particle drag is largely unexplored, but can in principle be resolved from detailed lattice Boltzmann simulations.

The frequency spectra of the measured and computed pressure drop fluctuations for configuration B show that the correspondence between the measurements performed at the University of Twente (NL) and the University of Birmingham (UK) is good indicating that the experimental results were reproducible. Both the shape and the power are in good agreement, although case B1, the intermediate / spout-fluidization regime (mono-disperse), displays a slight deviation in the shape of the frequency spectrum. The root mean square of the pressure drop fluctuations in Table 6.4 is also comparable.

Particle velocities

The measured and computed time-averaged particle velocity fields generally display good agreement. The particle flow patterns are very similar, although the computed particle flow patterns reach higher up into the bed. The likeliness of a particle to reach a large height increases with the measuring time. Therefore, the particles in the simulation (16 s/particle * $4.5 \cdot 10^4$ particles ~ 200 h) are more likely to reach high up in the bed than in the experiment (1 h/particle * 1 particles ~ 1 h).

Near the spout mouth the particle velocities are underestimated by PEPT since the actual velocity will be larger than the average velocity over 6 particle locations due to the rapid acceleration of the particle.

The measured and computed particle velocity profiles show good agreement. At a height of 0.15 m the shape of the computed profile differs slightly from the measured profile in all cases except for case B7, the jet-in-fluidized-bed regime (bi-disperse). The simulations show positive velocities in a larger region of the bed, while the velocities close to the wall are more negative than in the experiment.

At a height of 0.25 m, the agreement is very good, except for case B1, the intermediate / spout-fluidization regime (mono-disperse), and B2, the spouting-with-aeration regime (mono-disperse), where the particle velocity in the center of the bed is slightly overpredicted by the model. The cases with a bi-disperse size distribution, case B4 through B7, show that the velocities of large and small particles are virtually identical, which is also predicted by the model.

The time-averaged particle velocities at a height of 0.25 m generally show the same profile, which is typical for the fountain region; relatively high time-averaged particle velocities in the center and negative velocities near the walls. The negative particle velocities near the walls are approximately half as large as the positive velocities in the center.

The agreement between the measured and computed root mean square of the particle velocity is not as good as the time-averaged value. It is however better than expected, since the RMS of the experimental result is influenced by the noise in the PEPT signal, the filtering of this noise and the smoothing effect, which is caused by calculating the particle velocities over a range of six particle positions. The effect of this procedure on the numerical results is illustrated by the additional series in the profiles in Figure 6.24. This figure clearly demonstrates that the RMS, especially of the small particles, is significantly reduced by the procedure, while the time-averaged results are barely affected. Consequently, the RMS of the velocity of the small and large particles is much more similar. This explains why the experimental RMS is generally smaller than its computed counterpart. The shape of the profile of the RMS particle velocity is predicted correctly in most cases.
The averaging procedure would also explain why the model results of cases B4, B5 and B6, show a clear difference between the RMS of the small and large particles, while this effect cannot be observed as clearly in the experimental RMS data.
The profiles of the RMS in the horizontal (x) and vertical (z) direction generally show the same approximate trends, although the profile in the horizontal direction is generally smoother. The RMS in the vertical direction is on average about twice as large as the RMS in the horizontal direction.

The particle velocity field at z = 0.15 m shows that the velocity peak in the center of the bed is generally narrower in the experiments. When one assumes that the solids volume fraction distributions are comparable in the simulation and the experiment, the total upward particle flow will be smaller in the experiment. Since the upward flow needs to be balanced by a downward flow of equal magnitude, the total downward flow will also be smaller. Furthermore, the downward flow is spread over a larger area. This explains the observed differences between the computed and measured downward particle velocities.

Mono-disperse versus bi-disperse

A comparison between the behavior of the mono-disperse and the bi-disperse size distribution shows that the time-averaged particle velocities in the bi-disperse system are much higher than those in the mono-disperse system. Since the superficial gas velocity normalized with the minimum fluidization velocity was the same for both cases, this difference was not caused by the gas velocities. The most probable explanation is therefore that the bi-disperse size distribution allows for a more rapid acceleration due to its lower average inertia.

The larger particle velocities also explain the higher frequencies observed in the bi-disperse system. Since this trend is observed in both the experimental and the computed results, it is correctly predicted in the model.

From a theoretical point of view the small particles are expected to accelerate more rapidly because of their lower inertia and a larger ratio between the drag and gravity forces. When the small particles accelerate faster than the large particles, both types of particles will collide, despite the low solids concentration. The collisions will increase the velocity of the large particles and decrease the velocity of the small particles. The collisions are therefore most probably responsible for the similarity between the velocities of different sized particles, although the more rapid acceleration is still observed in the RMS. Because the experimental particle velocities were obtained after averaging over several points, these fluctuations will be diminished.

6.5 Detailed analysis of the numerical results

In the previous section, the numerical and experimental results were compared. In this section, the model results have been used to obtain more detailed information on the particle behavior, especially by studying the concentration of the particles, which was not available in the experimental results.

A surface plot of the time-averaged vertical particle flux at a height of 0.15 m, which is slightly below the packed bed surface position, is presented for all cases. For the cases with a bi-disperse size distribution, the concentrations and fluxes of small and large particles will be presented and discussed. The results consist of four parts, which respectively show:

a. the total time-averaged particle flux profile:

$$\left\langle \mathbf{\Phi}_p \right\rangle_{i,j,k} = \frac{1}{V_{cell} N_t} \sum_{N_t} \sum_{\forall a \in i,j,k} f_a^{i,j,k} m_a \mathbf{v}_a \tag{6.2}$$

where $f_a^{i,j,k}$ is the fraction of particle a in cell (i, j, k) and N_t is the number of time steps.

b. the relative difference between the time-averaged particle fluxes of the large $\left\langle \mathbf{\Phi}_{large} \right\rangle_{i,j,k}$ and the small particles $\left\langle \mathbf{\Phi}_{small} \right\rangle_{i,j,k}$:

$$\left\langle \mathbf{\Phi}_{diff}^{rel} \right\rangle_{i,j,k} = \frac{\left\langle \mathbf{\Phi}_{small} \right\rangle_{i,j,k} - \left\langle \mathbf{\Phi}_{large} \right\rangle_{i,j,k}}{\left\| \left\langle \mathbf{\Phi}_{small} \right\rangle_{i,j,k} + \left\langle \mathbf{\Phi}_{large} \right\rangle_{i,j,k} \right\|} \tag{6.3}$$

Note that if $\langle \mathbf{\Phi}_{small} \rangle_{i,j,k}$ and $\langle \mathbf{\Phi}_{p} \rangle_{i,j,k}$ have the same sign, $\langle \mathbf{\Phi}_{small} \rangle_{i,j,k} > \langle \mathbf{\Phi}_{large} \rangle_{i,j,k}$, otherwise $\langle \mathbf{\Phi}_{small} \rangle_{i,j,k} < \langle \mathbf{\Phi}_{large} \rangle_{i,j,k}$.

c. the total time-averaged solids volume fraction profile:

$$\langle \varepsilon_p \rangle_{i,j,k} = \frac{1}{V_{cell} N_t} \sum_{N_t} \sum_{\forall a \in i,j,k} f_a^{i,j,k} V_a \tag{6.4}$$

d. the profile of the time-averaged concentration of small particles:

$$\langle c_{small} \rangle_{i,j,k} = \frac{\langle \varepsilon_{p,small} \rangle_{i,j,k}}{\langle \varepsilon_{p,small} \rangle_{i,j,k} + \langle \varepsilon_{p,large} \rangle_{i,j,k}} \tag{6.5}$$

Since the system is symmetric, the average results of the left and right half of the xz-plane are shown. Consequently, the left part of each profile corresponds with the area close to the wall, while the right part corresponds with the center of the bed.

The surface plots of the time-averaged vertical particle flux given in Figure 6.38 show that the bed is displaying pseudo-2D behavior, since the fluxes near the front and back wall are positive, while the fluxes at the side walls are negative. The results obtained for the same regimes are usually similar, although the flux observed for the mono-disperse size distribution is generally larger than that of the bi-disperse size distribution. Case B7 differs from the other jet-in-fluidized-bed cases. The upward flux in the center of the bed is relatively low, but spread over a large portion of the bed. This is connected to the severe tilting and meandering of the spout channel, which can cause the flux in most of the bed to be both positive and negative. The patterns differ between the regimes, especially close to the front and back wall. For the jet-in-fluidized-bed regime, the flux close to these walls is similar to the flux in the center of the bed, while it is lower in the other regimes. It is however noted that the solids volume fraction and the particle velocities clearly differ for all regimes, but these differences appear to compensate one another for the jet-in-fluidized-bed regime.

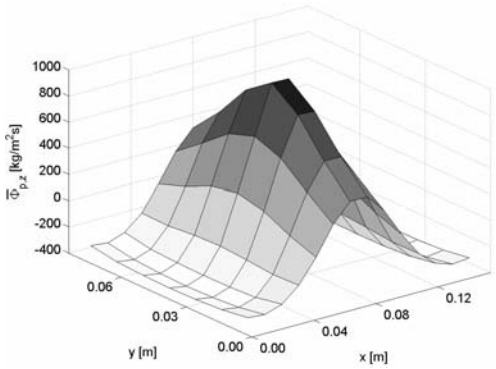

case B1, intermediate/spout-fluidization, mono

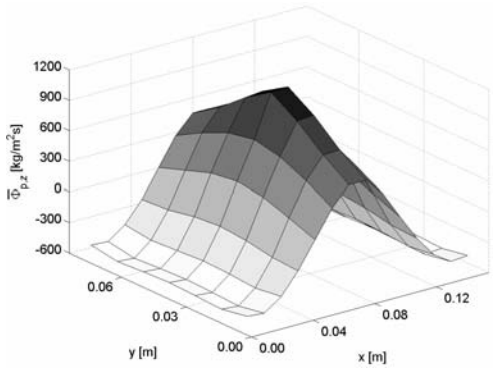

case B2, spouting with aeration, mono

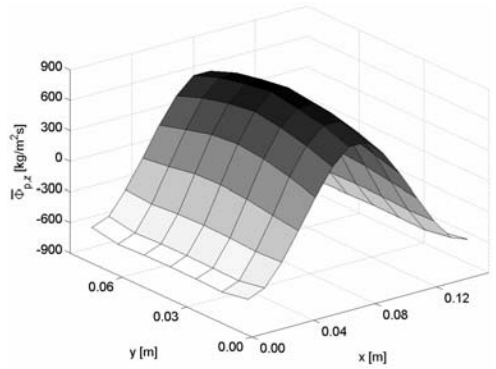

case B3, jet-in-fluidized-bed, mono

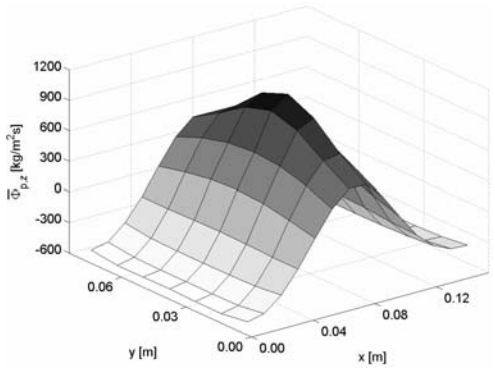

case B4, intermediate/spout-fluidization, bi

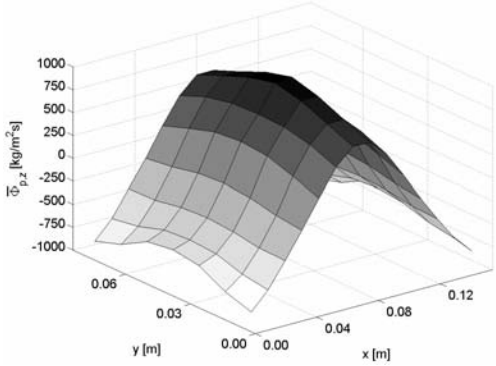

case B5, intermediate/spouting with aeration, bi

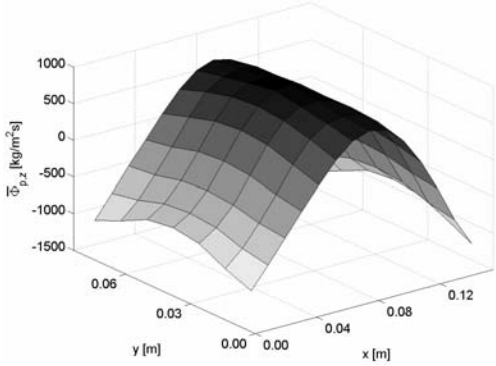

case B6, jet-in-fluidized-bed, bi

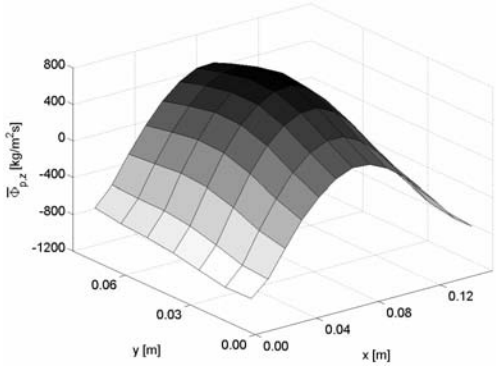

case B7, jet-in-fluidized-bed, bi

Figure 6.38 Surface plots of the time-averaged particle flux at z = 0.15 m.

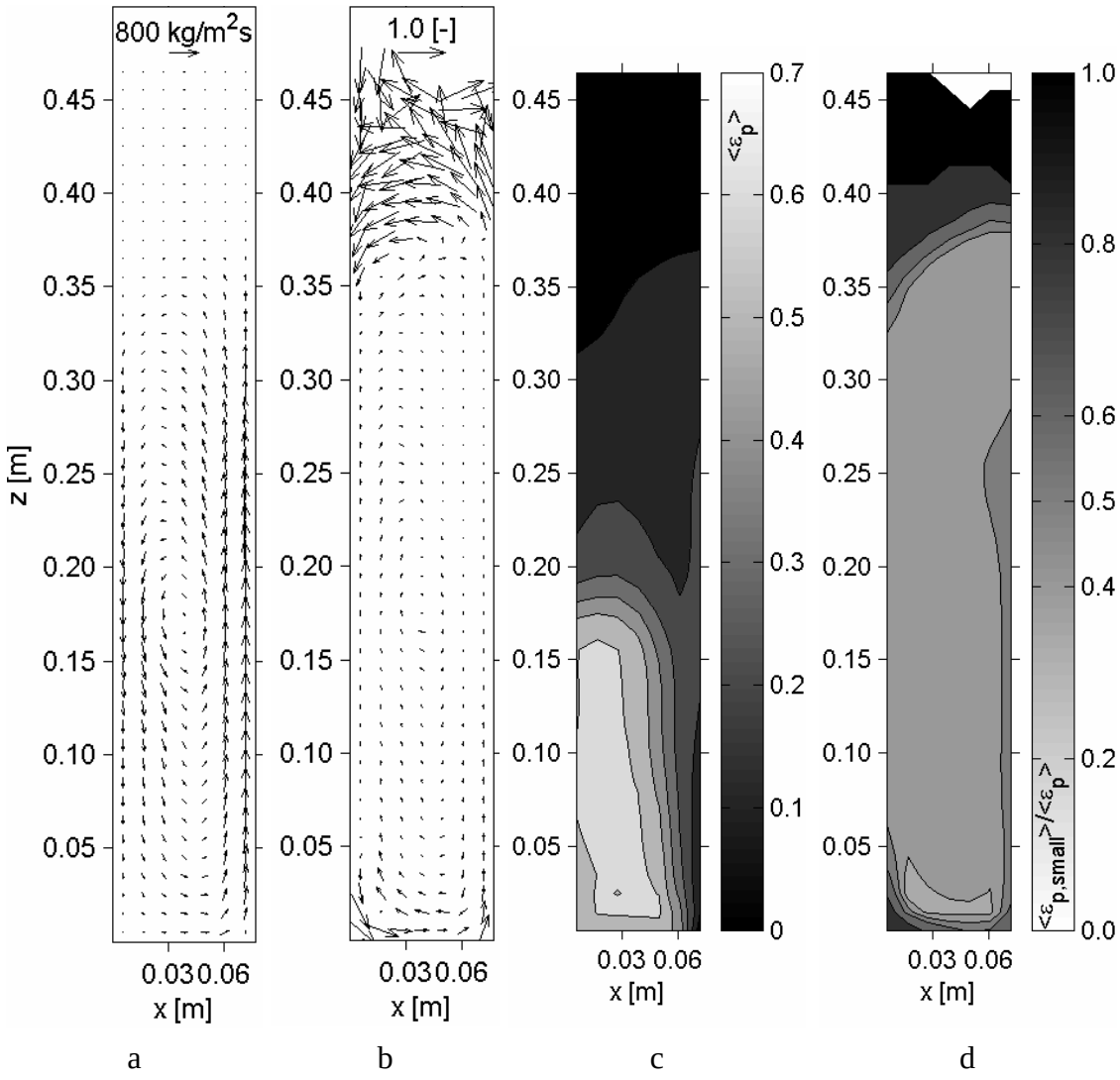

Figure 6.39 Time-averaged computed particle fluxes and concentrations in one half of the central xz-plane for case B4, the intermediate / spout-fluidization regime (bi-disperse), a) particle flux field b) $\left\langle \mathbf{\Phi}_{diff}^{rel} \right\rangle$ c) solids volume fraction d) concentration of small particles.

Figure 6.39 shows that the small particles reach higher up into the bed than the large ones, but the solids volume fraction in this region and consequently the solids flux are relatively small. The concentration of small particles in the bottom corner of the bed is large, which can be explained by the ability of the small particles to move into the void space between the large particles and the wall. Since the mean particle flux through this part of the bed is very small, the concentration of small particles in the stagnant parts of the bed is large. The small particles near the bottom of the annulus will eventually move into mouth of the spout channel. Consequently, the concentration of small particles in the lower part of the spout channel is also high. On

the other hand, the flux of the large particles in most of the annulus is slightly larger than that of the small particles.

Near the top part of the spout channel the time-averaged solids fraction increases. This is due to the periodic closing of the spout channel, which is typical for the spout-fluidization regime. The solids fraction in the annulus is very large, since no bubbles move through the annulus, which can be expected in the spout-fluidization regime.

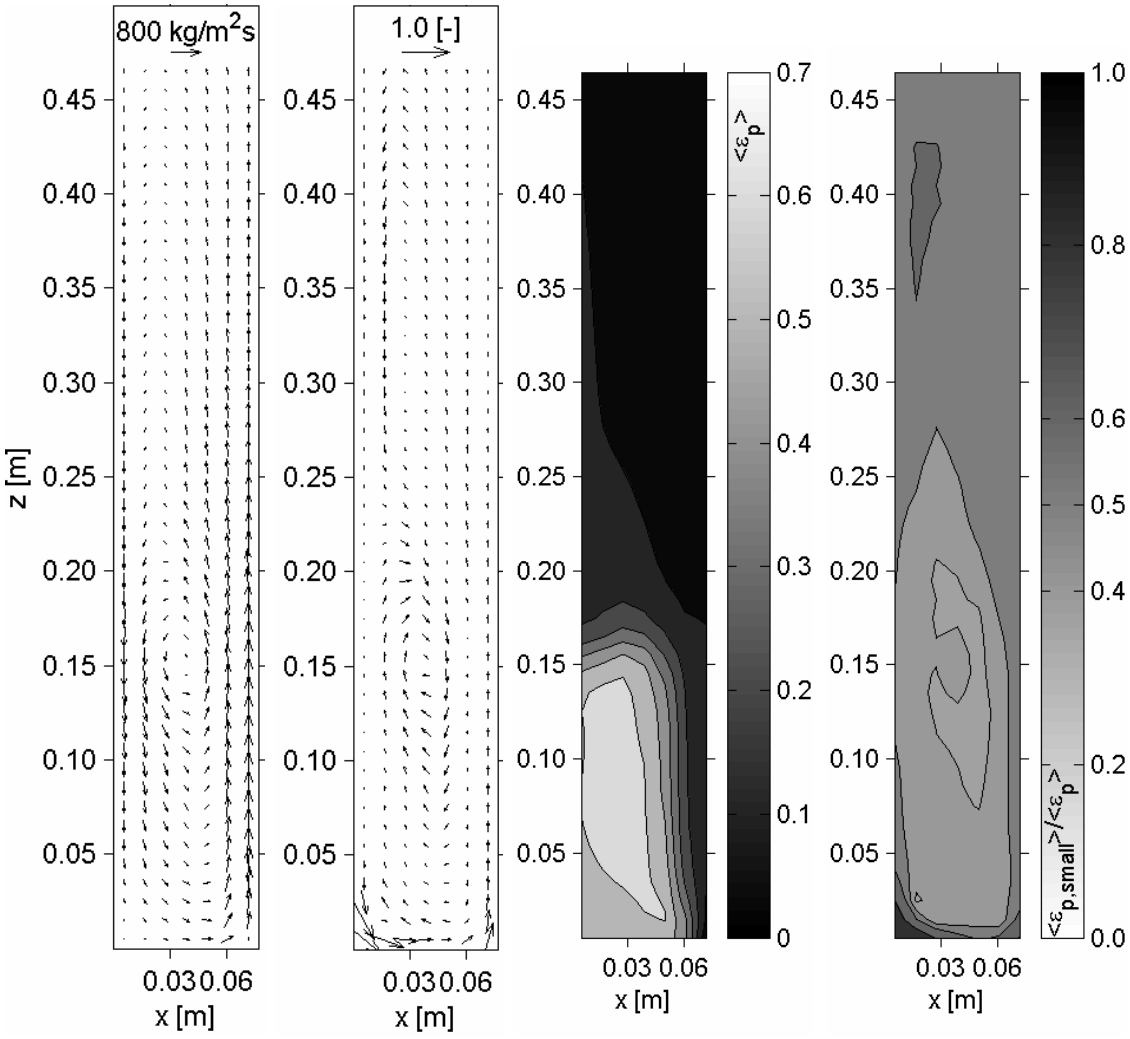

Figure 6.40 Time-averaged computed particle fluxes and concentrations in one half of the central xz-plane for case B5, the intermediate / spouting-with-aeration regime (bi-disperse), a) particle flux field b) $\left\langle \mathbf{\Phi}_{diff}^{rel} \right\rangle$ c) solids volume fraction d) concentration of small particles.

Figure 6.40 shows that a modest flux of both types of particles reaches high up into the bed, although the concentration of small particles is slightly larger in this part of the bed.

Furthermore, the flux of large particles in most of the annulus is larger than the flux of small particles. This effect is most profound close to the point around which the particles appear to circulate. The concentration of large particles around this point is relatively high, because the large particles from the spout channel decelerate more rapidly in the fountain region. This is caused by the decreasing solids volume fraction, which reduces the drag force acting on the large particles to a larger extent than that on the small particles, resulting in a faster deceleration of the large particles. The low solids volume fraction will also reduce the number of collisions between particles of both sizes, which reduces the momentum transfer rate from the small particles to the large particles in the spout channel. The difference in the deceleration is partially compensated for by the higher inertia of the large particles. Because of their enhanced deceleration, the large particles remain closer to the spout channel. These particles will subsequently enter the spout channel at a larger height and will consequently be accelerated to a lesser extent, which will keep them close to the spout channel in the fountain region.
The flux of small particles in the fountain region of the bed, close to the bottom of the bed and in the spout channel, is larger than that of the larger particles, which is predominantly due to the relatively high concentration of small particles in these areas.
The whole spout channel displays a low solids fraction, which is to be expected in the spouting-with-aeration regime. The solids volume fraction rapidly increases towards the annulus. The high solids volume fraction in the annulus is in agreement with the absence of bubble formation in the annulus.

Figure 6.41 shows that for case B6, similar to case B5, a modest flux of both types of particles reaches high up into the bed, although the concentration of small particles is slightly larger in that part of the bed.
Furthermore, the flux of large particles in most of the annulus is larger than that of the small particles. This effect is most profound close to the point around which the particles appear to circulate. In the vicinity of this point the concentration of large particles is somewhat higher.
The flux of small particles is however larger in the fountain region of the bed, close to the bottom of the bed and in the spout channel, which is predominantly due to the high concentration of small particles.
The solids volume fraction is low in the entire spout channel and in the lower part of the annulus it is lower compared to case B4, the intermediate / spout-fluidization regime (bi-disperse), and B5, the intermediate / spouting-with-aeration regime (bi-disperse), which is caused by the bubbles that are present in the bottom part of the annulus (see Figure 6.28).

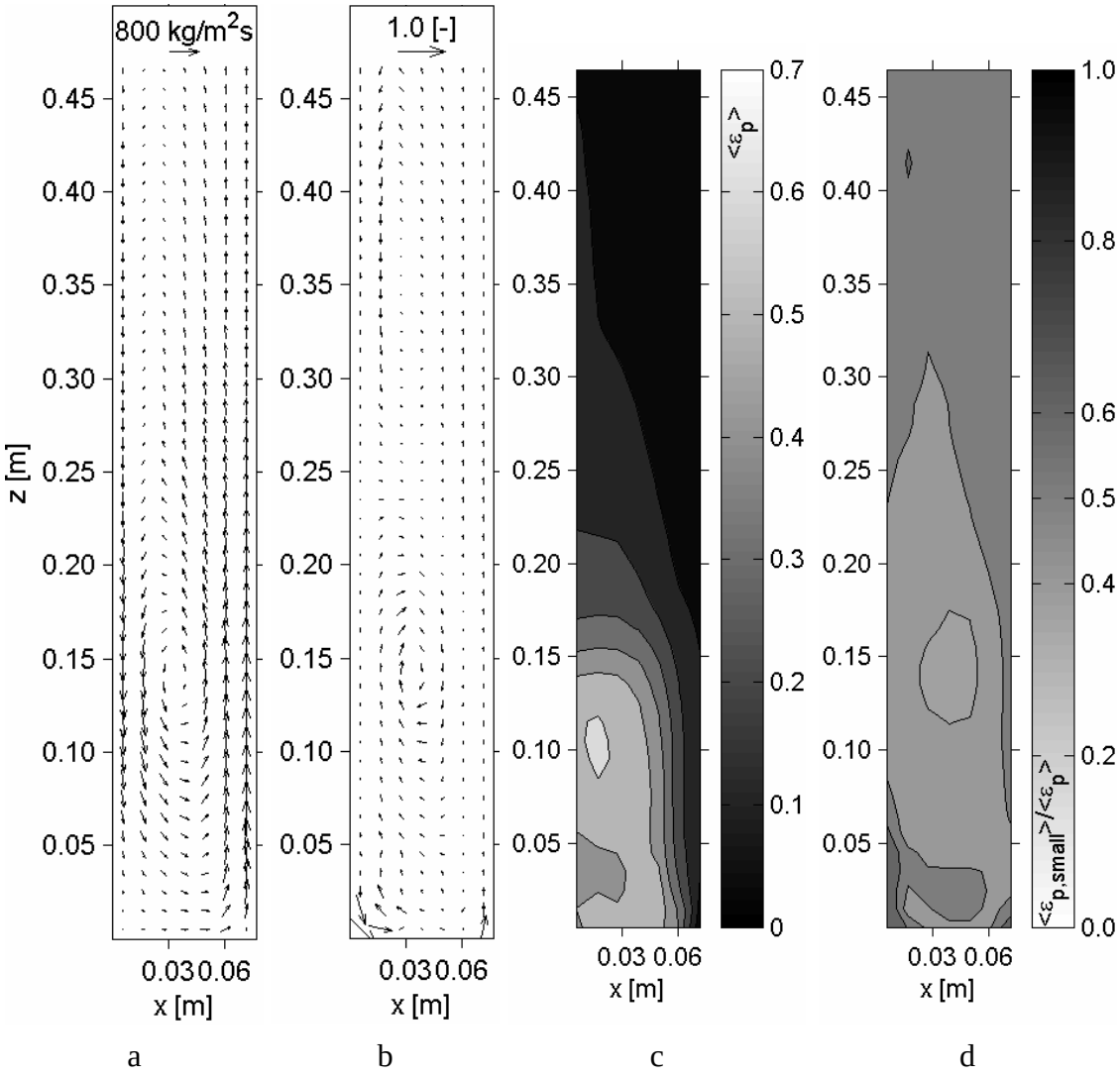

Figure 6.41 Time-averaged computed particle fluxes and concentrations in one half of the central xz-plane for case B6, the jet-in-fluidized-bed regime (bi-disperse), a) particle flux field b) $\left\langle \mathbf{\Phi}_{diff}^{rel} \right\rangle$ c) solids volume fraction d) concentration of small particles.

Figure 6.42 shows that the differences in the fluxes and concentrations of the large and small particles are very small for case B7 compared to the other cases.
The solids volume fraction in the spout channel is higher compared to the other cases. In this case the width of the spout channel increases with height indicating that bubbles are formed near the bottom of the bed, which increase in size and move through the centre of the bed (see Figure 6.30). Consequently the particle behavior approaches the behavior of a regular bubbling bed.

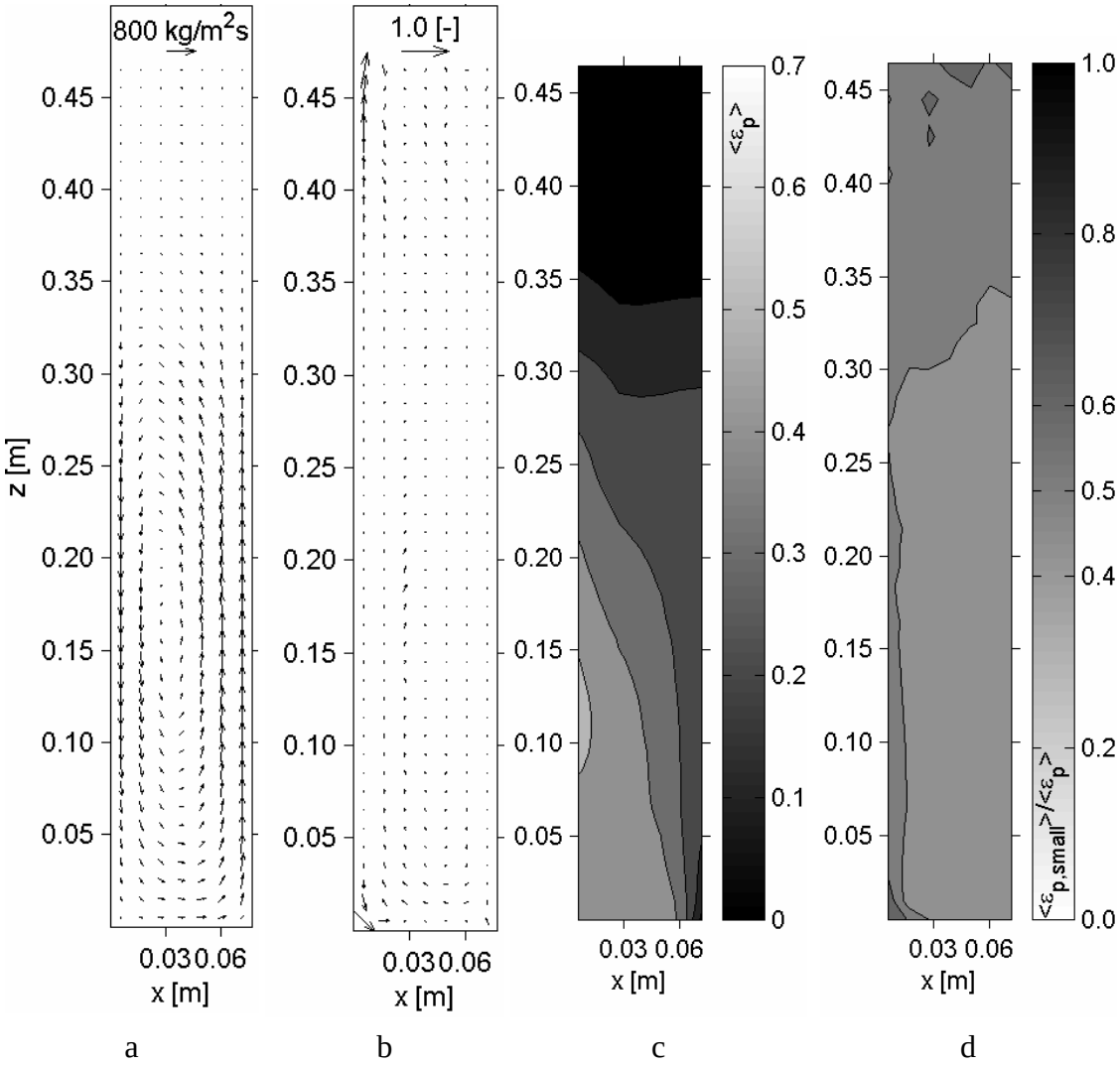

Figure 6.42 Time-averaged computed particle fluxes and concentrations in one half of the central xz-plane for case B7, the jet-in-fluidized-bed regime (bi-disperse), a) particle flux field b) $\left\langle \mathbf{\Phi}_{diff}^{rel} \right\rangle$ c) solids volume fraction d) concentration of small particles.

6.6 Particle circulation time

The particle circulation time is defined as the amount of time a particle requires to move from the bottom of the bed, up the spout, and back down through the annulus towards the bottom. The particle circulation times were determined using the method described in section 2.5.1. In this section the reproducibility of the particle circulation time distribution measurements will be studied first. Subsequently the particle circulation time distributions of large particles in a binary mixture will be compared with those of the small particles in the mixture. Finally the particle circulation time distributions of different flow regimes will be compared.

The particle circulation time distribution is prepared on a logarithmic horizontal axis, which is divided in a range of particle circulation times with equal width on that axis. On the vertical axis the fraction of time the particle spends in each range of particle circulation times is plotted. This was done to emphasize the importance of large particle circulation times, which would have been diminished in a regular histogram.
It was not attempted to obtain the particle circulation time distribution from the simulation results, since the simulations only produce results for a relatively short time interval (20 s), which will significantly affect the probability of longer particle circulation times.

Figure 6.43 shows the particle circulation time distribution of case B1, which is in the intermediate / spout-fluidization regime of the 3D-spout-fluid bed containing large particles. The distribution is approximately symmetric around a peak value that is observed at a particle circulation time of approximately 3 s, although a small tail towards larger particle circulation times can be observed. The tail is caused by a small number of cycles which require considerably more time. During these cycles the particle passes through the virtually stagnant lower corner of the bed, which only happens occasionally. Consequently, the statistics for the larger particle circulation time (> 10 s) are based on very few particles. The figure also shows that the reproducibility of the results is rather good, which was also found for the other cases.

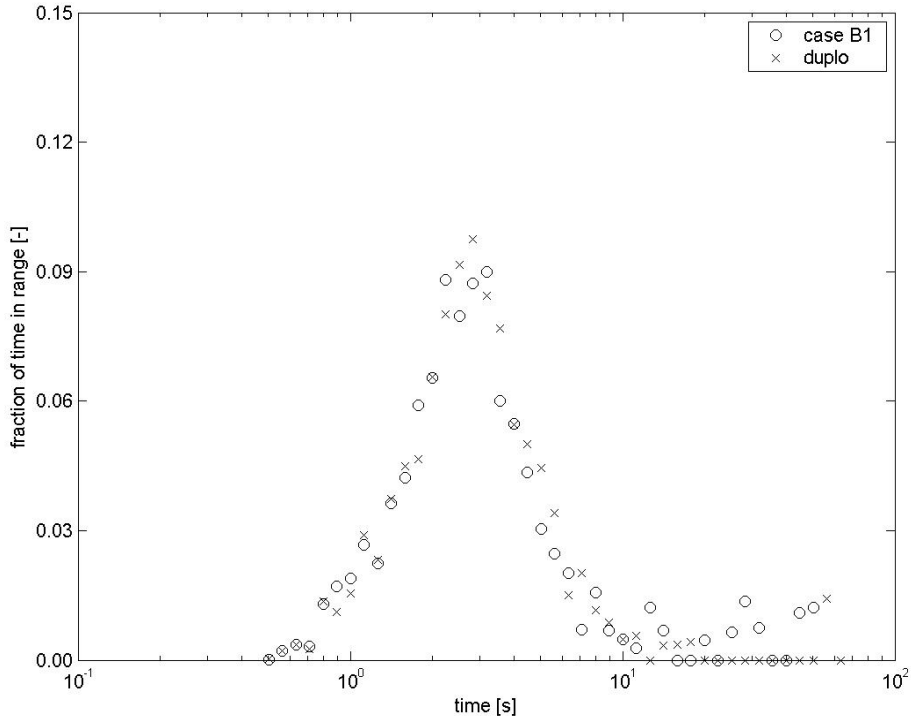

Figure 6.43 Measured particle circulation time distribution for case B1, the intermediate / spout-fluidization regime (mono-disperse).

Figures 6.44, 6.45 and 6.46 reveal that the behavior of particles with different sizes within a mixture appears to be very similar. The most noticeable differences are that the peak is higher for large particles and that the small particles are more likely to display larger particle circulation times. This is in agreement with the simulations results presented in section 6.5, which revealed that the concentration of small particles is higher in the more stagnant parts of the bed. Consequently, small particles are more likely to pass through these areas and therefore longer particle circulation times are more frequent.

It is noted that the number of spurious cycles (~ 10%) was much larger for case B7, the jet-in-fluidized-bed regime (bi-disperse), as compared to the other cases. This implies that the particles do not only move along the previously defined cycles, but also like particles in a regular bubbling bed.

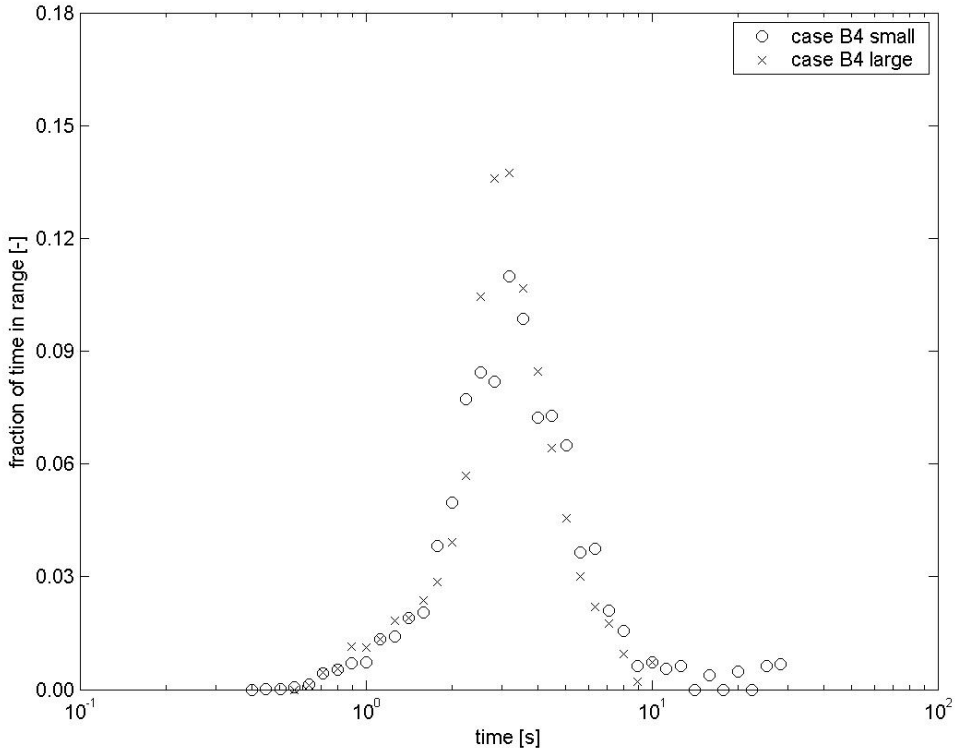

Figure 6.44 Measured particle circulation time distribution for case B4, the intermediate / spout-fluidization regime (bi-disperse).

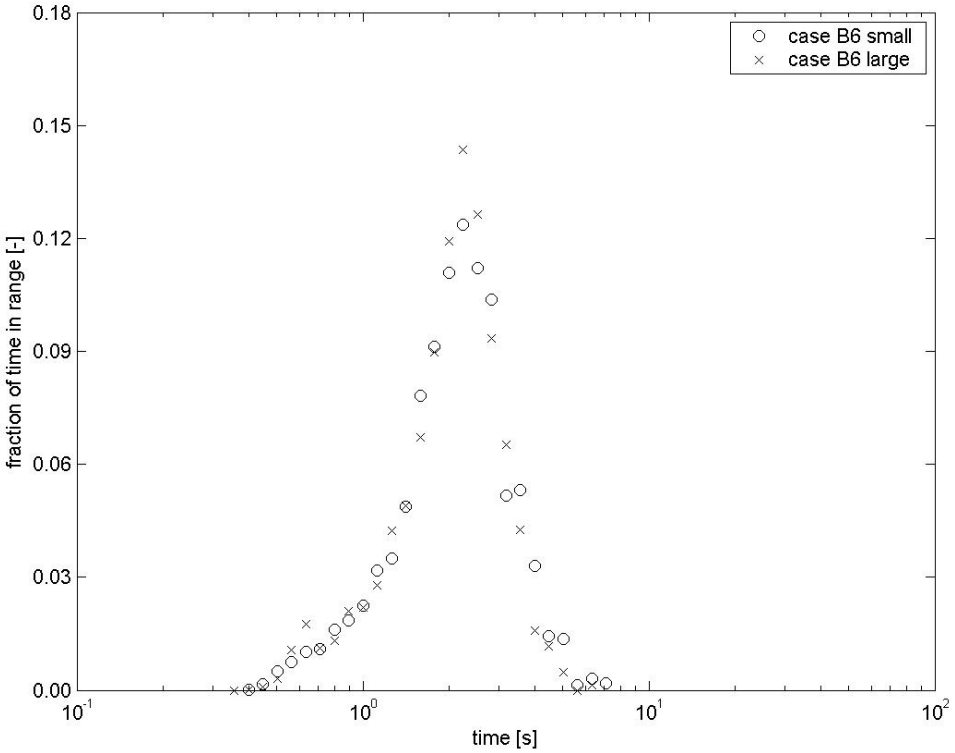

Figure 6.45 Measured particle circulation time distribution for case B6, the jet-in-fluidized-bed regime (bi-disperse).

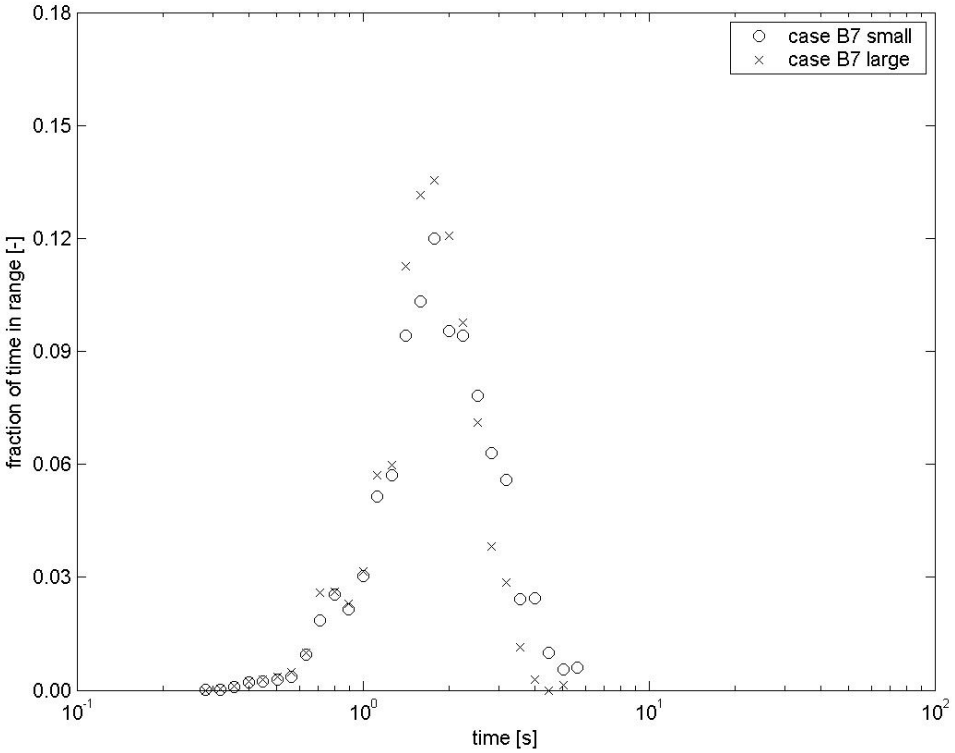

Figure 6.46 Measured particle circulation time distribution for case B7, the jet-in-fluidized-bed regime (bi-disperse).

Figures 6.47 and 6.48 show that the particle circulation time distributions differ between the flow regimes. For the mono-disperse size distribution shown in Figure 6.47, the jet-in-fluidized-bed regime (case B3) shows a relatively narrow particle circulation time distribution and a relatively low average particle circulation time.

The width of the peak is a measure for the spread in the particle circulation times. Particle circulation is important in processes, which predominantly take place in specific parts of the bed, like particle growth in a granulator. When all particles enter this part of the bed at approximately the same time intervals, which corresponds with a narrow particle circulation time distribution, the number of opportunities for growth is approximately the same for each particle. This will result in a narrow particle size distribution (PSD) provided that the amount of growth per circulation does not depend on the duration of the circulation.

A short particle circulation time means there will be more circulations in a fixed period of time, and less growth per circulation when the spraying rate is the same. This will result in a narrower PSD.

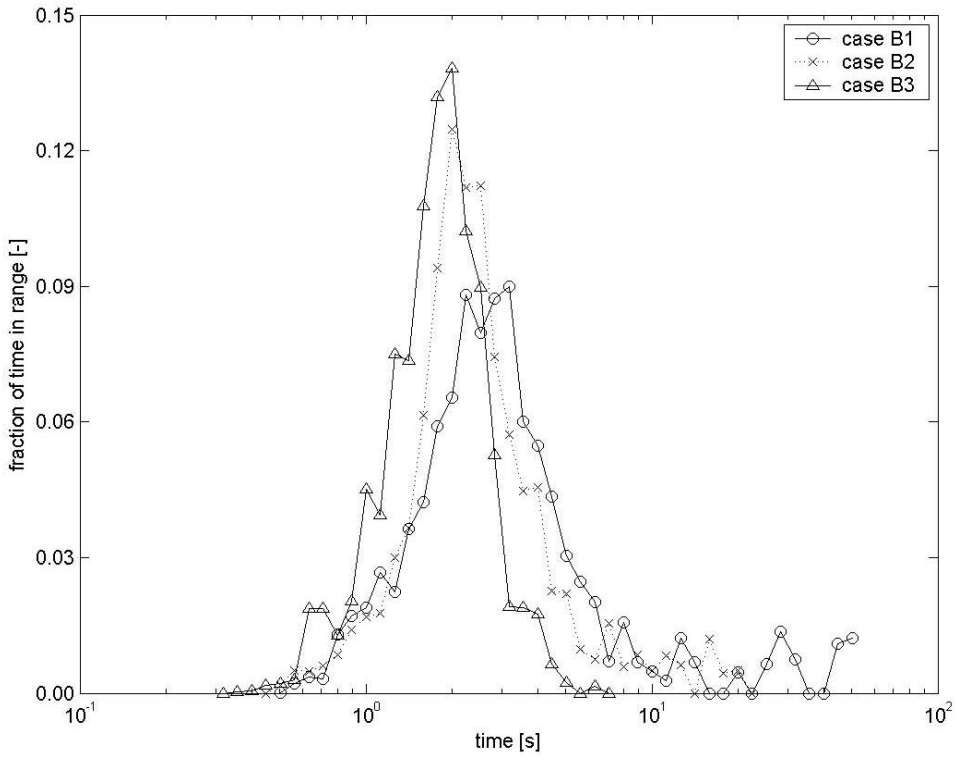

Figure 6.47 Measured particle circulation time distribution for all cases with a mono-disperse size distribution.

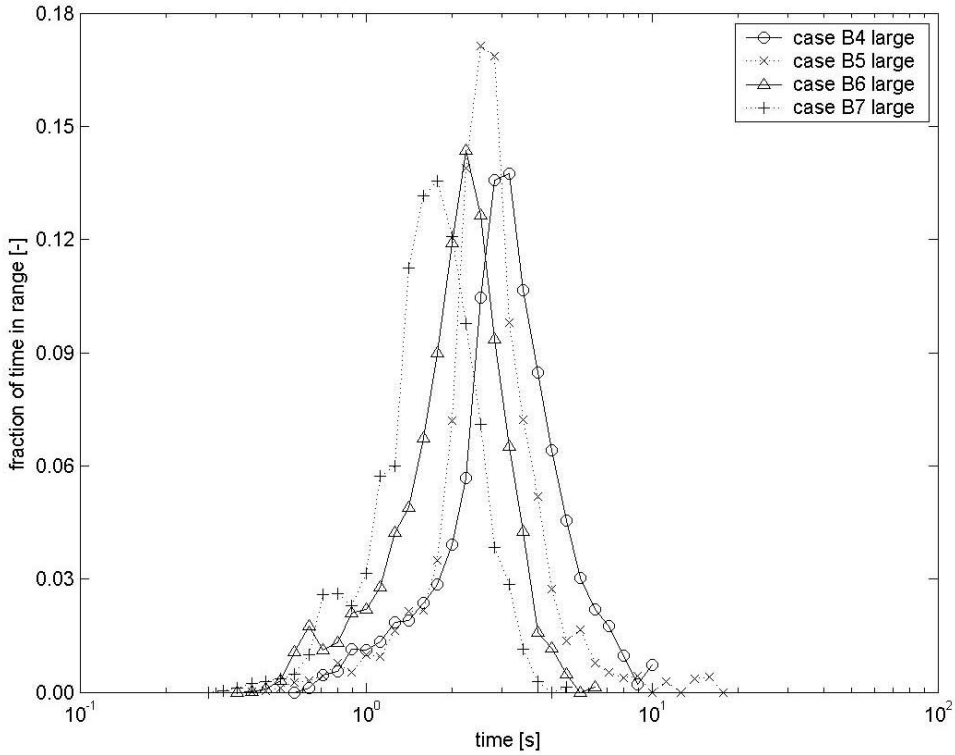

Figure 6.48 Measured particle circulation time distribution for all cases with a binary size distribution.

The particle circulation time distribution of case B2, the spouting-with-aeration regime (mono-disperse), is approximately as narrow as the jet-in-fluidized-bed regime, but this flow regime displays a larger average particle circulation time and a tail towards larger particle circulation times.

A tail towards larger particle circulation times indicates that the number of growth opportunities differs significantly between the particles. The size of the particles in the tail will differ significantly from the average particle size, which will result in a wider PSD and more particles that are off-spec.

Case B1, the intermediate / spout-fluidization regime (mono-disperse), shows a wider particle circulation time distribution around a high average particle circulation time with a long tail towards larger particle circulation times.

The particle circulation time distributions show that (the variation in) the number of growth opportunities differs significantly between the regimes. Case B3, the jet-in-fluidized-bed regime (mono-disperse), produces the most growth opportunities with little variation between the particles and is therefore most likely to result in a narrow PSD. Besides growth opportunities, there will be other factors influencing the actual growth, which will need to be assessed.

The results of the cases with a binary particle size distribution in Figure 6.48 (case B4, B5, B6 and B7) resemble those of the cases with a single particle size. The multi-frequency mode of the jet-in-fluidized-bed regime (bi-disperse, case B7) shows a narrow particle circulation time distribution around a low average particle circulation time. The single-frequency mode of the jet-in-fluidized-bed regime (bi-disperse, case B6) shows a less narrow particle circulation time distribution around a slightly higher average particle circulation time. The particle circulation time distribution of case B5, the intermediate / spouting-with-aeration regime (bi-disperse), is about as narrow as case B7, but this flow regime displays a larger average particle circulation time and a tail towards larger particle circulation times. Case B4, the intermediate / spout-fluidization regime (bi-disperse), shows a wider particle circulation time distribution around a high average particle circulation time with a short tail towards larger particle circulation times.
The particle circulation time distributions show the same trends as in the mono-disperse cases. Figures 6.44, 6.45 and 6.46 show that the small particles are more likely to display large particle circulation times than the large particles. This means that some particles that are already small also have fewer opportunities for growth, which will result in an even wider PSD. The multi-frequency mode of the jet-in-fluidized-bed regime (bi-disperse, case B7) produces most growth opportunities with little variation between the particles and is therefore most likely to result in a narrow PSD. It is however noted that the number of spurious cycles was high for this case.

For each of the cases not only the flow regime differs, but also the superficial gas velocity is different. Comparison of the particle circulation time distributions for different superficial gas velocities shows that with an increase of the superficial gas velocity the average particle circulation time is reduced. The only exception is case B7, the jet-in-fluidized-bed regime (bi-disperse), but this case displayed a lot of spurious cycles, which negatively affects the reliability of this particle circulation time distribution. The tail towards longer particle circulation times is generally longer for smaller background velocities, which can be explained by the presence of stagnant areas which are likely to be the cause of these tails.

6.7 Conclusions

In this chapter, the capability of the DPM was assessed to reproduce several of the important flow regimes observed in a 3D spout-fluid bed. For most of the cases, the model successfully predicted the flow regime, although some (small) differences with the experimental results were observed. In most cases, the frequency, at which the largest power is found, is overpredicted by the model. Furthermore, the fluctuations

predicted by the model are generally more regular than the measured fluctuations. Contrary to the experimental observations, the DPM did not predict any large slugs in the slugging-bed regime.
The remaining differences between the computed and experimentally observed bed behavior is most likely related to the representation of the effective fluid-particle interaction in the DPM, which relies on a homogeneous distribution of the particles on the length scale that is used to calculate the fluid-particle drag. The effect of heterogeneity on the fluid-particle interaction, which arises for example around gas bubbles, should be investigated. Lattice Boltzmann simulations would be well suited for this purpose.

The particle velocities for both mono-disperse and bi-disperse systems were investigated with the use of the model and positron emission particle tracking (PEPT). The computed results were compared with velocity maps determined from particle trajectories acquired using PEPT.
The DPM accurately reproduces measured time-averaged particle velocities for all investigated conditions and is therefore able to capture the details of the particle flow in various flow regimes. Surface plots of the particle velocity in the z-direction in a cross-section of the column do however show that the width of the spout channel, i.e. the region where upward particle velocities are encountered, is smaller in the experiments. At the border between the spout channel and the annulus, the same type of heterogeneity in the solids volume fraction is present that was already described in the discussion of the results for the pressure drop fluctuations. This supports the recommendation to study the effect of heterogeneity on the fluid-particle drag in more detail.
The computed root mean square of the particle velocity was in reasonable agreement with the measured values, especially when the various disturbances present in the experiments are taken into account.
The root mean square of the particle velocities in the vertical direction is about twice as large as that in the horizontal direction.
In the bi-disperse system the time-averaged particle velocities of the small and large particles were virtually identical in both the simulations and the experiments, despite the fact that the net force on, and consequently the acceleration of, the small particles is relatively larger. The excess velocity of the small particles is presumably transferred to the large particles through collisions. The computed root mean square was generally larger for the small particles, which was not as clearly observed in the experiments. This is probably related to the post-processing method of the experimental results.

The vertical particle flux through a plane showed that the 3D geometry that was used in this study does not display distinct 3D behavior. In the jet-in-fluidized-bed regime, the particle flux was virtually independent of position in the y-direction.
The DPM results for a mixture of large and small particles revealed that the flux of large particles is larger in the lower 0.25 m of the bed, but smaller higher up in the bed. The concentration of small particles is high in the corner of the walls and near the bottom plate, but low next to the spout at about 0.15 m above the bottom plate. Most differences in the particle concentrations disappeared at higher background velocities.

The experimental study of the particle circulation time distribution revealed that small particles are more likely to display long particle circulation times than large particles, which is in agreement with the high concentration of small particles in the stagnant corners of the bed that was observed with the DPM. The particle circulation time is reduced when the superficial gas velocity increases, whereas more outliers towards larger particle circulation times are obtained when the background velocity approaches the minimum fluidization velocity.
The jet-in-fluidized-bed regime displays the highest number of particle circulations within a fixed period of time and shows the most narrow particle circulation time distribution. Therefore this regime will probably provide the most (homogeneously distributed) growth opportunities in a granulator. To determine whether this regime is most suitable for granulation, the other factors influencing the growth in a granulator will need to be assessed, which is the subject of the next chapter.

Overall the model predicts the correct dynamics and quantitative particle velocities in a spout-fluid bed. There is however still room for improvement, especially regarding the treatment of the drag force at the boundary between dense and dilute areas around bubbles. Nevertheless, these results confirm the suitability of the DPM to study processes involving spout-fluid beds. That enables detailed studies of systems, which are difficult if not impossible to study experimentally, like the growth rate of each individual particle as a function of its location in a spout-fluid bed granulator.

Chapter 7

Numerical study of granulation using the DPM

Abstract

In this chapter an extension to the discrete particle model is presented, which facilitates the description of the gas-liquid-solid flow in a spout-fluid bed, including all relevant phenomena for the study of granulation.
The model is demonstrated for the case of a granulation process in a flat spout-fluid bed, containing four different initial particle size distributions. For each of the cases it was found that particle growth increases the mean of the particle size distribution, without affecting its standard deviation.

The amount of growth differs significantly for each individual particle and depends strongly on the position of the particle with respect to the spout mouth. Particle growth rapidly decreases with increasing distance from the spout mouth.

It was found that the growth rate scales with the projected surface area of the particle. Two types of growth have been identified in the simulations, ‘peak growth’ and ‘constant growth’. Peak growth occurs when particles are exposed to droplets over their entire projected surface area. The growth rate for this type of growth is very large, while the period over which growth occurs is very short (< 4 ms), due to the short residence time of the particles in the peak growth region.
Constant growth occurs when only a small fraction of the particle surface is exposed to the droplets, either because of the location of the droplet beam or because other particles are blocking part of its surface. The growth rate for this type of growth is relatively small, but it can be maintained over a longer period than peak growth.
The majority of the growth is caused by constant growth due to the low solids fraction above the spout mouth, which is caused by the large drag forces exerted by the gas phase on the particles in this region.

The smaller particles within a mixture of differently sized particles are slightly more likely to display peak growth, which is due to the larger concentration of these particles near the spout mouth. In the remainder of the bed all particles display similar growth rates per projected surface area.

For the particle size distributions examined in this work, the ones with a larger average particle size display larger peak growth rates per projected surface area due to longer residence times near the spout mouth. This is probably caused by the higher particle inertia.

Most of this chapter is accepted for publication in Chemical Engineering Science as:

Link, J.M., Godlieb, W., Deen, N.G., and Kuipers, J.A.M., 2006. Discrete element study of granulation in a spout fluidized bed.

7.1 Introduction

A detailed experimental study of granulation in a spout-fluid bed is very difficult, because (non-intrusive) access the spout channel is limited. Therefore computational models provide a powerful alternative for laborious experimental studies. The ultimate objective of a modeling study is to consider an industrial system, but due to the enormous variation in the length and time scales, continuum models constitute the only feasible option for the simulation of large scale spout-fluid bed granulators. To increase the predictive capabilities of these models more detailed information needs to be obtained from more sophisticated "learning" models, like the discrete particle model (DPM), which was presented in chapter 3.
The objective of this chapter is to assess the ability of the discrete particle model to study particle growth and to subsequently gain insight in the growth mechanisms present in a spout-fluid bed.
In a spout-fluid bed the particle diameters and velocities in the granulation zone are large. This implies that granulation in a spout-fluid bed generally progresses through coating, which means that droplets are added to a single particle and that they do not serve as a binder. Consequently, agglomeration will not be taken into account.

In this chapter, a learning model to study the spout-fluid bed spray granulation process will be presented. This model is based on the discrete particle model (DPM) described in chapter 3. Since the DPM has proven to be very successful in predicting the hydrodynamics of a spout-fluid bed, the focus of this chapter will be on the incorporation of the additional phenomena relevant for the granulation process, i.e. the treatment of the droplets. Subsequently the cases that were studied and the results of these cases are presented and discussed.

7.2 Granulation model

The granulation model is similar to the DPM extended with the description of the droplet dynamics. Similarly to particles, the droplets are assumed to be spherical, they are represented as discrete elements and they are subjected to the same forces. The main differences between the particles and the droplets are that the droplets are much smaller, they do not exist permanently, i.e. they are introduced and subsequently absorbed or elutriated, and they are present in much greater numbers, $\sim 20 \cdot 10^6$ droplets ($\sim 10^6$/s) versus $\sim 50 \cdot 10^3$ particles.

To be able to handle the large number of droplets, a number of simplifying assumptions was made:

1. Since the droplets are relatively small, they are assumed to move at their terminal velocity with respect to the gas phase. Consequently, the terminal velocity of each droplet only needs to be calculated once and is approximated assuming Stokes flow, i.e.:

$$v_\infty = u_{z,f} - v_{z,d} = \frac{d_d^2 \left(\rho_d - \rho_f \right) g}{18 \mu_f} \tag{7.1}$$

2. Because of their small size compared to the size of the solid particles, the droplets are assumed not to influence the porosity. Furthermore, the drag force that the droplets exert on the gas phase, is not taken into account in the source term, $\mathbf{S}_p$;
3. Since the volume fraction of droplets is very low ($< 1.10^{-6}$), the droplets are assumed not to interact, i.e. collide, with each other;
4. Since the impact of an individual encounter between a droplet and a particle is small, these encounters are not calculated. Instead, droplets are periodically probed for overlap with a particle. To minimize the number of times that droplets move through particles, the droplets are not allowed to move over a distance larger than the radius of a particle during the "droplet time step";
5. The droplets are assumed to have zero angular velocity.

The mechanism for particle growth is assumed to solely consist of the one-by-one addition of droplets to the particles, which leads to the following assumptions:

1. When overlap is detected, the mass and momentum of the droplet are immediately added to the particle:

$$m_p^{'} = m_p + m_d \tag{7.2}$$

$$\mathbf{v}_p^{'} = \frac{\mathbf{v}_p m_p + \mathbf{v}_d m_d}{m_p^{'}} \tag{7.3}$$

2. and subsequently the droplet is removed from the system.
3. It is assumed that the angular velocity is unaffected by the particle-droplet interaction:

$$\boldsymbol{\omega}_p^{'} = \boldsymbol{\omega}_p \tag{7.4}$$

4. The resulting particle remains solid and spherical and the position of the particle is not altered:

$$\mathbf{r}_p^{'} = \mathbf{r}_p \tag{7.5}$$

5. The radius of the particle increases:

$$r_p^{'} = \left(r_p^3 + r_d^3 \right)^{1/3} \tag{7.6}$$

6. When the particle growth causes overlap with another particle, particle growth is postponed until it does not result in overlap. In practice, this is rarely necessary, since the solids fraction in the region, where most of the growth takes place, is rather low.
7. Particles always collide with other particles, i.e. no agglomeration is assumed.
8. Droplets that hit the top boundary of the bed are removed from the system. Note that by definition droplets cannot hit other boundaries, since they follow the motion of the gas phase.

Table 7.1 summarizes the adopted interaction rules between droplets, particles and walls.

Droplets are introduced below the base of the spout channel, i.e. in the bottom cells through which the spout gas is introduced. The droplet velocity is related to the gas velocity and is consequently virtually constant. A continuous and homogeneous introduction of droplets can therefore be achieved by randomly distributing new droplets in all directions over the top portion of the cell, which is done at the beginning of each time step.

	Particle	**Droplet**	**Top wall**	**Other walls**
Particle	Collision	Coalescence	Collision	Collision
Droplet	Coalescence	Nothing	Droplet removed	Not applicable

Table 7.1 Overview of the adopted interaction rules between droplets, particles and walls.

7.3 Test cases

The objective of the simulations is to gain insight in the granulation process that occurs in a spout-fluid bed. In order to demonstrate the capabilities of the model within reasonable constraints for the required computational time, the simulation settings were chosen such that the total number of particles in the system is limited. To minimize computation time, a pseudo-2D configuration was selected to minimize the number of particles that is required. Furthermore, the hard sphere approach was used to model the collisions, since this approach is generally faster at high particle velocities. This approach is however not applicable to systems that display (local) defluidization. For this reason, glass particles were used in the simulation. These

particles have close to ideal collision properties, which are given in Table 7.2 and are based on the measured collision properties reported in chapter 5. Furthermore, the operating regime of a spout-fluid bed containing these particles can be predicted with a reasonable accuracy using the regime maps presented in chapter 4. This allows the selection of an operating regime, which displays no defluidization, even when the particles within the system grow to some extent.

Four cases, which are presented in Table 7.3 and Figure 7.1, with different particle size distributions (PSD's) were selected to study the spout-fluid bed granulation process. The total bed mass was the same for all cases, 1.36 kg, which corresponds to a stagnant bed height of approximately 0.23 m. A Gaussian particle size distribution was assumed for all cases:

$$P\left(d_p\right) = \frac{1}{\sigma\sqrt{2\pi}} e^{-\frac{\left(d_p-\mu\right)^2}{2\sigma^2}} \tag{7.7}$$

where μ represents the mean particle diameter and σ the standard deviation.
It needs to be noted here that the PSD's were obtained with a random number generator, which produced small deviations from a perfect Gaussian distribution due to the finite number of particles.

To mimic the different stages in the granulation process to some extent, three simulations were performed for PSD's with increasing mean particle diameter. The initial width of the particle size distribution was assumed to be unaffected by the granulation, i.e. σ was the same. The effect of the width of the particle size distribution was addressed by a simulation with twice the initial σ.

Property	**Value**	**Unit**
Material	Glass	-
ρ_p	2526	kg/m^3
$e_{n,\, p \leftrightarrow p}$	0.97	-
$e_{n,\, p \leftrightarrow w,\, glass}$	0.97	-
$\mu_{p \leftrightarrow p}$	0.10	-
$\mu_{p \leftrightarrow w,\, glass}$	0.10	-
$\beta_{0,\, p \leftrightarrow p}$	0.33	-
$\beta_{0,\, p \leftrightarrow w,\, glass}$	0.33	-

Table 7.2 Particle properties.

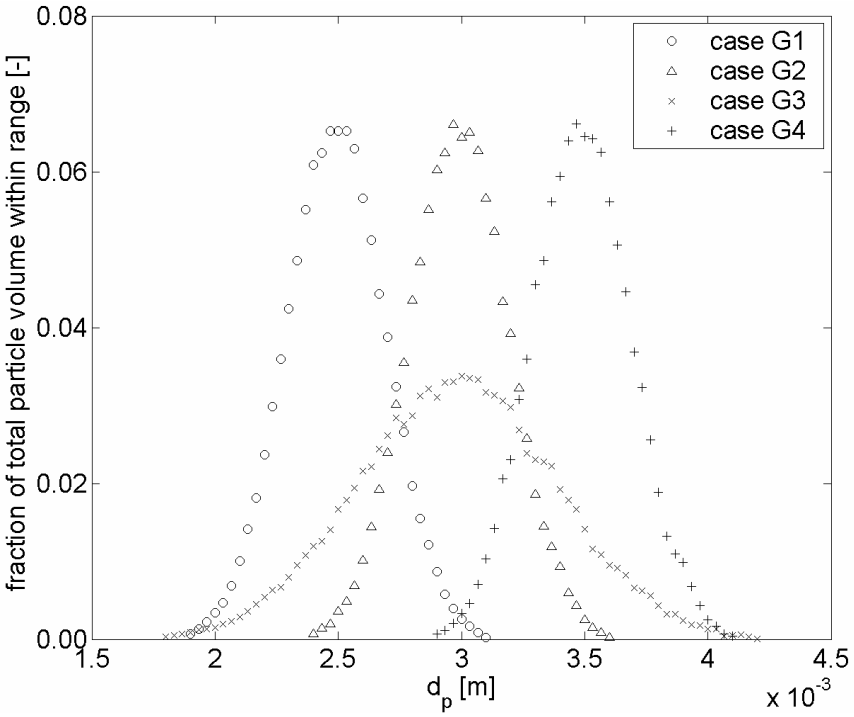

Figure 7.1 Initial particle size distribution for all cases.

Case	μ [mm]	σ [mm]	N_p	u_{mf} [m/s]
G1	2.5	0.2	$6.94 \cdot 10^4$	~1.34
G2	3.0	0.2	$3.97 \cdot 10^4$	~1.53
G3	3.0	0.4	$4.37 \cdot 10^4$	~1.53
G4	3.5	0.2	$2.48 \cdot 10^4$	~1.69

Table 7.3 Characteristics of the initial and final particle size distributions.

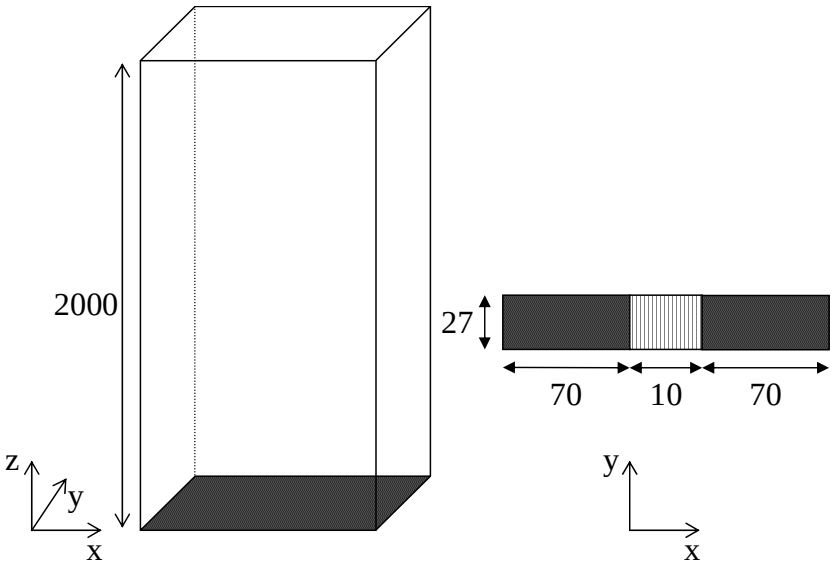

Figure 7.2 Schematic representation of the geometry of the pseudo-2D granulator, dimensions are given in mm.

Property	Value	Unit
N_X	30	-
N_Y	1	-
N_Z	240	-
t	20	s
Δt	$1.0 \cdot 10^{-4}$	s
u_{bg}	3.5	m/s
u_{sp}	40	m/s
d_{drop}	$2 \cdot 10^{-4}$	m
ρ_{drop}	2526	kg/m^3
Φ_{drop}	$2.2 \cdot 10^{-6}$	m^3/s
Δt_{drop}	$1.7 \cdot 10^{-5}$	s
v_∞	1.59	m/s
Mass loading ratio	0.082	-

Table 7.4 Numerical settings and droplet characteristics.

To avoid bridge formation between the back and front wall within the granulator, the depth of the system was chosen to be at least 6 times the diameter of the largest particles. The geometry of the bed is presented in Figure 7.2.
The characteristics of the droplets, e.g. flow rate and size, are chosen to approximate realistic conditions and are presented in Table 7.4 along with the numerical settings.

7.4 Results

During the simulations the radii of all particles and droplets along with their positions and velocities were recorded at a frequency of 250 Hz.
These results were used to determine the factors influencing the growth. First the resulting particle size distributions were studied, which can in principle also be obtained from experiments. Subsequently the simulation results were studied in more detail with special focus on the spatial distribution of the growth rates, which is far more difficult if not impossible to establish experimentally.

7.4.1 Resulting particle size distributions

Figure 7.3 shows how the particle size distributions (PSD's) change over a growing period of 20 s, while the properties of the distributions are presented in Table 7.5.
The mean particle diameter of the PSD increases slightly, but the shape of the PSD is hardly affected by the particle growth. The moderate changes in the PSD's are as expected, since the granulation period is relatively short. The standard deviation of the

PSD is virtually unaffected by the granulation in all cases, which suggests that the growth is uniformly distributed over all particle sizes. The increase in the mean particle diameter is however different for each case, but this is caused by the differences in the number of particles that were used.

The simulation results can be used to study the growth rate of each individual particle, and can therefore be used to check whether the growth is uniform for all particles as is suggested by the shift in the PSD. Figure 7.4 shows a scatter plot of the time-averaged growth rate for each individual particle for case G2 as a function of the particle diameter.
The results demonstrate that the growth rate is certainly not uniform. A small fraction of the particles (0.16%) does not grow at all and is therefore not represented in this figure. Furthermore, the growth rates differ up to three orders of magnitude.
The growth rate increases slightly with increasing particle diameter. This is in agreement with the observed uniform increase in particle diameter, see Figure 7.3, because the particle volume scales with d_p^3.

The enormous spread in the growth rates of individual particles suggests that improved understanding of the parameters influencing the growth process can provide means to influence the PSD. The influence of the following parameters on the growth rate will be assessed in more detail in the subsequent sections:

- Spatial position;
- Particle diameter;
- PSD.

Furthermore the time scale of the particle growth will be examined.

Case	**μ (t = 0s) [mm]**	**μ (t = 20s) [mm]**	**σ(t = 0s) [mm]**	**σ (t = 20s) [mm]**
G1	2.4424	2.5018	0.1991	0.1998
G2	2.9493	3.0209	0.1989	0.1981
G3	2.8123	2.8832	0.4034	0.4013
G4	3.4539	3.5374	0.1982	0.1985

Table 7.5 Mean and standard deviation of the particle size distribution before and after granulation for all cases.

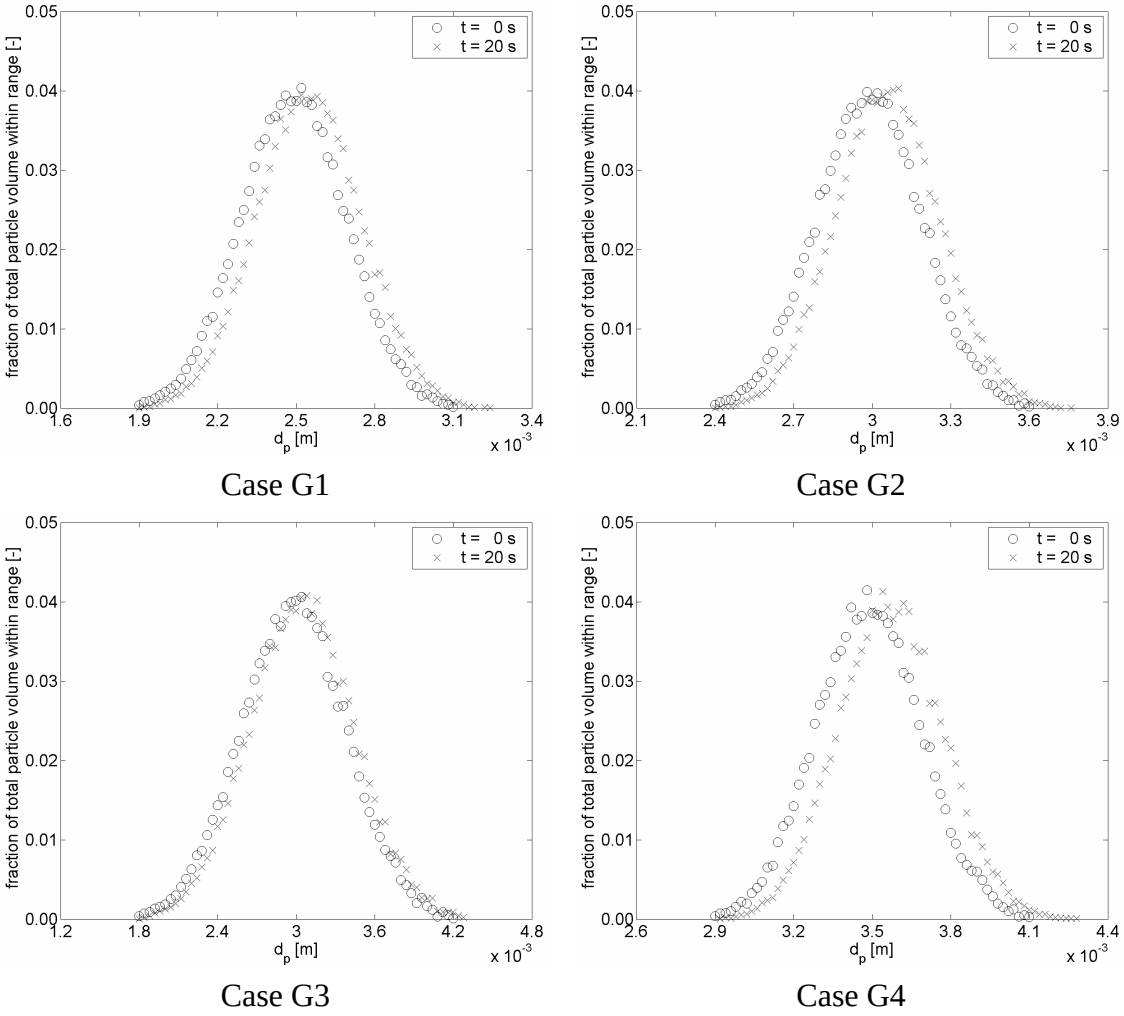

Figure 7.3 Particle size distribution before and after granulation for all cases.

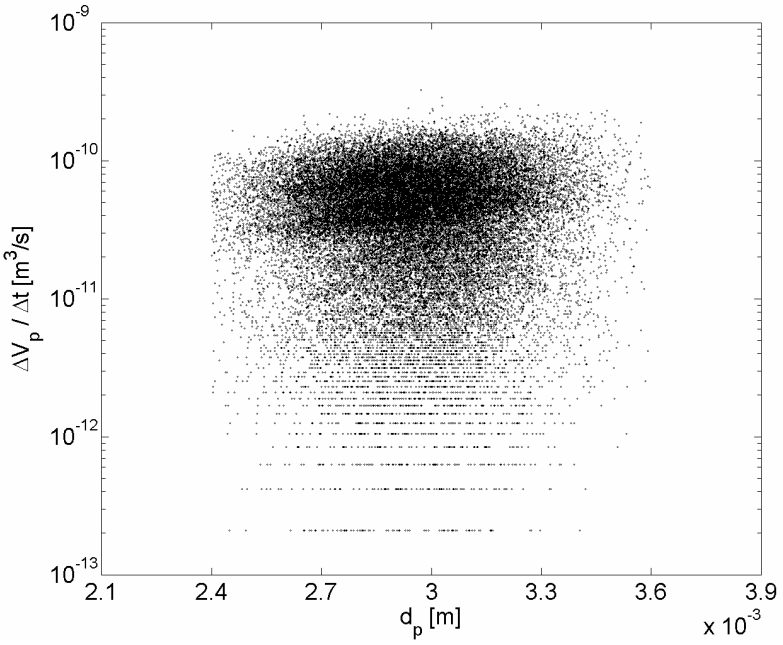

Figure 7.4 Average growth rate during a 20 s period versus particle diameter for case G2.

7.4.2 Influence of spatial position on the particle growth rate

In Figure 7.5, the location of the particle-droplet contact is presented in contour plots showing the cumulative fraction of droplets absorbed by the particles. To determine this quantity, the bed was divided into cells measuring 5 x 27 x 5 mm^3 (X x Y x Z). The number of droplets absorbed in each cell was determined by calculating the growth for each particle during a period of 4 ms (1 / 250 Hz) and subsequently assigning that growth to the cell, which contained the interpolated position of the particle. Finally, all cells were sorted based on the growth rate per cell, and the cumulative fraction of growth was determined by starting with the cell displaying most growth.

Figure 7.5 shows that most of the particle growth occurs in the region close to the spout mouth. For this reason, a close-up of this region is given in this figure as well. Since the presence of particles is required for growth, corresponding contour plots were also made for the solids fraction, which are given in Figure 7.6.

Figure 7.5 shows that half of the growth takes place in the first 0.03 m above the spout mouth. The solids fraction in this region is quite low ($\varepsilon_p < 0.2$). Consequently the growth can most likely be attributed to a relatively small number of particles with a high growth rate.

The differences between the cases are relatively small, and are mainly induced by differences in the meandering of the spout channel. Case G1, which contains the smallest particles, slightly differs from the other cases. The region where growth occurs is larger, especially higher up in the bed and next to the spout mouth, although the amount of growth within these regions is very small. The occurrence of growth next to the spout mouth appears to be related to the solids fraction, which is slightly lower in this region for case G1. This is probably related to the lower value of the minimum fluidization velocity for the mixture in case G1.

Particle growth requires the presence of both droplets and particles. Consequently, the growth rate will be affected by the concentration of both the droplets and the particles. Figure 7.7 shows the concentration of droplets as a function of the position in the vertical (z) direction for all cases, while Figure 7.8 shows the solids fraction in the spout channel for all cases.

Figure 7.7 shows that the concentration of droplets decreases with height. The rate at which the droplets disappear, and consequently the resulting magnitude of particle growth, varies with height. First, the droplet concentration is large, resulting in a large growth rate, thus decreasing the droplet concentration almost exponentially with height. Subsequently the rapid decrease of the droplet concentration is (partly) compensated by a rapid increase in the solids fraction in the spout channel, i.e. the area directly above the spout mouth, shown in Figure 7.8. This growth behavior

continues up to a height of approximately 0.05 m, where the solids fraction displays a maximum. When the solids fraction drops, the slope of the droplet concentration curve becomes less negative and stabilizes to some extent.

It is furthermore noted that the droplet concentration also decreases because the droplets are spread over a larger volume.

Some differences between the cases are observed, which most likely originate from the differences in the distribution of the solids over the bed, which is a result of the differences in the minimum fluidization velocity. Since the minimum fluidization velocity of case G4 is largest, the excess gas velocity is smallest, which results in the largest solids fraction.

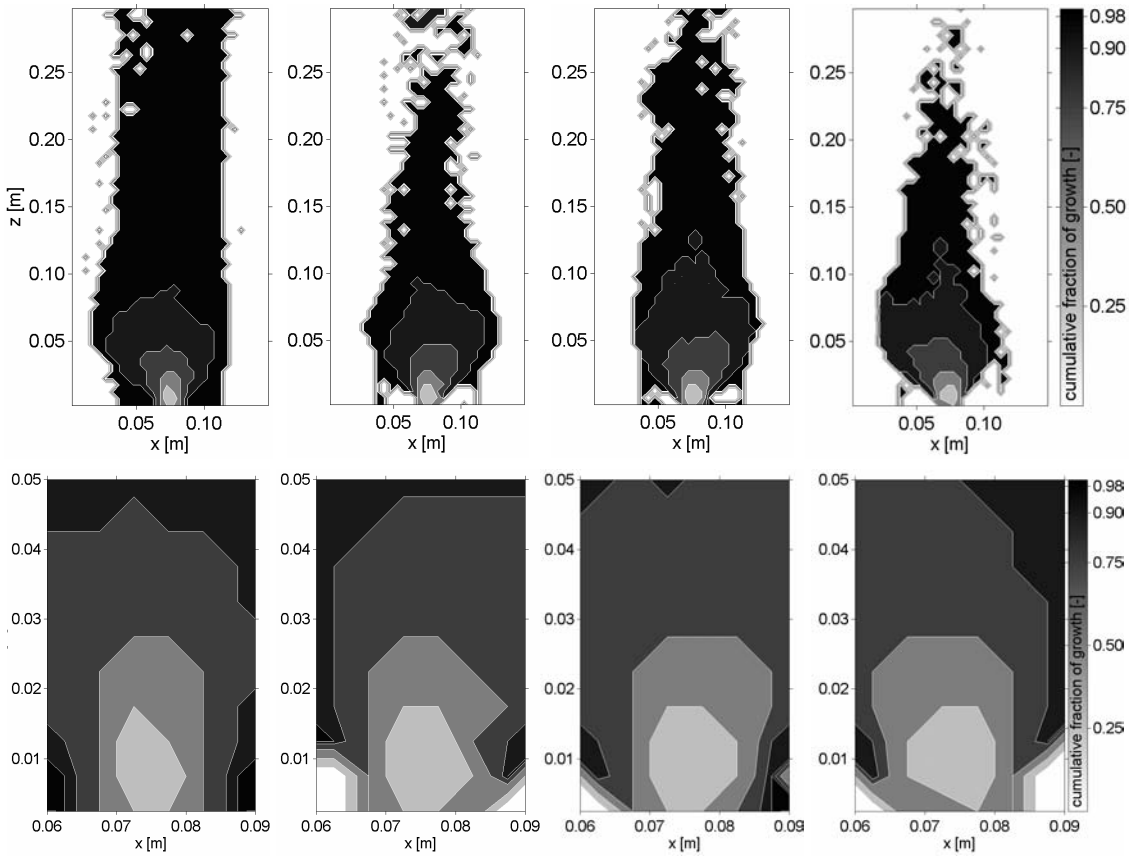

Figure 7.5 Contour plots of the cumulative fraction of growth for all cases.

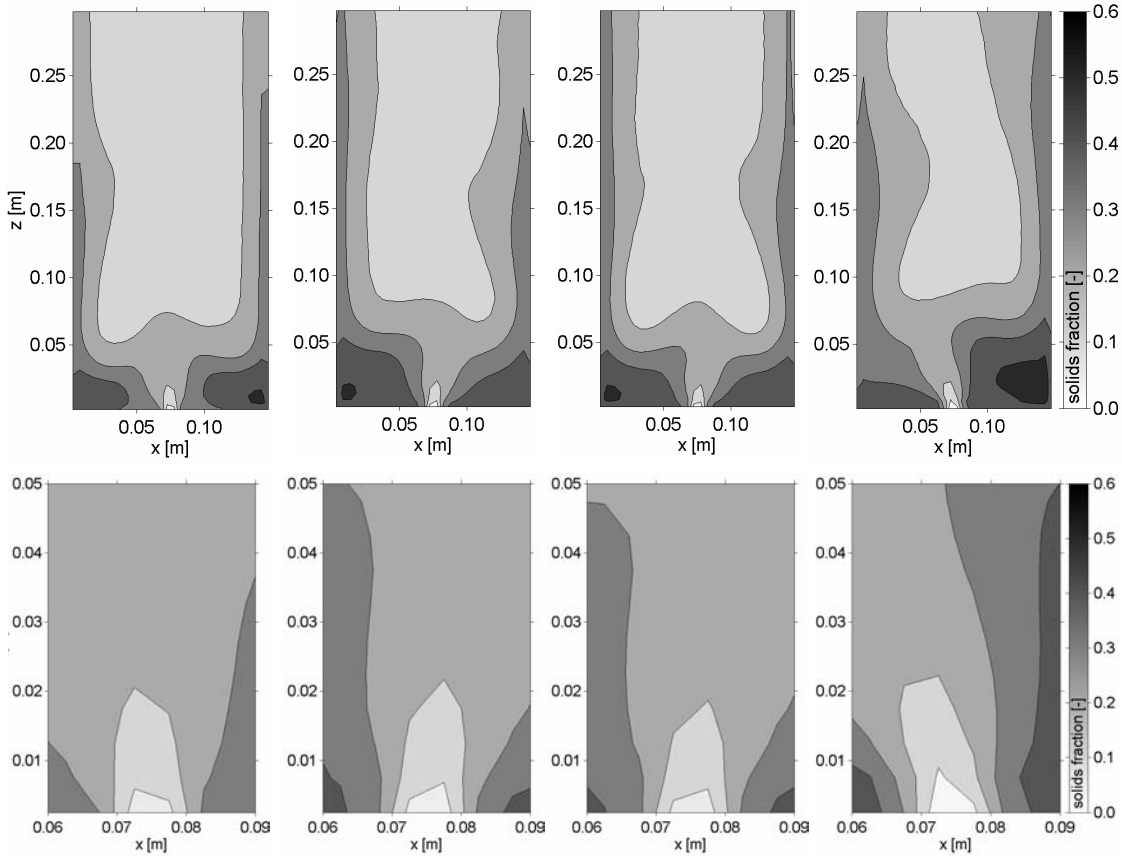

Figure 7.6 Contour plots of the solids fraction for all cases.

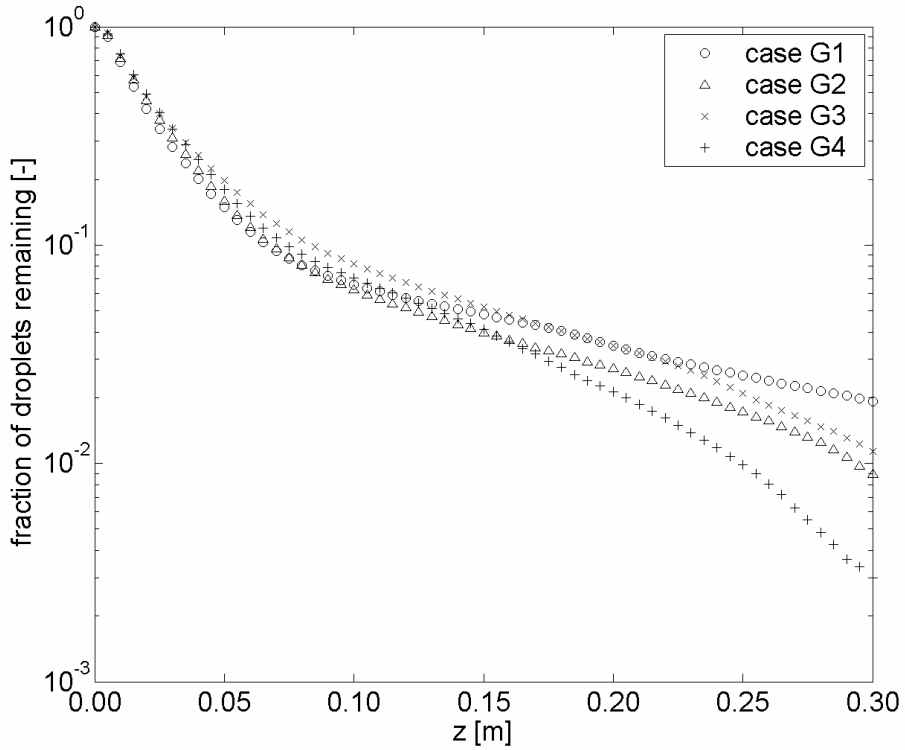

Figure 7.7 Fraction of droplets remaining as a function of the z-coordinate for all cases.

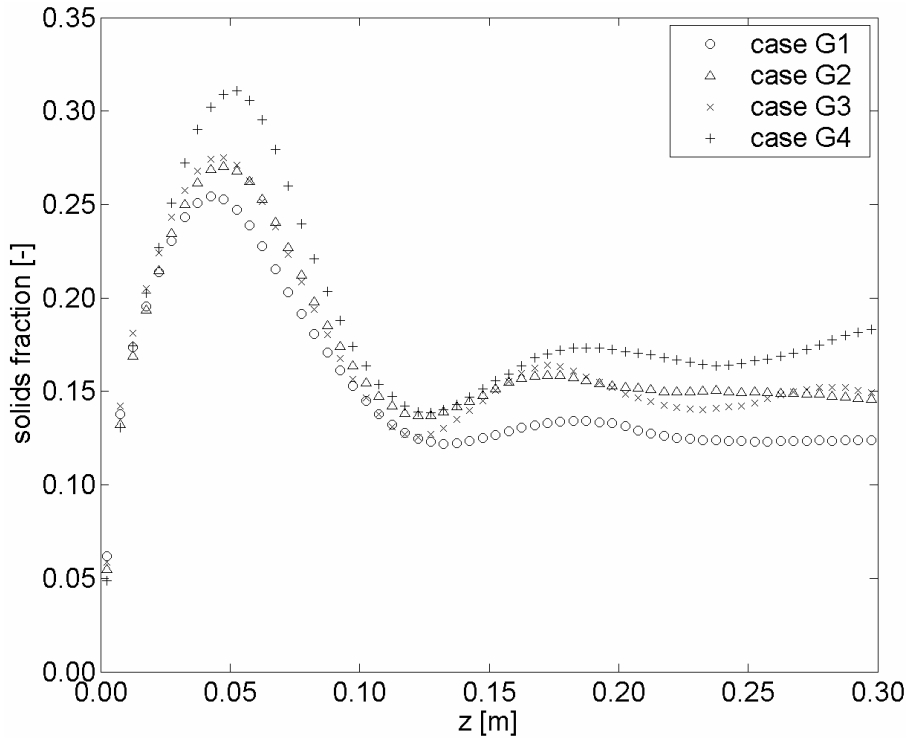

Figure 7.8 Solids volume fraction in the spout channel as a function of the z-coordinate for all cases.

7.4.3 Time scale of particle growth

To estimate the time scale for particle growth, the growth behavior of a single particle for the base case, case G2, is presented in Figure 7.9. Apart from the increase in particle volume as a function of time this figure also displays the position of the particle in the vertical (z) direction to emphasize that the particle position is of vital importance to the growth behavior.

The particle only grows substantially when it is very close to the spout mouth. The growth usually only requires a few time steps of 0.004 s, but due to the high growth rate the amount of growth during one pass through the growth zone can be substantial, e.g. ~2% in 0.028 s. After the particle leaves the growth area, it needs to travel back to the bottom of the bed before further growth can occur. Furthermore it can be observed that the particle does not always grow near the bottom of the bed.

Figure 7.9 illustrates that the time scale for particle growth is short. To determine whether the analysis period of 0.004 s is sufficiently short to capture the details of the growth process, the frequency at which each growth rate occurs was determined. Subsequently it was checked whether the frequency at which each growth rate can be observed is independent of the analysis period, which would indicate that the analysis period is sufficiently short. The results are plotted in Figure 7.10 and the results for

each period are the combined results of the number of periods that make up 20 s (e.g. the result for 0.02 s comprises 1000 periods).

Figure 7.10 shows that the results for a period of 0.004 s are the same as the results for a period of 0.008 s up to a growth rate of approximately 0.6 m^3/s. Most of the growth rates (~99%) are within that range. Therefore the analysis period is sufficiently short to study these growth rates in more detail. Since the results obtained using a period of 0.020 s differ from the results obtained with smaller periods, this period is not suitable to study the growth rates in more detail.

For larger growth rates (than 0.6 m^3/s), the growth rate observed for 0.004 s is approximately twice the growth rate observed for 0.008 s. This can only be the case, when the larger growth rates, which are only observed during a period of 0.004 s, are followed (and preceded) by a period of 0.004 s with negligible growth. Consequently, all larger growth rates are not observed for more than 0.004 s, which indicates that the growth period for larger growth rates is shorter than 0.004 s. Therefore the minimum analysis period (0.004 s) is probably too long to study these growth rates in more detail.

Note that the observed growth rates reach very large values: the highest growth rates cause a 10% volume increase during a period of 0.004 s. Furthermore, the close-up in Figure 7.10 shows that most particles display no growth at all, which is due to the small analysis period that is displayed in the figure.

Figure 7.10 showed that the minimum analysis period is too long to study growth rates larger than 0.6 m^3/s. On the other hand, this figure showed that these growth rates are rarely observed. To determine whether these growth rates are essential to understanding the growth process, the contribution of each growth rate to the total growth was determined and plotted in Figure 7.11 for the same periods that were used in Figure 7.10.

Figure 7.11 shows that the larger growth rates are only responsible for approximately 10% of the total growth. Therefore the minimum analysis period (0.004 s) is sufficiently short to study (most of) the growth process.

Furthermore, the figure shows that the fraction of growth is approximately constant for small growth rates. This type of growth is therefore termed constant growth.

When the growth rate increases beyond the constant growth, a parabolic shape can be discerned in the figure. Because of the occurrence of a local maximum associated with the parabolic shape, this type of growth is termed peak growth.

Note that the analysis period is too short to accurately determine the growth rates during peak growth. It is therefore likely that these growth rates will increase, when a smaller analysis period is used. This does however not affect the contribution of the peak growth to the total growth.

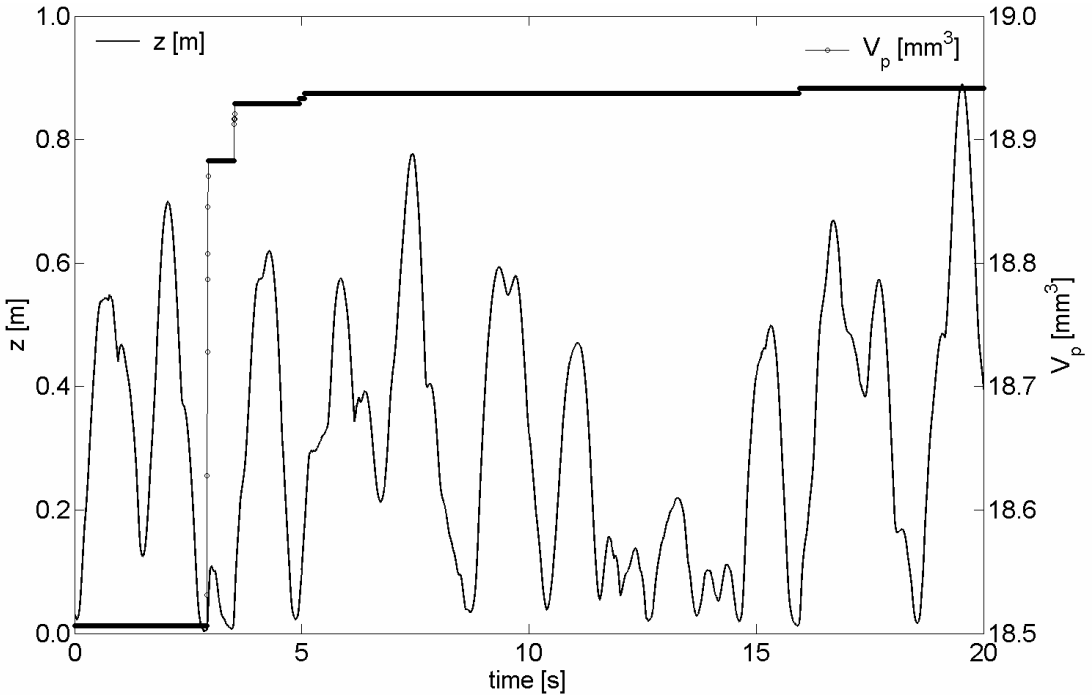

Figure 7.9 Radius and z-position of a particle for case G2.

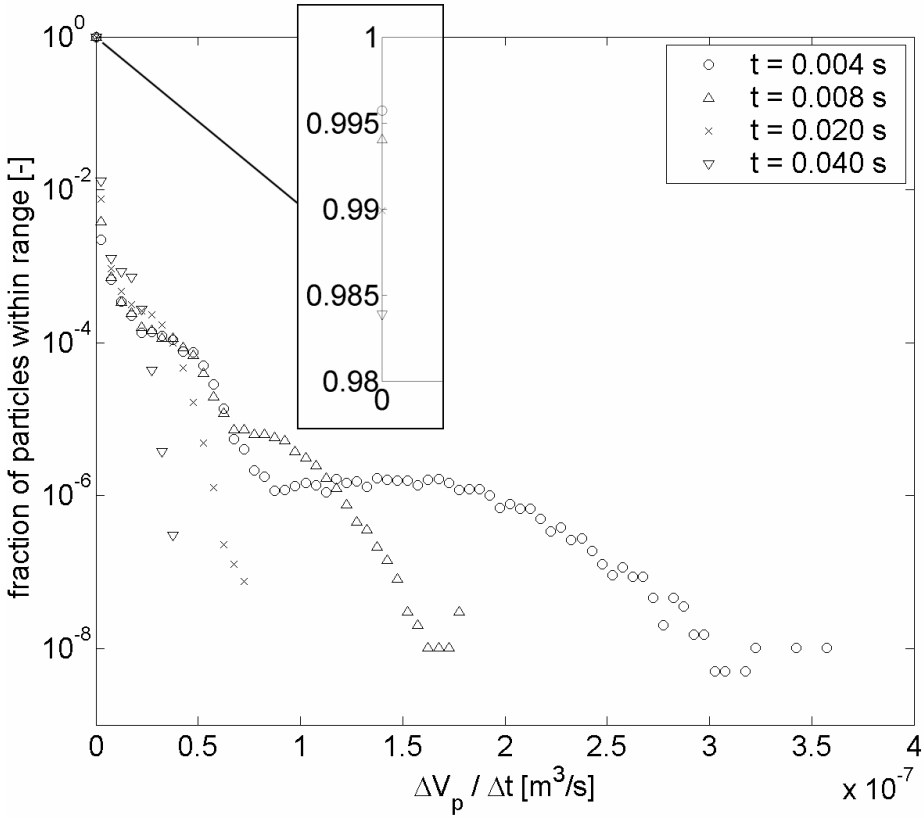

Figure 7.10 The distribution of the average growth rate obtained using different periods of time for case G2.

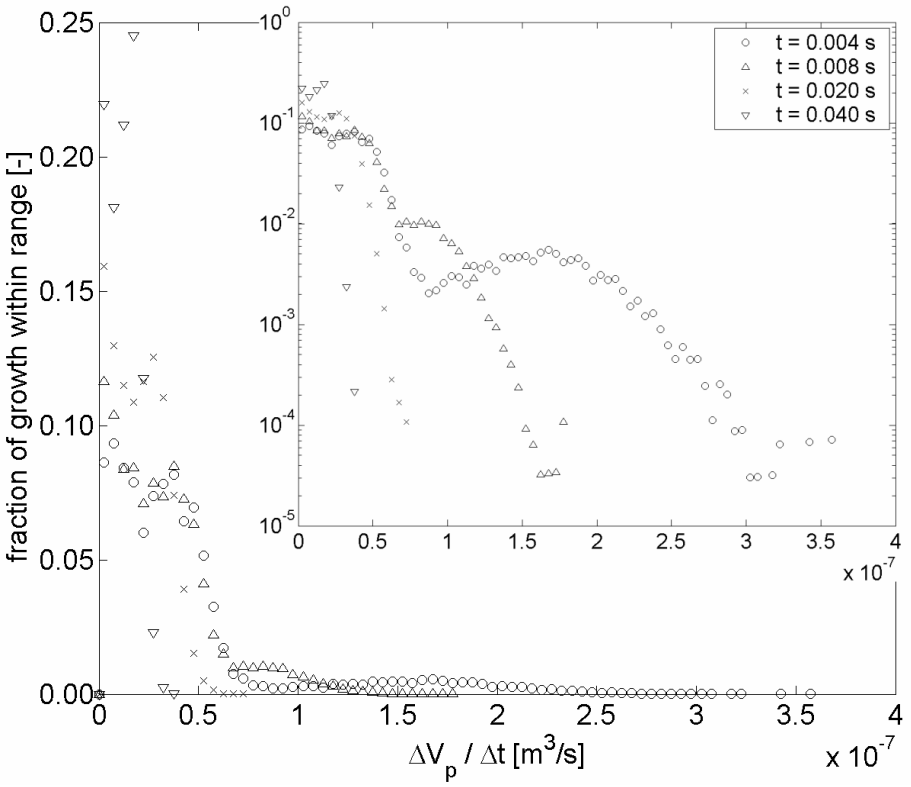

Figure 7.11 Fraction of growth versus growth rate obtained using different periods of time for case G2.

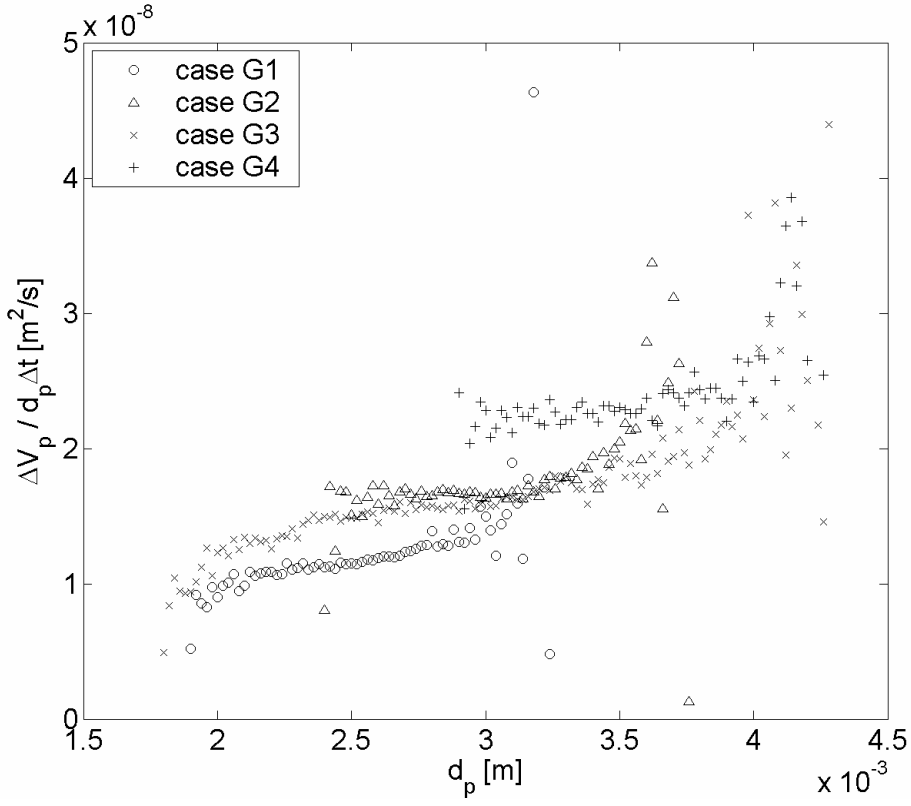

Figure 7.12 Average growth relative to the particle diameter versus particle diameter determined over 0.004 s-periods for all cases.

7.4.4 Influence of particle size

The average particle growth as a function of:

- the particle diameter,
- the projected particle surface, and
- the particle volume

were determined and are respectively shown in Figures 7.12, 7.13 and 7.14. For each of these results, the relative growth rate was determined during 5000 periods of 0.004 s. Consequently, the effect of the growing particle diameter was cancelled out.

When comparing Figures 7.12, 7.13 and 7.14, it appears that the average particle growth is a linear function of the projected particle surface. This means that the growth rate per projected area is a useful parameter to compare the behavior of different particle sizes under different conditions. Note that the scattering observed for each case at low and high particle diameters is caused by the small number of particles within both of these size classes.

7.4.5 Influence of the initial particle size distribution

The influence of particle size within a mixture on the experienced particle growth was assessed by dividing each PSD into three categories:

1. small: $d_p < \mu - \frac{1}{2}\sigma$
2. medium: $\mu - \frac{1}{2}\sigma < d_p < \mu + \frac{1}{2}\sigma$
3. large: $\mu + \frac{1}{2}\sigma < d_p$

The contribution to the total growth of each category was determined and plotted in Figure 7.15 in terms of the growth rate per projected surface area for case G2. The results for the other cases were found to be similar.

Figure 7.15 shows that the three categories display virtually the same trend. The constant growth and the peak growth are observed at the same growth rate per projected surface area, although the distribution between the types of growth differs slightly between the categories. The small particles display a little less constant growth and a little more peak growth.

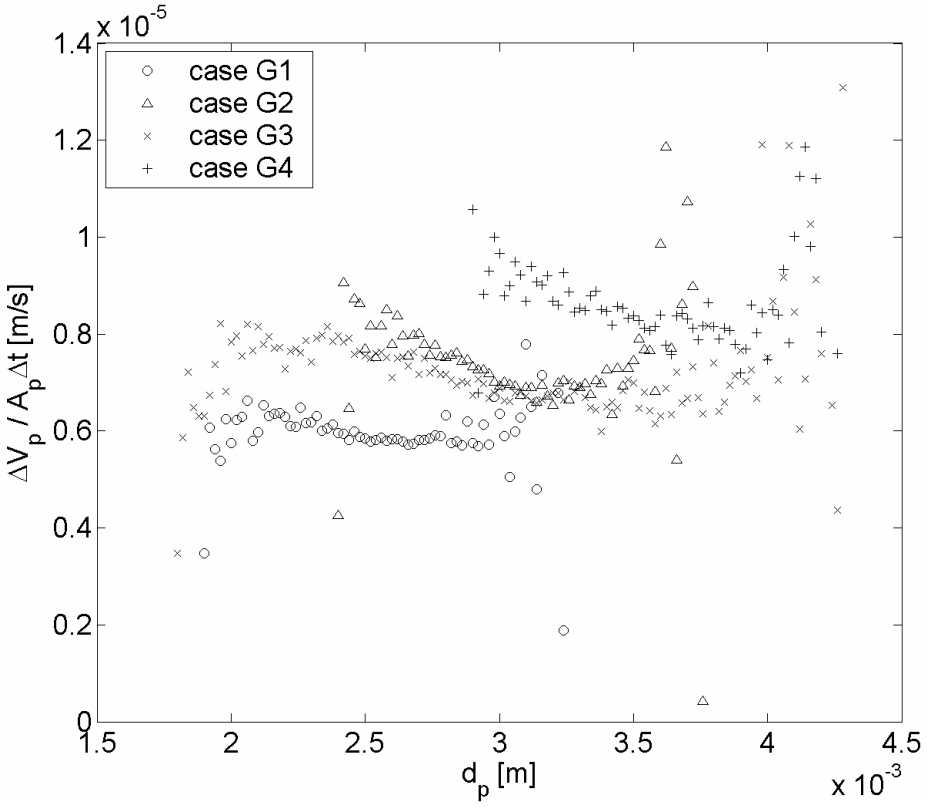

Figure 7.13 Average growth relative to the projected particle surface versus particle diameter determined over 0.004 s-periods for all cases.

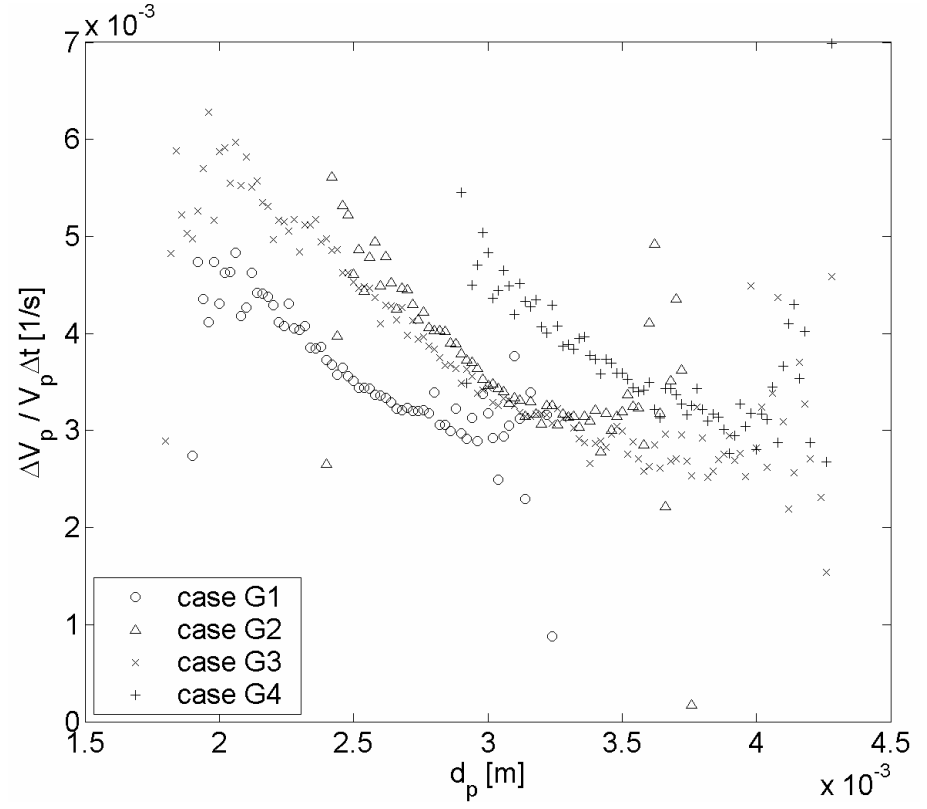

Figure 7.14 Average growth relative to the particle volume determined over 0.004 s-periods for all cases versus the particle diameter.

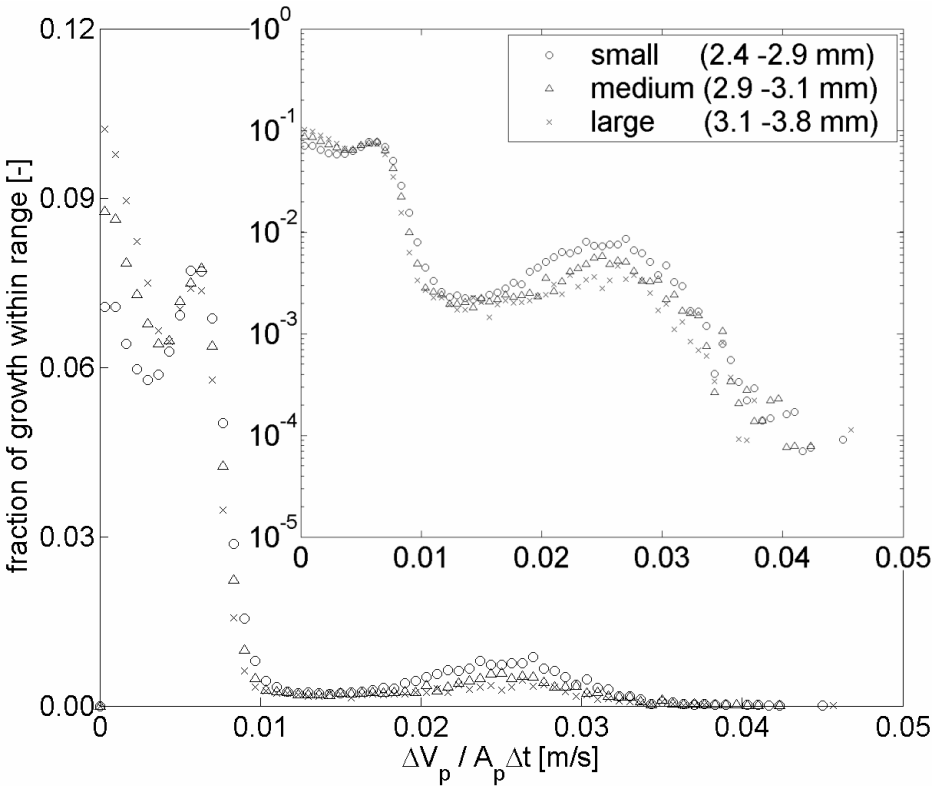

Figure 7.15 Fraction of growth versus growth rate per projected surface for different particle sizes determined over 0.004 s-periods for case G2.

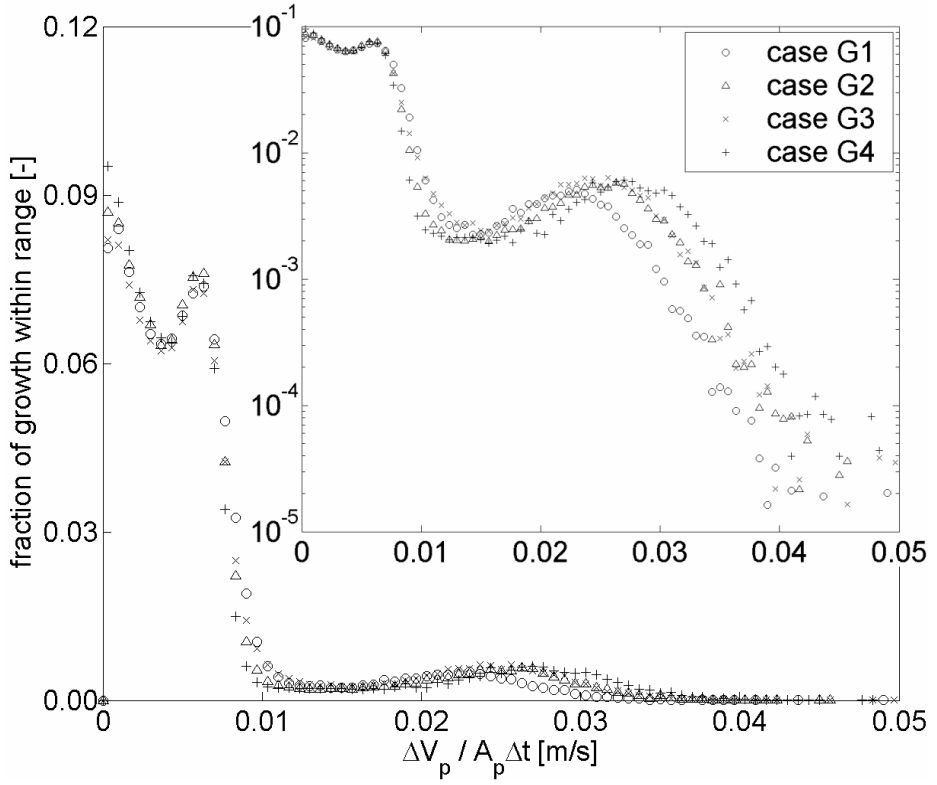

Figure 7.16 Fraction of growth versus growth rate per surface area as a function of the PSD determined over 0.004 s-periods.

In Figure 7.16, the results for the different cases are compared in the same manner. The trends for the cases are similar. For constant growth, the differences between the size categories within each case are larger than the differences between the cases. The growth rates per projected surface area for which peak growth is observed differ more between the cases than within each case, which can also be related to (excessive) length of the analysis period.

7.5 Discussion

Although the particle size distribution after granulation suggests that the growth process is uniform for all particle sizes, the detailed results show that enormous differences exist between the growth rates of the particles. When the nature of these differences is understood, means can be found to improve control over the particle size distribution. The nature of these differences was assessed through a number of parameters in the preceding sections, the results of which will be discussed in this section.

The spatial position of the particles relative to the spout mouth proves to be the dominant factor for growth in a spout-fluid bed granulator. The concentration of droplets and therefore the opportunity for growth is largest close to the spout mouth. This is however not the only important factor in particle growth, since the presence of particles is obviously required as well.

The amount of growth is closely related to the projected surface area of the particle. This can be understood when one considers how a single particle system would grow. In that extreme case droplets will only hit the particle on the projected surface area and since this area is larger for larger particles, particle growth will be larger for these particles. Growth through direct exposure to the droplets will however not occur frequently in a system with many particles, since part of the surface of particles will be blocked by the presence of other particles.

Particle growth is a very short term process, but the growth rates vary significantly and can be extremely high. The highest growth rates are probably due to particles that are largely or completely exposed to the droplet beam. These particles display this type of growth for very small periods. The length of the growing period is limited by the particle residence time in the growth zone, which will generally be very short for these particles, because the particles are accelerated by the momentum of the droplets and the gas that is traveling through this region at high velocity.

The particles displaying lower growth rates will not be accelerated to a large extent and therefore display stable growth during a longer period. Since the growth period at low growth rates is larger than the growth period at high growth rates, the total growth during a given period is much less heterogeneous than the growth rate itself.

Two types of growth behavior have been distinguished: peak growth, which is the high, short-term growth rate that occurs when particles are completely exposed to the droplet beam, and constant growth. The latter occurs at low growth rates, and is termed constant, since the fraction of total growth is approximately the same for all growth rates within its range. Consequently, the number of particles displaying each growth rate is inversely proportional to the growth rate itself.
The contribution of the constant growth to the total growth is much larger than the contribution of the peak growth. This can only be the case when particles are rarely exposed to the droplet beam over their entire surface. The contour plots of the porosity show that the solids concentration in the entire region above the spout mouth, i.e. the spout channel, is indeed rather low. The low concentration is due to the large drag force exerted by the gas phase. Furthermore, particles present in the lower part of the spout channel will block part of the surface of particles higher up in the spout channel.

The particle growth was found to scale with the projected surface area. Smaller particles display slightly more peak growth than larger particles, which is probably due to the larger concentration of small particles near the spout mouth, see Figure 7.17, which shows the concentration, i.e. the local particle fraction of the three types of particles divided by the total particle fraction.

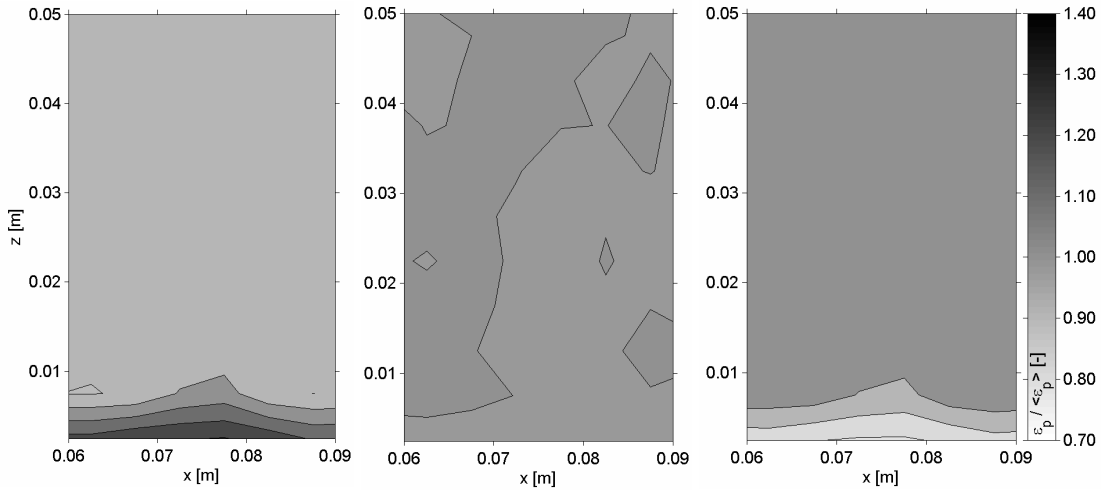

Figure 7.17 Relative concentration for different particle sizes for case G2.

Between the different particle size distributions, the particle growth rate per projected surface area, observed during peak growth, increases slightly with increasing average particle diameter. A larger average particle size results in a larger minimum fluidization velocity. The excess gas velocity and therefore the drag force on the particle will be less. Consequently the residence time near the spout mouth will be larger, causing more particle growth per projected surface area.

7.6 Conclusions

It has been demonstrated that the extended DPM can be used to study granulation processes in detail. Based on the simulations presented in this chapter, the following conclusions are drawn.

It was found that particle growth increases the mean diameter of the particle size distribution, without affecting its standard deviation.

The amount of growth differs significantly for each individual particle and depends strongly on the position of the particle with respect to the spout mouth. Particle growth rapidly decreases with increasing distance from the spout mouth.

It was found that the growth rate scales with the projected surface area of the particle.

Two types of growth have been identified in the simulations, peak growth and constant growth.
Peak growth occurs when particles are exposed to droplets over their entire projected surface area. The growth rate for this type of growth is very large, while the period over which the growth occurs, is very short (< 0.004 s) due to the large amount of momentum that is transferred to the particle. This limits the particle's residence time in the region where growth occurs.
Constant growth occurs when only a small fraction of the particle surface is exposed to the droplets, either because of the location of the droplet beam or because other particles are blocking part of its surface. The growth rate for this type of growth is relatively small, but it can be maintained over a longer period than peak growth.
The analysis period used in this work was sufficiently short to study constant growth, but too long to allow a detailed study of peak growth.
The majority of the growth is caused by constant growth, which is due to the low solids fraction above the spout mouth, which is caused by the large drag forces exerted by the gas phase in this region.

Within a particle size distribution, the smaller particles are slightly more likely to display peak growth, which is due to the larger concentration of these particles near the spout mouth. In the remainder of the bed all particles display similar growth rates per projected surface area.

For the particle size distributions examined in this work, the ones with a larger average particle size display larger peak growth rates per projected surface area due to longer residence times near the spout mouth. This is probably caused by the higher inertia of these particles.

In future work, the extensions to the model should be validated, in particular the particle-droplet and gas-droplet interaction.
Since there are a number of factors influencing the growth rate, the exact manner in which the growth rate depends on these parameters needs to be studied in more detail and for more realistic systems in order to obtain reliable relations for the growth. When the model is successfully validated, it will be a suitable tool to derive such relations.

Bibliography

Adrian, R. J., 1991. Particle-imaging techniques for experimental fluid mechanics, Annual Review of Fluid Mechanics, 23, 261-304.

Agarwal, P.K., Hull, A.S. and Lim, K.S., 1997. Digital image analysis techniques for the study of bubbling fluidized beds, in Chaouki, J., Larachi, F., and Dudukovic, M.P., Non-invasive monitoring of multiphase flows, Elsevier Science B.V., Amsterdam, The Netherlands, 407-454.

Anderson, T.B. and Jackson, R., 1967. A fluid mechanical description of fluidized beds, Industrial and Engineering Chemistry, Fundamentals, 6, 527-539.

Becker, H. A. and Sallans, H. R., 1961. Drying wheat in a spouted bed: On the continuous, moisture diffusion controlled drying of solid particles in a well-mixed, isothermal bed, Chemical Engineering Science, 13-3, 97-112.

Bird, R.B., Stewart, W.E. and Lightfoot, E.N., 1960. Transport phenomena, John Wiley & Sons, New York, pp. 79.

Campbell, C.S. and Brennen, C.E., 1985. Computer simulations of granular shear flows, Journal of Fluid Mechanics, 151, 167-188.

Choi, M. M. S. and Meisen, A., 1997. Sulfur coating of urea in shallow spouted beds, Chemical Engineering Science, 52-7, 1073-1086.

Cundall, P.A. and Strack, O.D.L., 1979. A discrete numerical model for granular assemblies, Géotechnique, 29, 47.

Deen, N.G., Westerweel, J. and Delnoij. E., 2002. Two-phase PIV of bubbly flows: status and trends", Chemical Engineering Technology, 25-1, 97-101.

Ergun S., 1952. Fluid Flow through Packed Columns, Chemical Engineering Progress, 48, 89-94.

Goldschmidt, M.J.V., Link, J.M., Mellema, S. and Kuipers, J.A.M., 2003. Digital Image Analysis Measurements of Bed Expansion and Segregation Dynamics in Dense Gas-Fluidised Beds, Powder Technology, 138-2-3, 135-159.

He, Y-L., Lim, C.J. and Grace, J.R., 1992. Spouted Bed and Spout-Fluid Bed Behaviour in a Column of Diameter 0.91 m, Canadian Journal of Chemical Engineering, 70, 848-857.

He, Y.-L., Lim, C.J., Grace, J.R., Zhu, J.-X. and Qin, S.-Z., 1994. Measurements of voidage profiles in spouted beds, Canadian Journal of Chemical Engineering, 72, 229-234.

Hoomans, B.P.B., Kuipers, J.A.M., Briels, W.J. and van Swaaij, W.P.M., 1996. Discrete Particle Simulation of Bubble and Slug Formation in a Two-Dimensional Gas-Fluidised Bed: A Hard-Sphere Approach, Chemical Engineering Science, 51-1, 99-118.

Hoomans, B.P.B., Kuipers, J.A.M., Mohd Salleh, M.A., Stein, M., and Seville, J.P.K., 2001. Experimental validation of granular dynamics simulations of gas-fluidised beds with homogeneous in-flow conditions using Positron Emission Particle Tracking. Powder Technology, 116, 166-177.

Jono, K., Ichikawa, H., Miyamoto, M. and Fukumori, Y., 2000. A review of particulate design for pharmaceutical powders and their production by spouted bed coating, Powder Technology, 113-3, 269-277.

Kawaguchi, T., Sakamoto, M., Tanaka, T. and Tsuji, Y., 2000. Quasi-Three-Dimensional Numerical Simulation of Spouted Beds in Cylinder, Powder Technology, 109, 3-12.

Keane, R.D. and Adrian, R.J., 1990. Optimization of particle image velocimeters: I. double pulsed systems, Measurement Science and Technology, 1, 1202-1215.

Kharaz, A.H., Gorham, D.A. and Salman, A.D., 1999. Accurate measurement of particle impact parameters, Measurement Science and Technology, 10, 31-35.

Koch, D.L. and Hill, R.J., 2001. Inertial Effects in Suspension and Porous-Media Flows, Annual Reviews of Fluid Mechanics, 33, 619-647.

Kucharski, J. and Kmiec, A., 1989. Kinetics of granulation process during coating of tablets in a spouted bed, Chemical Engineering Science, 44-8, 1627-1636.

Larachi, F., Grandjean, B. P. A. and Chaouki, J., 2003. Mixing and circulation of solids in spouted beds: particle tracking and Monte Carlo emulation of the gross flow pattern, Chemical Engineering Science, 58-8, 1497-1507.

Limtrakul, S., Boonsrirat, A. and Vatanatham, T., 2004. DEM modeling and simulation of a catalytic gas-solid fluidized bed reactor: a spouted bed as a case study, Chemical Engineering Science, 59-22+23, 5225-5231 (ISCRE18).

Link, J.M., Zeilstra, C., Deen, N.G. and Kuipers, J.A.M., 2004. Validation of a discrete particle model in a 2D spout-fluid bed using non-intrusive optical measuring techniques, Canadian Journal of Chemical Engineering, 82, 30-36.

Link, J.M., Cuypers, L.A., Deen, N.G. and Kuipers, J.A.M., 2005. Flow regimes in a spout-fluid bed: a combined experimental and simulation study, Chemical Engineering Science, 60-13, 3425-3442.

Litster, J. and Ennis, B., 2004. The science and engineering of granulation processes, Kluwer Academic Publishers, Dordrecht.

Littman, H., Morgan III, M.H., Narayanan, P.V., Kim, S.J. and Day, J.-Y., 1985. An Axisymmetric Model of Flow in the Annulus of a Spouted Bed of Coarse Particles. Model, Experimental Verification and Residence Time Distribution, Canadian Journal of Chemical Engineering, 63, 188-194.

Liu, L. X. and Litster, J. D., 1993a. Coating mass distribution from a spouted bed seed coater: Experimental and modelling studies, Powder Technology, 74-3, 259-270.

Liu, L. X. and Litster, J. D., 1993b. Spouted bed seed coating: The effect of process variables on maximum coating rate and elutriation, Powder Technology, 74-3, 215-230.

Lu Huilin, He Yurong, Liu Wentie, Jianmin Ding, Dimitri Gidaspow and Jacques Bouillard, 2004. Computer simulations of gas-solid flow in spouted beds using kinetic-frictional stress model of granular flow, Chemical Engineering Science, 59-4, 865-878.

Mathur, K. B. and Epstein, N., 1974. Spouted beds, Academic Press, New York.

Nagarkatti, A. and Chatterjee, Asok, 1974. Pressure and Flow Characteristics of a Gas Phase Spout-Fluid Bed and the Minimum Spout-Fluid Condition, Canadian Journal of Chemical Engineering, 52, 185-195.

Oliveira, W. P. de, Freire, J. T. and Coury, J. R., 1997. Analysis of particle coating by spouted bed process, International Journal of Pharmaceutics, 158-1, 1-9.

Parker, D.J., Broadbent, C.J., Fowles, P. Hawkesworth, M.R and McNeil, P., 1993. Positron Emission Particle Tracking - a technique for studying flow within engineering equipment. Nuclear Instruments and Methods in Physics Research, A326, 592-607.

Parker, D.J. and McNeil, P., 1996. Positron emission tomography for process applications. Measurement Science and Technology, 7, 287-296.

Pavarini, P. J. and Coury, J. R., 1987. Granulation of an insoluble powder in a spouted bed, Powder Technology, 53-2, 97-103.

Pianarosa, D.L., Freitas, L.A.P., Lim, C.J., Grace, J.R. and Dogan, O.M., 2000. Voidage and particle velocity profiles in a spout-fluid bed, Canadian Journal of Chemical Engineering, 78, 132-142.

Rovero, G., Piccinini, N., Grace, J. R., Epstein, N. and Brereton, C. M. H., 1983. Gas phase solid-catalysed chemical reaction in spouted beds, Chemical Engineering Science, 38-4, 557-566.

San José, M. J., Olazar, M., Peñas, F. J., Arandes, J. M. and Bilbao, J., 1995. Correlation for calculation of the gas dispersion coefficient in conical spouted beds, Chemical Engineering Science, 50-13, 2161-2172.

San José, M. J., Olazar, M., Alvarez, S., Izquierdo, M.A. and Bilbao, J., 1998. Solid cross-flow into the spout and particle trajectories in conical spouted beds, Chemical Engineering Science, 53-20, 3561-3570.

Schaaf, J. van der, Schouten, J. C. and Bleek, C. M. van den, 1998. Origin, propagation, and attenuation of pressure waves in gas-solid fluidized beds, Powder Technology, 95, 220-233.

Schiller, L. and Naumann, A., 1933. A drag coefficient correlation, VDI Zeitschrift, 77, 318-320.

Stein, M., Martin, T.W., Seville, J.P.K., McNeil, P.A. and Parker, D.J., 1997. Positron emission particle tracking: particle velocities in gas fluidised beds, mixers and other applications. in Chaouki, J., Larachi, F., and Dudukovic, M.P., Non-invasive monitoring of multiphase flows, Elsevier Science B.V., Amsterdam, The Netherlands, 161-184.

Stein, M., Ding, Y.L., Seville, J.P.K., and Parker, D.J., 2000. Solids motion in bubbling gas fluidised beds. Chemical Engineering Science, 55, 5291-5300.

Sutanto, W., Epstein, N. and Grace, J.R., 1985. Hydrodynamics of Spout-Fluid Beds, Powder Technology, 44, 205-212.

Takeuchi, S., Wang, S. and Rhodes, M., 2004. Discrete element simulation of a flat-bottomed spouted bed in the 3-D cylindrical coordinate system, Chemical Engineering Science, 59-17, 3495-3504.

Tsuji, Y., Kawaguchi, T. and Tanaka, T., 1993. Discrete particle simulation of two-dimensional fluidized bed, Powder Technology, 77, 79-87.

Vukovic, D.V., Hadzismajlovic, Dz.E., Grbavcic, Z.B., Garic, R.V. and Littman, H., 1984. Flow Regimes for Spout-Fluid Beds, Canadian Journal of Chemical Engineering, 62, 825-829.

Wen, Y.C. and Yu, Y.H., 1966. Mechanics of Fluidization, Chemical Engineering Progress Symposium Series, 62, 100-111.

Westerweel, J., 1993. Digital Particle Image Velocimetry - Theory and Application, University Press (Delft), PhD-thesis.

Westerweel, J., 1994. Efficient detection of spurious vectors in Particle Image Velocimetry Data, Experiments in Fluids, 16, 236 - 247.

Westerweel, J., 1997. Fundamentals of Digital Particle Image Velocimetry, Measurement Science and Technology, 8, 1379-1392.

Westerweel, J., Dabiri, D. and Gharib, M., 1997. The effect of a discrete window offset on the accuracy of cross-correlation analysis of digital PIV recordings, Experiments in Fluids, 23, 20-28.

Willert, C. E. and Gharib, M., 1991. Digital Particle Image Velocimetry, Experiments in Fluids, 10, 181-193.

Xu, J., Bao, X., Wei, W., Shi, G., Shen, S., Bi, H. T., Grace, J. R. and Lim, C. J., 2004. Statistical and frequency analysis of pressure fluctuations in spouted beds, Powder Technology, 140-1+2, 141-154.

Ye, M., 2005. Multil-level modeling of dense gas-solid two-phase flows, Ph.D. Thesis, University of Twente, Enschede, The Netherlands, 28-29.

Zhao, J., Lim, C. J., and Grace, J. R., 1987. Flow regimes and combustion behaviour in coal-burning spouted and spout-fluid beds, Chemical Engineering Science, 42-12, 2865-2875.

Zhang, J-Y and Tang, F., 2004. Classification and determination of flow regimes in spout-fluidized beds, Proceedings of the 11th int. conf. on fluidization, 491-498.

Zhu, H. P. and Yu, A. B., 2002. Averaging method of granular materials, Physical Review E, 66-021302, 1-10

Nomenclature

a	ratio between cube diameter and particle diameter, -
c	correction factor for the intensity of a pixel, -
C_D	drag coefficient, -
d	diameter, *m*
D	distribution function, -
D	depth of the bed, *m*
D_I	size of an interrogation area, -
e_n	coefficient of normal restitution, -
F_I	fraction of particles remaining in the interrogation area, - (despite in-plane displacement)
F_O	fraction of particles remaining in the interrogation area, - (despite out-of-plane displacement)
$\mathbf{F}_{ab}$	contact force, *N*
f	volume fraction, -
f_{sample}	sampling rate, $1/s$
freq( )	frequency in the frequency spectrum
$\mathbf{f}(t)$	input function for the Fourier transform
F( )	Fourier transform
g	gravitational acceleration, m/s^2
$\mathbf{g}$	gravitational acceleration, m/s^2
h	height, *m*
$\mathbf{H}$	rotation matrix, -
i	horizontal position on a grid, -

I	intensity of a pixel, -
I	moment of inertia, $N\,m$
I( )	imaginary part of the Fourier transform
$\mathbf{I}$	unit matrix, -
j	vertical position on a grid, -
j	discrete input signal indicator, -
J	impulse, $kg\,m/s$
$\mathbf{J}_{ab}$	impulse vector, $kg\,m/s$
k	discrete frequency indicator, -
k	spring stiffness, N/m
m_{ab}	effective mass, kg
m_p	particle mass, kg
M	total number of pixels in the vertical direction, -
M	image magnification, $1/m$
n	computational time step, -
$\mathbf{n}_{ab}$	normal unit vector, -
N	total number of pixels in the horizontal direction, -
N	number of frequencies in the frequency spectrum, -
N	number specified by subscript, -
N_I	initial number of particles in an interrogation area, -
p	pressure, Pa
P	probability, -
P( )	power of the frequency spectrum
$\mathbf{r}$	position, m
r	radius, m
R	correlation, -
R( )	real part of the Fourier transform

Re_p $= \dfrac{\varepsilon_f \rho_f \left|\mathbf{u}_f - \mathbf{v}_p\right| d_p}{\mu_f}$,particle Reynolds number, -

s spatially-averaged displacement in pixels, -

$\mathbf{s}$ spatially-averaged displacement in pixels, -

$\mathbf{s}_D$ particle image displacement in pixels, -

$\mathbf{S}_p$ particle drag sink term, N/m^3

$\mathbf{t}_{ab}$ tangential unit vector, -

t time, s

$\mathbf{T}$ torque, $N\,m$

u frequency variable, $1/s$

u fluid velocity, m/s

$\mathbf{u}_f$ fluid velocity, m/s

v speed, m/s

v_∞ terminal velocity, m/s

$\mathbf{v}$ particle velocity, m/s

$\mathbf{v}_{ab}$ relative velocity at the contact point, m/s

V volume, m^3

W width of the bed, m

x horizontal position, m

$\mathbf{x}$ position on the interrogation area grid, -

z vertical position, m

Greek Symbols

β inter-phase momentum transfer coefficient, $kg/m^3 s$

β_0 coefficient of tangential restitution, -

δ displacement, m

ε volume fraction, -

ϕ	general variable
η	damping coefficient, $N\,s/m$
λ_f	gas phase bulk viscosity, $kg/m\,s$
μ_f	gas phase shear viscosity, $kg/m\,s$
μ	dynamic friction coefficient, -
ρ	density, kg/m^3
$\boldsymbol{\tau}_f$	gas phase stress tensor, *Pa*
$\boldsymbol{\Phi}$	flux, $kg/m^2 s$
$\boldsymbol{\omega}$	angular velocity, $1/s$

Subscripts and superscripts

0	initial condition
1	first image
2	second image
2D	two-dimensional
3D	three-dimensional
a,b	particle indices
bg	background
C	mean intensity
cell	computational grid cell
D	intensity fluctuations
end	end of simulation
f	fluid phase
flow	flowsolver
F	mean with the fluctuating intensity
FOV	field of view
max	maximum
mf	minimum fluidization

move	remaining movement
n	normal direction
n	computational time step
p	particle
part	particles
s	solid phase
shift	correction by window shifting
sp	spout
t	tangential direction
T	threshold
walls	system walls
X	interrogation areas in the horizontal direction
z	in the vertical direction
Z	interrogation areas in the vertical direction

Mathematical symbols

–	spatial average
‹ ›	temporal average
`	after correction
`	root mean square
∞	infinity
d	step
e, e	natural logarithmic base
f	an unspecified function
i	$\sqrt{-1}$
δ	small difference
δ	delta function
Δ	difference

μ	mean
θ	unspecified number
σ	standard deviation

Abbreviations

2D	two-dimensional
3D	three-dimensional
CCD	charge-coupled device
CMOS	complementary metal-oxide-semiconductor
DPM	discrete particle model
FOV	field of view
FFT	fast Fourier transfer
MFM	multi-fluid model
NL	The Netherlands
PEPT	positron emission particle tracking
PIV	particle image velocimetry
PSD	particle size distribution
RMS	root mean square
SAPDF	spectral analysis of pressure drop fluctuations
TFM	two-fluid model
UK	United Kingdom

List of publications

Goldschmidt, M.J.V., Link, J.M., Mellema, S. and Kuipers, J.A.M., 2003. Digital image analysis of bed expansion in dense gas-fluidised beds, Powder Technology, 138, 135-159.

Link, J.M., Zeilstra, C., Deen, N.G. and Kuipers, J.A.M., 2004. Validation of a discrete particle model in a 2D spout-fluid bed using non-intrusive optical measuring techniques, Canadian Journal of Chemical Engineering, 82(1) 30-36.

Link, J.M., Deen, N.G. and Kuipers, J.A.M., 2004. Comparison of PIV measurements and a discrete particle model in a rectangular 3D spout-fluid bed, Proceedings of Fluidization XI, May 9-14, 2004, Naples, Italy, 539-546.

Link, J.M., Deen, N.G., and Kuipers, J.A.M., 2004. Discrete Particle Simulation of a Spout-Fluid Bed: Treatment of two-way Coupling and Effect of Drag Closure, Proceedings 5th International Conference on Multiphase Flow, ICMF'04, Yokohama, Japan, May 30-June 4, 2004, Paper No. 457.

Link, J.M., Cuypers, L.A., Deen, N.G. and Kuipers, J.A.M., 2005. Flow regimes in a spout-fluid bed: a combined experimental and simulation study, Chemical Engineering Science, 60(13), 3425-3442.

Link, J.M., Fan, X., Wood, J., Deen, N.G., Ingram, A., Parker, D.J. and Kuipers, J.A.M., 2005. Comparison of PEPT measurements and discrete particle simulations in a rectangular 3D spout-fluid bed, Proceedings 7th World Congress of Chemical Engineering, 10-14 July 2005, Glasgow, Scotland.

Link, J.M., Godlieb, W., Tripp, P., Deen, N.G., Heinrich, S., Peglow, M., Kumar, J., Kuipers, J.A.M., Schönherr, M. and Mörl, L., 2006. Comparison of fibre optical measurements and discrete element simulations for the study of granulation in a spout fluidized bed, Proceedings 5th World Congress on Particle Technology, 24-27 April 2006, Orlando, Florida, USA.

Link, J.M., Godlieb, W., Deen, N.G. and Kuipers, J.A.M., 2006. Discrete element study of granulation in a spout fluidized bed, accepted for publication in Chemical Engineering Science.

Levensloop

Jeroen Link werd op 11 november 1975 in Zevenaar geboren, alwaar hij de lagere school heeft doorlopen. In 1994 heeft hij aan het Liemers College te Zevenaar zijn VWO diploma behaald.

In september 1994 begon hij met de opleiding Chemische Technologie aan de Universiteit Twente in Enschede. In het kader van deze opleiding liep hij van februari tot en met april 1999 stage bij DSM in Geleen. In juni 2000 studeerde hij af bij de werkeenheid Fundamentele Aspecten van de Proceskunde (FAP) op de ontwikkeling van een methode voor het meten van segregatie in gefluïdiseerde bedden.

In oktober 2000 trad hij in dienst bij de werkeenheid FAP om als assistent in opleiding een promotieonderzoek te verrichten op het gebied van granulatie in “spout”-fluïde bedden. De resultaten van dit onderzoek staan beschreven in dit proefschrift.

Op 1 april 2005 is hij als onderzoeker in dienst getreden bij de onderzoeksafdeling ijzermaken van Corus.

Dankwoord

Na iets meer tijd dan oorspronkelijk de bedoeling was, is het dan toch gelukt om mijn proefschrift af te ronden. Gelukkig is de extra bestede tijd niet voor niks geweest en zijn de krenten, de PEPT metingen in Engeland en de implementatie van granulatie in het DPM, toch nog in de spreekwoordelijke pap terechtgekomen.
Ondanks dat er op een proefschrift maar één naam staat, ben ik natuurlijk niet de enige, die daar een bijdrage aan heeft geleverd. Ik wil daarom, middels dit dankwoord, mijn dank betuigen aan alle mensen, die daaraan hun steentje hebben bijgedragen.

In de eerste plaats wil ik mijn promotor, Hans Kuipers, van de vakgroep fundamentele aspecten van de proceskunde bedanken, omdat hij mij in de gelegenheid heeft gesteld om binnen zijn groep een promotieonderzoek uit te voeren. In het begin van het onderzoek heeft hij de dagelijkse begeleiding op zich genomen, waardoor ik goed uit de startblokken kon komen. In het vervolg van het onderzoek kon ik altijd gebruik maken van zijn indrukwekkende en brede kennis van het vakgebied. Het is dan ook vooral dankzij zijn hulp en die van zijn opvolger als dagelijks begeleider, Niels Deen, dat ik het onderzoek met veel plezier heb kunnen doen en er veel van heb geleerd. Met Niels heb ik verreweg de meeste discussies gevoerd over het onderwerp. Dankzij deze discussies en zijn waardevolle suggesties heeft hij een enorme bijdrage geleverd aan de kwaliteit en structuur van het proefschrift. Ook wist hij mij tijdens het afronden van het proefschrift ook op afstand goed gemotiveerd te houden. De andere UD's, Martin en Martin, hebben ook een niet te onderschatten bijdrage geleverd, met name op het gebied van de "drag" (van der Hoef) en het "grid" (van Sint Annaland).

Verder gaat mijn dank uit naar Per Brynildsen, Rob Stevens, Luc Vanmarcke, Roeland Elderson en André Kayaert van (de onderzoeksafdeling van) kunstmestproducent Yara gevestigd te Sluiskil voor de ondersteuning van het onderzoek. Door hun deelname in het project bleef ik me, ondanks de fundamentele aard van het onderzoek, toch altijd bewust van de praktische toepassing. Daarnaast hebben zij de ureumkorrels in diverse maten en kleuren geleverd, die nodig waren voor de experimenten. Ook wil ik Senter Novem bedanken voor de financiële ondersteuning.

Daarnaast wil ik mijn afstudeerders bedanken. Christiaan Zeilstra heeft in de beginfase van het onderzoek meegeholpen om de ontwikkeling van het model in gang te zetten en daarnaast heeft hij door middel van de metingen in de pseudo-2D opstelling een begin gemaakt met het experimentele werk. Wil Paping heeft vervolgens de drukmetingen in de 3D opstelling voorbereid in het kader van het practicum proceskunde. Deze metingen zijn uitgevoerd en geanalyseerd door Leon Cuypers. Emiel ten Velde heeft het meetprogramma in de pseudo-2D opstelling afgerond en Willem Godlieb is er net voor het einde van het promotieonderzoek nog in geslaagd om granulatie in het discrete deeltjes model te implementeren.

Vervolgens wil ik de vakgroeptechnici bedanken. Wim Leppink heeft de 3D opstelling gebouwd en daarmee een belangrijk gedeelte van het onderzoek mogelijk gemaakt. Hij heeft daarbij zelfs zijn rug (gelukkig tijdelijk) opgeofferd voor de wetenschap. Robert Meijer was verantwoordelijk voor de aansturing van de 3D opstelling en heeft daarnaast geassisteerd bij de experimenten, die uitgevoerd zijn in Birmingham (Engeland). Omdat ik toen nog geen rijbewijs had, mocht hij met een Nederlands busje vol met zeer verdachte balletjes aan de verkeerde kant van de weg rijden. Gelukkig werden we pas gecontroleerd toen het busje Engeland verliet. Gerrit Schorfhaar en Wim Leppink hebben ervoor gezorgd dat de metingen in de pseudo-2D opstelling succesvol verliepen. Bij de overige technici, Robert Brouwer, Benno Knaken en Henk Jan Moed, kon ik altijd terecht voor hulp en adviezen.
Verder wil ik de secretaresses, Nicole Haitjema en Ria Hofs-Winkelman, nog bedanken voor hun administratieve werk, hun persoonlijke interesse en de soepele manier, waarop allerlei zaken geregeld werden.
I would also like to thank Dadan Darmana, Christiaan Zeilstra and Robert Meijer for keeping the computer cluster online (at least for most of the time).

Bob Hoomans wil ik bedanken voor zijn pionierswerk in de ontwikkeling van het harde bollen DPM, Albert Bokkers voor de ontwikkeling van de volledig driedimensionale versie van het DPM en Christiaan Zeilstra en Mao Ye voor de implementatie van het zachte bollen DPM.
I would like to thank Professor Jonathan Seville of the University of Birmingham (UK) for offering me the opportunity to conduct PEPT measurements at his facility. The arrangement, preparation and assistance of Dr. Parker, Dr. Wood, Dr. Fan and Dr. Ingram with the experiments is greatly appreciated.
Professor Jerry Westerweel wil ik bedanken voor het beschikbaar stellen van zijn PIV software.

Verder heb ik ook een erg leuke tijd gehad met mijn collega's op het Vlugterlab. Om te beginnen wil ik mijn kamergenoot in de skybox van de vakgroep, Albert Bokkers, bedanken. Het was erg gezellig op de kamer, mede door de vele discussies en gesprekken met als favoriete onderwerpen gefluïdiseerde ballen en volleyballen. Ook de overige collega's wil ik van harte bedanken voor de discussies tijdens de koffiepauzes, het klaverjassen tijdens de lunchpauzes en de vele, gezellige en meestal nogal lange borrels.

Er was ook de nodige sportieve ontspanning: bij studentenvolleybalvereniging Harambee, waar ik onder andere met Haramgay, HarambInc en Brievolutions zowel binnen als buiten het veld een mooie tijd heb gehad, en bij de vakgroep met het volleyballen tijdens de lunchpauzes (voetballen kon ook, maar dat heb ik om onduidelijke redenen maar één keer mogen doen) en het zeilweekend. Verder werd er jaarlijks een skivakantie en het pan-/Waarbeekfeest georganiseerd door Liesbeth Kuipers, waarvoor ik haar van harte wil bedanken.
Ook wil ik mijn (oud-)huisgenoten, (oud-)commissiegenoten, overige vrienden en familie bedanken voor de leuke tijd.

En "last but not least" wil ik mijn ouders, mijn zusje Angèl en haar vriend Peter bedanken voor hun steun en interesse tijdens mijn promotie. Ondanks de voor mijn vader enigszins teleurstellende ontdekking dat chemische technologie weinig met chemie te maken had, hebben ze toch geprobeerd te begrijpen, waar ik mee bezig was. Gezien de vragen, die ze stelden toen ik ze (op hun eigen verzoek) mijn eindpresentatie liet zien, is dat nog redelijk gelukt ook.

Iedereen nogmaals van harte bedankt!

Jeroen